MARJAN MONSHI

GRAPHENE-METAL HYBRID PLASMONIC STRUCTURES: SYNTHESIS, MULTI-SPECTROSCOPIC CHARACTERIZATION, AND STABLE ANALYTE DETECTION

DOCTORAL DISSERTATION

Kaunas
2026

KAUNAS UNIVERSITY OF TECHNOLOGY

MARJAN MONSHI

GRAPHENE-METAL HYBRID PLASMONIC STRUCTURES: SYNTHESIS, MULTI-SPECTROSCOPIC CHARACTERIZATION, AND STABLE ANALYTE DETECTION

Doctoral dissertation
Natural Sciences, Physics (N 002)

2026, Kaunas

The dissertation has been prepared at the Institute of Materials Science of Kaunas University of Technology in 2020–2025.

The doctoral right has been granted to Kaunas University of Technology together with University of Southern Denmark.

Research supervisor:
Prof. Dr. Hab. Sigitas TAMULEVIČIUS (Kaunas University of Technology, Natural Sciences, Physics, N 002).

Edited by: English language editor Brigita Brasienė (Publishing House *Technologija*), Lithuanian language editor Aurelija Gražina Rukšaitė (Publishing House *Technologija*).

Dissertation Defence Board of Physics Science Field:
Prof. Dr. Diana ADLIENĖ (Kaunas University of Technology, Natural Sciences, Physics, N 002) – **chairperson**;
Prof. Dr. Hab. Arvaidas GALDIKAS (Kaunas University of Technology, Natural Sciences, Physics, N 002);
Prof. Dr. Liutauras MARCINAUSKAS (Kaunas University of Technology, Natural Sciences, Physics, N 002);
Assoc. Prof. Dr. Lina MIKOLIŪNAITĖ (Vilnius University, Natural Sciences, Chemistry, N 003);
Prof. Dr. Horst-Gunter RUBAHN (University of Southern Denmark, Denmark, Natural Sciences, Physics, N 002).

The dissertation defence will be held on 29 May 2026, at 10 a. m. at the Rectorate Hall of Kaunas University of Technology in the meeting of the Dissertation Defence Board of the Physics Science Field.

Address: K. Donelaičio 73-402, LT-44249 Kaunas, Lithuania.
Phone: +370 608 28 527; email doktorantura@ktu.lt.

The dissertation was sent out on 29 April 2026.
The dissertation is available on the website http://ktu.edu, at the library of Kaunas University of Technology (Gedimino 50, Kaunas) and the Library of the University of Southern Denmark (Campusvej 55, Odense).

KAUNO TECHNOLOGIJOS UNIVERSITETAS

MARJAN MONSHI

GRAFENO-METALO HIBRIDINĖS PLAZMONINĖS STRUKTŪROS: SINTEZĖ, MULTISPEKTROSKOPINIS VERTINIMAS, IR STABILUS ANALITĖS APTIKIMAS

Daktaro disertacija
Gamtos mokslai, fizika (N 002)

Kaunas, 2026

Disertacija rengta 2020–2025 metais Kauno technologijos universiteto Medžiagų mokslo institute.

Doktorantūros teisė Kauno technologijos universitetui suteikta kartu su Pietų Danijos universitetu.

Mokslinis vadovas:
prof. habil. dr. Sigitas TAMULEVIČIUS (Kauno technologijos universitetas, gamtos mokslai, fizika, N 002).

Redagavo: anglų kalbos redaktorė Brigita Brasienė (leidykla „Technologija“), lietuvių kalbos redaktorė Aurelija Gražina Rukšaitė (leidykla „Technologija“).

Fizikos mokslo krypties disertacijos gynimo taryba:
prof. dr. Diana ADLIENĖ (Kauno technologijos universitetas, gamtos mokslai, fizika, N 002) – **pirmininkė**;
prof. habil. dr. Arvaidas GALDIKAS (Kauno technologijos universitetas, gamtos mokslai, fizika, N 002);
prof. dr. Liutauras MARCINAUSKAS (Kauno technologijos universitetas, gamtos mokslai, fizika, N 002);
doc. dr. Lina MIKOLIŪNAITĖ (Vilniaus universitetas, gamtos mokslai, chemija, N 003);
prof. dr. Horst-Gunter RUBAHN (Pietų Danijos universitetas, Danija, gamtos mokslai, fizika, N 002).

Disertacija bus ginama viešame Fizikos mokslo krypties disertacijos gynimo tarybos posėdyje 2026 m. gegužės 29 d. 10 val. Kauno technologijos universiteto Rektorato salėje.

Adresas: K. Donelaičio g. 73-402, LT-44249 Kaunas, Lietuva.
Tel: +370 608 28 527; el. paštas doktorantura@ktu.lt.

Disertacija išsiųsta 2026 m. balandžio 29 d.
Su disertacija galima susipažinti interneto svetainėje http://ktu.edu, Kauno technologijos universiteto bibliotekoje (Gedimino g. 50, Kaunas) ir Pietų Danijos universiteto bibliotekoje (Campusvej 55, Odense).

TABLE OF CONTENTS

LIST OF TABLES **7**
LIST OF FIGURES **8**
LIST OF ABBREVIATIONS AND TERMS **12**
INTRODUCTION **14**
1. LITERATURE REVIEW **19**
  1.1. Fundamentals of Graphene and Graphene-Based Allotropes 19
  1.2. Graphene Synthesis Routes and Advanced Techniques 22
    1.2.1. Growth Mechanisms of Graphene on Catalyst Surface via PECVD 24
  1.3. Characterization of Carbon-Based Materials 28
    1.3.1. Raman Scattering Spectroscopy of Graphene-Based Materials 30
  1.4. SERS Platforms: Enhancement Principles and Challenges 32
    1.4.1. Graphene-Metal Hybrid SERS Platforms 36
2. MATERIALS AND METHODS **39**
  2.1. Preparation of Catalytic Substrates for Graphene Growth 39
    2.1.1. Nickel Foil (Case Study I) 39
    2.1.2. Silicon Dioxide (Case Study II) 39
    2.1.3. Copper Foil (Case Study III) 40
  2.2. Graphene Growth Process and Protocols 40
  2.3. Fabrication of Graphene Hybrid Ag-SERS Platforms (Case Study III) 41
    2.3.1. Synthesis and Assembly of Silver Nanocubes 41
    2.3.2. Graphene Dry Transfer from Copper 42
  2.4. Characterization Techniques 42
    2.4.1. Scanning Electron Microscopy/Energy Dispersive Spectroscopy 42
    2.4.2. X-ray Diffraction 43
    2.4.3. Spectroscopic Ellipsometry 44
    2.4.4. Atomic Force Microscopy 44
    2.4.5. X-Ray Photoelectron Spectroscopy 46
    2.4.6. Raman Scattering Spectroscopy 46
    2.4.7. UV-Vis-nIR Spectroscopy 48
    2.4.8. Transient Absorption Spectroscopy 49
  2.5. Statistical Analysis 49
3. RESULTS AND DISCUSSION **51**
  3.1. Case Study I: Preliminary Investigation of Nickel as Catalyst in PECVD 51
    3.1.1. Study Design and Parametric Optimization 51
    3.1.2. Surface Analysis 51
    3.1.3. Raman Analysis (Standard 4-band) 56
    3.1.4. Transition to Dielectric Substrates 59
  3.2. Case Study II: Nickel-Encapsulated Graphitic Shells for UV-SERS 61

3.2.1. Study Design: Full Factorial Matrix 61
3.2.2. Surface Analysis 62
3.2.3. Correlation Study 68
3.2.4. Spectroscopy Analysis 71
3.2.5. Dimensionality Reduction and Identification of Key Metrics 84
3.2.6. Feasibility Study of UV-SERS Measurement 86
3.3. Case Study III: Signal Stability of Graphene-Overlayered Resonant Silver Arrays 87
3.3.1. Study Design: Comparative Longitudinal Stability 88
3.3.2. Surface and UV-Vis Analysis 88
3.3.3. Analyte Raman Signal Measurement 91
3.3.4. Quantitative Analysis of Signal Retention 93
CONCLUSIONS 97
SANTRAUKA 99
LIST OF REFERENCES 111
CURRICULUM VITAE AND DESCRIPTION OF CREATIVE ACTIVITIES 134
LIST OF SCIENTIFIC PAPERS AND SCIENTIFIC CONFERENCES 136
ACKNOWLEDGEMENT 138
APPENDICES 140

LIST OF TABLES

Table 1. Graphene growth protocol for three distinct case studies 41
Table 2. Abbreviated notations used in the spectroscopic metrics of this study: examples for the 2D band 48
Table 3. Parametric optimization of PECVD growth on polycrystalline Ni foil 51
Table 4. Quantitative metrics derived from the spectral fitting of the average Raman profiles for each sample series 58
Table 5. Significant correlations identified between the input factors and spectroscopic metrics, as well as inter-metric correlations 70
Table 6. Identified Raman bands, specified the center of peaks, their fitted functions, and their related reference 73
Table 7. Fitting results for the graphene reference sample obtained using the 7-band fitting model 90
Table 8. Normalized intensities and calculated enhancement factors for characteristic Raman peaks of 2NT; peak I (766 cm^{-1}), located outside the SLR range, serves as the normalization reference 93

LIST OF FIGURES

Figure 1. (a) Atomic structure of a carbon atom, (b) energy levels of outer electrons in carbon atoms, (c) the formation of sp^2 hybrids, (d) the crystal lattice of graphene where A and B are carbon atoms belonging to different sub-lattices, a_1 and a_2 are unit-cell vectors, (e) sigma bond and pi bond formed by sp^2 hybridization [19]................... 19
Figure 2. (a) Single layer graphene structure, A and B denote carbon sites, (b) bilayer graphene stacking types, (c) three-layer graphene stacking types, (d) π bond and sigma bond positions in the graphene honeycomb lattice [20] 20
Figure 3. Different hybridizations for carbon materials; the vertices of the triangle represent the pure forms: diamond (sp^3), graphene (sp^2), and carbyne (sp) [33]...... 21
Figure 4. Schematic overview of graphene synthesis routes and classification of CVD techniques[39] 22
Figure 5. Schematic of the microwave plasma-enhanced CVD reactor [47] 23
Figure 6. Scheme for growing graphene on a catalytic substrate (copper in this case): red hexagons are the active sites of the Cu surface, and blue spots signify active carbon species [63] 24
Figure 7. Schematic diagram of graphene growth on a) copper and b) nickel substrates in the thermal CVD process [64] 25
Figure 8. Schematic diagrams for ambient pressure CVD graphene on (a) and (b) Ni(111) and (c) and (d) polycrystalline Ni films at (900–1,000 ºC) [79] 26
Figure 9. The optical image of the polycrystalline nickel surface after an annealing time of (a) 1 min, (b) 15 min, and (c) 40 min [86] 27
Figure 10. Gas mixing ratios of graphene films synthesized at 750 °C adopted from[88] 28
Figure 11. Schematic of the overall function of Raman spectroscopy from the laser source to the final spectrum on the computer [96] 29
Figure 12. Diagram illustrating Raman scatterings and Rayleigh scatterings [95] .. 29
Figure 13. (a) The three-stage model of carbon amorphization showing the evolution of the Raman I(D:G) ratio and G peak position with increasing disorder, (b) compiled empirical data of the I(D:G) ratio versus crystallite size (La), and (c) Raman spectrum of single-layer Graphene [105, 106] 30
Figure 14. The transformation from molecular to crystalline of non-graphitic carbons with their Raman line shape analysis of G and D mode [108] 32
Figure 15. Illustrated various enhancement mechanisms of SERS: (a) normal Raman scattering, (b) electromagnetic mechanism, (c) static chemical mechanism, (d) charge-transfer mechanism, and (e) resonance Raman mechanism [122] 34
Figure 16. Reactor schematic of the PECVD device [194] 40
Figure 17. PVA-mediated dry transfer process: a) lamination of the copper foil with graphene onto the PVA layer, b) laminated structure consisting of PVA and copper foil with graphene, c) detachment of copper foil from the PVA sheet 42
Figure 18. Illustration of the AFM blind tip deconvolution workflow: (a) the raw topographic AFM micrograph exhibiting tip-dilation artifacts, (b) the estimated geometry of the AFM probe tip, and (c) the final deconvoluted surface topography45
Figure 19. X-ray diffraction pattern of the homemade polycrystalline nickel foil... 52

Figure 20. The optical microscopy images of the polycrystalline nickel foil after carbon deposition: (a) foil directly on the cooling stage with 1 min grow duration and (b) foil on a custom metal holder in the PECVD chamber at a hydrogen-rich regime with 10 min grow duration 53
Figure 21. Optical images of nickel foil after the PECVD process in different regimes: (a) hydrogen-rich regime with a growth duration of 10 minutes and (b) carbon-rich regime with a growth duration of 10 minutes 53
Figure 22. Optical micrographs of foil surfaces after graphene growth through PECVD, using a high carbon flow and a growth duration of 10 minutes on: (a) untreated, (b) thermal argon annealed film on foil, (c) particle-decorated, and (d) laser-ablated Ni foil 54
Figure 23. SEM images of foil surfaces after graphene growth through PECVD, using a high carbon flow and a growth duration of 10 minutes on: (a) untreated, (b) thermal argon annealed film on foil, (c) particle-decorated, and (d) laser-ablated Ni foil 56
Figure 24. Raman spectra (532 nm excitation) of graphene grown on the four distinct Ni foil surfaces; each spectrum represents the mathematical average of measurements taken from at least three different locations on the sample, smoothing out local heterogeneities 57
Figure 25. SEM micrograph of the (a) 10 nm Ni film on SiO_2 after thermal annealing at 500 °C for 1 hour and (b) sample after PECVD process under a moderate regime .. 60
Figure 26. SEM micrograph of the particle-seeding strategy on SiO_2: (a) surface state after gravitational sedimentation of Ni nanoparticles and (b) post-PECVD growth morphology, revealing the predominant formation of carbon nanotubes 60
Figure 27. Summarized workflow of the fabrication and analysis process 62
Figure 28. AFM surface topography of Ni films: as-deposited (left), after dewetting (center), and after 60-minute carbon deposition (right) Series A–D 63
Figure 29. (a) RMS surface roughness in 60 min growth at each processing stage, (b) correlation between graphitic shell roughness and initial Ni thickness 64
Figure 30. SEM images with two magnifications from B series, dewetted Ni film (a, b), post-CVD process after 40 min growth (c, d) 65
Figure 31. EDS elemental mapping of B series after 60 minutes of growth showing distributions of (a) Ni, (b) Carbon, (c) Silicon, and (d) Oxygen 66
Figure 32. Size distributions of (a) dewetted islands for all nominal thicknesses, (b) post-CVD deposited carbon on sample C|60 with a fitted log-normal distribution curve and the average value of ~245 nm 67
Figure 33. Relative Ni film composition derived from the peak intensity of deconvolution high-resolution XPS spectra in the Ni 2p region of Ni films 67
Figure 34. High-resolution XPS spectra of Series B samples at varying deposition times: (a) Ni $2p_{3/2}$ region and (b) C 1s region 68
Figure 35. Representative Raman spectrum of sample A|40 fitted with the 11-band model 71
Figure 36. Averaged Raman spectra (solid lines), normalized to the quiet band and their standard errors (colored bands) of (a) A, (b) B, (c) C, and (d) D series in four durations of growth 72

Figure 37. Factorial influence plots of (a) relative intensity of the D band to G band and (b) relative area of D band to G band 74
Figure 38. Full width at half maximum of (a) D band, (b) G band 74
Figure 39. Relative intensity of (a) I(2D:D) and (b) C2D of all the samples 75
Figure 40. Factorial influence plots of less prominent Raman metrics: (a) intensities of D1″ and D2″ normalized with D band, (b) intensities of D1 ⋆ and D2 ⋆ normalized with D band 76
Figure 41. UV-Vis-nIR extinction spectra of (a) as-deposited Ni films, (b) dewetted islands, and (c) post-CVD graphitic shells (60 min growth) 78
Figure 42. Full UV–Vis–nIR extinction spectra acquired in the wavelength range of 170–1,000 nm for all sample series (A, B, C, and D) across the four distinct growth durations 79
Figure 43. Mean number of layers for all the samples prepared in this study 80
Figure 44. TAS spectra and traces for all samples prepared in this study; the series and duration labels are specified within each graph 81
Figure 45. TAS data for sample B|60: (a) contour plot, (b) spectra at the selected delays, (c) wavelength traces, and (d) normalized consolidated trace with exponential fit.. 82
Figure 46. Influence of input factors on TAS metrics: (a) decay time constants, (b) decay amplitudes, (c) normalized slow decay amplitude, and (d) absolute peak intensity. 83
Figure 47. Two significant correlations among Raman metrics and TAS amplitude: (a) scatter plot of W(G) vs. TAS intensity and (b) intensity ratio ID1 ⋆ :D2 ⋆ vs. TAS intensity 84
Figure 48. PCA biplot displaying sample scores (circles) and metric loadings (vectors) on the first two principal components 85
Figure 49. SERS detection of adenine on nickel-encapsulated graphite (sample A|40): (a) resonant excitation at 325 nm showing enhancement and (b) non-resonant control at 442 nm 86
Figure 50. Workflow of the fabrication and analysis process: (a) synthesis of Ag nanocubes, (b) fabrication of a templated substrate by replicating a silicon master, (c) deposition of Ag nanoparticles via CAPA method, (d) graphene growth on Cu foil by PECVD, (e) graphene transfer onto the assembled array via PVA dry method, (f) fabricated SERS samples "U" and "G", (g) exposure samples to the 2NT analyte and (h) track the signal over the year 88
Figure 51. (a) UV-Vis extinction spectrum and (b) SEM image of the periodic silver nanoparticle arrays on PDMS 89
Figure 52. A representative Raman spectrum of the reference graphene sample on Cu foil with fitted bands overlaid 90
Figure 53. (A) Normalized Raman spectra of reference materials (graphene, PDMS, 2NT), (B) temporal evolution of 2NT Raman spectra on protected (G) and unprotected (U) substrates over 344 days 91
Figure 54. Comparison of average Raman spectra normalized to the intensity of peak I for the 2NT reference (yellow) and SERS measurements (blue) 92
Figure 55. Scree plot showing the variance explained by each PCs in the Raman spectral dataset 94

Figure 56. (a) PCA score plot of reference signatures and time-resolved SERS observations, (b) calculated analyte detection scores for protected (G) vs. unprotected (U) samples over 344 days 94

PAVEIKSLŲ SĄRAŠAS

57 pav. Nikelio folijos paviršiaus SEM vaizdai po grafeno auginimo: (a) neapdorota, (b) termiškai argone atkaitinta plėvelė ant folijos, (c) dalelėmis padengta ir (d) lazeriu abliuota Ni folija. 102
58 pav. B|60 bandinio EDS elementų pasiskirstymo žemėlapiai, rodantys (a) Ni, (b) anglies, (c) silicio ir (d) deguonies pasiskirstymą. 105
59 pav. Adenino SERS aptikimas ant nikeliu kapsuliuoto grafito (A|40 bandinys): (a) rezonansinis žadinimas esant 325 nm, rodantis sustiprinimą, ir (b) nerezonansinis kontrolinis matavimas esant 442 nm. 106
60 pav. Apskaičiuoti analitės aptikimo balai apsaugotiems (G) ir neapsaugotiems (U) bandiniams per 344 dienas. 109

LIST OF ABBREVIATIONS AND TERMS

2D – Two-dimensional;
2NT – 2-Naphthalenethiol;
Abs (IR) – Absorption in the near infrared region;
Abs (UV) – Absorption in the ultraviolet region;
Abs (UV-IR) – Subtraction;
Abs (Vis) – Absorption in the visible region;
Abs (Vis:UV) – Division;
AFM – Atomic force microscopy;
Ag – Silver;
AgNCs – Silver nanocubes;
Au – Gold;
CAPA – Capillary assisted particle assembly;
CM – Chemical mechanism;
CT – Charge-transfer resonance;
Cu – Copper;
CVD – Chemical vapor deposition;
DFT – Density functional theory;
DMF – Dimethylformamide;
EDS – Energy dispersive spectrometry;
EF – Enhancement factor;
EM – Electromagnetic mechanism;
FWHM – Full width at half maximum;
GERS – Graphene enhanced Raman spectroscopy;
GIANs – Graphene-isolated Au nanoparticles;
I(2D) – Intensity of 2D band;
I(2D:G) – Intensity ratio of 2D band to G band;
I(D) – Intensity of D band;
I(D:G) – Intensity ratio of D band to G band;
I(G) – Intensity of G band;
La – Crystaline size;
LSPR – Surface plasmon resonance;
Ni – Nickel;
PCA – Principal component analysis;
PCs – Principal components;
PDMS – Poly dimethyl sulfide;
PECVD – Plasma-enhanced chemical vapor deposition;
Pos (G) – Position of the G band;
PVA – Polyvinyl alcohol;
RMS – Root mean square;
RRS – Resonance Raman scattering;
SEM – Scanning electron microscopy;
SERRS – Surface-enhanced resonance Raman scattering;
SERS – Surface-enhanced Raman spectroscopy;

SHINERS – Shell-isolated nanoparticle-enhanced Raman spectroscopy;
SLR – Surface lattice resonance;
TAS – Transient absorption spectroscopy;
UV – Ultraviolet;
UV-Vis-nIR – Ultraviolet-visible-near infrared;
W(2D) – Width of 2D band (typically FWHM);
W(D) – Width of D band (typically FWHM);
W(G) – Width of G band (typically FWHM);
XPS – X-ray photoelectron spectroscopy;
XRD – X-ray diffraction.

INTRODUCTION

Background and Motivation

Nanophotonics, the manipulation of light-matter interactions at the sub-wavelength scale, has revolutionized the ability to detect physical and chemical phenomena with unprecedented precision [1]. Within this field, Surface-Enhanced Raman Scattering (SERS) stands out as a powerful spectroscopic technique for trace-level molecular detection via ultra-sensitive platforms. By leveraging the massive amplification of Raman signals from molecules adsorbed on nanostructured metallic surfaces, SERS enables sensitivity levels capable of identifying single molecules [2].

The core of SERS lies in the unique optical properties of plasmonic nanomaterials acting as powerful nano-antennas to maximize the Raman signal. Currently, two mechanisms are widely recognized as the drivers of the SERS effect: electromagnetic enhancement (EM) provides the dominant contribution, while chemical enhancement (CM) plays mainly a supporting role. The EM mechanism arises primarily from localized surface plasmon resonances (LSPR), where free electrons in the metal oscillate collectively under specific wavelengths of light. In contrast, the CM mechanism involves chemical interactions between the adsorbed molecules and the surface, ultimately altering the polarizability of the system [3].

The efficacy of the SERS platform is fundamentally dictated by its plasmonic resonance, which is highly dependent on the material composition, shape, and dimensions of the nanostructures. While scientific literature has historically prioritized the amplification of electromagnetic fields, the practical deployment of these sensors in real-world environments is critically hindered by the chemical instability of the plasmonic nanomaterials [4]. The shelf life of SERS substrates is crucial for maintaining their sensitivity. If these substrates degrade or lose their enhancement properties over time, the detection results can become inconsistent. Standard substrates, typically composed of noble metals such as silver (Ag) or copper (Cu), are highly susceptible to rapid oxidation, sulfidation, and corrosion upon exposure to ambient air or aqueous analytes [5, 6]. Such degradation not only dampens the plasmonic resonance but also induces the desorption or decomposition of the target analyte, leading to the irretrievable loss of the molecular fingerprint over time. To address these challenges, substrates must be protected or should undergo additional treatments.

The isolation of graphene in 2004 [7], introduced a two-dimensional (2D) material uniquely equipped to address these shortcomings. Combining optical transparency, mechanical robustness, and atomic impermeability, graphene serves as an ideal hybrid integration for metallic nanostructures. It provides exceptional passivation, shielding the metal from environmental degradation without significantly decaying the near-field electromagnetic enhancement. Furthermore, it actively contributes to the CM of SERS, amplifying the signal by facilitating molecular adsorption and enrichment via $\pi - \pi$ stacking interactions [8, 9].

Despite this tremendous potential, current research on SERS stability predominantly focuses on short-term performance; typically spanning only weeks or months; where the massive initial EM enhancement dominates the sensor's response [10, 11]. Because of this short-term focus, the critical role of the CM in defining long-term sensor stability has been largely overlooked in literature. On bare metal substrates, direct chemical interactions between the target analyte and the highly reactive plasmonic surface actually accelerate metal degradation, leading to rapid, irreversible signal loss. While advanced two-dimensional coatings like graphene have been introduced to physically shield the metal, current literature has not quantitatively considered how the CM dictates extended operational lifetimes [12]. Consequently, there remains a critical lack of data regarding year-long signal stability, which is paramount for applications requiring environmental monitoring or forensic archiving, where evidence must remain stable for retrospective testing [13, 14].

Beyond the visible spectrum, extending SERS operation into the ultraviolet (UV) region offers profound analytical advantages [15]. UV excitation allows for the coupling of surface enhancement with molecular resonance Raman scattering (SERRS). This synergistic effect is particularly powerful for detecting specific biomolecules that exhibit electronic transitions in this spectral region, while simultaneously reducing interfering fluorescence backgrounds. However, traditional noble metals are ineffective in the UV regime due to severe optical damping caused by interband transitions. Consequently, UV plasmonic requires the use of alternative transitions or base metals. To date, the application of these non-noble metals is rarely addressed in the literature due to their extreme chemical reactivity and instantaneous surface oxidation [16–18].

This dissertation aims to shift this paradigm by demonstrating that while the EM mechanism provides the initial massive signal enhancment, a stable CM is the fundamental driver for long-term signal retention. To address these challenges, this study evaluates graphene-metal hybrid SERS platforms using two distinct approaches. First, the study examines the feasibility of utilizing novel nickel particles encapsulated in carbon shell architecture for ultraviolet SERS applications. Second, it investigates the integration of monolayer graphene onto a standard silver-based visible-SERS platform. This longitudinal approach allows for quantitative proof that over a year-long period, even as the EM field inevitably decays, the preservation of the CM, specifically mediated by robust $\pi - \pi$ stacking interactions between the analyte and the graphene overlayer, is the vital mechanism responsible for prolonged analyte detection.

Research Tasks

The following research tasks have been defined to achieve the dissertation objective:

1. Investigate the effects of the hydrocarbon flow regime in plasma-enhanced chemical vapor deposition (PECVD) as the primary technique for graphene growth, using nickel as a catalytic substrate, and the influence of this catalyst's surface on the quality of the deposited film.
2. Fabricate a hybrid design consisting of nickel and carbon shell by manipulating key catalytic and growth parameters while establishing an evaluation framework to determine the correlations between the synthesis factors and key structural characteristics of the shells.
3. Validate the functionality of the nickel-encapsulated architecture as an oxidation-resistant UV-SERS platform to confirm the protection of the metallic core and its plasmonic activity.

4. Establish a protocol for the transfer of PECVD-grown graphene to plasmonic arrays of silver nanoparticles.

5. Conduct a longitudinal study to quantify the role of the graphene layer in signal stability and sensor reliability over a year-long period.

Scientific Novelty

The following contributions represent the original scientific value of this dissertation:

1. Developed a new strategy to address the inherent non-uniformity of graphene growth on polycrystalline nickel foils, where nucleation mainly occurs at grain boundaries and specific grain orientations.

2. Established the first comprehensive correlation framework for evaluating the quality of graphitic shells encapsulated nickel particles, a highly disordered system where standard evaluation metrics were unreliable. By systematically screening 107 metrics across three spectroscopies: Raman (11-band model), ultraviolet-visible-near infrared (UV-Vis-nIR), and transient absorption spectroscopy (TAS), this work identified a specific set of indicators for independently tracking the key structural characteristics of the carbon shell (thickness and graphitization degree).

3. Systematically validated the interchangeable utilization of spectroscopy metrics, more specifically between the TAS and Raman spectroscopy for characterizing disordered graphitic structures. Specifically, for the first time, the study revealed that TAS peak intensity exhibits a deterministic negative correlation with Raman G-band width (W(G)) establishing it as a rapid, non-destructive proxy for crystallinity.

4. Introduced nickel-encapsulated graphitic shells as a viable, oxidation-resistant platform for ultraviolet SERS application. The research proved that the graphitic shell preserves the plasmonic activity of the non-noble metal core for over two years, enabling the resonant detection of biomolecules (adenine) at 325 nm, a spectral region rarely accessible to standard noble-metal SERS substrates.

5. Provided the first quantitative, longitudinal analyte signal retention on graphene-protected silver arrays over a one-year period. By developing a novel principal component analysis (PCA) based "analyte detection score", this work moved beyond qualitative observations to numerically quantify a $\sim 30\%$ signal retention after 344 days, stablished a benchmark for long-term monitoring applications.

Key Statements for the Defence

1. Pre-seeding polycrystalline nickel foils with nanoparticles lowers the activation energy for carbon precipitation and fundamentally decouples the graphene growth mechanism from the substrate’s underlying crystallographic orientation. This thermodynamic modification enables the synthesis of large domains planar graphene films even under carbon-rich PECVD conditions.

2. The structural quality of nickel-encapsulated graphitic shells is governed by two physical mechanisms, i.e., shell thickness and graphitization. A systematic multi-spectroscopic framework establishes that these features must be tracked separately: infrared absorbance ($\mathrm{Abs(IR)}$), the Raman $\mathrm{I(2D{:}\,D)}$ ratio and are the deterministic

proxies for shell thickness/flake density, whereas $\mathrm{Abs(Vis{:}UV)}$, $\mathrm{I(D_1^{\star}{:}\,D_2^{\star})}$, and D band width $(\mathrm{W(D)})$ from Raman isolates the degree of crystalline ordering.

3. Significant inter-metric correlations across Raman, UV-Vis-nIR, and TAS confirm that complementary techniques probe the same underlying structural defects in disordered carbon. Specifically, the TAS peak intensity serves as an interchangeable proxy for crystallinity (strongly correlating G-band width), while the TAS slow decay ratio $(\mathrm{A_2/(A_1 + A_2)})$ inversely tracks shell thickening (correlating with Raman $\mathrm{I(2D{:}\,D)}$). These relationships validate the interchangeable use of these methods for non-destructive quality assessment.

4. Nickel-encapsulated graphitic shells function as stable UV-SERS platforms because the graphitic shell provides a sealed barrier against oxidation for over two years without dampening the near-field enhancement. The successful detection of adenine at 325 nm is driven by surface-enhanced resonance Raman scattering, a synergistic effect where the excitation wavelength simultaneously aligns with the UV plasmonic resonance of the nickel core and the intrinsic electronic transitions of the analyte, while the carbon shell facilitates target adsorption via $\pi - \pi$ stacking.

5. The integration of monolayer graphene on resonant silver lattice arrays extends the SERS operational lifetime from weeks to over one year. While the EM of the underlying silver lattice degrades, the graphene overlayer effectively provides both physical and electronic passivation, thereby preserving the CM. As quantified by PCA, this preservation of the $\pi - \pi$ interaction between the aromatic analyte and the sensor surface is the primary mechanism allowing for $\sim 30\%$ signal retention after 344 days.

Author's Contribution

The research presented in this dissertation was primarily conceptualized, designed, and executed by the author, who assumes full responsibility for the validity of the experimental data and conclusions. The author independently led the experimental design and carried out the majority of sample synthesis and preparation protocols. The technical assistance with specific deposition steps was provided by Dr. Andrius Vasiliauskas (metal film deposition and thermal processing) and Dr. Nadzeya Khinevich (assistance with SERS substrate assembly). The data analysis and interpretation were conducted independently by the author. Maziar Moussavi provided assistance with data curation and the visualization of complex datasets (specifically statistical modeling and PCA).

Specialized characterization data were collected in collaboration with subject matter experts at the Institute of Materials Science, while the interpretation of these results remained the responsibility of the author.

Prof. Dr. Tomas Tamulevičius provided scanning electron microscopy (SEM) and energy-dispersive x-ray spectroscopy (EDS) data; Dr. Algirdas Lazauskas conducted X-ray diffraction (XRD) measurements; Dr. Erika Rajackaitė performed atomic force microscopy (AFM); Dr. Domantas Peckus carried out transient absorption spectroscopy (TAS) measurements; Assoc. Prof. Dr. Mindaugas Andrulevičius conducted X-ray photoelectron spectroscopy (XPS) measurements.

Additionally, Dr. Martynas Talaikis (Center for Physical Sciences and Technology) provided the target analyte and conducted specialized UV-SERS measurements.

The work was conducted under the scientific guidance and supervision of Prof. Dr. Hab. Sigitas Tamulevičius.

Thesis Structure

The dissertation is organized as a monograph comprising five main chapters with a summary, described as follows:

Introduction establishes the research context, defines the primary aim and specific tasks, details the scientific novelty, presents the key statements for defence, and clarifies the author's contribution to the work.

Literature Review provides a comprehensive overview of the state-of-the-art, covering the fundamental properties of graphene-based materials, the mechanisms of PECVD synthesis on catalytic metals, and the current challenges in SERS stability.

Materials and Methods details the experimental protocols employed throughout the study, including the preparation of catalytic substrates, PECVD growth parameters, and the fabrication of hybrid SERS platforms. It as well describes the characterization techniques and statistical methodologies used for the data analysis.

Results and Discussion presents the experimental findings, divided into three interconnected case studies: Case Study I: Preliminary Investigation of Nickel as Catalyst in PECVD (presents a fundamental investigation designed to elucidate the behavior of the nickel catalyst under PECVD graphene growth conditions); Case Study II: Nickel-Encapsulated Graphitic Shells for UV-SERS (establishes a multi-spectroscopic framework for evaluating disordered graphitic structures and validates the feasibility of protected nickel cores for UV-range sensing); Case Study III: Signal Stability of Graphene-Overlayered Resonant Silver Arrays (quantifies the protective efficacy of monolayer graphene on resonant silver arrays, demonstrating year-long signal retention).

Conclusions summarizes the main scientific findings, reiterates the validated scientific novelty, and proposes directions for future research.

Santrauka provides a comprehensive summary of the dissertation in the Lithuanian language.

1. LITERATURE REVIEW

1.1. Fundamentals of Graphene and Graphene-Based Allotropes

In order to understand the basic properties of graphene [19], first, one must consider the fundamental structure of the carbon atom. The nucleus of a carbon atom is surrounded by six electrons: two in a deep inner shell and four outer electrons that are important for bonding (shown in Figure 1a, b). In graphene, the carbon atom mixes one (s) orbital, with two (p) orbitals from the outer shell to form sp^2 hybridized state. These sp^2 orbitals lie flat in a plane, oriented at 120° angles to one another, while the remaining unhybridized pz orbital extends perpendicularly above and below this plane (Figure 1c). Carbon atoms utilize these three planar sp^2 orbitals to form strong covalent sigma (σ) bonds with three neighboring atoms, establishing the robust hexagonal honeycomb lattice characteristic of monolayer graphene (Figure 1c, d). Concurrently, the perpendicular pz orbitals overlap with those of adjacent carbon atoms to form weaker pi (π) bonds. The electrons within these π bonds are not localized; they rather form a highly delocalized electron cloud that can move freely across the entire two-dimensional sheet, granting graphene its remarkable electrical conductivity and facilitating strong $\pi - \pi$ interactions with aromatic molecules.

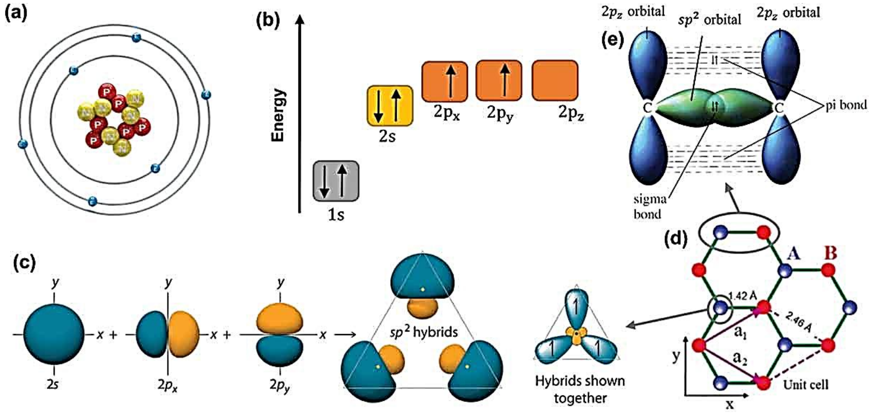

Figure 1. (a) Atomic structure of a carbon atom, (b) energy levels of outer electrons in carbon atoms, (c) the formation of sp^2 hybrids, (d) the crystal lattice of graphene where A and B are carbon atoms belonging to different sub-lattices, a_1 and a_2 are unit-cell vectors, (e) sigma bond and pi bond formed by sp^2 hybridization *[19]*

The exceptional mechanical robustness and flexibility of graphene are fundamentally governed by its in-plane σ bonds, while the delocalized π bonds regulate the out-of-plane interactions between adjacent graphene layers (**Figure** *2*).

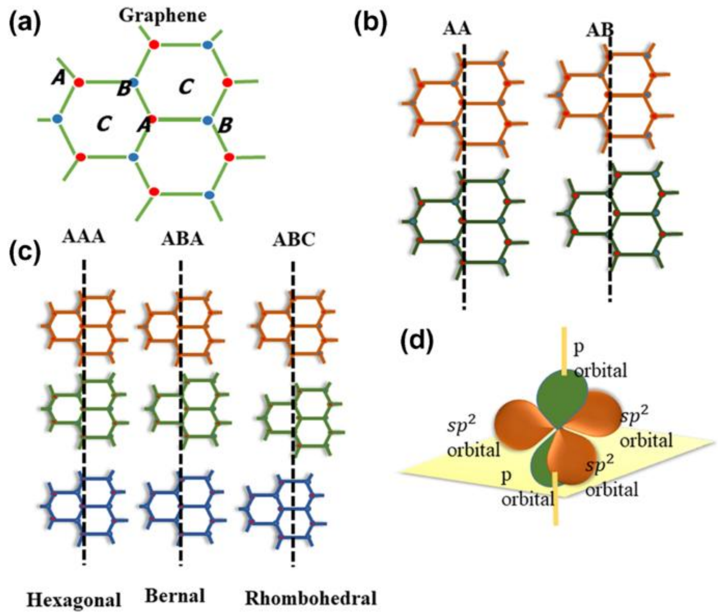

Figure 2. (a) Single layer graphene structure, A and B denote carbon sites, (b) bilayer graphene stacking types, (c) three-layer graphene stacking types, (d) π bond and sigma bond positions in the graphene honeycomb lattice *[20]*

This distinct atomic arrangement endows graphene with a unique combination of physical properties that make it highly advantageous for hybrid sensing platforms [21]. It is optically transparent (97.4% transmission) [22], mechanically robust (with a Young's modulus of 1 TPa) [23], and, most critically for the objectives of this study, atomically impermeable to standard gases [24]. This exceptional impermeability allows graphene to function as an ultimate passivation layer, shielding reactive metallic substrates from environmental degradation and oxidation. Furthermore, the electronic structure of graphene-based materials evolves rapidly with the number of layers, approaching the three-dimensional limit of bulk graphite at approximately 20 layers. Monolayer and strictly bilayer graphene exhibit relatively simple electronic spectra, behaving as zero-gap semiconductors (or zero-overlap semimetals) with distinct electron and hole charge carriers [25]. However, as the structure thickens to three or more layers, the electronic spectra become increasingly complex due to the emergence of multiple charge carriers and significant overlapping of the conduction and valence bands. Consequently, monolayers, bilayers, and few-layers (3 to <10) graphene are classified as physically distinct 2D crystalline systems [26].

Beyond ideal 2D planar sheets, graphene can exist in a multitude of dimensional forms. These include zero-dimensional wrapped cages (such as fullerenes and carbon dots) [27], one-dimensional rolled-up structures (single- and multi-walled carbon nanotubes) [28, 29], and complex three-dimensional architectures like vertically aligned nanosheets or encapsulated shells [30]. The graphene and its related forms can be broadly classified into two distinct categories, i.e., chemically modified derivatives and structural variations. Chemically modified derivatives, such as hydrogenated graphene (graphane), fluorinated graphene (fluorographene), oxidized graphene (graphene oxide), and graphene, introduced by acetylenic chains (graphyne and graphdiyne) [31], are synthesized by intentionally introducing functional groups that chemically alter the intrinsic sp^2 lattice [32]. In contrast, the structural variations, commonly referred to as graphene-based materials, encompass monolayer graphene, few-layer assemblies, graphitic flakes, and highly defective architectures containing amorphous carbon phases. The diverse properties of these structural variations arise primarily from the changes in nanoscale morphology, defect density, and hybridization state, rather than deliberate chemical functionalization.

The structural evolution of these carbon materials is fundamentally governed by the hybridization state of the carbon atoms (sp^1, sp^2, sp^3), a relationship often visualized using a ternary phase diagram (Figure 3).

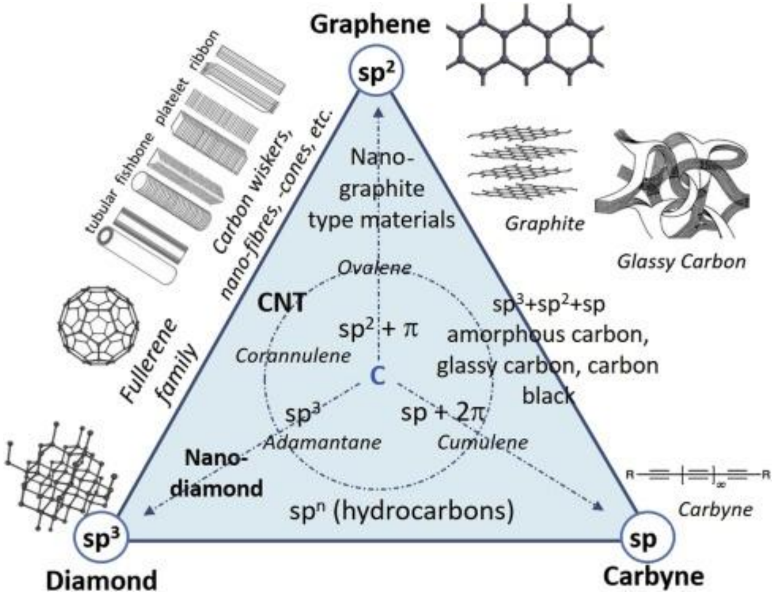

Figure 3. Different hybridizations for carbon materials; the vertices of the triangle represent the pure forms: diamond (sp^3), graphene (sp^2), and carbyne (sp) *[33]*

In this framework, pristine graphene is located near the sp^2 vertex, consisting entirely of a planar monolayer of sp^2-bonded carbon atoms. As additional layers or defects are introduced, the material develops a more bulk-graphitic or disordered character. The materials situated along the edges or within the interior of the ternary diagram, such as carbon nanotubes, fullerenes, and glassy carbon, exhibit mixed or transitional bonding states. While predominantly sp^2-hybridized, these structures introduce local sp^3 characteristics due to the physical curvature or lattice disorder. Closer to the center of the diagram lies highly disordered forms, such as amorphous carbon, which contain a complex, randomized mixture of sp^2, sp^3, and sp-hybridized atoms [33]. Lacking long-range crystallographic order, these amorphous and highly defective graphitic phases display significantly broadened electronic and vibrational properties [34, 35], posing a critical challenge for accurate qualitative and quantitative characterization.

1.2. Graphene Synthesis Routes and Advanced Techniques

In 1999, Ruoff et al., [36] first proposed that micrometer-to-nanometer-sized graphene sheets could theoretically be obtained from highly oriented pyrolytic graphite. Building on this concept, Novoselov et al., [7] successfully isolated few-layer graphene via mechanical exfoliation (the "scotch tape" method) in 2004, a groundbreaking achievement that earned them the 2010 Nobel Prize in Physics. Since this pioneering isolation, graphene has become one of the most extensively studied 2D materials over the past two decades [37, 38].

Since its initial discovery, numerous techniques, broadly categorized into top-down (e.g., exfoliation) and bottom-up approaches, have been developed to synthesize high-quality monolayers with a wide range of morphologies. Figure 4 illustrates a schematic overview of these synthesis routes [39].

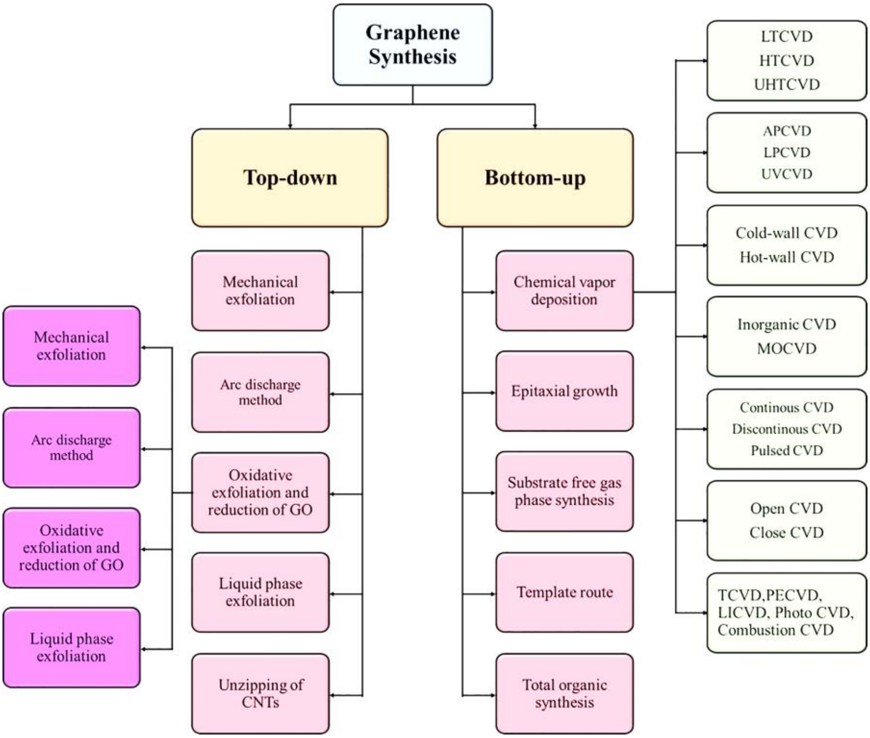

Figure 4. Schematic overview of graphene synthesis routes and classification of CVD techniques*[39]*

Among the bottom-up methods, thermal Chemical Vapor Deposition (CVD) has established itself as a standard for high-quality, large-area graphene synthesis. CVD typically involves the catalytic decomposition of hydrocarbon precursors (e.g., methane: CH_4) on the surface of transition metal substrates at elevated temperatures

[40]. While thermal CVD is the primary technique for producing planar graphene films, it fundamentally requires high temperatures (often exceeding 1,000 °C) to overcome the thermodynamic activation energy barriers associated with hydrocarbon dissociation and crystalline ordering. However, the integration of graphene into temperature-sensitive substrates and devices necessitates a shift toward lower-temperature processing. This requirement has catalyzed the adoption of advanced plasma-assisted techniques that leverage electromagnetic energy to initiate the chemical reactions that would otherwise be thermodynamically unfavorable at reduced thermal regimes [41, 42].

In plasma-enhanced CVD (PECVD), energetic ionized gases enable graphene synthesis at significantly lower substrate temperatures (≤700 °C) [43]. As illustrated in the schematic in Figure 5, the system comprises several key components. A microwave guide directs power into the discharge chamber, where high-energy electrons ionize and dissociate precursor gases, producing a highly reactive plasma plume consisting of radicals (e.g., CH_3, CH_2, C), ions (CH_3^+, H^+), and atomic hydrogen and carbon [44]. These reactive species adsorb onto the substrate (primarily catalytic metals), where subsequent chemical reactions and structural rearrangements lead to the formation of carbon allotropes [45].

The substrate holder positions the sample within the plasma zone and regulates its temperature, while gas outlets continuously remove by-products and maintain stable chamber pressure [46]. Additional diagnostic components may be as well integrated to monitor plasma and film growth in real time.

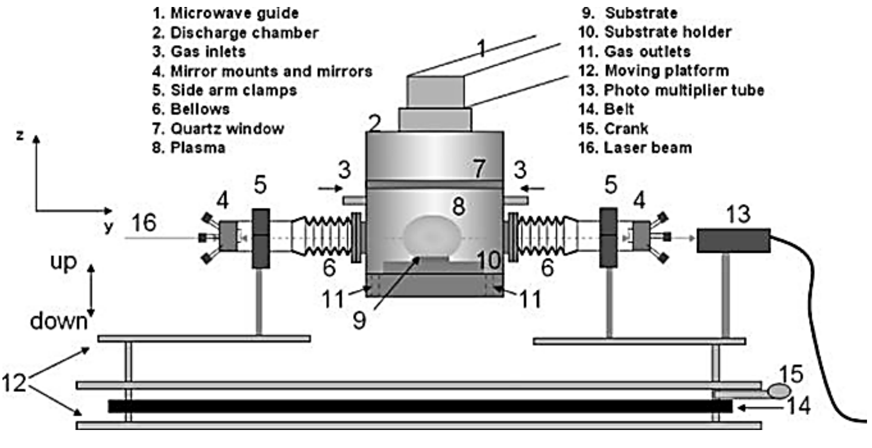

Figure 5. Schematic of the microwave plasma-enhanced CVD reactor *[47]*

Consequently, several interdependent parameters, such as process temperature [46, 48], plasma power [46, 48], precursor type [46, 49, 50], etching gas ratios [51], operating pressure [46, 50, 52] and depositing time [46, 50, 53], can be adjusted to directly control the characteristics of the synthesized material. However, the optimization of these parameters is highly dependent on the nature of the catalytic substrate used for the growth process.

1.2.1. Growth Mechanisms of Graphene on Catalyst Surface via PECVD

Beyond operational parameters, the nature of the underlying substrate plays a profound role during the PECVD graphene growth process. The substrate can directly affect the number of graphene layers that are grown [54], the types of structural defects present [55], residual strain [56], and more [57]. This influence arises from the fundamental differences in the growth mechanism of catalytic substrates [58], insulating surfaces (e.g., Si wafers, quartz) [59] or transition metals (e.g., Co, Ni, Pt, Ge, Pd, Al) [60].

While successful low-temperature growth has been reported on non-catalytic quartz [61], the grow process suffers from impractically slow rates. Consequently, copper (Cu) and nickel (Ni) remain the two most common catalytic substrates, typically yielding monolayer and few-layer graphene, respectively [62]. According to the proposed unified model for catalytic substrates, active carbon species formed from the dissociation of precursor gases tend to aggregate into thermodynamically stable formations at the active sites on the surface. This process initiates the growth of graphene layer, on the surface (see **Figure *6***) [63].

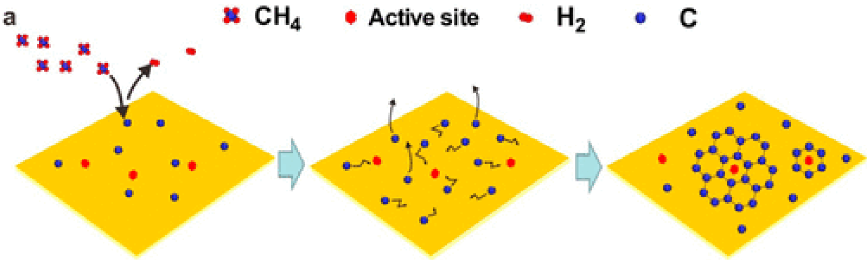

Figure 6. Scheme for growing graphene on a catalytic substrate (copper in this case): red hexagons are the active sites of the Cu surface, and blue spots signify active carbon species *[63]*

While the dissociation process is similar, the actual growth mechanisms on Cu and Ni differ significantly (**Figure 7**), as initially reported by Muñoz and Gómez [64].

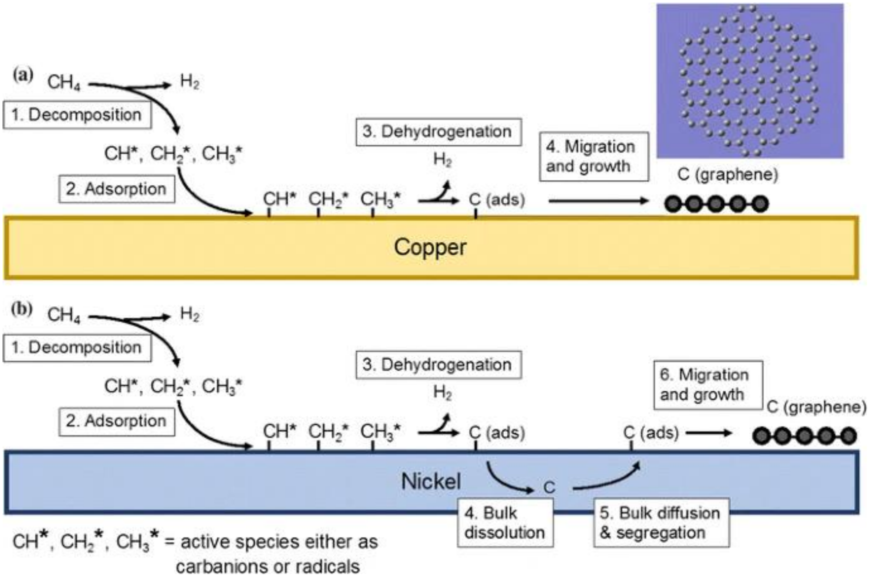

Figure 7. Schematic diagram of graphene growth on a) copper and b) nickel substrates in the thermal CVD process [64]

Copper promotes strictly surface-mediated growth; once a monolayer forms, the catalytic surface is passivated, stopping further decomposition in a "self-limiting" manner. Because this mechanism is strictly confined to the surface, the structural uniformity of the resulting graphene is highly sensitive to the substrate's initial topography [65]. During synthesis, decomposed carbon atoms accumulate and preferentially form nuclei at high-energy surface irregularities, such as grooves, scratches from mechanical rolling, or surface impurities [58]. Consequently, the most critical factor in achieving a uniform, high-quality planar film on copper is suppressing this heterogeneous nucleation. As demonstrated in recent studies, physically smoothing the copper surface prior to the synthesis drastically reduces the density of active nucleation sites, thereby minimizing the unwanted localized growth of additional, non-uniform graphene layers [66].

While copper is ideal for continuous monolayer generation due to its strictly surface-mediated, self-limiting behavior, transition metals like nickel, which have higher carbon solubility, exhibit a fundamentally different growth paradigm. Graphene growth on nickel typically follows a dissolution-segregation-precipitation mechanism in high-temperature (~1,000 °C) thermal CVD [67]. Carbon atoms diffuse into the bulk nickel and, upon cooling or saturation, segregating back to the surface, makes the cooling rate critical for uniformity [68, 69]. However, in plasma-assisted processes, the mechanism is highly influenced by reduced surface temperatures. Carbon solubility in nickel drops from approximately 1.3 at. % at 1,000 °C [60, 70] to roughly 0.6 at. % at 700 °C. At these intermediate temperatures, the system operates near the dissolution-precipitation limit, heavily modified by the continuous plasma flux. At even lower thermal regimes ($\leq$500 °C), bulk solubility drops significantly [71], as a threshold dissolution temperature around 475 °C has been reported. In this regime, the growth becomes primarily surface-mediated, forming largely through the transformation of surface-confined nickel-carbide (Ni_2C) phases [72]. Plasma plays a crucial role in enhancing the local surface temperature. The "plasma ball" hovering just above the substrate acts as an intense heat source [73], which differs from the set controlled by the stage heater [74]. Plasma ball ensures exhaustive dissociation of the hydrocarbon feedstock [75]. Carbon concentration is defined by the ratio of carbon species to the total gas volume. Hydrogen plays a dual role in this process: it reduces the native oxide layer on the metal surface and further acts as an etchant, removing amorphous carbon ($a - C$) and highly defective sp^3 phases [76].

The relationship between the Gibbs free energy (ΔG) and carbon supersaturation ($\Delta\mu$) governs this nucleation process [77]. In PECVD, high dissociation rates create a large saturation that drives the phase transformation. However, nucleation is rarely homogeneous; it follows a heterogeneous pathway where the energy barrier is significantly lowered at specific active surface sites, such as steps, grain boundaries, and protrusions. Furthermore, the local geometry of the catalyst plays a pivotal role. The Gibbs-Thomson effect suggests that the regions of high curvature possess a higher chemical potential, which intensely facilitates carbon precipitation and localized growth. Understanding this thermodynamic preference is essential for engineering strategies that aim to control the grow process [78]. For instance, such thermodynamic behavior poses a significant challenge when using commercial polycrystalline nickel foil, which is composed of domains with varying crystal orientations separated by the grain boundaries.

Zhang et al., [79] were the first to systematically investigate this phenomenon by comparing graphene growth on single crystal versus polycrystalline nickel foils (Figure 8).

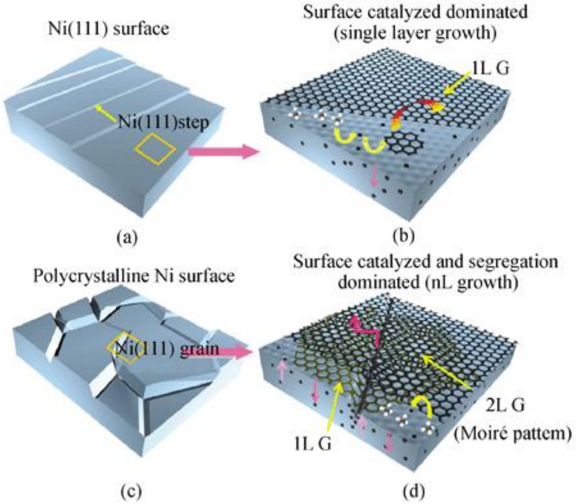

Figure 8. Schematic diagrams for ambient pressure CVD graphene on (a) and (b) Ni(111) and (c) and (d) polycrystalline Ni films at (900–1,000 ºC) *[79]*

On monocrystalline surfaces, single layer growth dominates, whereas on polycrystalline substrates, highly uneven multilayer growth prevails. This disparity arises because catalytic activity and carbon diffusion coefficients are strictly dictated by the exposed crystal facet and grain boundaries. Consequently, carbon diffusion rates vary significantly, causing graphene to grow thicker on specific grains while remaining thin on the others [80]. This non-uniformity is further exacerbated during the cooling phase, where massive accumulations of carbon segregate at the high-energy grain boundaries [81].

Despite using single-crystal Ni with a unified orientation would theoretically resolve these uniformity issues [57, 82–84], pure monocrystalline foils are prohibitively expensive. Furthermore, complete elimination of grain boundaries is not always desirable; recent studies suggest that controlling the density and distribution of grain boundaries can be used to modulate the electronic and mechanical properties of the graphene film [85]. Therefore, engineering polycrystalline foils is a highly practical alternative.

Thiele et al., [86] have identified a direct correlation between the grain type of the underlying nickel and the thickness variations of the resulting graphene, noting that the Ni(111) orientation is the most favorable for achieving the lowest number of layers. This preference is crystallographically driven: the Ni(111) plane possesses a hexagonal atomic arrangement that closely matches the honeycomb lattice of graphene, thereby promoting epitaxial alignment [84]. In contrast, the (100) and (110) planes exhibit square or rectangular symmetries that do not support epitaxial growth, leading to the fragmentation and rotationally disordered multilayer domains.

They also reported that by annealing the polycrystalline Ni film at high temperatures (~1,000 ºC) in hydrogen and argon environments, internal stress minimized, which promoting the secondary recrystallization of the favorable Ni(111) grains as illustrated in Figure 9.

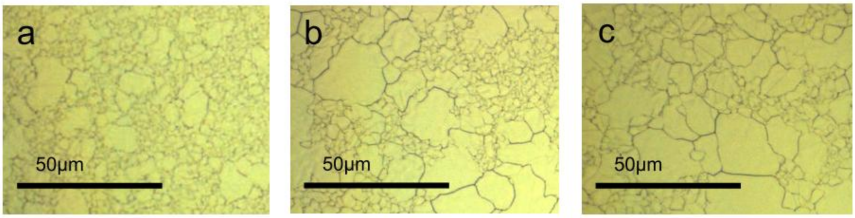

Figure 9. The optical image of the polycrystalline nickel surface after an annealing time of (a) 1 min, (b) 15 min, and (c) 40 min *[86]*

Recently, as noted by Kicińskia et al., [87], the catalytic activity of nickel during graphene growth is fundamentally governed by its electronic configuration, specifically the presence of vacancies in the 3d electron shell. Transition metals with completely filled d-orbitals (e.g., Cu, $3d^{10}$) interact weakly with carbon, strictly favoring the surface-adsorption mechanisms that lead to self-limited monolayer growth. In contrast, nickel ($3d^{8}$) possesses moderate d-vacancies that allow for significant orbital overlaps with carbon p-electrons without forming the irreversible, refractory carbides characteristic of early transition metals. This unique electronic structure dictates the dissolution-precipitation mechanism, which naturally favors the formation of multilayer graphene.

Kim et al., [88] shown the optimum gas ratio for synthesis high-quality, planar monolayer graphene on polycrystalline foil requires a hydrogen-rich environment to suppress secondary nucleation via aggressive etching (**Figure *10***).

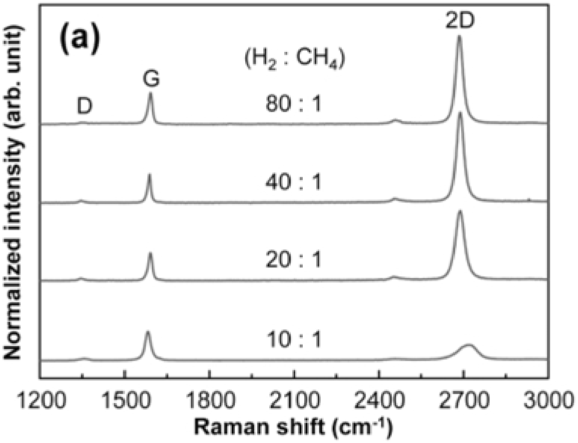

Figure 10. Gas mixing ratios of graphene films synthesized at 750 °C adopted from*[88]*

Recent mechanistic studies have demonstrated a shift towards a carbon-rich environment, leading to the formation of non-planar structures [89–91] . This carbon-rich kinetic imbalance promotes significant secondary nucleation at grain edges and high-energy defect sites. Under these supersaturated conditions, the precipitating carbon lattice cannot relax into a thermodynamically stable planar 2D sheet. Instead, in order to accommodate the high influx of carbon and minimize surface energy, the growing layers are compelled to curve, resulting in the encapsulation of catalytic particles or the vertical extrusion of nanowalls [92]. Such a disordered system has proven to be more challenging for the evaluation process, which will be explained further.

1.3. Characterization of Carbon-Based Materials

Among the various characterization techniques used for carbon-based materials [93], Raman spectroscopy stands out as a versatile, non-destructive tool that probes molecular vibrational modes and is highly sensitive to the sp^2 bonding network [94].

Figure 11 illustrates the standard setup of a Raman spectrometer. The process begins with monochromatic light (typically a laser) directed through a microscope objective onto the sample. The interaction of the incident photons (ω) with the molecular bonds results in scattering. While the vast majority of light scatters elastically (Rayleigh scattering) with no change in energy, a very small fraction scatters inelastically (see Figure 12). This inelastic scattering occurs via two mechanisms: stokes scattering, where the incident photon transfers energy to the molecule (creating a phonon), resulting in scattered light with lower energy (ω – ων), and anti-stokes scattering, where the photon absorbs energy from an excited molecule, resulting in higher energy (ω ± ων) [94, 95].

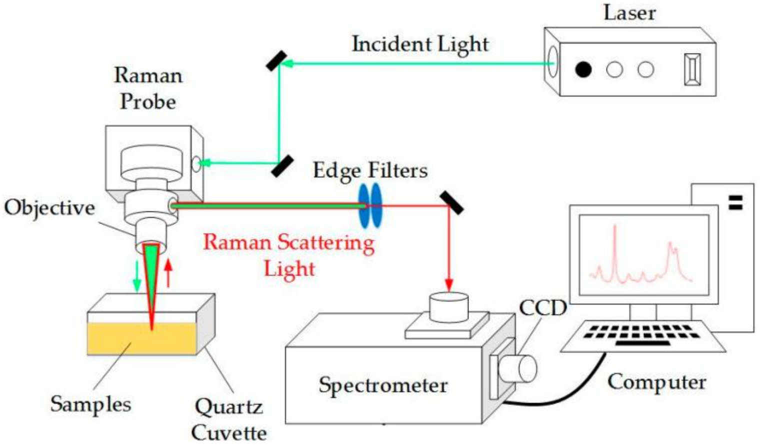

Figure 11. Schematic of the overall function of Raman spectroscopy from the laser source to the final spectrum on the computer *[96]*

It should be noted that for a vibrational mode to appear in a Raman spectrum, it must be "Raman-active". This occurs only when the vibration induces a change in the molecule's polarizability, essentially, how easily the electron cloud is distorted by the laser's electric field. Therefore, the changes in the shape or orientation of the electron cloud during vibration determine the activity of a specific mode [97].

The instrument's optics collect the scattered light, filter out the intense Rayleigh scattering, and direct the remaining signal to a spectrometer. The energy difference between the incident and scattered light is recorded as the Raman shift (in cm^{-1}).

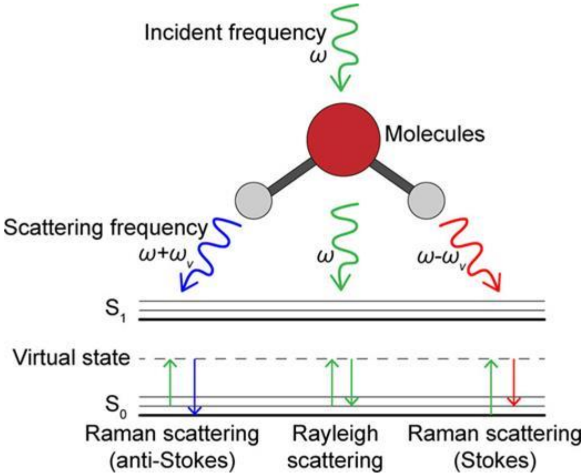

Figure 12. Diagram illustrating Raman scatterings and Rayleigh scatterings *[95]*

Although the spectrum contains both Stokes and Anti-Stokes peaks, Stokes scattering is significantly more intense at room temperature because the population of molecules in the ground state is far greater than in the excited states (Boltzmann distribution). Consequently, Stokes-shifted peaks are conventionally used for the spectral analysis [98].

1.3.1. Raman Scattering Spectroscopy of Graphene-Based Materials

Graphene-based materials absorb photons across a wide energy range, bringing multiple phonon modes into resonance [99]. The spectrum of high-quality graphene is characterized by three principal bands. The 2D band (~2,700 cm^{-1}) is a second-order overtone and is the key indicator of layer number in monolayers, appearing as a single, sharp Lorentzian peak. The G band (~1,580 cm^{-1}) arises from the in-plane stretching of sp^2 carbon pairs and represents the crystalline graphitic lattice [99–103]. Finally, the D band (~1,350 cm^{-1}), a defect-activated band involving intervalley scattering and appears only when the perfect honeycomb lattice is broken by edges, vacancies, or structural disorder [104].

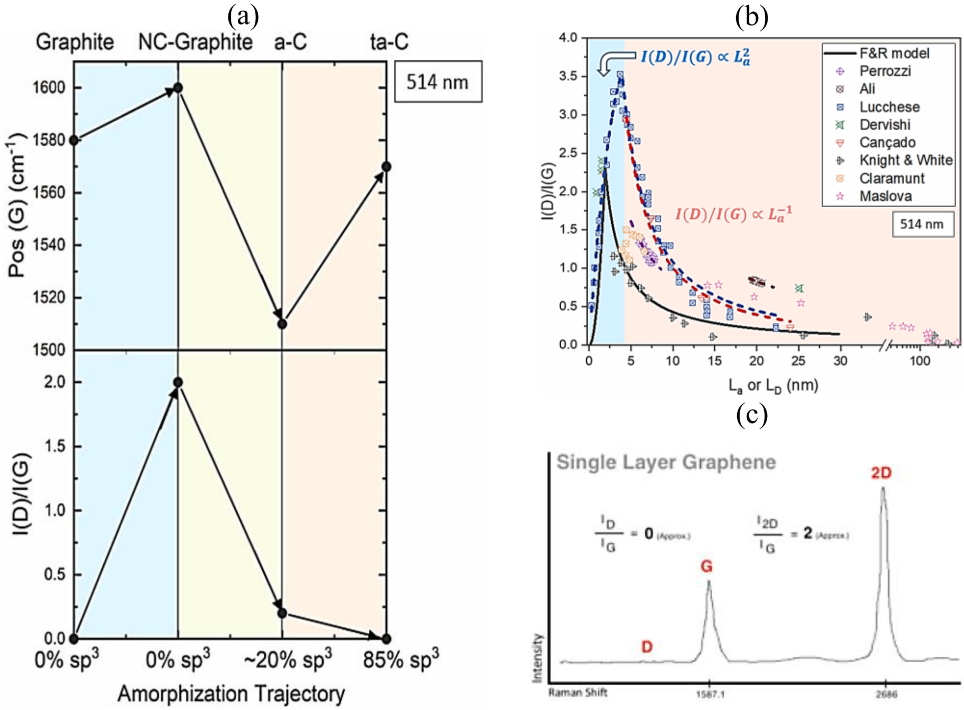

Figure 13. (a) The three-stage model of carbon amorphization showing the evolution of the Raman I(D:G) ratio and G peak position with increasing disorder, (b) compiled empirical data of the I(D:G) ratio versus crystallite size (La), and (c) Raman spectrum of single-layer Graphene *[105, 106]*

While the principal Raman bands are prominent and sharply defined in pristine monolayer and few-layer graphene (Figure 13c), their spectral behavior fundamentally changes as the material transitions towards a bulk graphitic or highly defective state. As crystallite domains become smaller and a higher density of structural defects is introduced into the sp^2 hybridized lattice, the interpretation of the Raman spectrum requires significantly more scrutiny. For instance, standard empirical metrics established for pristine graphene, such as utilizing the relative intensity of 2D band to G band (I(2D:G)), intensity ratio to determine the number of layers, become intractable as the material approaches the three-dimensional limit of graphite, causing the 2D band to broaden and the electronic bands to overlap. Similarly, the relative intensity ratio of the D band to the G band (I(D:G)), which is a well-known and reliable metric for quantifying defect density in lightly disordered samples, becomes ambiguous and loses its linear reliability in highly defective nano-architectures.

In general, the intensity of the D peak is directly correlated with the level of disorder. The foundational framework for understanding this evolution is the "three-stage model" proposed by Ferrari and Robertson [105]. This model describes how the G peak position (Pos G) and relative intensity of I(D:G), change with progressive amorphization (Figure 13a).

Stage 1 (Graphite to Nanocrystalline Graphite): Disorder is introduced primarily by grain boundaries. As average crystallite domain size (L_a) reduces, the I(D:G) increases according to Tuinstra-Koenig relationship [107]. The Pos(G) typically remains relatively stable or shows a slight blueshift.

Stage 2 (Nanocrystalline to Amorphous Carbon): As disorder increases further, the sp^2 clusters become smaller, and the rings distort. As illustrated by the compiled empirical data in Figure 13b, the standard Tuinstra-Koenig relationship fails in this highly disordered regime. Instead of increasing with disorder, the I(D:G) ratio reaches a maximum and subsequently drops according to the Ferrari and Robertson correlation, $\mathrm{I(D:G)\alpha La^2}$. This renders standard defect calculations based solely on this ratio highly ambiguous for heavily disordered carbons. Additionally, Pos(G) generally shows a significant decrease as the sp^2 bonds become more distorted and chain-like structures begin to form.

Stage 3 (Amorphous C to Tetrahedral a-C): The sp^3 content increases significantly (from 20 to 85%) and the remaining sp^2 sites are often confined to short chains rather than rings. The Raman spectrum loses distinct features, and the I(D:G) goes to zero.

Schuepfer et al., [108] demonstrated that the empirical formulas that are based solely on I(D:G) ratio often fail in highly disordered systems because defect formation is extrinsic and complex. When structural transformation is incomplete (typical in low-temperature synthesis), the spectrum exhibits broadened peaks and elevated photoluminescence (PL) backgrounds, as shown in **Figure *14***. In such disordered architectures, spectral features, such as the G-band Full Width at Half Maximum (W(G)) and the PL background slope, become critical indicators of structural bond disorder and hydrogen content, respectively [97, 106, 109].

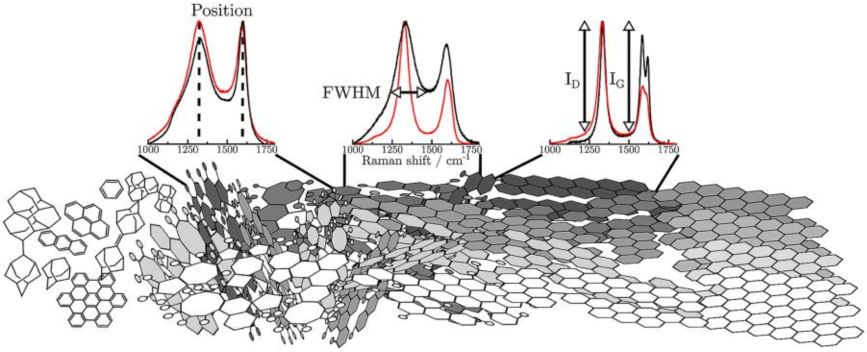

Figure 14. The transformation from molecular to crystalline of non-graphitic carbons with their Raman line shape analysis of G and D mode *[108]*

Therefore, to accurately deconvolute mixed phases, it is necessary to look beyond the prominent bands and analyze the "hidden" vibrational modes. This emphasizes the need to refine Raman evaluation metrics, especially in relation to the novel morphologies that have emerged following the isolation of graphene [110].

To address this, Couzi et al., [111] pioneered the re-examination of the first-order Raman spectrum of defective carbons, identifying low prominent modes in the 1,000–1,300 cm^{-1} region (D'' bands), and distinguished two dispersive and non-dispersive components. Similarly, Moseenkov et al., [112] investigated bands in the 1,400–1,500 cm^{-1} region and attributed them to the amorphous phases. Recognizing the complexity of heterogeneous datasets of disordered structures, recent studies have begun employing statistical methods [113] and machine learning to interpret spectral data [109].

1.4. SERS Platforms: Enhancement Principles and Challenges

The core of surface-enhanced Raman scattering lies in the unique optical properties of plasmonic nanoparticles. Unlike pure bulk metals, which have a strict maximum limit on the wavelength size they can effectively couple with, plasmonic nanoparticles can couple their electron density with electromagnetic radiation of wavelengths significantly larger than the particle itself. This phenomenon is driven by the unique nature of the dielectric-metal interface. [114, 115]. Fundamentally, plasmons arise from the collective oscillation of free electrons. When exposed to an electromagnetic wave, the oscillating light forces these electrons to migrate, creating a dynamic dipole moment that oscillates at the incident light's frequency.

Due to these highly tunable scattering and coupling properties, plasmonic nanoparticles serve as exceptional candidates for trace-level spectroscopy analyte detection, by significantly enhancing the signal [116, 117]. A key performance indicator, the enhancement factor, quantifies the signal increase under SERS conditions compared to a conventional Raman experiment without the nanostructured substrate [118, 119]. The total enhancement is a product of two distinct mechanisms, i.e., EM and CM. Electromagnetic enhancement is the dominant contributor and an intrinsic property of the plasmonic substrate, independent of the specific analyte molecule. This enhancement comes from a twofold phenomenon [120], involving the amplification of both the incident and scattered light. (1) Incident field enhancement: the localized surface plasmon resonance of the nanostructure generates a greatly enhanced local electric field right at the molecule's location, causing the molecule to be excited more intensely by the incident laser [2, 121]. Therefore, strong enhancement can be achieved when the localized surface plasmon resonance or LSPR maximum is aligned with the excitation laser wavelength. (2) Scattered field enhancement: the Raman-scattered light emitted by the molecule, which is at a different wavelength (the Stokes-shifted wavelength), can itself excite the plasmon resonance. This causes the outgoing Raman signal to be amplified a second time as it leaves the surface [119]. Total EM mechanism is a product of these two effects.

It should be note that while aligning the LSPR with the laser provides significant enhancement, the maximum effect is often achieved when the plasmon resonance wavelength (λ_{StLSPR}) is positioned between the excitation wavelength (λ_{Stokes}) and the Stokes-shifted wavelength (λ_{Stokes}). This "bridging" position allows for substantial enhancement of both the incoming excitation field and the outgoing Raman scattered field. The Stokes-shifted wavelength (λ_{Stokes}) can be calculated from the laser wavelength and the Raman shift (Δν in cm^{-1}) [120] by using equation (1).

$$\frac{1}{\lambda_{Stokes}} = \frac{1}{\lambda_{laser}} - \frac{\Delta\upsilon}{10^7} \qquad (1)$$

In contrast to the universally applicable EM, the chemical mechanism provides a smaller, molecule-specific amplification. The CM fundamentally relies on the direct interaction between the adsorbed molecule and the plasmonic surface, which modifies the intrinsic polarizability of the adsorption complex [3, 122]. This enhancement arises from three distinct photophysical and chemical contributions: static chemical interactions, charge-transfer (CT) resonance, and molecular resonance Raman scattering (RRS) [122, 123] as illustrated in Figure 15c-e.

The first contribution, static chemical interaction, occurs when the target molecule chemically binds to the substrate in its ground state. This binding alters the structural geometry and electronic distribution of the adsorbate, thereby increasing its Raman scattering cross-section. However, the enhancement provided by this static perturbation is relatively modest, typically yielding an enhancement factor of 10 to 100 [123]. The second contribution, CT mechanism, is driven by the photoinduced electron tunneling between the metal substrate and adsorbed molecule during laser excitation [124]. The CT phenomenon is a resonance-like process that strictly depends on the alignment of the incident laser energy, the molecular energy levels, and the Fermi level of the metallic or semiconducting substrate. When the energy of the exciting photon matches the energy gap for this metal-to-molecule (or molecule-to-metal) electronic transition, the Raman scattering is significantly amplified. The enhancement factor attributed to the CT mechanism typically reaches two to four orders of magnitude. The most substantial chemical contribution arises from the molecular RRS. This occurs when the incident laser photon energy coincides directly with an intrinsic electronic transition within the analyte molecule at the interface. When this molecular resonance is coupled with the near-field electromagnetic enhancement of the plasmonic surface, the combined phenomenon is termed surface-enhanced resonance Raman scattering or SERRS [15]. The SERRS contribution can be exceptionally powerful, yielding additional enhancement factors of four to six orders of magnitude. Consequently, SERRS enables extremely high sensitivity, often reaching the single-molecule detection limit, particularly for biomolecules that are analyzed in the visible and ultraviolet spectral regions [15, 122].

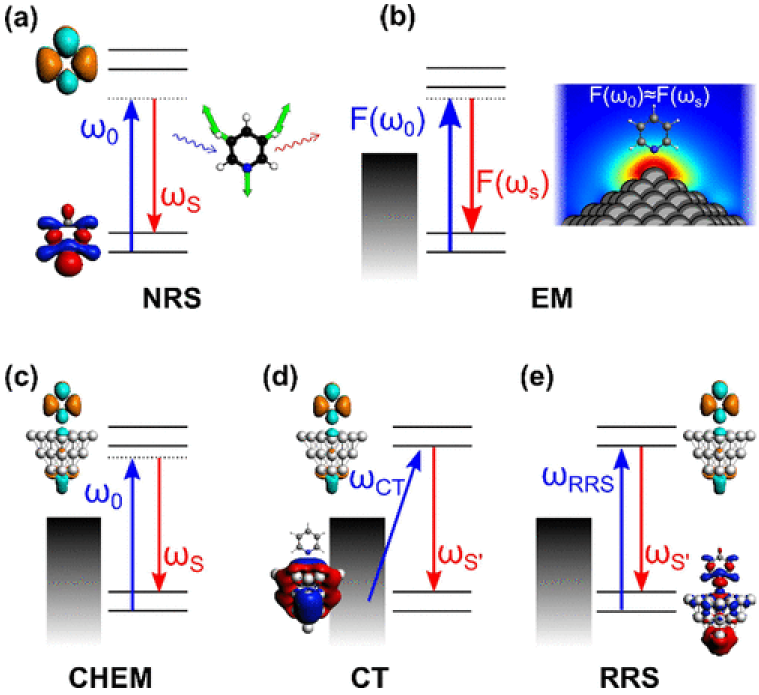

Figure 15. Illustrated various enhancement mechanisms of SERS: (a) normal Raman scattering, (b) electromagnetic mechanism, (c) static chemical mechanism, (d) charge-transfer mechanism, and (e) resonance Raman mechanism *[122]*

Ultimately, while the CM can yield high enhancement factors under specific resonant conditions, it is inherently selective and heavily dependent on the chemical structure of the target molecule. The scientific community widely agrees that while the EM provides the vast majority of the overall signal amplification, the CM plays a vital complementary role. Specifically, the CM is responsible for the finer, analyte-specific details of SERS spectra, such as specific frequency shifts, alterations in relative peak intensities, and the emergence of new vibrational bands that are absent in normal Raman scattering [3, 123].

While EM and CM principles govern the enhancement of individual nanoparticles or random aggregates, engineering the macroscopic arrangement of these nanostructures into periodic arrays introduces a higher resonance Q-factor value $Q = \frac{\lambda}{\Delta\lambda} \sim 100$, due to a fascinating optical phenomenon called surface lattice resonance (SLR) [125, 126]. This effect occurs when the LSPR spectrally aligns with the Rayleigh anomaly (the scattering of the light into specific directions in a periodic structure). SLR manifests as a narrow, high-quality resonance peak in the optical spectrum [127]. Although the EM field becomes more delocalized through this hybridization, the overall field enhancement in the vicinity of the nanoparticles increases [128–131]. In SERS, this resonance can be optimized [132–135] with peak enhancement expected when the SLR wavelength is positioned between the excitation and Stokes-shifted wavelengths of the analyte [136], as validated in multiple studies [114, 137, 138].

The selection of a plasmonic metal for SERS applications is typically guided by its optical properties within the desired spectral region (UV, Visible, Near-IR) and can be tailored based on specific measurement requirements. Silver is one of the most effective and widely used noble metals for SERS in the visible range (compatible with commercial Raman systems) due to its pronounced LSPR properties and exceptionally low optical losses [130, 139–142]. While traditional SERS heavily relies on the noble metals (such as Ag, Au), transition metals (e.g., Pt, Pd, Rh, Co, Ni) offer distinct advantages that address specific sensing limitations. First, unlike chemically inert noble metals, transition metals are widely used in industrial catalysis [143]. Consequently, SERS substrates that are composed of these materials can function simultaneously as the catalyst and the sensor, enabling the in-situ monitoring of chemical reactions on the surface. Second, and highly significant for this work, transition metals exhibit plasmonic resonances that are naturally shifted towards the UV spectral range [144, 145]. As previously established, the operation in the UV offers significant analytical advantages, including the avoidance of fluorescence backgrounds and the ability to leverage resonance Raman enhancement for biomolecules (e.g., DNA, amino acids) that absorb strongly in the UV [15, 17]. This unique optical capability has recently motivated the exploration of alternative UV-SERS platforms [146], including those based on Rhodium [147] and Cobalt [16].

The plasmon resonance frequency of nanoparticles can be adjusted by modifying their shape, dimensions, and material composition. However, the practical applications of these platforms are significantly limited by chemical degradation. Many metals commonly used for SERS fabrication are susceptible to rapid oxidation when exposed to ambient conditions [148]. This oxidation causes a shift in their plasmonic resonance and leads to a severe loss of SERS activity. Common silver-based SERS substrates often lose their efficacy within days or weeks. Quantitative studies on anisotropic silver nanoparticles (spheres, cubes, and disks) have shown that even moderate temperatures can initiate surface oxidation that fundamentally reorganizes the optical resonance landscape [5]. The degradation process is further accelerated by the atmospheric pollutants and moisture. For instance, the longitudinal experiments on silver and gold nanoparticles that are stored in seawater revealed a dramatic loss of SERS activity: the Raman signal dropped to 50% after four weeks, 15% after eight weeks, and was completely extinguished within twelve weeks [149].

The shelf life of SERS substrates is crucial for maintaining their sensitivity. If these substrates degrade or lose their enhancement properties over time, the detection results can become inconsistent and unreliable [150]. Moreover, the high chemical reactivity of metal surfaces can result in undesirable interactions with detectable analytes, causing spectral distortions, photocarbonization, and photobleaching under intense laser illumination [13, 14]. To address these challenges, substrates must be protected or should undergo additional treatments. This is particularly critical in applications where evidence needs to remain stable for retrospective testing, as well as in environmental monitoring, where sensors are exposed to harsh aqueous or atmospheric conditions for extended periods [4, 12, 151].

1.4.1. Graphene-Metal Hybrid SERS Platforms

In order to mitigate the inherent chemical instabilities of standard SERS platforms, the integration of graphene and its derivatives have emerged as a transformative strategy for designing the next generation of sensors [152–155]. Owing to its exceptional electronic properties, atomic impermeability, and chemical stability [156], graphene enhances SERS performance through multiple synergistic avenues: surface passivation, molecular adsorption, fluorescence quenching and chemical enhancement [157–159]. While graphene can be integrated with plasmonic metals in various configurations, this section primarily focuses on two foundational architectures that are directly relevant to this dissertation:

Graphene Overlayers and Planar Shielding

The overlayer configuration involves the transfer or direct deposition of a 2D graphene sheet onto prefabricated plasmonic nanostructures. This structural configuration primarily acts as a robust, impermeable physical barrier against environmental degradation: a paramount requirement for noble metal substrates where rapid oxidation and sulfidation are the leading causes of signal decay. Topsakal et al., [160] were the first to demonstrate that while oxygen molecules (O_2) can weakly physisorb onto the graphene surface, they cannot penetrate the lattice to react with the underlying metal. Furthermore, the dissociation of O_2 into reactive atomic oxygen is kinetically inhibited on the chemically inert basal plane. Empirically, Losurdo et al., [161] demonstrated the effectiveness of this barrier in preventing the oxidation of non-ordered silver plasmonic structures, maintaining the metal in a metallic state over months of air exposure. Similarly, Chen et al., [162] proved that the CVD grown graphene directly on the catalytic metals (Ni, Cu) can protect them from oxidizing gases and liquid solutions. However, Yu [163] noted a critical caveat: while graphene significantly retards oxidation, continuous exposure can lead to localized corrosion initiating at defect sites, as common CVD-grown graphene inevitably contains imperfections. Suzuki et al., [164] demonstrated that a graphene-overlayered silver substrate could sustain operational integrity as high as 150 °C. This capability is vital for the in-situ monitoring of catalytic reactions, as the graphene layer effectively traps analyte molecules within the sensing volume, preventing thermal desorption. This can function of the substrate's ability to withstand laser-induced damage during the measurement process.

Beyond physical shielding, the graphene overlayer provides critical electronic passivation. In standard SERS experiments, direct contact between the highly reactive metal surface and the analyte often leads to metal-catalyzed molecular degradation or the formation of strong chemisorbed bonds, which severely distort the intrinsic vibrational spectrum [165–167]. By physically separating the metal from the molecule, the hybrid platform ensures that the resulting SERS signal reflects the true vibrational fingerprint of the analyte, free from spurious peaks associated with side reactions or photocarbonization.

Functioning as an infinite polycyclic aromatic hydrocarbon, graphene exhibits a profound affinity for other aromatic molecules through non-covalent $\pi-\pi$ stacking interactions, contributes to the CM of SERS [116, 140, 158, 168–170]. Density functional theory (DFT) calculations reveal that this adsorption is driven by a combination of dispersion forces and electrostatic interactions, leveraging the large polarizability of the graphene sheet to strongly enrich the analyte concentration directly above the plasmonic near-field [171–173]. This $\pi-\pi$ interaction facilitates efficient charge transfer between the graphene surface and the analyte, increasing the molecular polarizability and providing a highly stable, fluorescence-free background for vibrational fingerprinting [174]. It is important to note that pristine graphene is highly conductive, which is essential for rapid charge transfer, but it is also chemically inert. Efficient molecular adsorption often requires specific binding sites. While defects within graphene can create useful binding sites, excessive defect density can disrupt the delocalized network and degrade the material's conductivity. Quantitative studies [175], have identified an optimal defect density. For instance, mildly reduced graphene oxide has been shown to provide enhancement factors an order of magnitude higher than pristine exfoliated graphene, as oxygen functional groups facilitate stronger binding [176]. Similarly, introducing dopants, such as boron or nitrogen, creates new electronic states that maximize chemisorption and charge transfer without compromising the structural integrity of the lattice [177].

Several studies have demonstrated that using graphene as an overlayer on plasmonic substrates can maintain the plasmonic effects of irregularly distributed aggregates [178, 179] as well as periodic structures [180, 181]. However, there is still a lack of real quantitative long-term signal stability data, which is essential for the industrial and clinical adoption of these sensors.

Graphene Encapsulation and Core-Shell Architectures

In order to overcome the morphological limitations and the unpredictable aggregation of bare nanoparticles, shell-isolated nanoparticle-enhanced Raman spectroscopy (SHINERS) was pioneered by the research group of Tian et al., in 2010 [182]. This revolutionary architecture encapsulates individual plasmonic cores within a chemically inert shell. The thickness of this shell plays a vital role in this architecture since electromagnetic enhancement decays exponentially with a distance (r^{-10}) from the metal surface [167]. As Li et al., [183] demonstrated, typically, the thickness of several nanometers is needed to ensure pinhole-free coverage of the particles.

While early SHINERS utilized dielectric insulators, such as silica (SiO_2) and alumina (Al_2O_3), the integration of graphitic shells has emerged as a transformative advancement [184, 185]. Unlike dielectric shells, graphene derivatives contribute an additional chemical enhancement mechanism termed graphene-enhanced Raman spectroscopy (GERS). Mediated primarily by charge transfer and $\pi-\pi$ stacking, GERS aligns the molecular energy levels of the adsorbed aromatic analyte with the Fermi level of the graphitic shell, facilitating resonant transitions that significantly increase the Raman cross-section [186, 187].

Furthermore, encapsulation provides a 3D physical barrier that prevents nanoparticle agglomeration: a ubiquitous issue when bare metallic sensors are exposed to proteins, organic acids, or high-salinity environmental samples [188]. A critical advantage of these shells, reported to be their superlative ability to quench fluorescence interference, which can otherwise overwhelm the Raman signal [189]. While the degree of Raman enhancement in GERS is highly dependent on the band alignment between the graphene and the analyte molecules [190], to avoid intrinsic spectral interference, it is recommended to utilize customized dielectric substrates to reduce the background noise and employ finely tuned laser excitation to selectively amplify the analyte via molecular resonance [191, 192].

Addressing the critical gaps identified in the literature, the primary objective of this dissertation is to evaluate graphene-metal hybrid platforms through two distinct architectural approaches. First, the study assesses the feasibility of a novel, three-dimensional nickel-encapsulated graphitic architecture for inaccessible UV-SERS applications. Second, it integrates a planar monolayer graphene shield onto highly reproducible, resonant silver lattice arrays to quantitatively investigate the specific roles of graphene in surface passivation and signal stability via chemical enhancement over an unprecedented year-long period.

2. MATERIALS AND METHODS

2.1. Preparation of Catalytic Substrates for Graphene Growth

2.1.1. Nickel Foil (Case Study I)

Fabrication: the polycrystalline nickel foils used in Case Study I were fabricated by the technical staff at the Technology Development Laboratory (Institute of Materials Science, Kaunas University of Technology) and provided to the author for this research. The foils were produced via electrodeposition using a sulfamate electrolyte (pH 4.0, 40 ºC, density 1.25 g/cm^3) containing boric acid and surfactant additives. In this process, a glass plate coated with a thin evaporated silver layer served as the cathode substrate. The edges were connected via conductive copper tape and sealed with silver paste to ensure uniform current distribution. Electrodeposition was initiated at a low current density (0.25–0.30 A/dm^2) and gradually increased to 2.2–2.5 A/dm^2 until the total charge of approximately 22 A·h/dm^2 was transferred. The resulting nickel layer (~150 µm) was mechanically detached from the substrate, and the sacrificial silver seed layer was selectively removed by immersion in an aqueous ammonia-peroxide solution.

Cleaning: in order to remove the organic contaminants, the Ni foil was cut into 20 × 20 mm squares and immersed in boiling dimethylformamide for 10 minutes, followed by boiling acetone for 10 minutes. Finally, the samples were thoroughly rinsed with deionized water and dried under a nitrogen gas stream. This cleaning protocol was standard for all substrates used in following studies.

Surface modifications: prior to carbon deposition, the homemade Ni foil underwent three distinct pre-treatments to evaluate the influence of surface engineering:

1. Thermal annealing: a 6nm nickel film was first evaporated on cleaned nickel foil by magnetron sputtering onto a nickel foil. The foil was then placed in a quartz furnace at atmospheric pressure with a 200 sccm flow of pure argon (99.999%) and annealed at 500 °C for 1 hour.
2. Nanoparticle pre-deposition: a dispersion was prepared using commercial Ni nanoparticles (Nanochemazone Canada, NCZ4601, purity >99.9%, average size ~80 nm). A mixture containing 100 µl solution of Ni nanoparticles dispersed in water (containing 0.0007 grams of Ni) was added to 5 mL of dimethyl sulfoxide. The cleaned foil was immersed in this suspension 24 hours at room temperature to allow for gravitational sedimentation of the particles onto the surface.
3. Laser ablation: the nickel foil was micro-structured using a 1,064 nm fiber laser (50 W average power, 20 kHz repetition rate). The surface was scanned line-by-line horizontally to create a defined texture.

2.1.2. Silicon Dioxide (Case Study II)

Ultrathin Ni films with four distinct nominal thicknesses (4, 6, 8, and 10 nm) were deposited on silicon dioxide (SiO_2) substrates (15 × 15 mm) via direct-current magnetron sputtering. The deposition performed at a working distance of 23 cm from a 3-inch pure Ni target (99.99%) at a base pressure of ~10^{-5} Pa in constant current mode. These initial thicknesses served as the primary independent variable (Series A–D). In order to transform the films into islands (seeding layer), the samples underwent a dewetting process in a quartz furnace at 500 ºC for 1 hour with a 200 sccm flow of pure argon.

2.1.3. Copper Foil (Case Study III)

Commercial Cu foil (45 µm thickness, 20 × 20 mm) was used for monolayer graphene growth. The cleaned foil was annealed in a quartz furnace at atmospheric pressure under pure argon for 1 hour. This pretreatment promotes the formation of a surface Cu_2O layer, which suppresses nucleation density and facilitates the growth of large continuous layer via plasma-enhanced chemical vapor deposition [193].

2.2. Graphene Growth Process and Protocols

Graphene synthesis was performed using a microwave plasma-enhanced chemical vapor deposition system that features a 2.45 GHz microwave plasma source and a temperature-controlled substrate holder within a cylindrical stainless-steel chamber. This configuration allows for independent control of the substrate temperature and plasma power. Methane ($CH_4 > 99.9\%$ purity) served as the carbon precursor, while hydrogen ($H_2 > 99.999\%$) acted as the reducing and etching gas. Figure 16 illustrates reactor schematic.

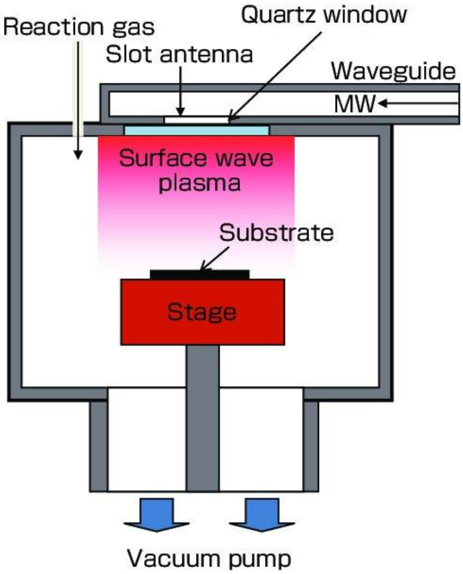

Figure 16. Reactor schematic of the PECVD device *[194]*

Cleaned substrates were loaded into the chamber and heated to the set temperature. Hydrogen was introduced to reduce the surface oxides and etch residues. Subsequently, methane was introduced according to the optimized parameters for each case study. After the deposition period, the plasma was extinguished, and the system was allowed to cool naturally (~25 °C/min). The growth protocol gas flow ratios, power, pressure and deposition time and temperature for the three distinct cases are provided in Table 1.

Table 1. Graphene growth protocol for three distinct case studies

Case Study-Type of substrate	H_2 flow (sccm)	Pre-treatment (time/ temp)	Plasma power (kW)	Pressure (mbar)	CH_4 flow (sccm)	Deposition (time/temp)
Case Study I - Ni foil	Varied	10 min/ 600-750 °C	1.4	27-40	Varied	1-10 min/ 600-750 °C
Case Study II -SiO_2/Ni	200	10 min/ 500 °C	1.3	30	75	10, 20, 40, 60 min/ 500 °C
Case Study III -Cu foil	200	10 min/ 550 °C	1.1	24	25	10 min/ 550 °C

Specific Configurations

Thermal management (Case Study I & III): metal foils were mounted on a specialized metal holder with a central aperture. This elevated the foils above the stage, minimizing thermal contact and heat loss during synthesis.

Protective shielding (Case Study II): a custom-built stainless-steel shield (5 mm height) was placed over the substrates to promote the growth of encapsulated morphologies and protect the delicate nickel islands from excessive plasma etching [195].

2.3. Fabrication of Graphene Hybrid Ag-SERS Platforms (Case Study III)

2.3.1. Synthesis and Assembly of Silver Nanocubes

Synthesis: monodisperse silver nanocubes (AgNCs) with an average edge length of 77 ± 3 nm were synthesized at the National Institute for Materials Science (NIMS) in Japan by Dr. Joel Henzie and provided for this study. The synthesis followed a modified polyol method, utilizing polyvinylpyrrolidone as a capping agent to direct the shape evolution and stabilize the cubic morphology [196].

Assembly process: periodic arrays were fabricated using capillarity-assisted particle assembly (CAPA) [197]. First, a polydimethylsiloxane (PDMS) template was created by soft lithography replication of a silicon master stamp [198]. The stamp featured a 20 × 20 mm array of pillars (180 nm diameter, 100 nm height, 400 nm periodicity). The AgNCs suspension was concentrated for assembly by centrifugation and redispersed in a 1:2 ethanol/dimethylformamide solution [198]. The assembly was conducted on a custom-built setup where the PDMS template moved at a controlled speed of 1 μm/s relative to a fixed droplet of the nanoparticle suspension [128]. Following assembly, the substrates were rinsed with 0.1 M hydrochloric acid for 30 seconds, followed by ethanol and deionized water to remove polyvinylpyrrolidone.

2.3.2. Graphene Dry Transfer from Copper

A modified dry transfer method was employed to transfer graphene from the Cu growth substrate to the Ag-SERS platform:

6. **Lamination:** a commercial water-soluble polyvinyl alcohol (PVA) film (30 µm thick, paper-backed) was laminated onto the graphene/Cu foil using a hot-roll laminator at 110 °C [199].
7. **Detachment:** Cu foil was oxidized by overnight immersion in deionized water to weaken the graphene-metal interface, allowing the PVA/graphene stack to be mechanically peeled off (Figure 17).
8. **Transfer:** the PVA/graphene film was laminated onto the target Ag-SERS substrate. The paper backing was removed, and the PVA was dissolved by immersing the sample in deionized water at room temperature overnight, leaving the graphene monolayer protecting the silver arrays.

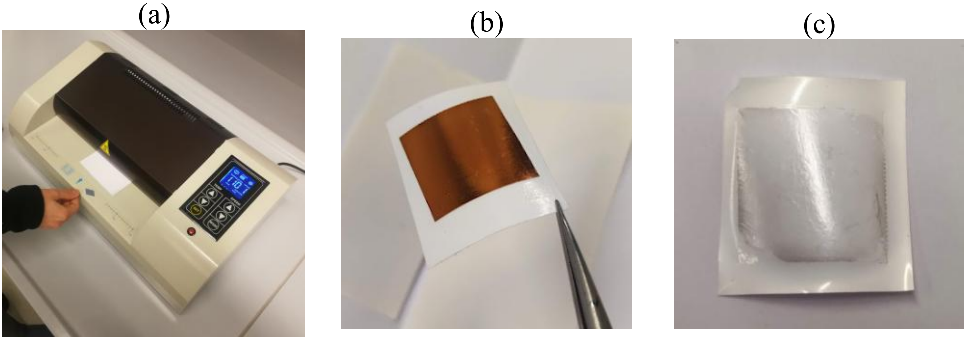

Figure 17. PVA-mediated dry transfer process: a) lamination of the copper foil with graphene onto the PVA layer, b) laminated structure consisting of PVA and copper foil with graphene, c) detachment of copper foil from the PVA sheet

2.4. Characterization Techniques

2.4.1. Scanning Electron Microscopy/Energy Dispersive Spectroscopy

Surface morphological analysis and elemental mapping were conducted using high-resolution electron microscopy to characterize the nanostructure evolution of the catalytic substrates and hybrid platforms.

High-resolution SEM imaging parameters: the primary morphological characterization was performed using an FEI Quanta 200 FEG scanning electron microscope. This system is equipped with a Schottky-type field emission electron gun, which provides a high-bright, coherent electron beam that is essential for nanoscale imaging.

Topographic imaging: routine surface imaging was conducted under high-vacuum conditions using an accelerating voltage of 30 kV. This high-energy beam was selected to maximize the lateral resolution (achieving up to 1.2 nm), providing the necessary contrast to resolve the fine boundaries of the dewetted nickel islands and the sharp edges of the silver nanocubes.

Morphological assessment: the system was used to track the transformation of continuous metal films into discrete islands during the dewetting process and verify the uniformity of the capillary-assembled silver arrays on the PDMS templates.

Elemental EDS mapping: the elemental analysis was performed using an integrated EDS spectrometer. A critical methodological optimization was applied to the accelerating voltage to ensure accurate compositional data for the thin-film structures:

Low-voltage mapping: while imaging required high energy, EDS was conducted at a lower accelerating voltage of 5 kV.

Interaction volume optimization: this reduction was essential to minimize the interaction volume of the electron beam within the sample. By limiting the penetration depth, the excitation was confined primarily to the surface layers. This allowed for the precise discrimination of the graphitic shells and nickel cores from the underlying silicon dioxide or bulk substrates, preventing the background signal from overwhelming the spectral signature of the nanomaterials.

Data processing: three steps have been followed for the data processing: deep learning segmentation, algorithm training, and statistical extraction.

Deep learning segmentation: in order to move beyond qualitative observation, the quantitative analysis of the nanostructure size distributions was performed using a semi-automated computational workflow. Raw SEM micrographs, specifically those of the dewetted nickel islands and subsequent graphitic shells, were processed using "Ilastik", an interactive machine-learning toolkit.

Algorithm training: a deep-learning pixel classification algorithm was trained on representative image subsets to recognize and segment the nanoparticles from the complex substrate background.

Statistical extraction: this segmentation enabled the automated extraction of morphological statistics, including particle density and equivalent disk diameters (d_{eq}), ensuring that the size distribution histograms were statistically robust and reproducible.

2.4.2. X-ray Diffraction

In order to determine the crystallographic orientation and phase purity of the synthesized Nickel foil, X-ray diffraction analysis was performed using a Bruker D8 Discover diffractometer (Bruker AXS GmbH).

Instrument configuration: the measurements were conducted in a parallel beam geometry using Cu Kα radiation ($\lambda = 1.54$ Å) as the X-ray source. This configuration was selected to minimize the errors arising from sample roughness, ensuring accurate peak positioning for the electrodeposited nickel foils.

Scanning parameters: diffractograms were acquired over a 2θ angular range of 40° to 100°, covering the primary reflection planes of face-centered cubic (fcc) nickel.

Data processing: the resultant diffraction patterns were processed using DIFFRAC.EVA software. The phase identification was performed by matching the experimental peaks against standard reference patterns from the ICDD (International Centre for Diffraction Data) database. Specifically, the analysis focused on the relative intensity ratios of the (111), (200), and (220) reflections to quantify the degree of polycrystalline texture.

2.4.3. Spectroscopic Ellipsometry

In order to precisely verify the thickness of the deposited nickel thin films prior to dewetting process in Case Study II, variable angle spectroscopic ellipsometry was performed using a Semilab GES5-E rotating compensatory ellipsometer. This system is equipped with a high-intensity Xenon arc lamp, covering a broad spectral range from 185 nm to 2,000 nm.

Measurement protocol: to ensure statistical reliability and account for any potential non-uniformity in the sputtering process, the data were acquired from three distinct locations on each sample. For each spot, the change in polarization state (Ψ and Δ) was recorded at six different angles of incidence, ranging from 50° to 75° in 5° increments. This multi-angle approach is critical for minimizing the correlation effects between the film thickness and optical constants during the fitting process.

Optical modeling: the data analysis was performed using the Semilab spectroscopic ellipsometry analyzer software. The thickness extraction was based on a stratified three-layer optical model:

1. *Substrate*: silicon dioxide with optical constants fixed to standard literature values.
2. *Active layer*: the metallic nickel film; the dispersion curves (n and k) were initially taken from the software's material database and refined to fit the experimental data.
3. *Ambient air*: the film thickness was determined by minimizing the mean squared error between the measured polarization data and the model-generated curves.

2.4.4. Atomic Force Microscopy

AFM was performed using a JPK NanoWizard 3 system (JPK Instruments, Germany) to quantify the three-dimensional surface topography and roughness evolution of the substrates.

Operational parameters and mode selection: high-resolution topographic images were acquired using I-shaped silicon cantilevers (AppNano, USA) equipped with tetrahedral tips.

Intermittent contact mode: all measurements were conducted in intermittent contact mode (AC/tapping mode) rather than standard contact mode. This methodological choice was critical due to the mechanical fragility of the graphitic shells formed in Case Study II. Contact mode scanning exerts significant lateral shear forces that were found to damage or detach the delicate carbon structures, particularly in samples with shorter growth durations (10 min). By oscillating the cantilever near its resonance frequency and sensing the dampening of the amplitude, the intermittent mode minimized the tip-sample interaction forces, preserving the integrity of the nanostructures.

Scanning protocols: in order to capture both the macroscopic uniformity and microscopic details of the dewetted islands, the scans were performed over two distinct field sizes: 10 × 10 μm for general survey and roughness statistics and 2.5 × 2.5 μm for high-resolution single-particle analysis.

Data processing and artifact correction: the raw topographic data were processed using Gwyddion (open-source software for SPM data analysis). The workflow included four steps:

1. *Leveling*: polynomial background subtraction was applied to remove sample tilt and scanner bow.
2. *Noise reduction*: line-by-line median filtering was used to eliminate high-frequency scanning noise.
3. *Tip deconvolution*: a crucial step in analyzing the lateral dimensions of nanoparticles is correcting for the finite radius of the AFM tip, which can artificially broaden features. A morphological dilation algorithm (tip deconvolution) was applied to reconstruct the true lateral geometry of the nickel islands.
4. *Statistical analysis*: the root mean square (RMS) roughness (R_q) was calculated from the height distribution data.

In order to rectify the tip-sample convolution artifacts inherent in AFM imaging, a blind tip estimation and surface reconstruction algorithm was applied to the raw topographic data. Since the finite radius of the probe tip artificially broadens the lateral dimensions of nanostructures, a direct analysis of raw scans leads to an overestimation of particle size.

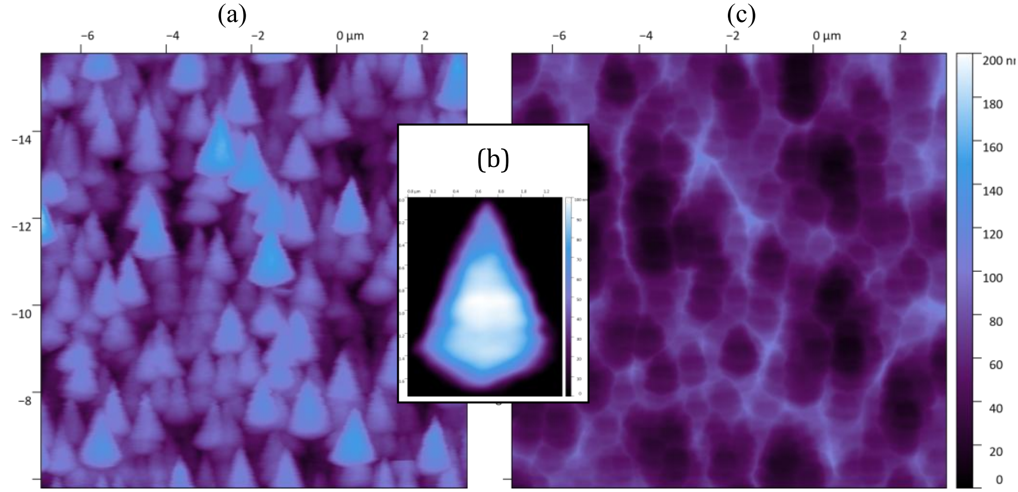

Figure 18. Illustration of the AFM blind tip deconvolution workflow: (a) the raw topographic AFM micrograph exhibiting tip-dilation artifacts, (b) the estimated geometry of the AFM probe tip, and (c) the final deconvoluted surface topography

As illustrated in Figure 18a, the deconvolution workflow first utilizes the steepest slopes within the raw micrograph to numerically reconstruct the geometry of the AFM tip (Figure 18b). This estimated tip shape is then mathematically “eroded” from the original data, yielding a deconvoluted surface topography (Figure 18c). This correction was essential for accurately resolving the boundaries of the dewetted nickel islands and ensuring the validity of the statistical size distribution analysis, as presented in case study II of the next chapter.

2.4.5. X-Ray Photoelectron Spectroscopy

In order to determine the elemental composition, stoichiometry, and precise chemical bonding states of the surface layers, XPS was performed using a Kratos XSAM800 spectrometer (Kratos Analytical, UK).

Instrumentation and environmental conditions: photoelectrons were excited using non-monochromatic Al Kα radiation (hν = 1,486.6 eV). All measurements were conducted under ultra-high vacuum conditions to prevent surface contamination and electron scattering with a base pressure in the analytical chamber maintained below 5.8×10^{-8} Pa. To ensure the accuracy of the binding energy (E_B) scale, the system was calibrated using the standard reference peaks of Au $4f_{7/2}$ (84.0 eV), Ag $3d_{5/2}$ (368.3 eV), and Cu $2p_{3/2}$ (932.7 eV).

Data acquisition protocols: spectra were acquired using a hemispherical electron energy analyzer configured for high-resolution analysis. Wide-scan survey spectra were collected with a step size of 0.5 eV to identify all elements present on the surface. Detailed spectra of the C 1s (carbon) and Ni 2p (nickel) regions were acquired with a fine step size of 0.1 eV. Notably, these scans were performed at a fixed pass energy of 20 eV. This low pass energy was selected to maximize the energy resolution, allowing for the deconvolution of closely spaced oxidation states (e.g., distinguishing metallic Ni^0 from Ni^{2+}).

Spectral deconvolution and curve fitting: the data analysis was performed using XPSPEAK 4.1 software. A Shirley-type background subtraction was applied to all spectra to account for the background arising from inelastic electron scattering. A specific peak-fitting strategy was employed to accurately model the physics of the photoemission process for conductive vs. non-conductive phases:

Conduction electron interaction (asymmetric peaks): for the metallic nickel core (Ni^0) and the graphite carbon shell (sp^2 C=C), the lineshapes were modeled using an asymmetric function. This asymmetry arises from the interaction of the photohole with conduction electrons in metallic systems. These peaks were fitted using a sum of Lorentzian–Gaussian functions with a ratio of 70:30.

Dielectric/oxide phases (symmetric peaks): for insulating or semiconducting components, such as nickel oxide/hydroxide ($Ni(OH)_2$) and defect-related carbon (sp^3 C-C), the peaks were modeled using a symmetric function. These were fitted using a product of Lorentzian–Gaussian functions with a ratio of 30:70.

2.4.6. Raman Scattering Spectroscopy

Raman measurements were performed to probe the vibrational phonon modes of the synthesized carbon films and detect the spectral fingerprints of SERS analytes. All spectra were acquired using a Renishaw InVia Raman spectrometer equipped with a confocal microscope (Leica) and a thermoelectrically cooled CCD detector.

Instrumentation and optical configuration: the measurements were conducted utilizing multiple laser excitation sources tailored to the specific resonance requirements of each case study. A diode-pumped solid-state laser with a wavelength of 532 nm (2.33 eV) was utilized as the primary source for the structural characterization of graphene-based materials and visible-range SERS evaluation in Case Study III. The measurements for the specialized ultraviolet SERRS feasibility study (Case Study II) were conducted at the Center for Physical Sciences and Technology, utilizing a 325 nm continuous-wave He-Cd laser to align with the intrinsic electronic transitions of the analyte and the plasmonic resonance of the nickel cores. A 442 nm He-Cd laser was additionally employed for non-resonant control experiments. The laser beams were focused onto the sample surface using a 50× objective lens, providing a spot diameter, sufficient to smooth out the local microscopic heterogeneities.

Acquisition protocols: to accommodate the varying thermal sensitivities of the samples and specific enhancement mechanisms, three distinct acquisition protocols were defined:

Protocol A (structural characterization): for the analysis of graphene on metal foils and graphitic shells (532 nm excitation), a laser power of 2.25 mW and an integration time of 10 seconds were employed. This power level provided a high signal-to-noise ratio without inducing thermal damage to the carbon lattice.

Protocol B (Ag-SERS measurements): for the silver-based SERS platforms in Case Study III (532 nm excitation), the laser power was strictly limited to 0.3 mW with an exposure time of 60 seconds to prevent localized plasmonic heating and photo-degradation of the 2NT analyte.

Protocol C (UV-SERRS measurements): for the detection of adenine on the nickel-encapsulated shells (Case Study II), the 325 nm UV laser was utilized at an appropriately low power threshold to prevent the photo-carbonization of the biomolecule while maximizing the resonant signal amplification.

Spectral deconvolution and fitting models: the post-processing was performed using OriginPro and custom MATLAB scripts. Depending on the structural disorder of the sample, one of two peak-fitting models was applied using the Levenberg–Marquardt algorithm:

Standard 4-to-7 band model: used for high-quality graphene (Case I and III). This model fits the prominent D band (~1,350 cm^{-1}), G band (~1,580 cm^{-1}), D' band (~1,620 cm^{-1}) and 2D band (~2,680 cm^{-1}). In monolayer graphene samples (Case III), additional weak components were included to accurately account for the spectral background.

Extended 11-band model: used for disordered graphitic shells (Case II). In order to disentangle the complex contributions of amorphous carbon and specific defect types, a comprehensive model incorporating 11 vibrational modes was adopted. This included specific Gaussian components for amorphous phases ($D_1^\star$ at 1,450 cm^{-1}, $D_2^\star$ at 1,500 cm^{-1}) and "hidden" defect modes in the valley region (D_1'' at 1,100 cm^{-1}, D_2'' at 1,230 cm^{-1}).

Normalization strategies: in order to ensure comparability across datasets with different signal intensities, two specific normalization techniques were implemented:

band normalization: for the disordered shells (Case Study II), where the absolute intensity of the G-band varies significantly with film thickness, raw spectra were also normalized to the integrated average intensity of the "quiet band" (1,900–2,200 cm^{-1}) and D band. As quiet band is completely free from first- or second-order Raman features, this method avoids the mathematical artifacts introduced by standard G-band normalization. Following normalization, the spectra were subjected to baseline correction using the least squares method to effectively remove the photoluminescence background. Finally, the peak fitting process was performed using Levenberg–Marquardt algorithm without prior smoothing to preserve subtle spectral features.

Euclidean normalization: for the longitudinal SERS stability study (Case Study III), where absolute intensity fluctuations occur over months, the spectra were pre-processed with Savitzky–Golay filter (for noise reduction) and a non-quadratic asymmetric Huber function (for baseline removal). The final spectra were normalized by dividing the intensity vector by its Euclidean norm (L^2-norm) to standardize the total signal energy for PCA analysis. This will be explained in detail further.

Metric definitions: Table 2 presents the abbreviated notations used to define the Raman spectroscopic metrics employed in this study.

Table 2. Abbreviated notations used in the spectroscopic metrics of this study: examples for the 2D band

Notation	Conventional Expression	Description
$\mathrm{C(2D)}$	Center of 2D band	The peak position of the 2D band.
$\mathrm{W(2D)}$	$\mathrm{FWHM_{2D}}$	The full width at half-maximum of the 2D band.
$\mathrm{A(2D)}$	$\mathrm{A_{2D}}$	The total integrated area under the 2D band.
$\mathrm{I(2D)}$	$\mathrm{I_{2D}}$	The peak intensity of the 2D band.
$\mathrm{I(2D\!:Q)}$	$\mathrm{I_{2D}/I_Q}$	The intensity of the 2D band, normalized to the quiet band average intensity ($1{,}900-2{,}200\ \mathrm{cm^{-1}}$).
$\mathrm{I(2D\!:D)}$	$\mathrm{I_{2D}/I_D}$	The ratio of the intensities of 2D and D bands.
$\mathrm{A(2D\!:T)}$	$\mathrm{A_{2D}/A_{total}}$	The area of the 2D band, normalized to the total spectroscopic response after background removal.

2.4.7. UV-Vis-nIR Spectroscopy

In order to characterize the optical properties of the synthesized materials, steady-state extinction spectra were acquired using an AvaSpec-2048 fiber-optic spectrometer (Avantes).

Instrumentation and acquisition: a collimated AvaLight-DHc source, combining deuterium and halogen lamps, was used to cover a broad spectral range from 170 nm to 1,100 nm. The spectra were collected with a spectral resolution of 1.4 nm. An integration time of 250 ms was used to ensure high signal-to-noise ratios, and 20 individual scans were averaged for each measurement.

The measurements were taken at three distinct spots on each sample for statistical reliability. Absorbance (Abs) was derived from the transmittance T_λ, data using the Beer–Lambert relation ($\mathrm{Abs}_\lambda = -\log T_\lambda$), under the assumption that scattering and reflection contributions were negligible within the experimental context, thereby allowing the absorption to be directly inferred from the transmission measurements.

Metric derivation and normalization: besides identifying the wavelength of maximum absorbance (λ_{max}), the absorbance was evaluated at three specific regions: ultraviolet ($\mathrm{Abs(UV)}{\sim}250\ nm$), visible ($\mathrm{Abs(Vis)}{\sim}450\ \mathrm{nm}$), and infrared (Abs(IR)~$1{,}000$ nm). Various normalization strategies from absorbance ratios of divisions (Abs(Vis:UV),Abs(UV:IR)) and subtraction (Abs(UV-IR)) Abs(Vis-IR) were applied for comparison and further used in the correlation study.

2.4.8. Transient Absorption Spectroscopy

In order to probe the ultrafast carrier relaxation dynamics, specifically electron-phonon (thermalization) and phonon-phonon (cooling) scattering, pump-probe spectroscopy was performed using a HARPIA spectrometer (Light Conversion).

Optical setup: the primary source was a Yb:KGW laser (Pharos, Light Conversion) emitting pulses of 290 fs duration at a fundamental wavelength of 1,030 nm. A collinear optical parametric generator (Orpheus) coupled with a harmonic generator was used to produce excitation pulses at 350 nm (3.54 eV). The pump fluence was maintained at $26.4\ \mu J/cm^2$ to ensure linear excitation regimes. A white-light supercontinuum probe, covering the spectral range of 477–780 nm, was generated by focusing a portion of the fundamental laser output into a 2 mm thick sapphire plate. The pump and probe beam diameters were approximately 700 µm and 500 µm, respectively, ensuring that the probed region was uniformly excited.

Data processing: to address the low signal-to-noise ratio inherent in disordered graphitic samples (particularly those with short growth durations), a specialized "consolidated trace" workflow was developed:

1. *Normalization*: instead of relying on a single wavelength trace, 207 individual spectral traces (ranging from 538 to 792 nm) were extracted. Each trace was normalized by its negative peak amplitude at time zero ($t = 0$).
2. *Averaging and interpolation*: normalized traces were averaged to construct a single, high-fidelity relaxation curve. The data was interpolated to 10,000 points using a spline function to facilitate robust fitting.
3. *Bi-exponential fitting:* relaxation dynamics were quantified by fitting the consolidated curve to a bi-exponential decay function to extract the thermalization and cooling time constants.

2.5. Statistical Analysis

In order to systematically analyze the Raman signal obtained from the 2NT analyte in SERS measurement (Case Study III), a multi-step data processing workflow was implemented, as previously mentioned. The Raman spectra obtained from each sample were imported and pre-processed using a custom MATLAB script. The noise in the raw spectra was mitigated using a Savitzky–Golay filter to enhance signal clarity. The spectral baseline was corrected using a non-quadratic asymmetric Huber function [200], which minimizes a non-quadratic cost function to effectively remove broad non-specific background signals while preserving analyte-specific Raman signatures. Following baseline correction, all spectra were normalized by dividing the intensity values by the Euclidean norm of the spectral vector to ensure comparability across datasets.

Principal component analysis: PCA is a multivariate statistical technique typically employed to extract significant components from high-dimensional data [201, 202]. Mathematically, the algorithm standardizes the input data (e.g., centering and scaling), computes the covariance matrix, and extracts the principal components (PCs) that represent the orthogonal directions of maximum variance. In this dissertation, PCA was utilized for two distinct purposes:

Metric reduction (Case Study II): to reduce the complexity of a dataset containing 107 derived metrics, facilitating the visualization of latent correlations between Raman, UV-Vis-nIR, and TAS parameters.

Signal stability tracking (Case Study III): to quantify the "analyte detection score". By building a model based on the spectral signatures of reference materials (2NT, PDMS, and Graphene), time-resolved SERS spectra were projected onto the defined PCs, allowing for the precise monitoring of signal stability over a 344-day period.

3. RESULTS AND DISCUSSION

3.1. Case Study I: Preliminary Investigation of Nickel as Catalyst in PECVD

This section presents a preliminary investigation to clarify the behavior of nickel as a catalyst in the PECVD graphene growth technique, while analyzing the surface effects on the deposited carbon film.

3.1.1. Study Design and Parametric Optimization

This study involved a comparative analysis of two substrate classes (polycrystalline nickel foil and nickel seeded on silicon dioxide) and various gas regimes (hydrogen-rich, carbon-rich, and moderate).

The investigation began with a standard hydrogen-rich recipe [88] on polycrystalline nickel foil. Following the identification of thermal and kinetic limitations, the process was shifted to a carbon-rich regime [203] to evaluate three distinct surface engineering strategies on the foil: (1) argon-annealed Ni film, (2) Ni particle-decorated surface, and (3) laser-ablated micro-structures.

Finally, in order to translate the morphology observed on rough foils to a dielectric substrate (the primary objective of Case Study II), the investigation culminated in a comparative study on SiO_2, for which a moderate gas regime [53] was selected. The details of the parametric operation in PECVD are outlined in Table 3.

Table 3. Parametric optimization of PECVD growth on polycrystalline Ni foil

Phase	Substrate Config	Ratio H_2:CH_4	Pressure (mbar)	Power (kW)	Temp / Time	Observation
Hydrogen-Rich	Ni foil (on stage)	80:1	27	1.4	600 °C /1 min	No continuous film
Hydrogen-Rich (thermal treatment)	Ni foil (on metal holder)	80:1	27	1.4	600 °C /10 min	Improved thermal stability, low growth rate
Carbon-Rich (Ni foil)	Ni foil (metal holder)	1.3:1	30	1.4	770 °C /10 min	Recipe used for surface engineering on Ni foil
Moderate-Regime on (SiO_2)	SiO_2 (on stage)	3:1	40	1.3	750 °C /10 min	Recipe used on insulator substrate

3.1.2. Surface Analysis

The crystallographic structure of the electrodeposited nickel foil was analyzed via X-ray diffraction. As shown in Figure 19, the diffraction pattern exhibits three distinct sharp peaks corresponding to the (111), (200), and (220) lattice planes. The presence of these multiple reflections confirms the polycrystalline nature of the substrate.

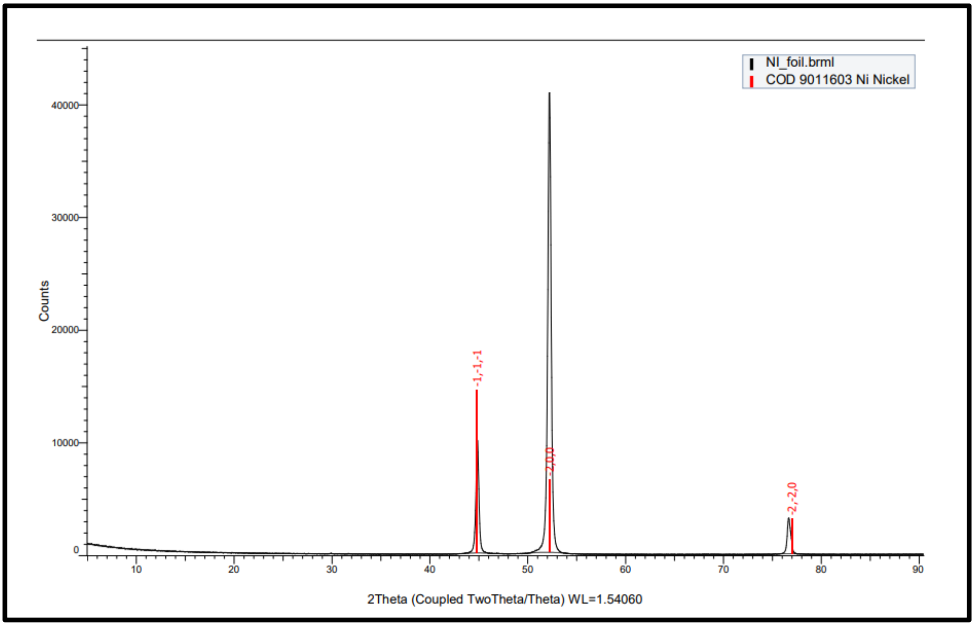

Figure 19. X-ray diffraction pattern of the homemade polycrystalline nickel foil

Initial trials employed a standard hydrogen-rich regime (H_2:CH_4 ~80:1): a ratio typically cited in literature for high-quality monolayer synthesis. However, when the nickel foil was placed directly on the water-cooled substrate stage, the process yielded insufficient film growth. As shown in the optical micrograph in **Figure *20***a, the surface exhibits pronounced grain boundaries with no visible optical contrast change, indicating that the high atomic hydrogen flux etched carbon species faster than they could nucleate on the surface. This is due to a short duration of the growth process (1 min) and direct contact with the cooled stage, which prevents the nickel foil from reaching the critical temperature required for efficient carbon solubility.

In order to address this, the process was refined by introducing a custom metal holder to physically isolate the foil from the cooled stage. This geometric modification fundamentally altered the thermodynamic environment. As evidenced in **Figure *20***b, the surface exhibited a distinct brownish discoloration and less intense grain boundary contrast.

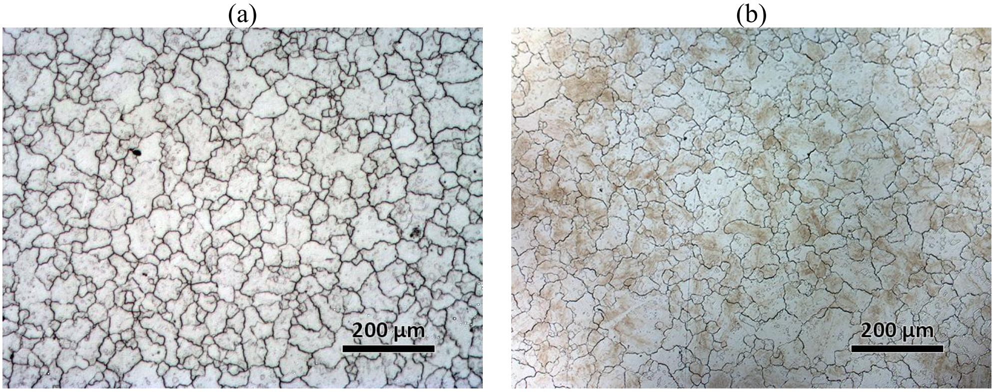

Figure 20. The optical microscopy images of the polycrystalline nickel foil after carbon deposition: (a) foil directly on the cooling stage with 1 min grow duration and (b) foil on a custom metal holder in the PECVD chamber at a hydrogen-rich regime with 10 min grow duration

By elevating the foil, the holder minimized conductive thermal losses to the stage, and longer grow duration allowed the plasma ball to effectively heat the substrate to the reaction temperature. While this configuration enabled nucleation and grow on the grains based on their orientations, the growth rate under the 80:1 regime remained impractically low for the target application, necessitating the transition to the carbon-rich regime described in the following section.

Figure ***21***b displays representative optical images after graphene growth on polycrystalline nickel foil using high carbon precursor flow (H_2:CH_4 ~20:15 sccm) with 10 minutes grow time.

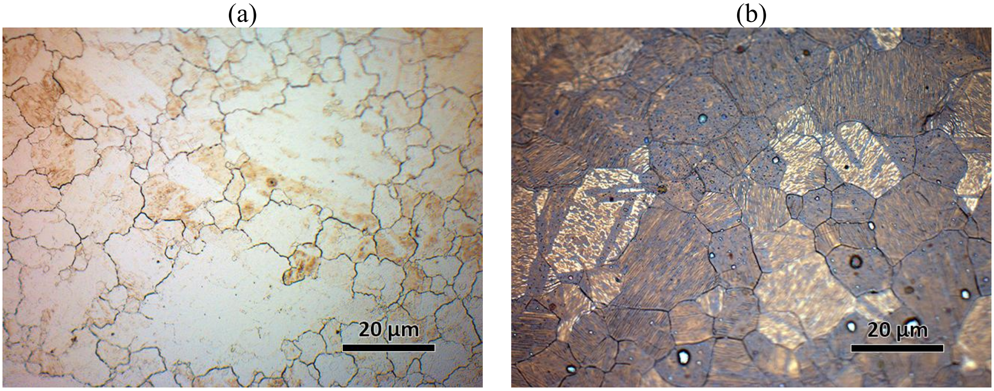

Figure 21. Optical images of nickel foil after the PECVD process in different regimes: (a) hydrogen-rich regime with a growth duration of 10 minutes and (b) carbon-rich regime with a growth duration of 10 minutes

Comparing optical images of nickel foil after the PECVD process at low carbon and high carbon regime reveals a common heterogeneous growth on both samples, where the graphene distribution strictly follows the underlying grains. This observation aligns with the findings of Kozlova et al.,[84], who demonstrated that the crystallographic orientation of individual nickel grains dictates carbon solubility and diffusion rates. The dark lines are carbon atoms that naturally segregated and precipitated at high-energy grain boundaries during cooling.

To investigate the effect of the catalytic surface on the final deposited carbon film, the same carbon-rich recipe was applied to three distinct surface-engineered nickel substrates: thermal-annealed nickel foil with a pre-deposited nickel film, nickel foil with pre-decorated nickel particles, and laser-ablated micro-structured surfaces. The preparation of all these surfaces is detailed in Chapter 2. **Figure *22*** presents optical micrographs with same scale bar of the nickel foil surfaces after graphene growth through plasma-enhanced CVD, using high carbon flow and a growth duration of 10 minutes.

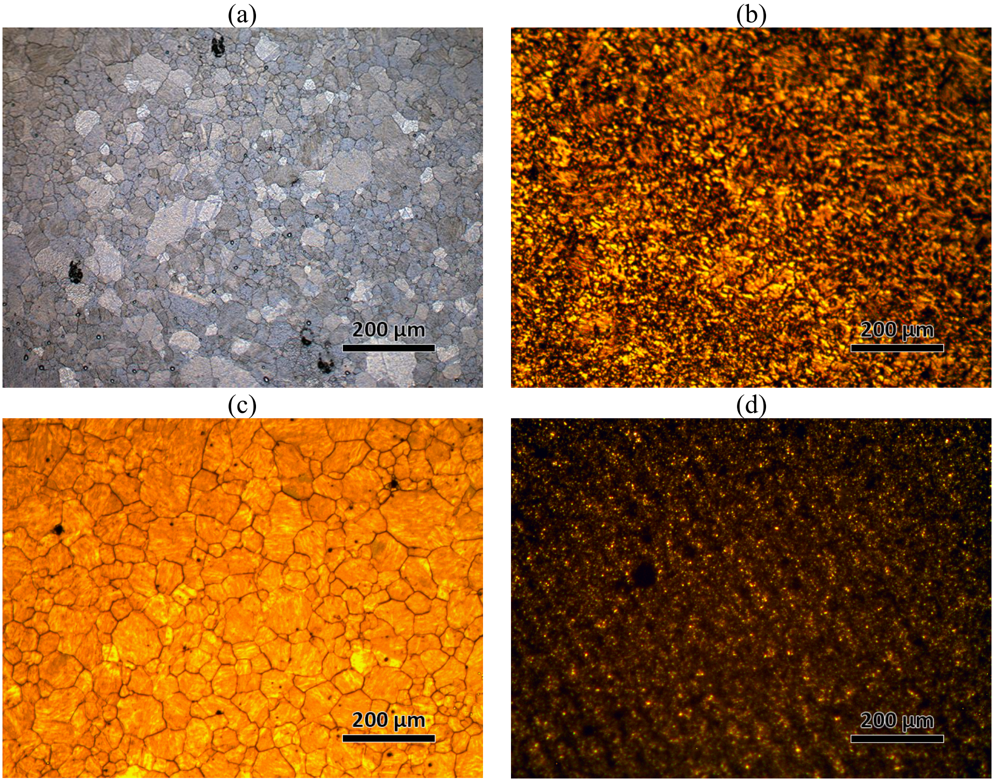

Figure 22. Optical micrographs of foil surfaces after graphene growth through PECVD, using a high carbon flow and a growth duration of 10 minutes on: (a) untreated, (b) thermal argon annealed film on foil, (c) particle-decorated, and (d) laser-ablated Ni foil

Figure *22*a presents a broader view of the untreated reference foil that presented in **Figure *21***b. As discussed, earlier surface exhibits a distinct lack of homogeneity with carbon film growth kinetics are strictly dictated by the underlying crystallographic orientation of individual nickel grains. The thermal-annealed sample (Figure 22b), prepared by evaporating a thin amorphous Ni film and annealing at 500 ºC exhibits evidence of complex surface restructuring. Sputtered Ni films typically exhibit a columnar microstructure with a weak fiber texture. While previous studies as discussed in earlier established that annealing in hydrogen and argon atmospheres at high temperatures (~1000 ºC) minimizes internal stress and promotes the secondary recrystallization of large, favorable Ni(111) grains, the lower thermal regime (~500 ºC) employed here was insufficient to drive massive grain enlargement. Furthermore, the lattice mismatch between the deposited thin film and the underlying bulk foil likely restricted uniform structural relaxation. Consequently, the recrystallization process resulted in the formation of numerous small, secondary grains separated by a highly dense network of grain boundaries, manifest as the pronounced dark lines visible in the optical micrograph.

However, the particle-decorated surface (**Figure** *22*c), yielded the most uniform coverage compared to the previous surfaces. This homogeneity can be rationalized by a high-surface-energy nucleation model. The deposited Ni nanoparticles introduce regions of high geometric curvature across the flat foil. According to the Gibbs–Thomson effect, these curved nanoscale surfaces possess a higher chemical potential, which significantly lowers the local activation energy required for carbon dissociation and precipitation. Effectively, these deposited particles act as a dense network of active seeds. By providing these highly favorable, localized precipitation sites across the entire foil, this strategy fundamentally decouples the graphene growth mechanism from the varying carbon diffusion rates and solubilities of the underlying crystallographic grains.

Lastly, is the laser-ablated substrate (Figure 22d) exhibits significant topological roughness which is expected to prevent planar film formation. As described by the energy balance theory [204], the rapid melting and re-solidification induced by the laser pulse created “cauliflower-like” nickel microstructures. Furthermore, as reported by Koda et al., [205], the intense interaction between the laser plasma and ambient air promotes simultaneous aggregation and surface oxidation. This complex defect-rich topology disrupts the continuity required for 2D film formation, instead favoring the localized encapsulation of the nickel features [89].

In order to gain deeper insight into these morphologies, SEM imaging that was performed is displayed in Figure 23.

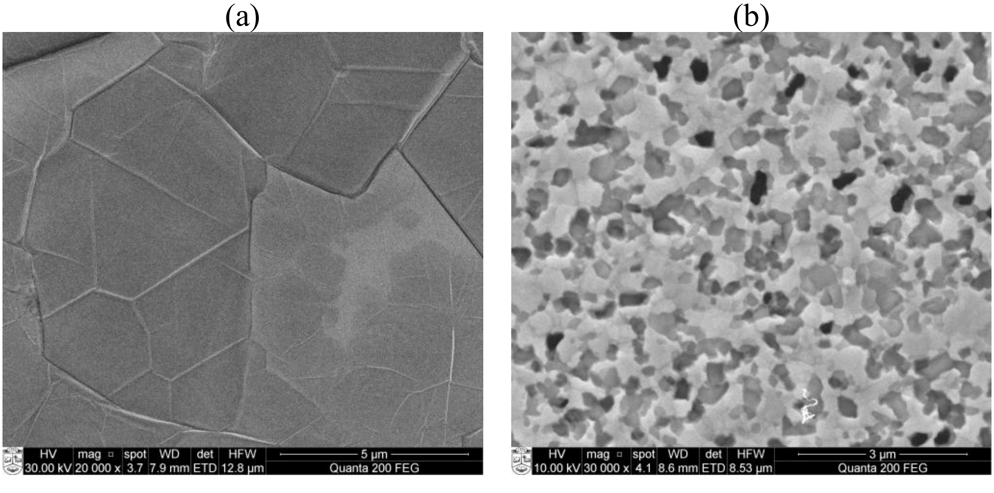
(a) (b)

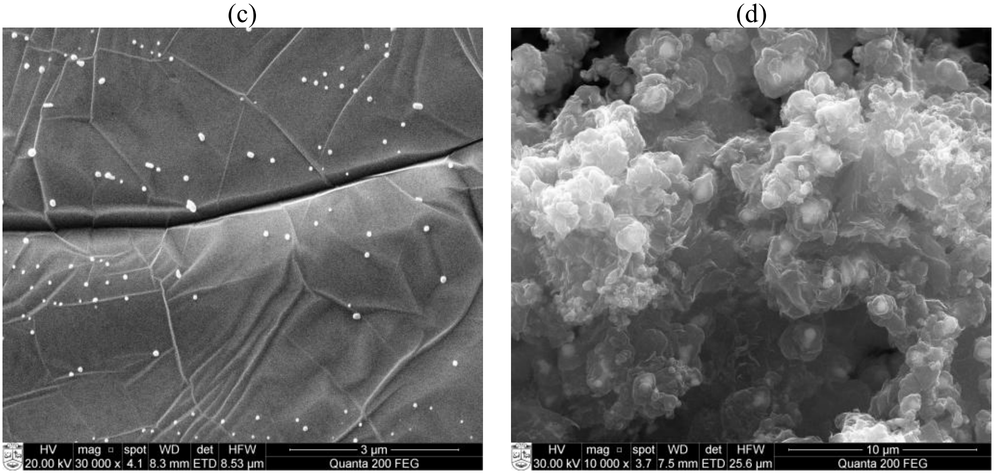

Figure 23. SEM images of foil surfaces after graphene growth through PECVD, using a high carbon flow and a growth duration of 10 minutes on: (a) untreated, (b) thermal argon annealed film on foil, (c) particle-decorated, and (d) laser-ablated Ni foil

The SEM micrographs reveal a fundamental divergence in film continuity driven by the surface engineering strategies. The untreated reference foil (**Figure** *23*a) and particle-decorated foil (**Figure** *23*c) show a continuous graphene film spanning across the foil, while the argon-annealed surface (**Figure** *23*b) and laser-ablated foil (**Figure** *23*d) failed to support continuous large-area growth, though for distinct reasons. The reference sample shows heterogeneity and patchy coverage, with certain areas visibly lacking growth. Conversely, the particle-decorated surface displays a more uniform, blanket-like morphology characterized by a dense network of wrinkles. These wrinkles should not be viewed as defects, as suggested by Moun et al., [206], but rather as stress-relief features. They arise from the relaxation of compressive strain between the graphene lattice and the nickel substrate during the cooling phase. Notably, the electrical transport current is several orders of magnitude higher in these wrinkled areas compared to the flat regions of the graphene films. The annealed foil is characterized by small, planar domains constrained by the crystallographic orientation of the secondary recrystallized grains, as previously discussed. Meanwhile, the laser-ablated surface features small, randomly oriented graphitic flakes that form atop dense topological defects, which act as uncontrolled active sites. As a result, instead of creating a planar sheet, the carbon wraps around the rough nickel features, leading to localized encapsulation.

3.1.3. Raman Analysis (Standard 4-band)

A low-magnification optical survey was first used to identify planar regions within the nickel grains, avoiding grain boundary steps. High-resolution Raman spectra were subsequently acquired from a minimum of three distinct locations on each sample type. To mitigate site-specific variations, these individual scans were mathematically averaged to generate a single consolidated spectral profile for each surface modification. Figure 24 presents average spectra, providing a representative overview of the carbon film vibrational properties. The quantitative metrics listed in Table 4 were derived from the spectral fitting of averaged profiles, ensuring that the reported values reflect the mean structural characteristics of the synthesized film.

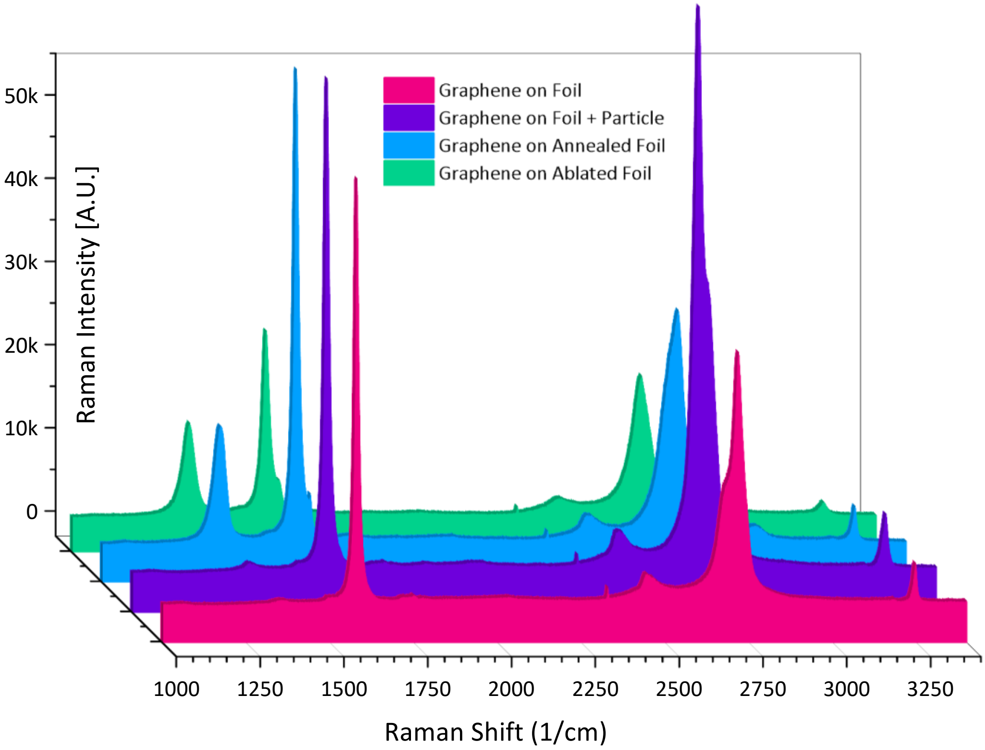

Figure 24. Raman spectra (532 nm excitation) of graphene grown on the four distinct Ni foil surfaces; each spectrum represents the mathematical average of measurements taken from at least three different locations on the sample, smoothing out local heterogeneities

The spectra display four characteristic peaks associated with graphene-based materials, each arising from distinct vibrational phonon modes within the carbon lattice. The G band (~1,580 cm^{-1}) band originates from the in-plane stretching of sp^2 hybridized carbon pairs, representing the intrinsic crystalline graphitic lattice. In contrast, the D band (~1,350 cm^{-1}) is a defect-activated band involving intervalley scattering; it arises only when the perfect honeycomb lattice is disrupted by edges, vacancies, or structural disorder. Similarly, the D' band (~1,620 cm^{-1}) is a defect-induced double-resonance mode, though it is driven by intra-valley scattering processes. Finally, the 2D band (~2,680 cm^{-1}) is a second-order overtone of the D band, acting as a critical indicator of the material's layer count and stacking order. Additionally, Raman bands resulting from interactions between layers cause the 2D band to split into two lower-intensity bands, located around 2,400 cm^{-1} and 3200 cm^{-1}, respectively. A small peak at approximately ~2,300cm^{-1} is also identified as a diagnostic marker for surface chemistry, rather than an intrinsic feature of graphene. This peak may be caused by trace nitrile or alkyne functionalities, likely resulting from the decomposition of DMF solvent residues on the catalytic nickel surface.

The 2D band, as discussed in the literature, is highly sensitive to the number of graphene layers and their stacking order (<5 layers). As the number of layers increases, the 2D band changes in shape and broadens, often splitting into multiple low-intensity peaks due to the changes in the electronic band structure and interlayer interactions [207]. In the case of a monolayer, this band appears as a single, sharp Lorentzian peak. In high-quality graphene, the double-resonance process involves two phonon interactions, making the 2D band particularly intense [207]. Generally, a sharper and narrower 2D band, full width at half maximum (FWHM) of ~40 cm^{-1} [54], and a higher I(2D:G) ratio (typically ≥2 for monolayer and ≥1 for bilayer graphene) [208], along with a lower I(D:G) ratio (<0.1) [98], indicate higher quality in PECVD-grown films.

Table 4. Quantitative metrics derived from the spectral fitting of the average Raman profiles for each sample series

Sample	I(D)	I(G)	I(2D)	W(2D)	I(D:G)	I(2D:G)	La (nm)
Reference Foil	377	50,508	27,182	52.9	0.01	0.5	2,572.6
Particle Decorated	818	58,724	60,475	47.8	0.01	1.0	1,378.3
Annealed Foil	13,932	56,068	26,145	74.0	0.2	0.5	77.3
Ablated Foil	10,872	21,884	15,927	65.3	0.5	0.7	38.6

The minor D band in both particles decorated sample and reference sample confirms that the phonon coherence length exceeds the laser spot size, indicating large graphene domains on the flat grains that heal defects. The particle-decorated sample exhibits the narrowest 2D band (FWHM ~47.8 cm^{-1}) and an I(2D:G) ratio of ~1.0, indicative of high-quality bilayer graphene across the flat grains. It is worth mentioning that the electronic structure rapidly evolves with the number of layers and only monolayers, and to good approximation, its bilayer has simple electronic spectra (both zero-gap semiconductors or zero-overlap semimetals) with one type of electron and one type of hole [25]. The spectra become increasingly complicated for three or more layers: several charge carriers appear, and the conduction and valence bands start notably overlapping [26].

In contrast, the significant D bands in thermal annealed foil and ablated samples reflect the force by high-energy surface defects. Based on Cançado et al., [209], the average crystallite size for graphene domains with G band linewidth of (15–20 cm^{-1}) can be calculated from equation 2, based on the relative area ratios of two prominent bands:

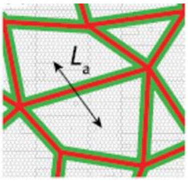

$$L_a\ (nm) = \frac{560}{E_L^4\left(\frac{AD}{AG}\right)}; \qquad (2)$$

where E_L is the excitation laser energy in eV, and A(D:G) is the ratio of the integrated peak area of the D band to the G band. Based on these calculations, the reference foil exhibits the largest calculated crystallite size ($La{\sim}2{,}572\ nm$), but suffers from highly patchy and non-uniform macroscopic coverage. In contrast, the particle-decorated sample yields a smaller calculated size ($La{\sim}1{,}378\ nm$). However, this reduction in La does not indicate a degradation of the intrinsic lattice; rather, it is primarily a spectral artifact driven by the dense network of surface wrinkles. Because these wrinkles act as geometric scattering centers that artificially enhance the D mode intensity, the calculated is reduced despite the fact that these features are actually beneficial stress-relief mechanisms. Ultimately, the particle-decorated strategy successfully yields vastly superior macroscopic continuity and higher overall film quality. Conversely, the significant D band contributions observed in the pre-annealed and laser-ablated samples confirm that these defect-rich Ni topologies restrict growth, strictly promoting the formation of highly fragmented, nanocrystalline graphene domains.

3.1.4. Transition to Dielectric Substrates

In order to exploit the encapsulated morphology for UV-SERS (the objective of Case Study II), it was necessary to examine these structures on a dielectric substrate (SiO_2) to avoid spectral interference from the graphene shell, as pointed in Chapter 1. Since laser ablation was not feasible on the quartz surface, a preliminary investigation compared the two remaining seeding strategies: (1) thermal argon annealing of a thin film and (2) nanoparticle deposition. Surface preparation was of the same protocol as described in Chapter 2. For the thermal annealing process, a 6 nm nickel film was deposited via magnetron sputtering and subsequently annealed at 500 °C for 1 hour to induce island formation. Conversely, for the particle deposition strategy, a dispersion was prepared by adding 100 μL of aqueous Ni nanoparticles to 5 mL of DMSO. The quartz substrate was immersed in this suspension for 24 hours at room temperature to allow for gravitational sedimentation of the particles onto the surface.

Both substrate types were subjected to PECVD using the thermal parameters listed in Table 3. However, a critical adjustment was made to the gas composition: the hydrogen-to-methane ratio was modified to 3:1 (moderate regime). This adjustment was necessary to maintain carbon supersaturation while preventing the vertical nanowall growth often observed on dielectrics.

Comparative SEM analysis of thermal annealed before and after PECVD growth revealed a fundamental distinction in the final morphology. As shown in **Figure *25***, the annealed 6 nm film underwent solid-state dewetting, effectively breaking the continuous film into discrete, island-like nickel seeds (**Figure *25***a). These islands subsequently acted as specific nucleation sites for carbon species, facilitating the growth of 3D encapsulated shelled structure (**Figure *25***b).

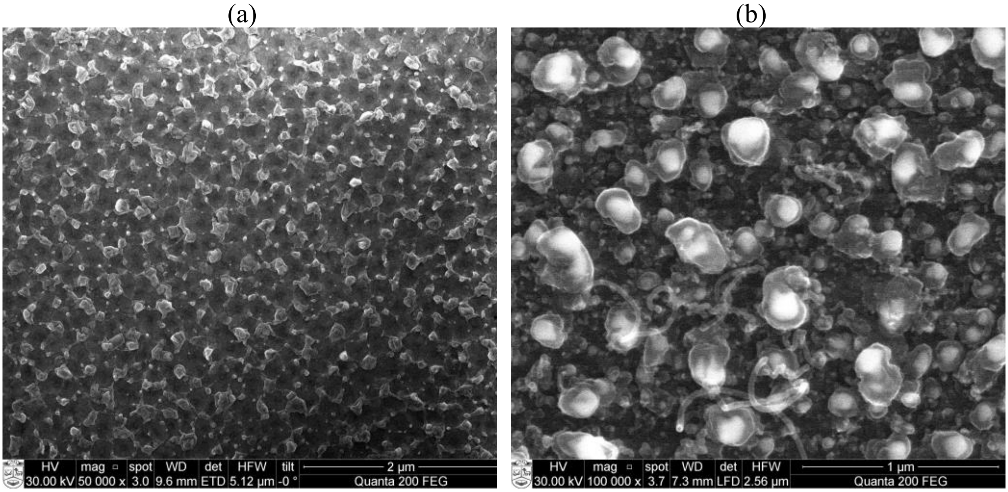

Figure 25. SEM micrograph of the (a) 10 nm Ni film on SiO_2 after thermal annealing at 500 °C for 1 hour and (b) sample after PECVD process under a moderate regime

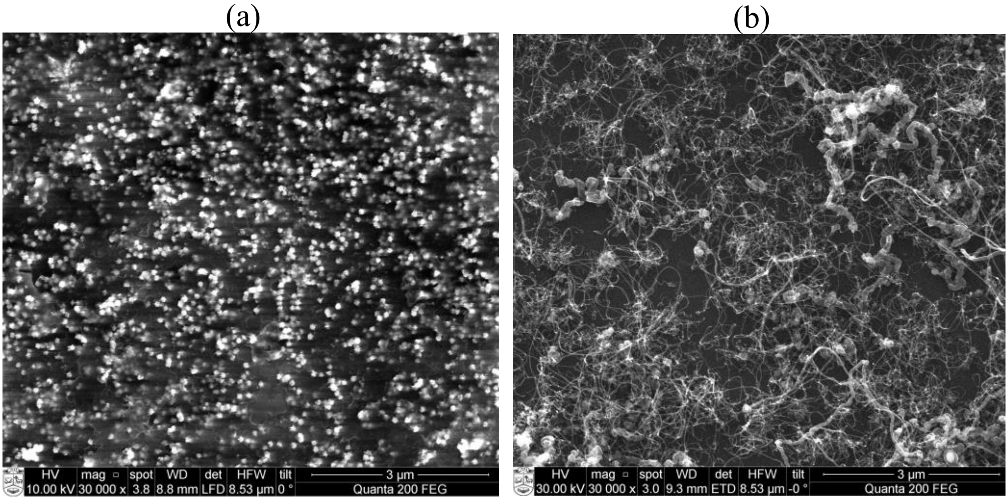

Figure 26. SEM micrograph of the particle-seeding strategy on SiO_2: (a) surface state after gravitational sedimentation of Ni nanoparticles and (b) post-PECVD growth morphology, revealing the predominant formation of carbon nanotubes

In contrast, the second strategy involved a direct deposition of Ni nanoparticles via gravitational sedimentation on SiO_2. As shown in **Figure *26***a, the sedimentation process yielded a relatively uniform distribution of particles on the surface without significant agglomeration. However, following the PECVD process, the morphological outcome was fundamentally different. As observed in **Figure *26***b, the surface is dominated by the formation of carbon nanotubes forest. This indicates that the synthesis outcome is strictly governed by the dimensions and curvature of the catalytic seed. The nanoparticles, having a smaller diameter and higher surface curvature than the dewetted islands, favored the diffusion-driven one-dimensional extrusion mechanism (tip-growth or base-growth) characteristic of nanotubes [210].

Thus, these preliminary studies established two fundamental insights. First, the experiments on polycrystalline foil demonstrated that introducing high-curvature features (via nanoparticle decoration) effectively decouples graphene nucleation from the underlying crystallographic grains. These particles create active sites that lower the activation energy for the precipitation of carbon species, promoting uniform high-quality bilayer graphene by a dense network of wrinkles as stress-relief features. Second, the transition to dielectric substrates revealed the carbon deposited morphology is strictly governed by the catalyst diameter. While the 80 nm gravitational sedimentation nanoparticles favored the formation of carbon nanotubes on SiO_2, the solid-state dewetting of 6 nm thin films produced specific dewetted islands geometry that is required to grow a shelled structure, the ideal architecture to adopt for Case Study II.

3.2. Case Study II: Nickel-Encapsulated Graphitic Shells for UV-SERS

This case study investigates the synthesis and characterization of nickel nanoparticles encapsulated within the graphitic shells. Building on the findings of the preliminary investigation, a critical modification was introduced to the PECVD configuration. A rectangular stainless-steel enclosure was placed over the samples within the chamber. As detailed in recent literature [203], this shielding creates a remote plasma environment, effectively decouples the substrate from the aggressive ion bombardment of the main plasma sheath, thereby preventing the excessive etching of the delicate nickel nano-islands while maintaining a sufficient flux of active radicals for the shell growth. The objective of this study is to evaluate the feasibility of hybrid structure as a stable UV-SERS platform. The investigation focuses on two critical performance metrics:

1. Passivation efficacy: verifying the protective capability of the graphitic shell in preserving the metallic nickel core against oxidation.
2. Structural assessment: conducting a comprehensive quality assessment of the disordered carbon structure. Given the complex nature of these shells, a multi-spectroscopic correlation framework (integrating Raman, UV-Vis, and TAS) is established to identify reliable quality indicators beyond standard metrics.

The results presented here have been published in *Carbon* (2025, Vol. 232, 119704).

3.2.1. Study Design: Full Factorial Matrix

In order to establish a diverse sample space, a full factorial experimental design was implemented involving two independent variables:

1. ***Initial nickel film thickness:*** deposited via magnetron sputtering at four nominal levels. These are labeled as series: A, B, C, and D, respectively.
2. ***Carbon deposition time:*** grown via PECVD at four-time intervals (10, 20, 40, and 60 minutes).

This design resulted in a matrix of 16 distinct sample types (e.g., sample “C|60” represents Series C with 60 minutes of growth). This structured diversity allowed for a robust statistical analysis of 107 dependent metrics derived from spectroscopy, ensuring that the identified quality indicators remain valid across different morphological regimes. The summarized workflow of the fabrication and analysis process is shown in Figure 27.

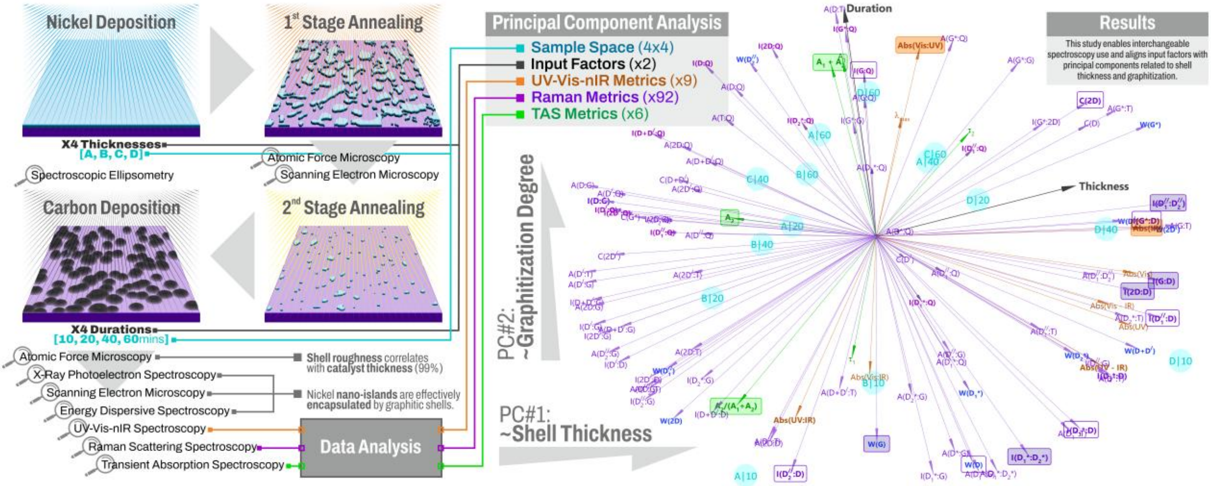

Figure 27. Summarized workflow of the fabrication and analysis process

3.2.2. Surface Analysis

Spectroscopic ellipsometry confirmed the initial thicknesses of the sputtered nickel films as 3.8 ± 0.8 nm (A), 6.7 ± 1.1 nm (B), 9.6 ± 1.0 nm (C), and 16.3 ± 1.2 nm (D). The morphological transformation of these films was tracked via AFM at three stages: as-deposited, after dewetting, and post-carbon deposition (Figure 28).

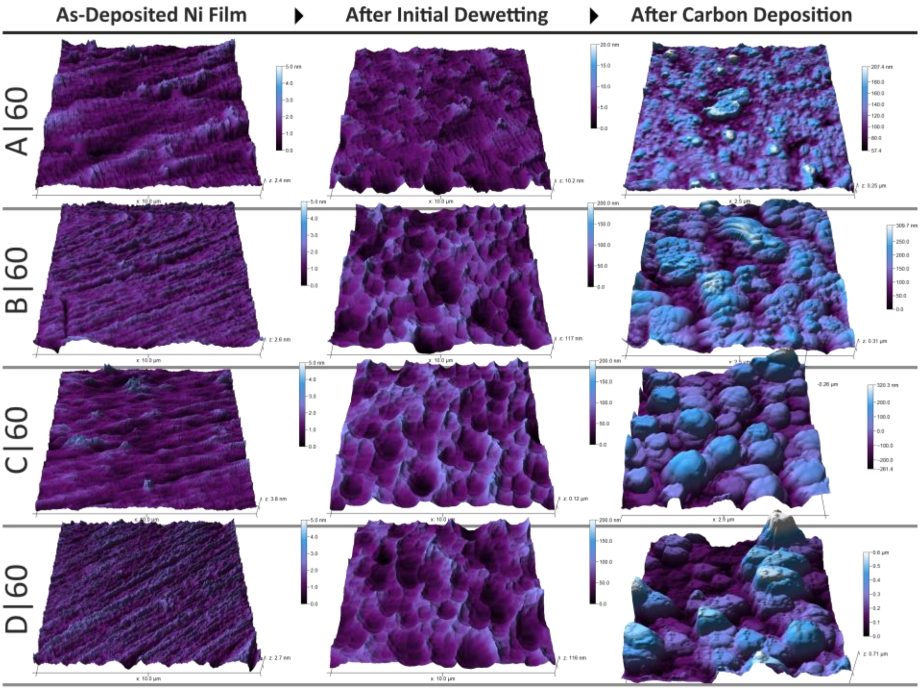

Figure 28. AFM surface topography of Ni films: as-deposited (left), after dewetting (center), and after 60-minute carbon deposition (right) Series A–D

As-deposited films exhibited a wrinkled surface with sub-nanometer ridges. upon annealing at 500 °C (dewetting), the continuous films transformed into discrete Ni islands. This process is driven by surface tension minimization [211]. According to the vapor-liquid-solid model at low temperatures, the catalytic growth occurs as carbon dissolves into these Ni islands until the metal-carbide particle reaches saturation, causing carbon to flow out and rapidly accumulate as amorphous carbon, which then encapsulates the catalyst particles. After about two minutes of encapsulation, the carbon atoms begin to graphitize, forming graphitic islands that serve as nucleation sites for further carbon growth, as previously reported in the literature [212–215].

Figure 29a presents the RMS roughness (R_q) evolution. While Series A (thinnest) showed minimal roughness increase after dewetting, Series B, C, and D developed larger islands. This aligns with the findings from other research studies [216, 217]. It is important to note that the choice of selecting R_q over average roughness (R_a) was based on the specific morphology (isolated domes/islands rather than a continuous film). While R_a provides a general baseline for surface texture, R_q is more sensitive to large vertical deviations from the mean line. Given that the sample morphology consists of discrete dome-shaped graphitic shells separated by a flat substrate (which will be further proven by EDS mapping), R_q provides a more accurate representation of the volumetric distribution and vertical extent of these features. Although AFM topography does not directly resolve the atomic layer count of the encapsulating walls, the R_q value serves as a proxy for the effective shell thickness and height. Crucially, the post-CVD roughness exhibited a strong linear correlation (99%) with the initial Ni film thickness

(Figure 29b). This confirms that the initial metal volume dictates the final dimensions of the graphitic domes. Thicker films yield larger Ni islands, which in turn support the growth of larger/thicker graphitic shells. This result will be further proved by spectroscopy analysis.

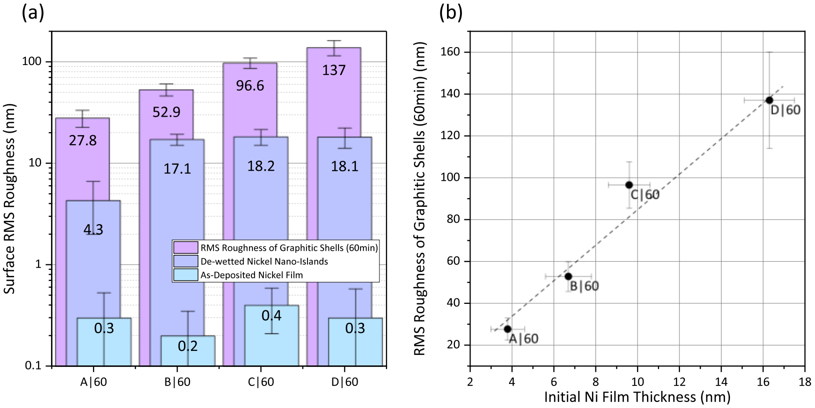

Figure 29. (a) RMS surface roughness in 60 min growth at each processing stage, (b) correlation between graphitic shell roughness and initial Ni thickness

Thus, the thickness is a proxy for surface roughness, effectively linking it to the initial Ni films.

Figure 30 is showcasing the transformation from the initially dewetted surface to the post-CVD process. In samples with higher initial Ni content, a clustering of islands was observed. It reveals that the isolated graphitic domes are separated by the exposed SiO_2 substrate. On a larger scale, the morphology appears uniform, consisting predominantly of encapsulated shells, though rare, isolated short nanotubes are occasionally observed.

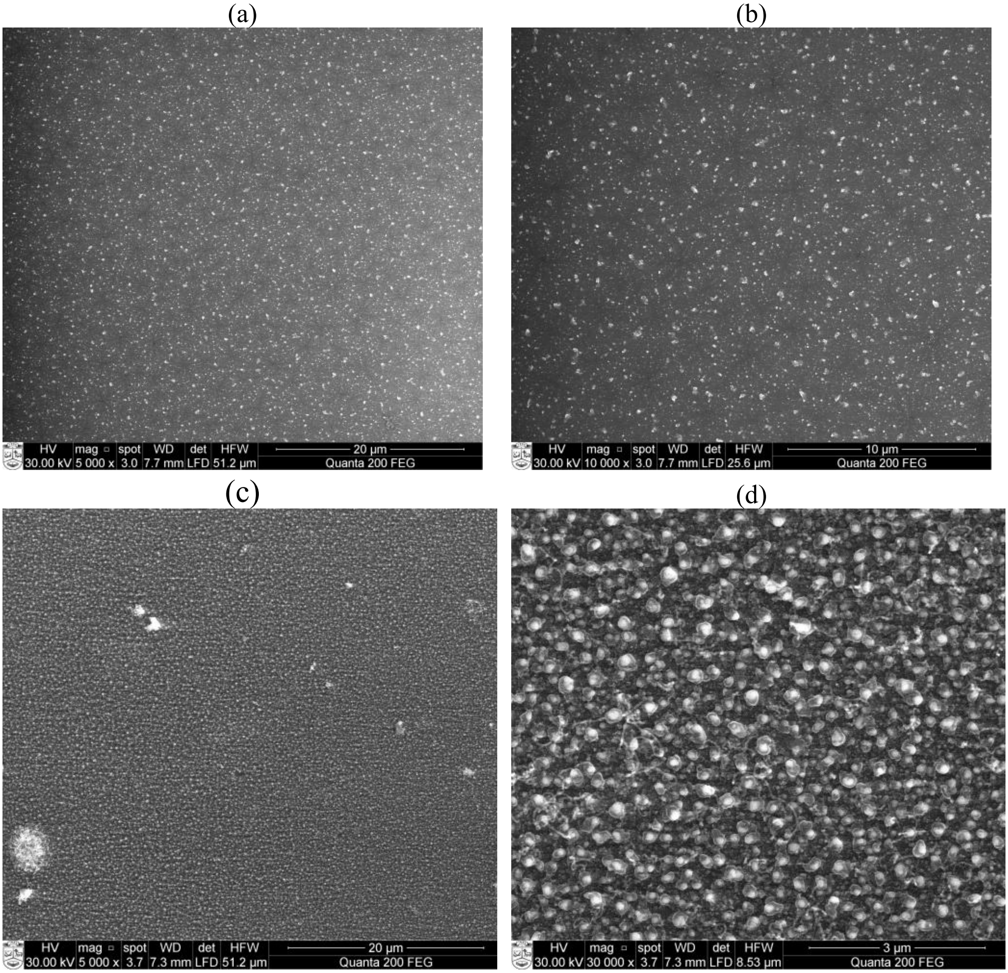

Figure 30. SEM images with two magnifications from B series, dewetted Ni film (a, b), post-CVD process after 40 min growth (c, d)

EDS mapping (Figure 31) confirms the core-shell architecture. The elemental maps show nickel cores (purple) perfectly spatially aligned with carbon shells (blue). Crucially, while oxygen was detected on the SiO_2 substrate, the Ni cores remained oxygen-free post-synthesis, suggesting successful reduction and encapsulation during the PECVD process.

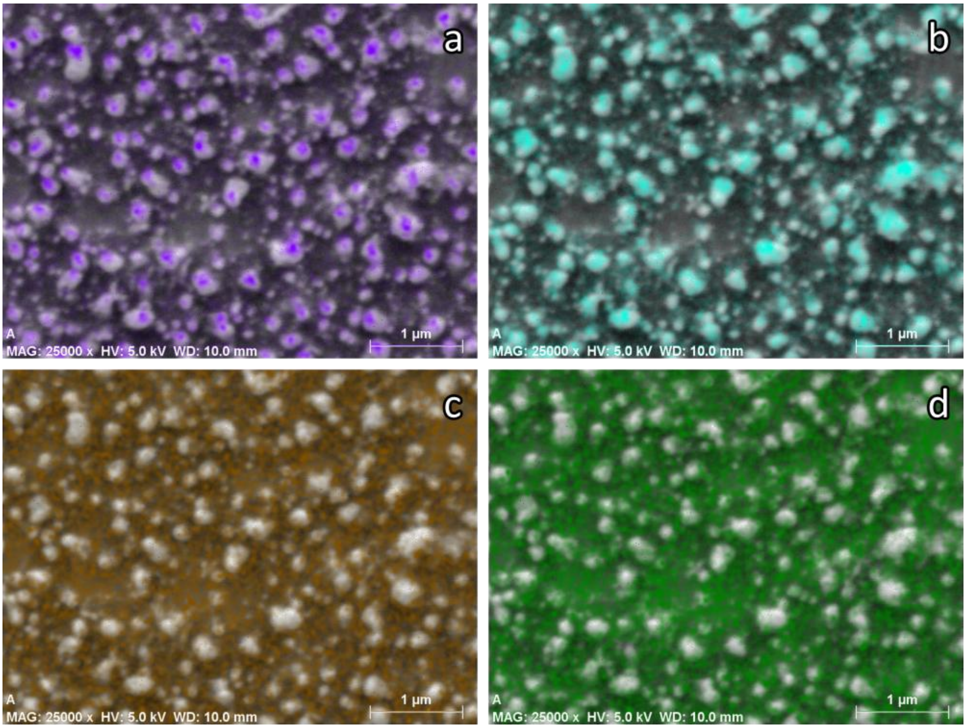

Figure 31. EDS elemental mapping of B series after 60 minutes of growth showing distributions of (a) Ni, (b) Carbon, (c) Silicon, and (d) Oxygen

It is noteworthy that a recent study [218] indicates that the growth of carbon on Ni catalyst predominantly occurs on Ni particles with an average size of ~20 nm. This has been linked to the optimal solubility of carbon in Ni at 500 °C, which is considered to be the ideal temperature for this size range. Considering this, the equivalent disk diameters of dewetted Ni islands and formed graphitic shells were calculated using the formula $d_{eq} = 2\sqrt{S/\pi}$, where (S) represents the observed area of the islands and shells from the SEM images. The distribution of these equivalent disk diameters is exemplified by sample C|60, as depicted in Figure 32.

The histogram in Figure 32a indicates that the initial dewetted islands display a scale-free size distribution with a mean equivalent disk diameter below 50 nm dominating across all series. Series A, having the lowest nominal thickness, shows the highest number of fine particles. Conversely, the samples with higher Ni content tend to form more clustered islands, aligning with RMS surface roughness result, as discussed earlier. Additionally, the distribution of graphitic shells (Figure 32b) mirrors the scale-free distribution of the nano islands, even showing a similar plateau from 200 to 400 nm that was observed in the sample C|60. The correlation between the scale of deposited carbon and the size of catalytic islands has as well been noted in other studies [211].

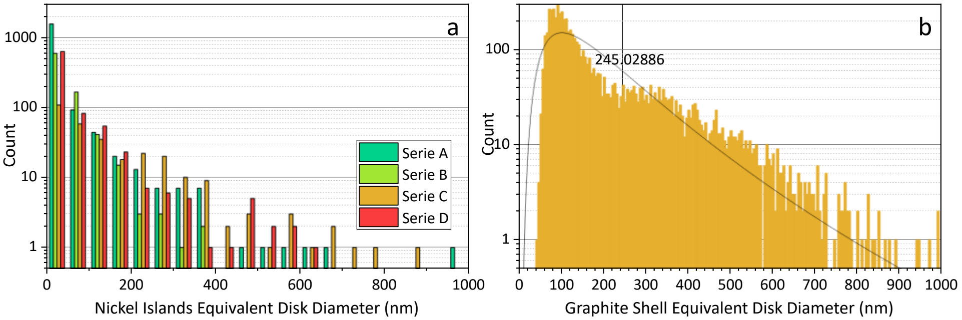

Figure 32. Size distributions of (a) dewetted islands for all nominal thicknesses, (b) post-CVD deposited carbon on sample C|60 with a fitted log-normal distribution curve and the average value of ~245 nm

XPS analysis was employed to verify the chemical state of the nickel and the quality of the carbon shell. As-deposited films in the Ni $2p_{3/2}$ region showed a mix of metallic Ni (852.6 eV) and $Ni(OH)_2$ (855.9 eV). The Ni film composition (**Figure *33***), derived from the peak intensity of deconvoluted high-resolution XPS spectra of the as-deposited Ni films across four nominal thicknesses (Series A–D), indicates that metallic Ni content increased with film thickness.

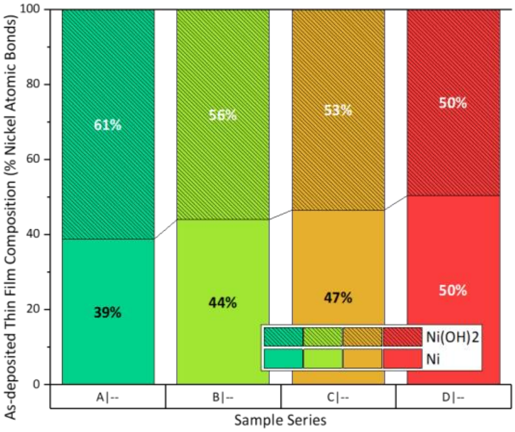

Figure 33. Relative Ni film composition derived from the peak intensity of deconvolution high-resolution XPS spectra in the Ni 2p region of Ni films

Figure 34 presents high-resolution XPS spectra for the graphitic shell encapsulated NiNPs in the Ni $2p_{3/2}$ and C 1s regions for the B series after depositing carbon. As evidenced by Figure 34a, the disappearance of the $Ni(OH)_2$ peak indicates that the PECVD environment reduced the oxide, and at least 20 min or more is needed to fully encapsulate the Ni core, and subsequently prevent re-oxidation upon exposure to air.

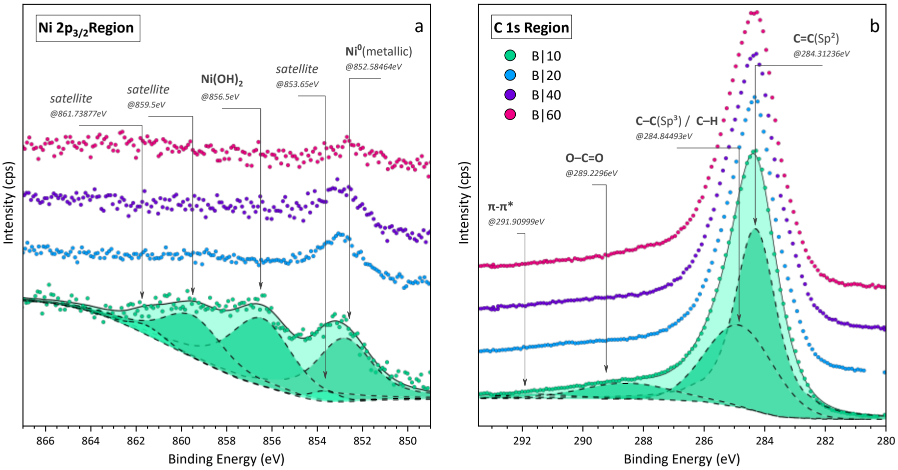

Figure 34. High-resolution XPS spectra of Series B samples at varying deposition times: (a) Ni $2p_{3/2}$ region and (b) C 1s region

The C1s spectra (Figure 34b) were dominated by the sp^2 graphitic peak (284.3 eV), constituting 82–87% of the carbon content [219–225]. A minor peak at 285.2 eV corresponds to sp^3 hybridized carbon (defects) [226, 227]. Two very low intensity peaks at 289.3 eV and 291.4 eV correspond to the carbon bonds in O-C=OH [221] and the π–π* satellite peak [224] respectively.

3.2.3. Correlation Study

These graphitic shell structures represent a highly disordered system where standard Raman metrics (more specifically I(D:G)) might be ambiguous. Thus, the necessity for a more solid multi-spectroscopic framework was underscored by challenges. To resolve this, a systematic correlation study was conducted to identify physically meaningful relationships between the input factors (thickness, time) and spectroscopic metrics.

Two samples (C|10 and C|20) exhibited low signal-to-noise ratios and were identified as outliers; they were excluded to ensure statistical robustness. The final dataset consisted of 14 observations. The full correlation matrix (presented in supplementary information) serves as a statistical map connecting the experimental input factors (synthesis parameters) to the output structural properties (spectroscopic metrics). In order to interpret this matrix effectively, the data should be viewed through three distinct lenses: statistical significance, dimensionality reduction, and physical causality.

Statistical definition: the matrix utilizes Pearson correlation coefficients (r) to quantify the linear relationship between variable pairs. The interpretation of these values is governed by two strict thresholds established for this study:

- Magnitude (r): the coefficient ranges from -1 to $+1$. The value of $|r| \geq 0.5$ is defined as the threshold for a strong correlation. A positive value indicates that a spectral feature intensifies as the synthesis parameter increases, while a negative value implies an inverse relationship.

- Confidence (p-value): to ensure that the observed trends are not artifacts of random noise or sample heterogeneity, only correlations with a p-value < 0.05 (two-tailed test) are considered statistically significant. This provides a 95% confidence level that the relationship is genuine.

Screening methodology (from 107 metrics to key indicators): the full matrix (provided in Appendix 1, Table S1) contains over 10,000 data pairs. To distil this into the manageable dataset presented in the main text, a rigorous filtering process was applied:

- Statistical significance: only correlations with $p < 0.05$ and $|r| \geq 0.5$ were retained.
- Exclusion of intra-technique redundancy: the correlations between metrics derived from the same spectroscopic technique (e.g., correlating Raman $I(G)$ with Raman $I(G{:}D)$) were systematically screened out. These "intra-technique" relationships are often mathematically dependent or trivial. Instead, inter-technique (cross-spectroscopic) correlations (e.g., TAS vs. Raman) were prioritized. This approach isolates the most valuable scientific insight: the validation that independent physical mechanisms (optical absorption vs. phonon scattering) are tracking the same structural evolution.
- PCA alignment: finally, the metrics that aligned strongly with the principal components (PC1 and PC2) were selected, ensuring they represent the fundamental drivers of shell thickness and graphitization.

Physical interpretation logic: beyond statistics, the correlations must be physically meaningful. The matrix should be interpreted by associating the input factors with specific physical growth mechanisms:

- Correlations with nickel thickness: these track thermodynamic and volumetric evolutions. A significant correlation here implies that the metric is sensitive to the volume of the catalytic island, the density of flakes, or the total amount of carbon deposited.
- Correlations with growth duration: these track the kinetic and structural evolutions. A significant correlation here indicates that the metric is sensitive to the healing of the carbon lattice, the reduction of amorphous phases, or the degree of graphitization over time.
- Inter-metric correlations: when a metric from one technique (e.g., TAS) correlates strongly with a metric from another (e.g., Raman), it validates the physical interchangeability. This implies that both techniques are probing the same underlying defect density or electronic state, allowing them to be used as complementary or substitute quality control tools.

Table 5. Significant correlations identified between the input factors and spectroscopic metrics, as well as inter-metric correlations

		Input Factors		**Selected TAS Metrics**			**Selected OES Metrics**		
		Thickness	Duration	$A_1 + A_2$	A_2	$\frac{A_2}{A_1 + A_2}$	Abs(IR)	Abs(UV − IR)	Abs (Vis:UV)
Input	Thickness				- 75%	-77%	82%	52%	
	Duration							-53%	71%
TAS	Abs(IR)	82%			-	-61%			
	Abs(Vis − IR)	61%							
	Abs(Vis:UV)		71%			-70%			
Selected Raman Metrics	I(D_1'':D)	55%					85%	82%	
	I(D_1'': D_2'')	54%					78%	54%	
	I(D_2'':D)		-69%	-54%					-52%
	W(D)		-70%	-56%				71%	
	I($D_1^\star$:D)		-69%	-60%			60%	92%	
	I($D_1^\star$: $D_2^\star$)		-73%	-69%				82%	-58%
	I($D_2^\star$:D)		-57%				74%	90%	
	W(G)		-60%	-70%		63%			-84%
	I(G:Q)			51%		-51%			62%
	I(G:D)	64%					86%	70%	
	I($G^\star$:D)	82%			-		87%	67%	
	C(**2**D)	60%				-64%	60%		
	I(**2**D:D)	70%			-		78%	65%	
	W(D+D′)	52%			-		80%	84%	

The key correlations are summarized in Table 5, and a comprehensive list of all explored correlations is available in the supplementary information. From this part forward, significant correlations ($|r| \geq 0.5$, $p < 0.05$) that have been found among data obtained from three spectroscopies (Raman, UV-Vis-nIR, and TAS) and the two main input factors, plus significant correlation among spectroscopy metrics, will be explained in detail.

3.2.4. Spectroscopy Analysis

3.2.4.1. Raman Analysis (Extended 11-Band Model)

Unlike the planar graphene in Case Study I, the nickel-encapsulated shells exhibit a complex, disordered morphology that cannot be accurately described by the standard 4-band model. In order to deconvolute the contributions of defects, an extended 11-band model was applied (Figure 35), incorporating specific bands for amorphous phase. It should be noted that all spectra were normalized to the "quiet band" (1,900–2,200 cm^{-1}) to allow for absolute intensity comparisons, avoiding the pitfalls of normalizing to the variable G-peak. All spectra are provided in Figure 36 for comparison.

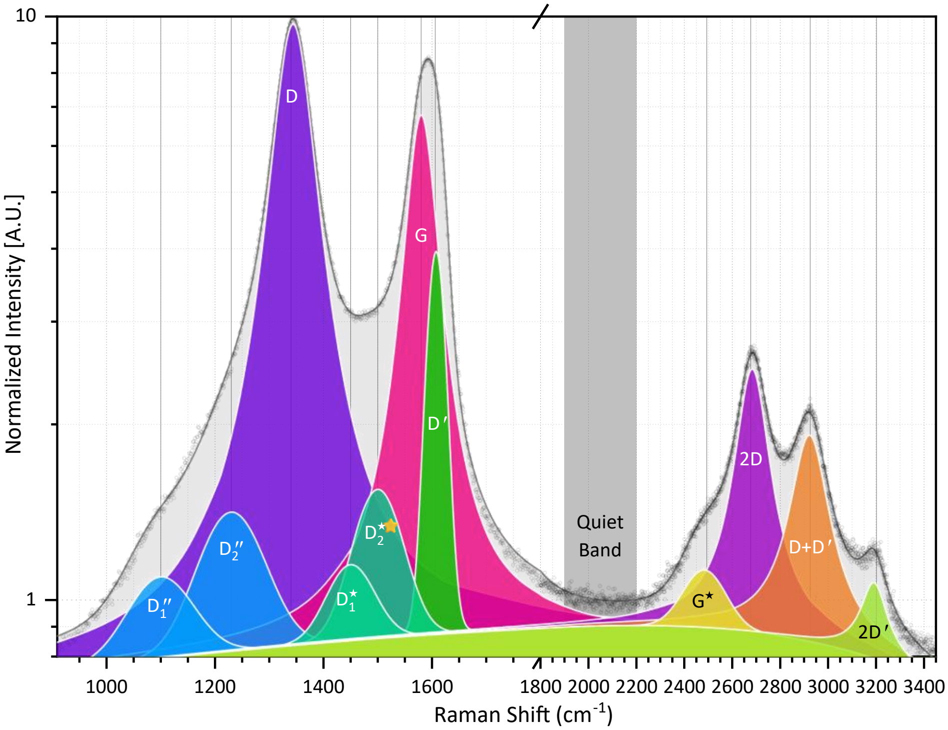

Figure 35. Representative Raman spectrum of sample A|40 fitted with the 11-band model

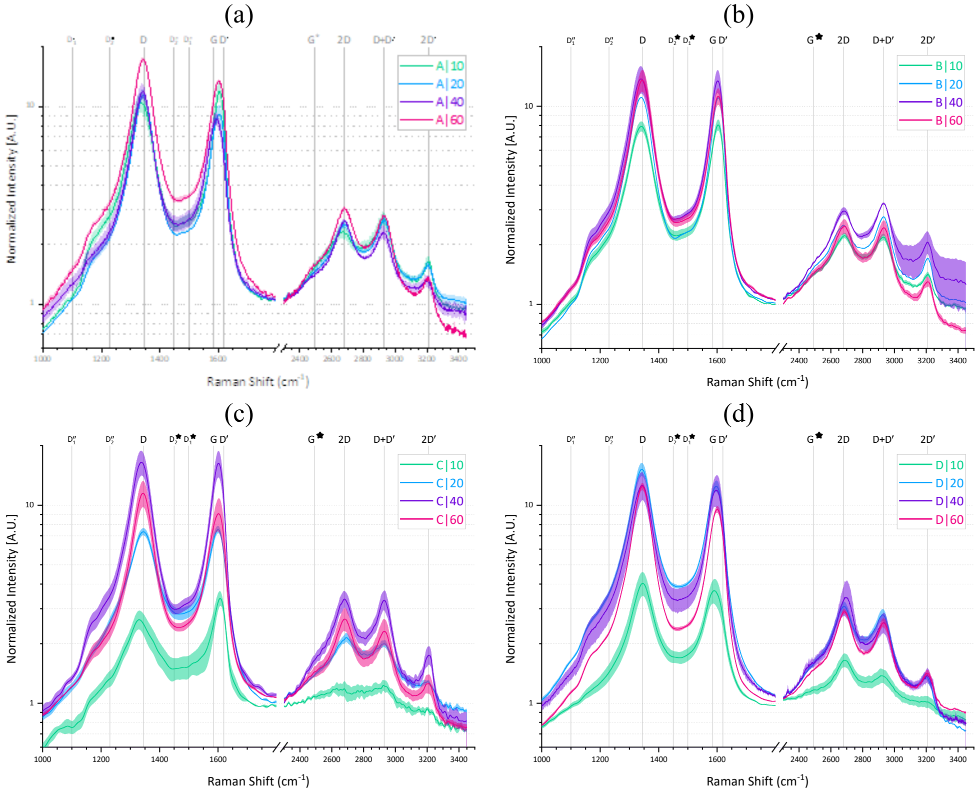

Figure 36. Averaged Raman spectra (solid lines), normalized to the quiet band and their standard errors (colored bands) of (a) A, (b) B, (c) C, and (d) D series in four durations of growth

Inspired by a recent study [112], this study employed a multi-peak fitting model incorporating 11 distinct bands; their specific positions and fitted functions are detailed in Table 6. It should be noted that due to the presence of seven overlapping peaks in the first-order region, the positions of specific bands were fixed during fitting to avoid the convergence toward unrealistic results [228]. Finally, the averaged values and standard deviations were calculated for each sample to ensure statistical accuracy.

Table 6. Identified Raman bands, specified the center of peaks, their fitted functions, and their related reference

Band Name	Center ($1/cm$)	Function	Reference
D_1''	1,100 (fixed)	Gaussian	[111]
D_2''	1,230 (fixed)	Gaussian	[111]
D	1,341.5 ± 2.3	Voigt	[229]
$\mathrm{D}_1^\star$	1,450 (fixed)	Gaussian	[112]
$\mathrm{D}_2^\star$	1,500 (fixed)	Gaussian	[112]
G	1,580 (fixed)	Lorentzian	[230]
D'	1,606.1 ± 0.9	Gaussian	[231]
$\mathrm{G}^\star$	2,492.2 ± 10.1	Voigt	[232]
2D	2,679.7 ± 5.3	Voigt	[233]
D+D'	2,926.0 ± 2.6	Voigt	[234]
2D'	3,201.6 ± 5.0	Voigt	[234]

The decision to fix the position of the G band at 1,580 cm^{-1} was based on the understanding that the variations in this mode typically arise from the changes in the Fermi level[94], strain, or temperature, factors that were not the primary focus of this specific fitting model. During the fitting process, it has been observed that the apparent shifts in the spectral envelope between 1,550–1,650 cm^{-1} arose primarily from the amplitude fluctuations of the neighboring D' peak rather than intrinsic shifts of the G band. Consequently, the position of the D' peak was allowed to vary freely.

It is worth mentioning that the D' peak was consistently observed at 1,606 cm^{-1} with a narrow standard deviation of 0.85 cm^{-1} across all samples. This finding suggests that the visual shift in the 1,550–1,650 cm^{-1} region is attributable to the relative changes in the G and D' peak ratios. Notably, this observed position (1,606 cm^{-1}) deviates from the commonly reported value of ~1,620 cm^{-1} [42]. However, this discrepancy is reconciled when examining the second-order 2D'band. In literature, the samples exhibiting a D' peak at 1,625 cm^{-1} typically show a 2D' feature around 3,250 cm^{-1}. In contrast, the study recorded the 2D' band at 3,201 ± 5 cm^{-1}. This correlates perfectly with a fundamental frequency of ~1,600 cm^{-1}, thereby strictly validating the assignment of the D' band to 1,606 cm^{-1}.

Raman metrics from prominent bands: the Raman analysis incorporated four prominent bands: D, G, D', and 2D, alongside seven less-prominent modes: D_1'', D_2'', $\mathrm{D}_1^\star$, $\mathrm{D}_2^\star$, $\mathrm{G}^\star$ or $(\mathrm{D} + \mathrm{D}'')$, D+$\mathrm{D}'$ and 2D', respectively. The D mode (~1,340 cm^{-1}), appearing in the first-order Raman spectrum, corresponds to the structural disorder. It can be activated by various defect types, including edge defects in small crystallites, vacancies, sp^3 hybridized carbon atoms, grain boundaries, and doping [229].

The D' band (1,600–1,650 cm^{-1}) represents a double-resonance mode activated by disorder in the graphitic lattice; its intensity increases proportionally with defect density. While related to lattice vibrations similar to the G mode, it involves intra-valley scattering processes. As Eckmann et al., [231] observed, at high defect densities, the D' band begins to merge with the G mode, making it challenging to deconvolute their individual contributions.

Figure 37 displays the factorial influence on the relative intensity ratio I(D:G) and its normalized area. These metrics are commonly employed in literature as the primary indicators of disorder in graphene-based materials.

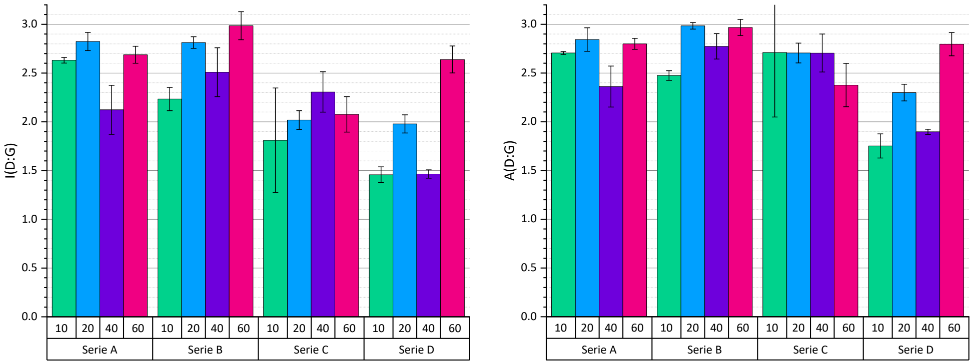
(a) (b)

Figure 37. Factorial influence plots of (a) relative intensity of the D band to G band and (b) relative area of D band to G band

The relative intensity ratio I(D:G) exhibits a negative correlation ($r = -0.64$) with nominal Ni thickness. As discussed extensively in the literature review, in spectra characterizing high defect concentrations (Stage 2 amorphization), the I(D:G) ratio reaches a maximum value and subsequently begins to decrease as disorder intensifies [105, 231]. This ambiguity renders it an unreliable metric for the highly disordered shells. Consequently, alternative indicators were evaluated.

The FWHM of the primary modes proved to be more robust. Especially both W(D) with $r = -70\%$ and W(G), with $r = -59\%$ show a strong negative correlation with growth duration, becoming narrower over time. This narrowing indicates a rise in the content of sp^2 bonds and an increasing degree of graphitization as the synthesis proceeds (**Figure *38***).

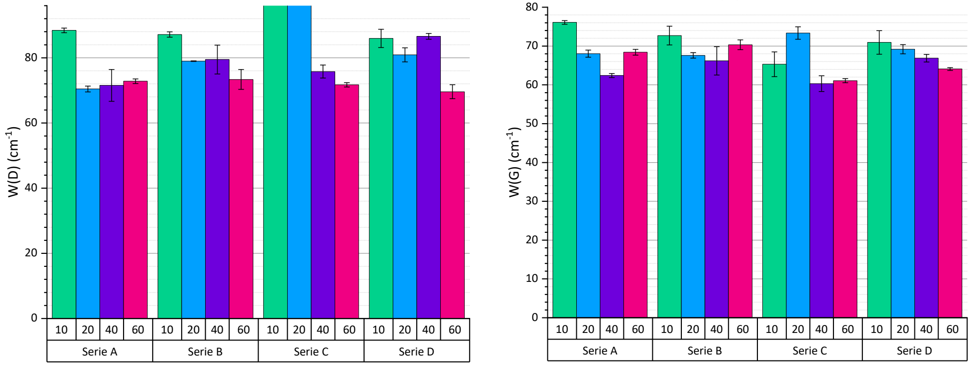
(a) (b)

Figure 38. Full width at half maximum of (a) D band, (b) G band

Regarding 2D mode, which serves as a third prominent band in graphene-based materials (2,696–2,700 cm^{-1}), its narrowing is typically associated with increased crystallinity in few-layer graphene [94]. In this study, the 2D peak position (C2D) was identified as a reliable indicator, showing a distinct upshift as the nominal Ni thickness increased (**Figure *39***a). This shift is associated with the development of a more graphitic character in the thicker series D samples. It is worth noting that while the intensity ratio I (2D:G) is the standard metric for identifying layer number in pristine graphene, it showed no significant correlation with the input factors in this study, likely due to the complex morphology of the encapsulated shells.

In order to address this, the approach of Kuznetsov et al., [236], who proposed using the ratio I(2D:D) as a proxy for the density of graphitic flakes deposited on the surface with a higher ratio indicating a higher flake count. In this study, I(2D:D) exhibited a strong positive correlation with nominal thickness (**Figure *39***b). This suggests that thicker Ni films (Series D) promote the nucleation of a higher density of graphitic flakes. Theoretically, a higher density of flakes implies more edges and grain boundaries, which should increase the disorder signal detected by the Raman. However, as previously established, the sensitivity of the standard intensity decreases in the high-defect density regime, further validating the use of I(2D:D) as a superior morphological metric for these samples.

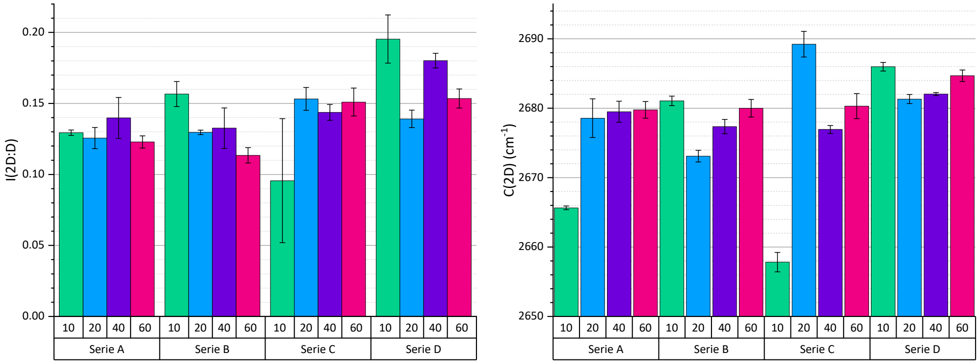
(a) (b)

Figure 39. Relative intensity of (a) I(2D:D) and (b) C2D of all the samples

The average crystallite size (L_a) was calculated using the equation outlined by Eckmann et al., [231] and ranged from 6 to 13 nm across the samples. Regarding the nature of defects, the intensity ratio $I(D{:}\,D')$, as suggested by Jiang et al., [237], initially pointed towards the “on-site” defects. Subsequently, the analysis using the area ratio $A(D'{:}D)$, based on the work of Lopez-Diaz et al.,[238] indicated that the vacancies are the dominant defect type. However, these calculated parameters did not exhibit statistically significant correlations with the input two factors in the correlation table.

A key consideration is the structural evolution of the carbon lattice. Graphite consists of hexagonal layers of sp^2 hybridized carbon atoms. When an atom is missing, the neighboring atoms may rearrange, causing lattice distortions or the formation of sp^3 bonds [239]. The accumulation of vacancy defects and the onset of sp^3 bond formation signal a transition from nanocrystalline graphite to an amorphous carbon structure[240]. In literature, this transition is often marked by the I(D:G) ratio, reaching a maximum value (typically around 2) before decreasing [105]: a trend that has been observed in the gathered samples as well. Therefore, in order to accurately assess the proportions of sp^2-sp^{3,} and amorphous phases in these vacancy-rich shells, it is crucial to analyze the less prominent bands in the first and second-order Raman spectra.

Raman metrics from less prominent bands (first order region): within the frequency range of 1,000–1,300 cm^{-1}, the components identified as D_1'' are suggested to be associated with defective carbonaceous structures. This area was initially reported in a previous study[241] and approved by the other researchers [242]. The first mode D_1'' signifies a composite of vibrational patterns, resulting from chain elongation containing vinyl groups, C-H oscillations, the presence of sp^2 carbon atoms within the defects and amorphous phases, as well as the existence of polyene fragments within the amorphous carbon structure [243]. Herziger et al., [242] as well attributed features in the 1,050–1,150 cm^{-1} range (in ion-irradiated graphene) to double-resonant intervalley scattering of longitudinal acoustic phonons [244]. The second compound (D_2''), as determined by performing the DFPT simulation by Lee et al., [245], has been shown to originate from the vibration of the carbon atoms restricted by the oxygen-containing groups, and its relative intensity to the G band correlates with the carbon to oxygen ratio.

Recently, Couzi et al., [246] revisited the first-order Raman spectra of defective graphitic carbons in this region. They identified up to three modes dependent on the excitation energy, relating them to the phonon modes from different dispersion branches. They recommended a two-mode fitting approach for nano graphite with La ~9 nm (similar to the obtained samples).

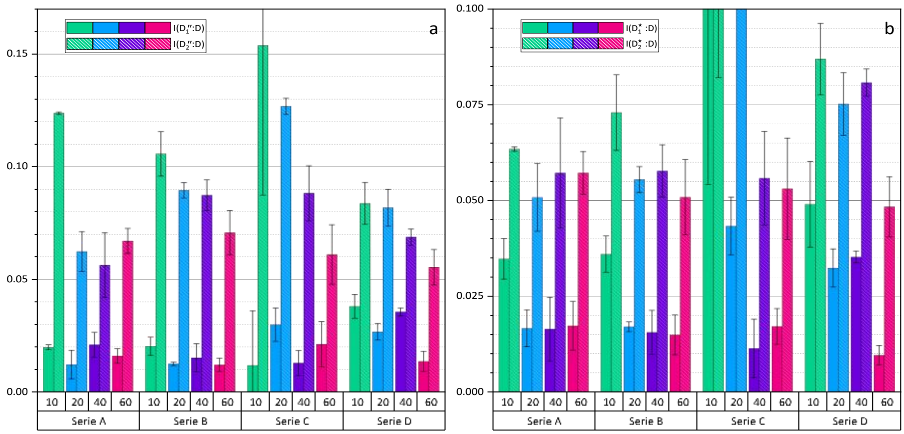

Figure 40. Factorial influence plots of less prominent Raman metrics: (a) intensities of D_1'' and D_2'' normalized with D band, (b) intensities of $D_1^\star$ and $D_2^\star$ normalized with D band

A two-mode approach was as well adopted in this region for the samples in this study: D_1'' located at 1,100 cm^{-1} and D_2'' at 1,230 cm^{-1}. Figure 40a shows the relative intensity ratio of D_1'' and D_2'' normalized with the D band for all the samples prepared in this study.

In the graph presented in Figure 40a, the D_2'' shows a more significant contribution, and its normalized intensity decreases over time. In contrast, $\mathrm{I}(\mathrm{D}_1''\text{:D})$ has a positive correlation with nominal thickness. This trend has as well been observed in another recent study, described as a shoulder below 1,250 cm^{-1}, when the temperature was increased [112]. In this study, the relative intensity (or area) of $\mathrm{I}(\mathrm{D}_1'':\mathrm{D}_2'')$ demonstrates a positive correlation with nominal thicknesses, offering an increase of defective carbonaceous structures. This is the novel metric found in this study that can be used for more accurate evaluation.

Figure 40b shows two bands assigned to $\mathrm{D}^\star$, which are related to the frequency range of 1,450–1,550 cm^{-1} between the D and G modes, where it is suggested to be fitted with two compounds [112]. In this study, $\mathrm{D}_1^\star$ is located around (1,450 cm^{-1}), while $\mathrm{D}_2^\star$ is located around (1,500 cm^{-1}), and both are associated with the presence of amorphous carbon film included in the composition [247]. As Figure 40b indicates, the relative intensity ratios of $\mathrm{I}(\mathrm{D}_1^\star\text{:D})$ and $\mathrm{I}(\mathrm{D}_2^\star\text{:D})$ diminish with the extension of growth duration. Their relative intensity (or area) ratio $\mathrm{I}(\mathrm{D}_1^\star:\mathrm{D}_2^\star)$ was as well found to have a strong negative correlation ($r = -0.72$) with a duration of growth with a pronounced contribution of $\mathrm{D}_1^\star$. This area, very recently, has been considered in the Moseenkov et al., [112] study, while analyzing carbon black heated from 800 °C to 2,600 °C and reported that the same relative ratio decreases from 2.2 for the initial CB to 0.9 for heated structures, where they mainly correspond to this reduction to $\mathrm{D}_1^\star$ (1,400–1,550 cm^{-1}) from graphene fragments smaller than 1.7 nm. The reduction in intensity of bands in this area in this study indicates that over time, the atoms have more opportunity to arrange into a crystalline structure. Many other research studies have as well indicated temperature sensitivity in this region [100, 248]. It should be noted that no significant correlation was observed between $\mathrm{D}_1^\star$ and $\mathrm{D}_2^\star$ and nominal thicknesses through the Raman spectra analysis.

Raman metrics from less prominent bands (second-order region): the second-order region (2,300 cm^{-1} to 3,300 cm^{-1}) typically begins with $\mathrm{G}^\star$, as well referred to ($\mathrm{D}+\mathrm{D}''$), located around 2,480–2,500 cm^{-1} frequency range. Its line shape and position are consistent with previous reports [232] which attribute it to a combination mode involving an inactive D phonon and the D'' mode [249]. This band in the present study is located at 2,492 cm^{-1}, and its relative intensity ratio is normalized with the D band; $\mathrm{I}(\mathrm{G}^\star\text{:D})$ has one of the strongest positive correlations, (r=0.8) with nominal thicknesses.

Two additional weak modes were analyzed in the higher frequency range: ($\mathrm{D}+\mathrm{D}'$) at 2,920–2,929 cm^{-1} and $2\mathrm{D}'$ around 3,200 cm^{-1}, and neither of them is a high-intensity signal [234]. The $2\mathrm{D}'$-band represents a second harmonic of the D' peak, while ($\mathrm{D}+\mathrm{D}'$) mode combines the D and D' resonances as indicated by its name. Both their FWHM increase with nominal thickness in this study. This broadening suggests a reduction in phonon lifetime, likely associated with the increased scattering caused by the higher density of graphitic flakes in thicker samples.

To summarize, the systematic correlation analysis allows to distinguish between two concurrent structural evolutions:

1. Graphitization (time-dependent): the narrowing of D band and G band, shown to be a more reliable metric for evaluating the degree of graphitization over time. In other words, crystallinity can as well be estimated by a decrease in sp^2-bonded carbon within the defect and amorphous phase, which is evidenced by a reduction in relative intensities $\mathrm{I}(\mathrm{D}_2'':\mathrm{D})$ and $\mathrm{I}(\mathrm{D}_1^\star:\mathrm{D}_2^\star)$ from less prominent bands over time.

2. Morphological disorder (thickness-dependent): conversely, metrics such as $\mathrm{I}(\mathrm{G}:\mathrm{D})$, $\mathrm{I}(2\mathrm{D}:\mathrm{D})$, and $\mathrm{C}(2\mathrm{D})$ are shown to be only related to nominal thickness or shell thickening, potentially leading to the rise of sp^2–sp^3 disorder bonds. The estimation of such disorder is as well supported by increases in $\mathrm{I}(\mathrm{G}^\star:\mathrm{D})$, $\mathrm{I}(\mathrm{D}_1'':\mathrm{D})$, or $\mathrm{I}(\mathrm{D}_1'':\mathrm{D}_2'')$ that is caused by such enhancement and can be a proof of the unreliability of conventional metrics, such as $\mathrm{I}(\mathrm{D}:\mathrm{G})$ and $\mathrm{I}(\mathrm{D})$, respectively.

3.2.4.2. UV-Vis-nIR Analysis

The extinction spectra were collected for as-deposited Ni films, dewetted islands, and post-CVD graphitic shells. Figure 41 displays the results for all four series at a 60-minute growth duration.

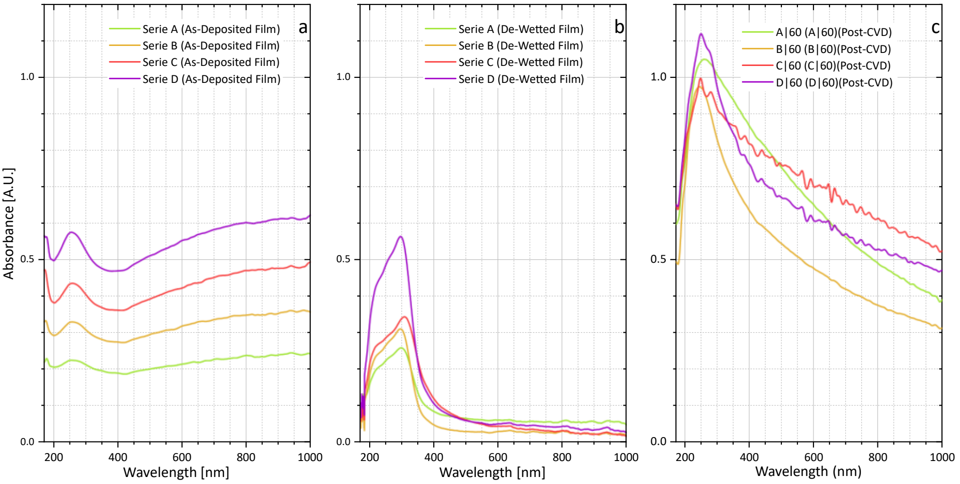

Figure 41. UV-Vis-nIR extinction spectra of (a) as-deposited Ni films, (b) dewetted islands, and (c) post-CVD graphitic shells (60 min growth)

Following the dewetting process (Figure 41b), significant absorption occurs primarily in the UV region (250–350 nm). This is attributed to the LSPR of the Ni island distribution, which is likely covered by a thin native oxide layer. The spectral profile remains consistent throughout the four series with the overall absorption intensity scaling with the initial nominal thickness of the Ni film.

Further in the post-CVD (Figure 41c) spectra, the absorption peak narrows and shifts to (λ_{max}~270 nm). This peak position is consistent with the characteristic absorption of graphene, but in this hybrid system, it represents a convolution of the graphitic shell absorption and the LSPR of the now-reduced metallic nickel core. This intense UV absorption is a critical feature that enables the UV-SERS application demonstrated later in this study. Post-CVD from all the samples is provided in **Figure *42***.

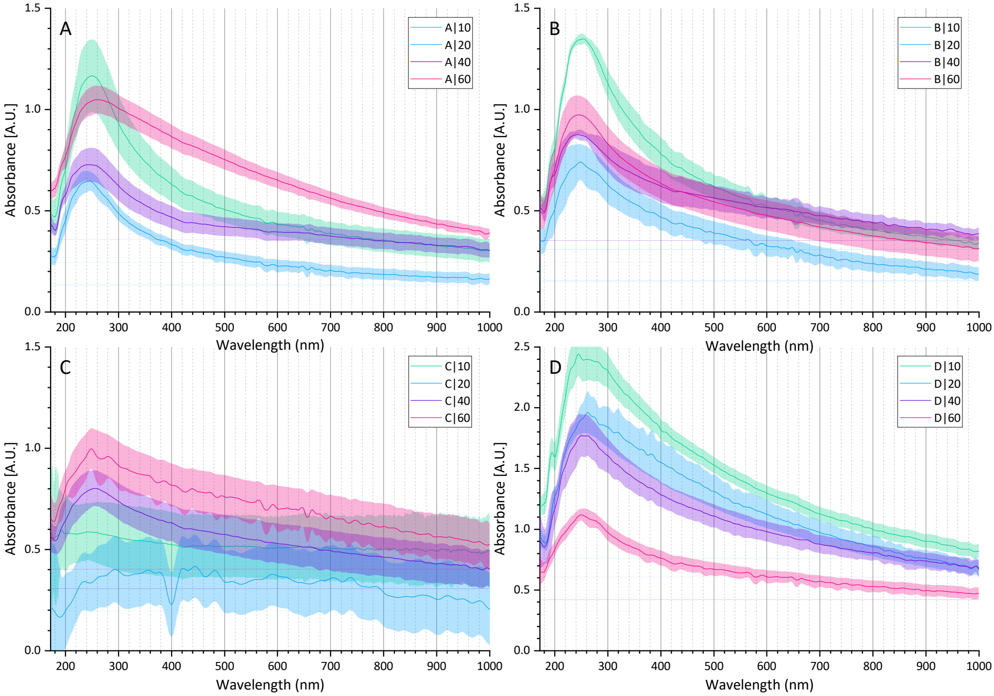

Figure 42. Full UV–Vis–nIR extinction spectra acquired in the wavelength range of 170–1,000 nm for all sample series (A, B, C, and D) across the four distinct growth durations

While the shift in λ_{max} is often used to estimate the layer number in exfoliated graphene, it is unreliable due to the overlapping Ni resonance. Instead, the integrated relative extinction ratio proposed by Backes et al., [250] was employed, calculated from equation (3):

$$N_{\text{Layers}} = 35.7\,\varepsilon_{@550}/\varepsilon_{@325} - 14.8; \tag{3}$$

where ε represents the extinction coefficient at the specified wavelengths. As shown in **Figure *43***, the estimated mean number of layers for the samples ranges from ~20 to ~30. It is important to note that the absolute accuracy of this calculation is influenced by the underlying Ni particles. However, since the Ni core contribution is constant for a given series, the relative variation in the $\varepsilon_{@550}/\varepsilon_{@325}$ or likewise the ratio of absorbance in the visible to the ultraviolet regions ($\text{Abs}(\text{Vis:UV})$) remains a reliable indicator for tracking changes in the carbon shell structure.

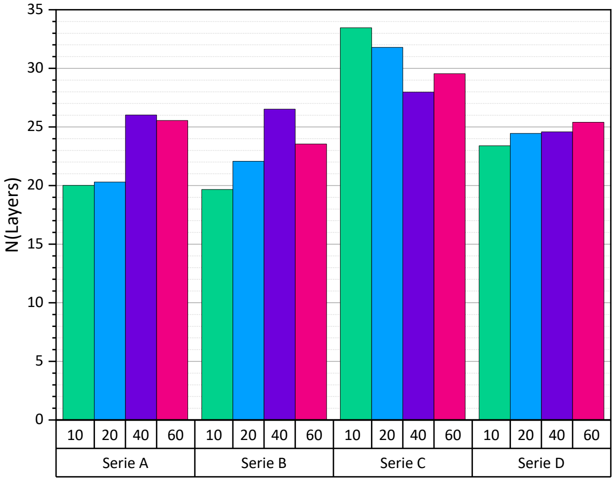

Figure 43. Mean number of layers for all the samples prepared in this study

Over the systematic study among the metrics, these correlations were found to be strongest among extinction spectra and Raman spectra:

***Crystallinity indicators**:* Abs(Vis: UV) exhibits a strong positive correlation with growth duration (r=+0.71) and a strong negative correlation with the Raman G-band width (r=-0.84). Since a narrower W(G) signifies higher crystalline quality, the increase in this optical ratio effectively tracks the graphitization process. This is further supported by its negative correlation with the amorphous carbon Raman markers $I(D_2'':D)$ and $I(D_1^\star:D_2^\star)$, confirming that as the shell quality improves (steeper spectral slope), the amorphous content decreases.

***Layer density indicators*:** positive correlations were found between the absorption in the UV (66%), higher in Vis (73%), and the strongest (82%) in the IR region with nominal thicknesses. Abs(IR) as well showed strong positive correlations with all Raman metrics, including I(2D:D), C(2D), $I(G^\star:D)$, $I(D_1'':D)$, and $I(D_1'':D_2'')$. This confirmed that Abs(IR) serves as a robust proxy for the density of graphitic flakes; thicker initial Ni films produce more numerous/dense shells, which scatter and absorb more light in the infrared region.

3.2.4.3. TAS Analysis

TAS was employed as a complementary tool to probe ultrafast carrier dynamics, offering insights into how photoexcited carriers interact and lose energy within the graphitic shells. The process begins with laser excitation (pump), which promotes electrons from the valence to the conduction band, leaving holes behind. This results in a non-equilibrium state where carriers initially interact via electron-phonon scattering (thermalization, τ_1), achieving a thermalized distribution within hundreds of femtoseconds. Subsequently, over picosecond timescales, phonon-phonon scattering redistributes this energy, cooling the lattice (τ_2) [251–253].

As shown in **Figure** ***44*** ($\Delta T/T$), all samples were negative. This is consistent with the Pauli blocking principle (phase-space filling), where the initial pump pulse populates states in the conduction band, reducing the absorption probability of the subsequent probe pulse [254].

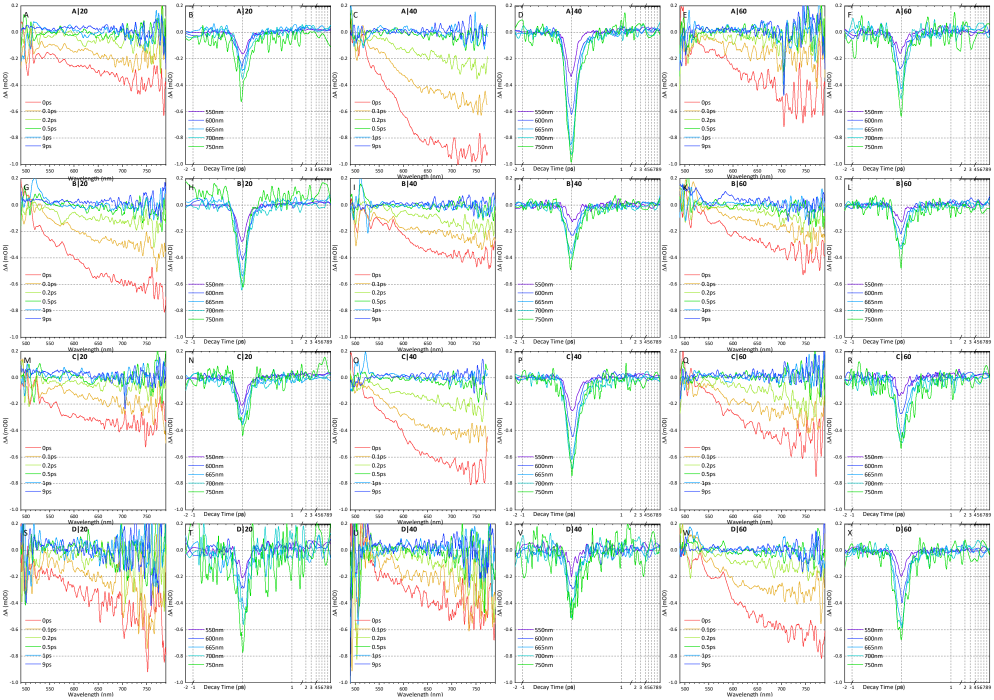

Figure 44. TAS spectra and traces for all samples prepared in this study; the series and duration labels are specified within each graph

Figure 45 illustrates a typical transient absorption measurement data, showing a contour plot of all data, spectra at five selected delay times, and traces at five selected wavelengths, respectively. Unlike previous studies that relied on singular traces [255], this work adopted an intricate analytical workflow to enhance the signal-to-noise ratio, particularly for samples with weak responses (e.g., 10-minute growth duration). Individual spectral traces (ranging from 538 nm to 792 nm) were normalized by their peak negative amplitude (at t=0). This scaled all traces to a common reference point (0 to 1). These normalized traces were averaged to construct a consolidated relaxation curve.

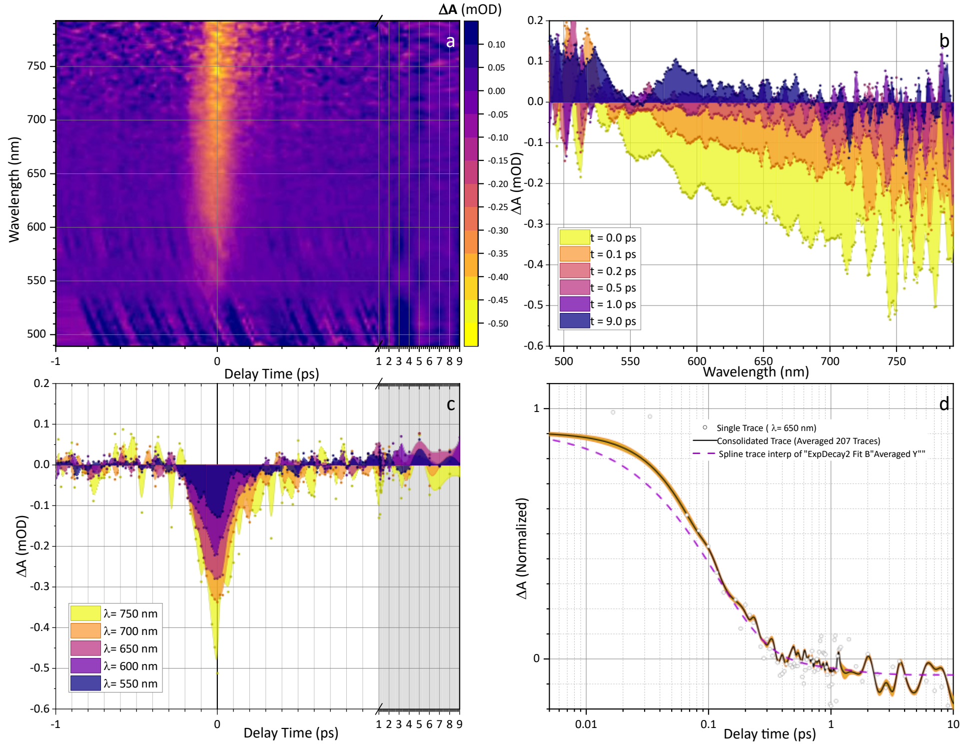

Figure 45. TAS data for sample B|60: (a) contour plot, (b) spectra at the selected delays, (c) wavelength traces, and (d) normalized consolidated trace with exponential fit

The curve was fitted using a bi-exponential decay function (equation 4):

$$I(t) = I_0 + A_1 \exp(-t/\tau_1) + A_2 \exp(-t/\tau_2) \tag{4}$$

In this equation, τ_1 and τ_2 represent the thermalization and cooling decay time constant, while A_1 and A_2 represent their corresponding amplitudes.

Analysis of decay time constants: the fast thermalization decay (τ_1) ranged from 100 fs to 150 fs across all samples (Figure 46a). These values align with literature reports for graphene; however, no statistically significant correlation was found with the input factors[251]. It should be noted that these timescales approach the temporal resolution limit of the instrument, making trend identification difficult.

In contrast, the slower cooling decay (τ_2) exhibited a statistically significant positive correlation (r=0.65) with nominal Ni thickness (Figure 46a). As suggested by Carpene et al., [35], photoexcited carriers can become trapped at defect sites, altering the decay dynamics. The increase in (τ_2) with thickness suggests that the larger/thicker shells (which have been established to have higher flake density) introduce specific phonon bottlenecks or trapping mechanisms that prolong the cooling phase. Other studies as well indicated that the changes in the structural defects of graphene affect the carrier relaxation dynamics [53, 255, 256].

Amplitude analysis and novel correlations: the most significant findings of this section lie in the analysis of the decay amplitudes (A_1 and A_2). The amplitude of the slow component A_2 and its normalized ratio, $\mathrm{A}_2/(\mathrm{A}_1 + \mathrm{A}_2)$, decreased significantly as the nominal Ni thickness increased (Figure 46c). This metric showed strong negative correlations with Raman metrics associated with flake density I(2D:D) and C(2D). This indicates that as the density of graphitic flakes increases (thicker Ni films), the relative contribution of the slow cooling channel diminishes.

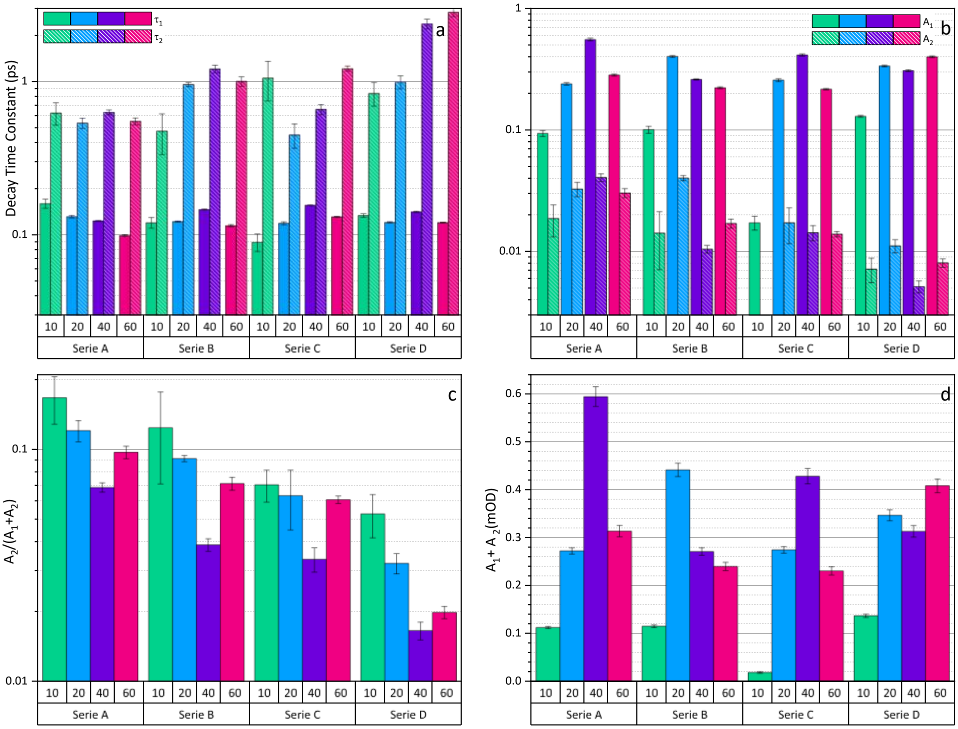

Figure 46. Influence of input factors on TAS metrics: (a) decay time constants, (b) decay amplitudes, (c) normalized slow decay amplitude, and (d) absolute peak intensity

The absolute peak intensity of the TAS signal (dominated by A_1) proved to be a powerful proxy for structural quality (Figure 46d). The samples with short duration of growth (10 min) as well exhibited very weak TAS signals due to the high prevalence of amorphous carbon. A strong negative correlation was found between the TAS intensity and the Raman G-band width (r=-0.84) and the amorphous band ratio $\mathrm{I}(\mathrm{D}_1^{\star}{:}\mathrm{D})$ and $\mathrm{I}(\mathrm{D}_1^{\star}{:}\,\mathrm{D}_2^{\star})$, as it can be seen in Figure 47b. This establishes a physically meaningful relationship: graphitic shells with higher crystallinity and lower amorphous content yield significantly higher TAS intensities.

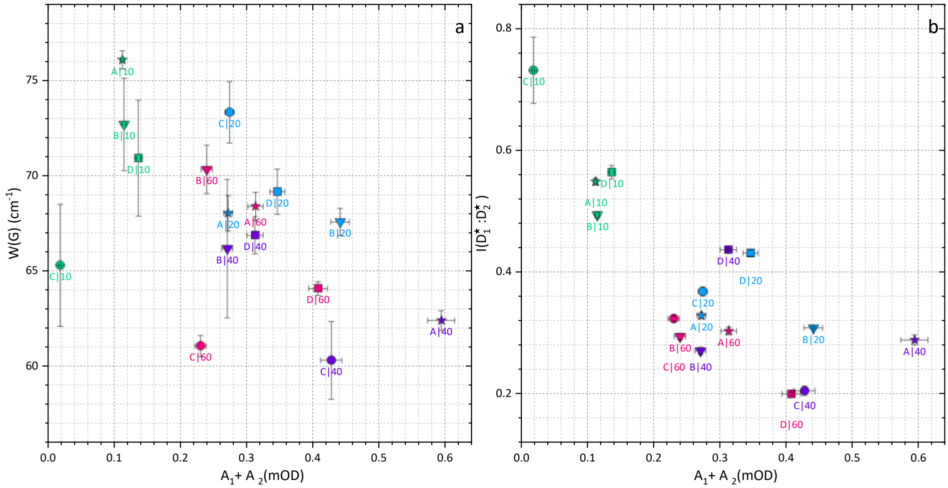

Figure 47. Two significant correlations among Raman metrics and TAS amplitude: (a) scatter plot of $\mathrm{W(G)}$ vs. TAS intensity and (b) intensity ratio $\mathrm{I}(\mathrm{D}_1^\star\!:\mathrm{D}_2^\star)$ vs. TAS intensity

Finally, considering the correlations between UV-Vis-nIR spectroscopy and decay amplitudes of TAS, it has been found that normalized $\mathrm{A}_2/(\mathrm{A}_1+\mathrm{A}_2)$ is as well negatively correlated with $\mathrm{Abs(Vis: UV)}$, which was earlier discussed that it relates to the mean number of monolayers. Additionally, both the absolute intensity of A_2 and its normalized value negatively correlates with IR absorption from the extinction spectrum, as detailed in Table 5.

3.2.5. Dimensionality Reduction and Identification of Key Metrics

In this study, generating a matrix of 107 dependent metrics from a relatively small sample size (16 samples) presents a challenge for interpretation. In order to resolve this, PCA was employed to navigate the extensive correlation matrix and extract the dominant trends hidden within the Raman (92 metrics), UV-Vis-nIR (9 metrics), and TAS (6 metrics) dataset.

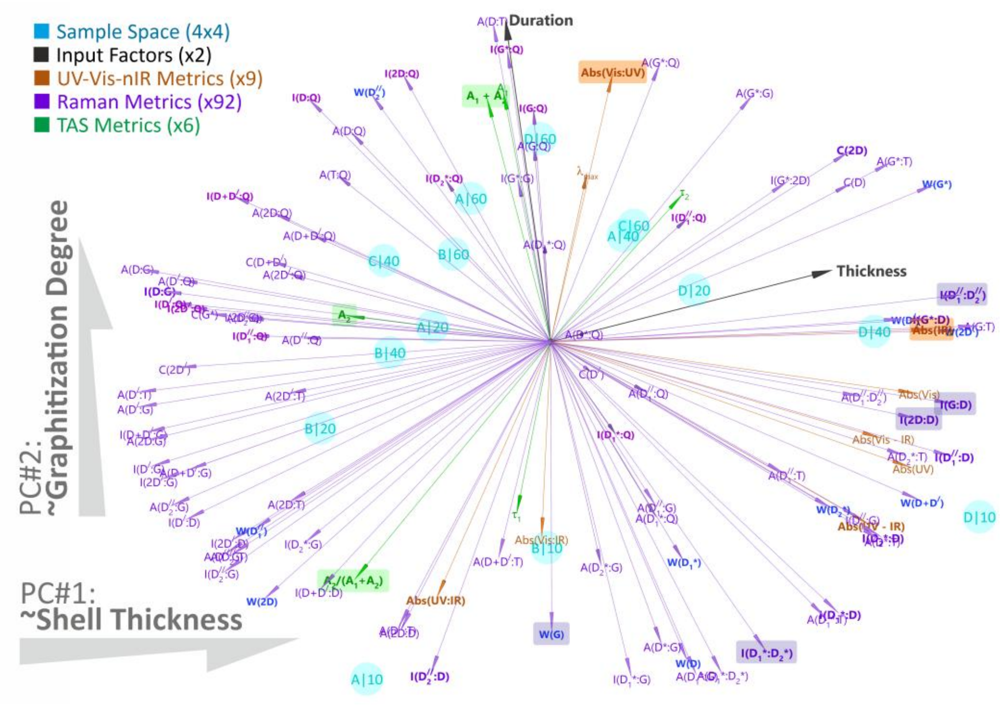

Figure 48. PCA biplot displaying sample scores (circles) and metric loadings (vectors) on the first two principal components

The analysis reveals that the first two components (PC1 and PC2) account for the majority of the variance. The biplot serves as a powerful tool for filtering redundant or unreliable metrics. For instance, among the various normalization strategies for the Raman 2D band (e.g., I(2D: Q), I(2D: D), I(2D: G), or A(2D: T)), the vector for I(2D: D) showed the strongest alignment with PC1 (the axis is largely defined by the morphological changes).

This statistical evidence reinforces the conclusion drawn in the Raman analysis section: I(2D: D) is the most robust metric for tracking the physical thickening and flake density of the shells, whereas standard metrics, such as I(D: G), are statistically less descriptive in this specific disordered regime.

Considering all reliable metrics and their physical significance, it can be concluded that the structural evolution of the samples is governed by two distinct mechanisms: (1) graphitization, driven by growth duration, which is best tracked by the narrowing of Raman peak widths (WG), and the increase in TAS peak intensity and (2) graphitic shell thickness, driven by initial Ni thickness, best tracked by the I(2D:D) ratio and infrared absorbance.

To assess the feasibility of this material as a UV-SERS platform, it is necessary to select a sample that balances high graphitic quality (for chemical stability) with low background scattering. Therefore, sample A|40 was selected as the representative candidate for the feasibility study. This sample proves to have the lowest flake density and the highest crystallinity regarding maximum TAS intensity. Moreover, it was shown that at 40 minutes, the nickel was fully encapsulated and included pinhole-free shell.

3.2.6. Feasibility Study of UV-SERS Measurement

Following the sample selection, a feasibility test was conducted to evaluate the potential of the nickel-encapsulated graphitic shell as a UV-SERS platform. A UV excitation wavelength of 325 nm was selected to spectrally align with the optical absorption band of the nickel core (~270 nm), thereby maximizing the potential for electromagnetic enhancement via the "bridging" effect. Adenine was chosen as the model analyte due to its strong electronic absorption in the ultraviolet region. Its structure consists of a pyrimidine ring fused to an imidazole ring, forming a complete aromatic system capable of interacting with the graphitic shell.

A drop of a 10^{-4} M adenine solution was applied to the sample surface and subsequently dried in a furnace for 30 minutes at 200 °C. **Figure *49***a presents the Raman spectra of the substrate with the analyte, the bare substrate, and the calculated difference spectrum (detected analyte).

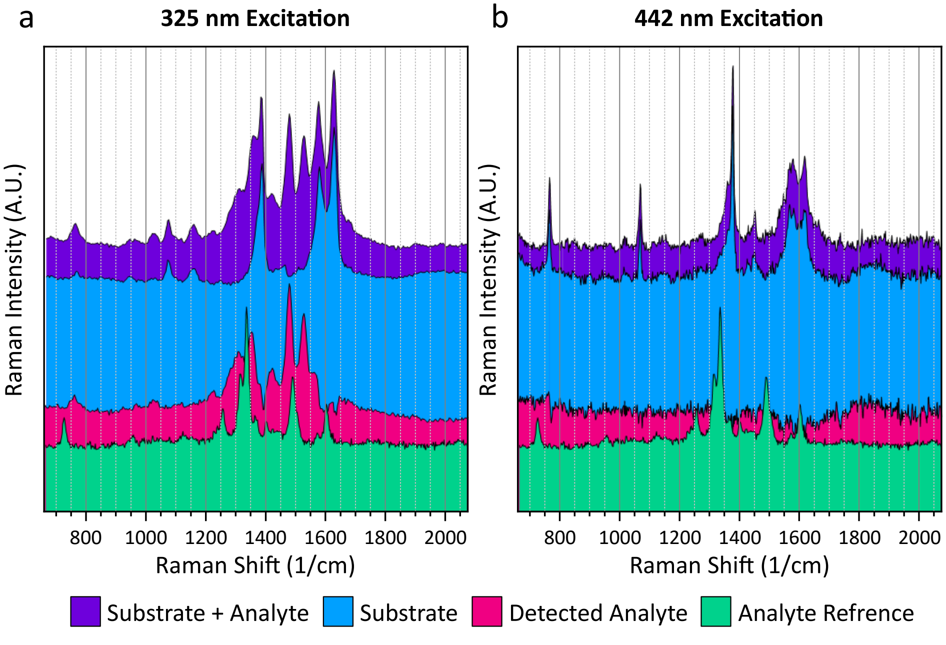

Figure 49. SERS detection of adenine on nickel-encapsulated graphite (sample A|40): (a) resonant excitation at 325 nm showing enhancement and (b) non-resonant control at 442 nm

The reference adenine spectrum exhibits characteristic bands at 727 cm^{-1}, 1,336 cm^{-1}, 1,489 cm^{-1}, and 1,601 cm^{-1}. The adenine core structure consists of two fused rings: a pyrimidine ring and an imidazole ring, forming a complete aromatic two-ring system [257]. Its most dominant band, assigned primarily to the stretching vibration of the C8–H bending mode of the purine ring, is located at ~1,464 to 1,489 cm^{-1} [146].

On the nickel-encapsulated substrate, the enhanced Raman peaks are clearly resolved, particularly in the fingerprint region (1,487 and 1,527 cm^{-1}), which corresponds to the stretching and bending modes of the purine nucleobase.

The observed signal arises from a powerful synergistic effect known as SERRS, which combines the following contributions:

Electromagnetic mechanism**:** driven by the localized surface plasmon resonance (LSPR) of the Ni core (~270 nm) that is fully encapsulated in graphite. As established in the literature, when the excitation laser (325 nm) closely aligns with the maximum optical absorption of the metallic nanostructure, it generates a substantial near-field electromagnetic enhancement.

Molecular resonance and chemical mechanism**:** adenine exhibits strong intrinsic electronic transitions in the ultraviolet region; thus, the excitation at 325 nm triggers molecular resonance Raman scattering. Furthermore, the hexagonal carbon network of the encapsulating shell interacts with the aromatic rings of adenine through non-covalent $\pi - \pi$ stacking. This interaction enriches the analyte concentration directly within the enhanced near-field and prevents thermal desorption.

Crucially, this measurement was performed two years after the initial synthesis of the substrate. During this period, the sample was stored under standard laboratory conditions. The successful detection of adenine confirms that the graphitic shell effectively protected the metallic nickel core from oxidation, a feat impossible for bare nickel nanoparticles, which would have degraded into non-plasmonic oxides within a few seconds in ambient air.

To confirm the resonant nature of this enhancement, a control experiment was conducted using a non-resonant 442 nm laser (**Figure *49***b). No discernible adenine peaks were detected, verifying that the massive signal amplification is directly linked to the coupling of the analyte's molecular resonance with the UV plasmon resonance of the nickel core. For the first time, this proof-of-concept demonstrates the viability of nickel-encapsulated graphitic shells as highly stable non-noble metal platforms for trace analyte detection via UV-SERRS.

3.3. Case Study III: Signal Stability of Graphene-Overlayered Resonant Silver Arrays

This case study addresses the critical challenge of oxidative degradation in noble-metal SERS substrates. While silver (Ag) offers superior plasmonic enhancement compared to nickel, its practical utility is limited by rapid sulfidation and oxidation. Thus, the author of the dissertation investigates the synergistic integration of a graphene monolayer with periodic arrays of silver nanocubes with a focus on quantifying stability. By employing a rigorous longitudinal assessment, the aim was to determine the "analyte detection score" of protected versus unprotected substrates over a period of one year. The results presented in this case study have been published in *The Journal of Physical Chemistry C* (2025, Vol. 129, 14983–14992).

3.3.1. Study Design: Comparative Longitudinal Stability

In order to isolate the protective effect of graphene from the intrinsic degradation of the silver, a comparative experimental design was implemented involving two parallel sets of samples fabricated via CAPA assembly technique:

1. ***Sample U (unprotected):*** a periodic array of bare silver nanocubes (edge length ~77 nm) assembled onto a PDMS template.

2. ***Sample G (protected):*** an identical Ag nanocube array covered with a CVD-grown monolayer graphene sheet, transferred via the PVA dry-transfer method.

A critical design parameter was the spectral alignment of the plasmonic resonance. The lattice periodicity (400 nm) was engineered to generate an SLR peak near 570 nm. This wavelength was specifically chosen to bridge the excitation laser (532 nm) and the Stokes-shifted emission of the target analyte, ensuring maximum electromagnetic enhancement. An overview of the workflow from the fabrication to the analysis process is presented in **Figure *50***.

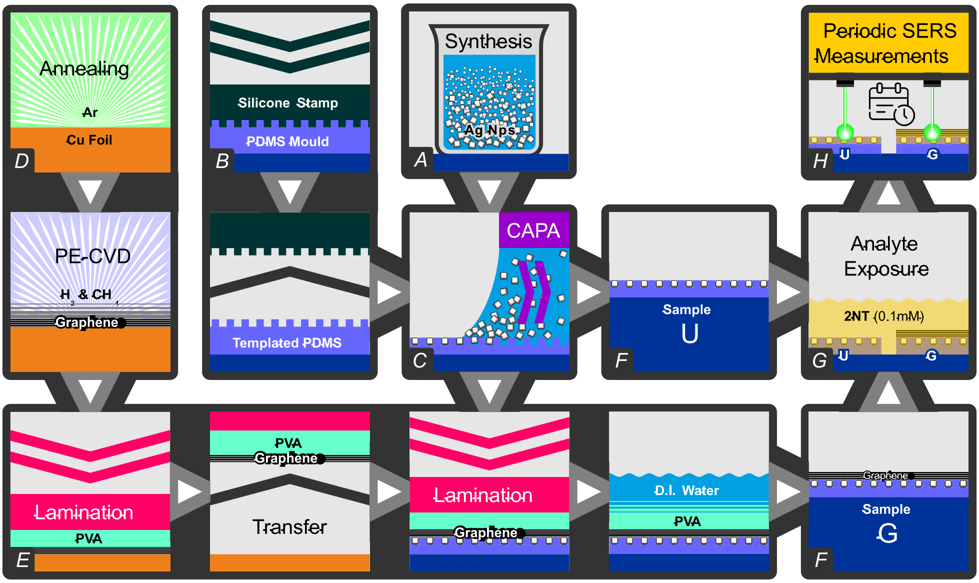

Figure 50. Workflow of the fabrication and analysis process: (a) synthesis of Ag nanocubes, (b) fabrication of a templated substrate by replicating a silicon master, (c) deposition of Ag nanoparticles via CAPA method, (d) graphene growth on Cu foil by PECVD, (e) graphene transfer onto the assembled array via PVA dry method, (f) fabricated SERS samples "U" and "G", (g) exposure samples to the 2NT analyte and (h) track the signal over the year

3.3.2. Surface and UV-Vis Analysis

Figure 51a presents the UV-Vis extinction spectrum of the periodic silver nanoparticle arrays on PDMS, measured at normal incidence. The spectrum exhibits two distinct features: a broad peak centered around 430 nm and a sharper resonance near 570 nm. The broad peak is attributed to the quadrupolar LSPR of the individual silver nanocubes. The dipolar LSPR, while not distinct as an isolated peak, hybridizes with the photonic Rayleigh anomaly mode[258], manifesting as a sharp lattice resonance peak at ~570 nm. For a square grating in PDMS, the RA wavelength at normal incidence is defined by the equation $\lambda_{RA} = \Lambda \times n$. Given the lattice periodicity (Λ = 400 nm) and the refractive index of PDMS (n =1.4), the theoretical RA wavelength is calculated to be ~560 nm [128, 132, 258]. The observed SLR peak at 570 nm is consistent with this calculation, as the SLR mode typically emerges slightly red-shifted relative to the Rayleigh anomaly.

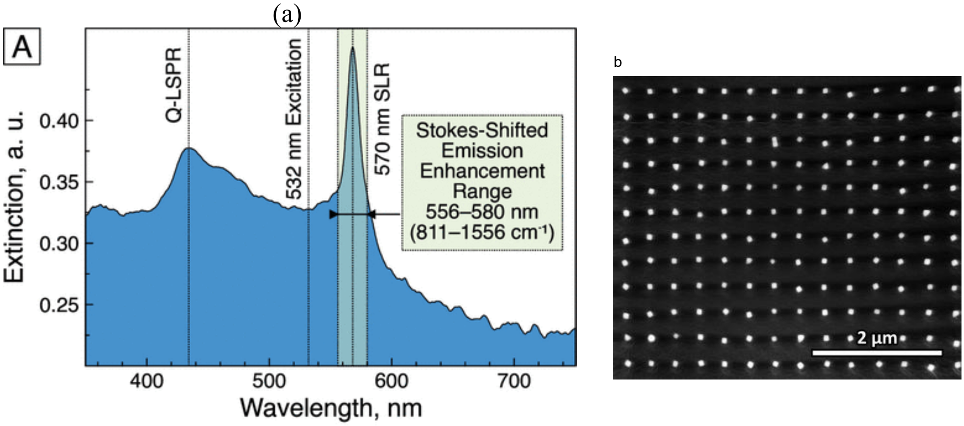

Figure 51. (a) UV-Vis extinction spectrum and (b) SEM image of the periodic silver nanoparticle arrays on PDMS

Figure 51b presents a SEM micrograph of the assembled plasmonic structure. The high uniformity of particle occupancy within the lithographic traps ensures consistent periodicity and geometry across the array, which is essential for the reproducibility and scalability of the substrate. The SERS enhancement on this resonant lattice is governed by the spectral positioning of the SLR. Centered at 570 nm, the SLR represents a high-quality plasmonic mode, characterized by a narrow linewidth and strong electromagnetic field localization. As illustrated in Figure 51a, the 532 nm excitation laser is positioned on the high-energy shoulder of this SLR peak. This alignment ensures efficient coupling of the incident light into the plasmonic system while reserving the resonance maximum for the scattered light.

For a 532 nm excitation source, the characteristic Raman vibrational modes of 2NT, spanning 811−1,556 cm^{-1}, correspond precisely to the wavelength range of 556−580 nm. This ensures that the inelastic scattering process occurs within the maximum electromagnetic enhancement window provided by the SLR. By positioning the SLR peak between the excitation laser and the Stokes-shifted scattering wavelengths, a dual-enhancement mechanism is achieved: first, by localizing the incident electric field and second, by providing a high density of optical states that amplify the outgoing Raman signals.

Figure 52 presents the Raman spectrum of the reference graphene on copper foil used in this study. While four prominent bands (D, G, D′, and 2D) were the primary focus of the analysis, three less-prominent bands (G*, D + D′, and 2D′) were as well included in the fitting process, as listed in Table 7.

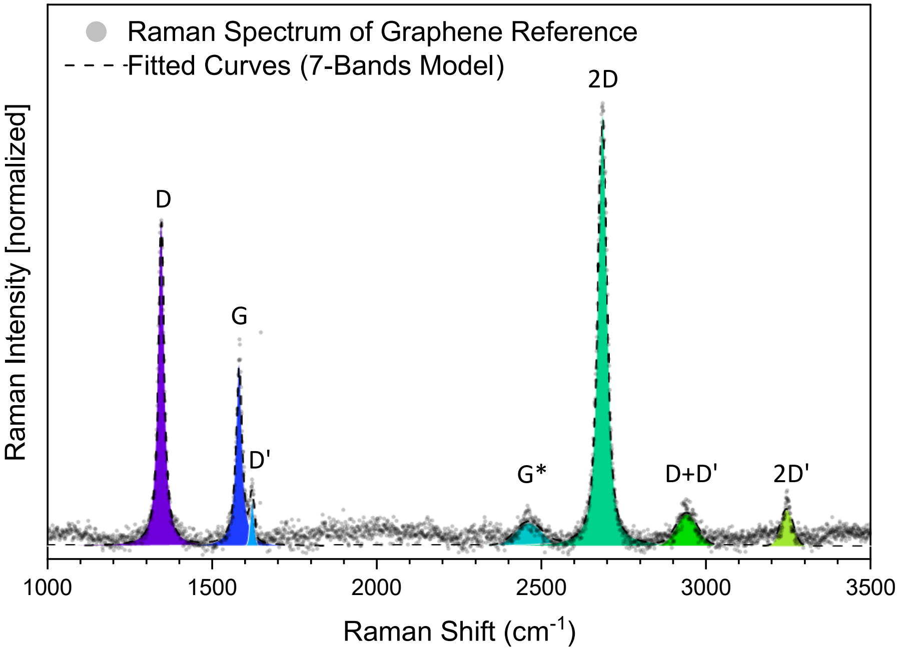

Figure 52. A representative Raman spectrum of the reference graphene sample on Cu foil with fitted bands overlaid

Table 7. Fitting results for the graphene reference sample obtained using the 7-band fitting model

Band	**Center (cm^{-1})**	**FWHM (cm^{-1})**	**Intensity**	**Fit Type**
D	1,345.1	20.8	1.76	Voigt
G	1,581.6	21.8	1.00	Voigt
D'	1,621.9	15.0	0.24	Gaussian
G*	2,461.2	95.0	0.13	Gaussian
2D	2,685.5	33.8	2.34	Voigt
D+D'	2,940.8	76.1	0.17	Gaussian
2D'	3,244.9	45.2	0.20	Gaussian

Considering prominent bands, the Raman spectrum confirms the synthesis of single-layer graphene with a specific structural defect. Sharp, symmetric, and well-fitted by a single Voigt function of the 2D mode confirmed the monolayer structure. This is further supported by the high I (2D:G) intensity ratio of ~2.68 [54]. The I(D:G) ratio of ~2.2 suggests a high concentration of defects as well, which is expected from a low-temperature growth process.

3.3.3. Analyte Raman Signal Measurement

The Raman signal of 2NT, a simple aromatic molecule with an extended π-conjugated system, was collected on two SERS substrates (U and G) after immersion in a 10^{-4} M solution. The measurements were conducted at eight discrete time intervals: immediately after exposure and after 10, 16, 24, 35, 108, 303, 344 days. This quasi-exponential temporal spacing was strategically designed to capture the rapid initial degradation kinetics of the highly reactive silver surface during the first month, while progressively extending the measurement intervals to effectively monitor the long-term baseline stability and signal retention over the remainder of the year. All samples at all time points were measured at least three times with an exposure time of 60 seconds and a 50× objective lens, which was later included in the PCA analysis. The reference samples of pure 2NT, PDMS, and graphene were measured as well to establish a reference dataset for the evaluation purposes.

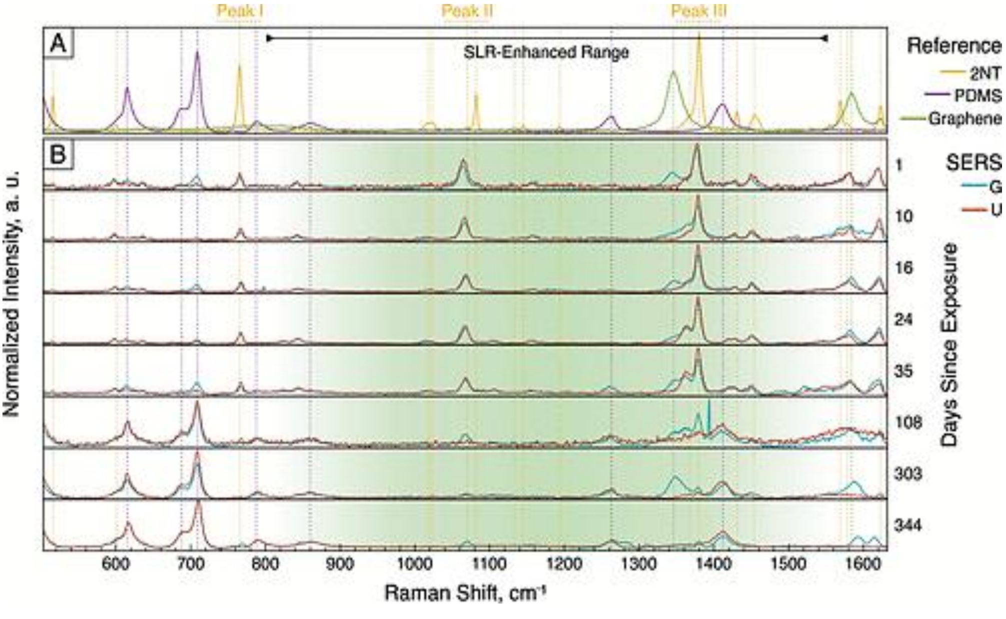

Figure 53. (A) Normalized Raman spectra of reference materials (graphene, PDMS, 2NT), (B) temporal evolution of 2NT Raman spectra on protected (G) and unprotected (U) substrates over 344 days

Figure 53a presents the average Raman spectra (480 cm^{-1} to 1,650 cm^{-1}) obtained from the measurements of reference samples, including PDMS, graphene, and 2NT molecules, along with the temporal evolution of SERS measurements on unprotected and graphene-protected substrates over time (Figure 53b).

The PDMS reference spectrum exhibits distinct peaks at 612 cm^{-1}, 705 cm^{-1}, 1,260 cm^{-1}, and 1,410 cm^{-1} [132, 259]. The 2NT molecule peaks are observed as well at 515 cm^{-1}, 599 cm^{-1}, 766 cm^{-1}, 1,020 cm^{-1} (correspond to the ring deformation and C-H bending), 1,082 cm^{-1} (associated with ring breathing coupled with C–S stretching and in-plane C–H bending), 1,380 cm^{-1} (representing the D-mode of the aromatic rings), 1,433 cm^{-1} and 1,455 cm^{-1} (attributed to in-plane C-H bending coupled with ring C=C stretching and C–S stretching), 1,570 cm^{-1} and 1,622 cm^{-1} (corresponding to the characteristic C=C stretching modes of the aromatic ring).

To assess the enhancement provided by the SLR, three relatively dominant and isolated characteristic Raman peaks of 2NT were analyzed: peak I at approximately 766 cm^{-1}, peak II at 1,082 cm^{-1}, and peak III at 1,380 cm^{-1}, as shown in **Figure *54***.

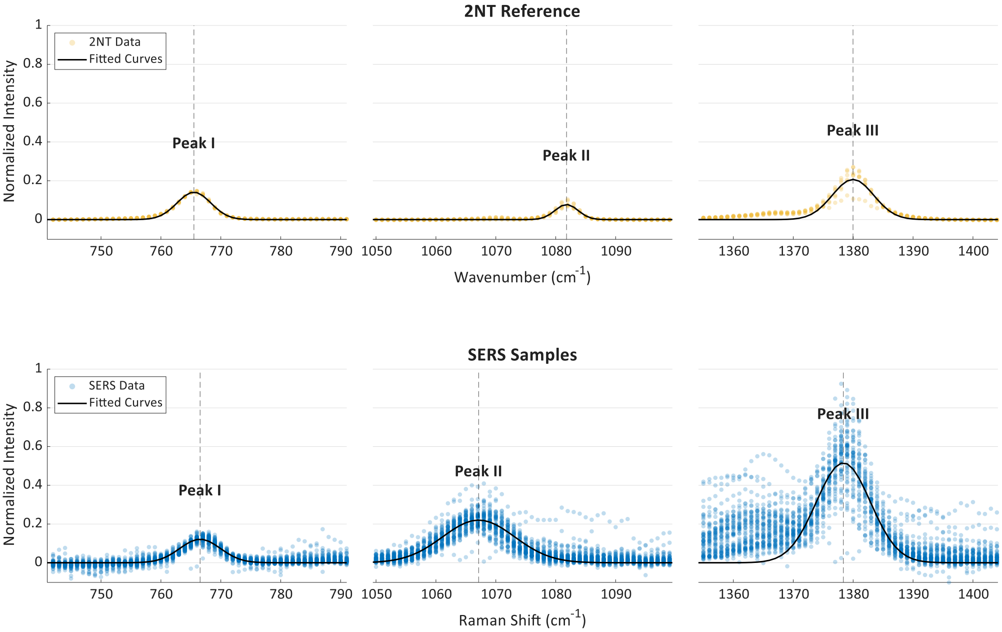

Figure 54. Comparison of average Raman spectra normalized to the intensity of peak I for the 2NT reference (yellow) and SERS measurements (blue)

Peak I lies outside the SLR enhancement range, which is expected to remain unaffected by the SLR and thus serves as an internal reference to measure EF, whereas peaks II and III are positioned within the SLR resonance region (green shaded area in Figure 53). These latter peaks are expected to be selectively enhanced by the SLR effect. Gaussian peak fitting was applied to both the 2NT reference and the SERS spectra from both samples obtained during the initial month, providing normalized peak intensities relative to peak I. The calculated EF (.

Table **8**) reflects selective amplification of peaks II and III under SERS conditions.

Table 8. Normalized intensities and calculated enhancement factors for characteristic Raman peaks of 2NT; peak I (766 cm^{-1}), located outside the SLR range, serves as the normalization reference

Peak	**Position (cm^{-1}) (reference)**	**Normalized intensity (reference)**	**Normalized intensity (SERS)**	**Enhancement factor (EF)**
I (off resonance)	766	1	1	x1
II (on resonance)	1,082	0.38 ± 0.03	3.39 ± 0.16	x8.92 ± 0.78
III (on resonance)	1,380	1.92 ± 0.11	6.80 ± 0.30	x3.54 ± 0.26

The comparison clearly illustrates the relative increase in intensity for peaks II and III, suggesting that their enhancement correlates directly with the position of the SLR peak.

3.3.4. Quantitative Analysis of Signal Retention

The Raman spectral data of reference samples (collected from pure crystalline 2NT, the PDMS substrate, and graphene monolayer) were subjected to PCA to identify the patterns of variance.

It is important to note that Raman analysis often relies on relative peak intensity ratios or peak fitting to derive metrics. However, these methods struggle with overlapping peaks and trace concentrations, as they reduce the spectral dataset to a single parameter, leading to a loss of critical information [260]. PCA addresses these challenges by leveraging the entire spectral dataset, capturing both prominent and subtle variations and generating a set of robust metrics known as principal components (PCs). The scree plot confirms that PC1 and PC2 together explain nearly 94% of the total variance, with an elbow point at PC3, justifying the selection of the first two components for spectral differentiation. PC1 captures 59.35% of the variance, primarily distinguishing the 2NT analyte signal from the PDMS background, while PC2 accounts for 34.55% effectively separating the graphene reference and graphene-protected (G) samples. The elbow point occurs at PC3 (2.82%), indicating that additional components contribute only marginal variance, which is mainly related to minor peak shifts in SERS measurements compared to the references (**Figure 55**). Given that PC1 and PC2 together explain nearly 94% of the variance, they were selected for further analysis to effectively represent spectral differentiation and long-term analyte retention.

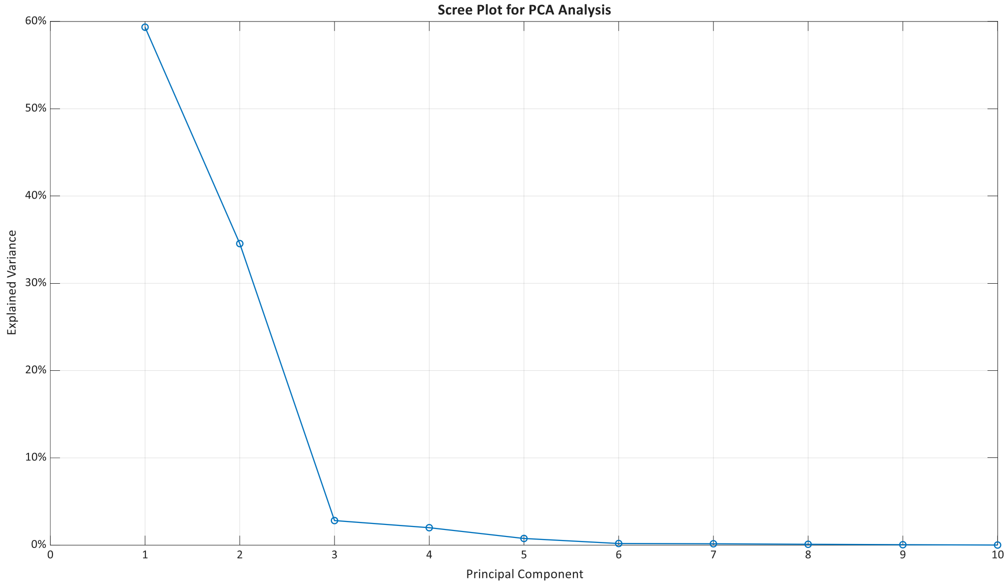

Figure 55. Scree plot showing the variance explained by each PCs in the Raman spectral dataset

By plotting the observation points against the first two principal components (see Figure 56a), 95% of the variance was visualized in the high-dimensional spectral dataset with PC1 capturing ~60% and PC2 accounting for ~35% of the variance.

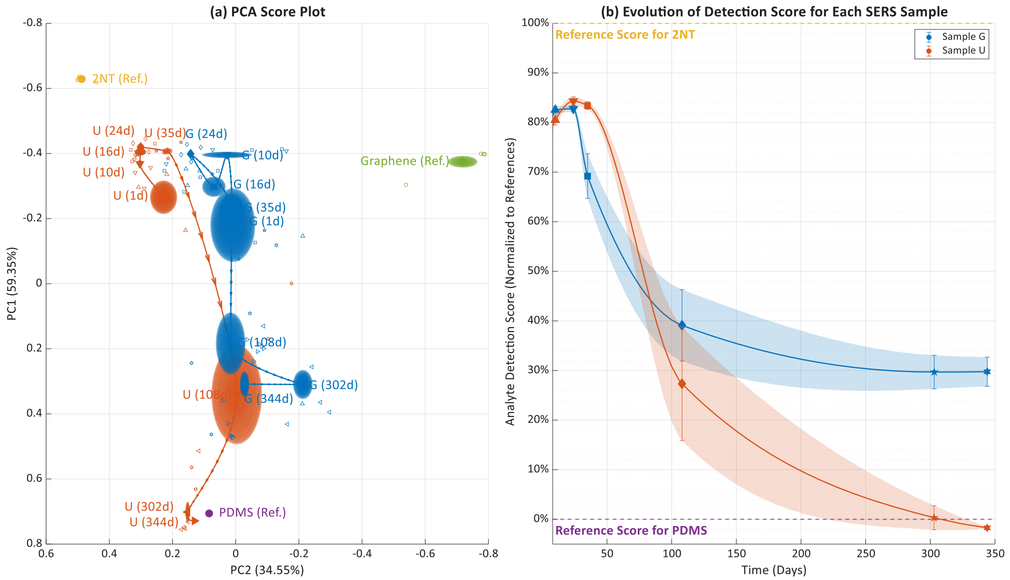

Figure 56. (a) PCA score plot of reference signatures and time-resolved SERS observations, (b) calculated analyte detection scores for protected (G) vs. unprotected (U) samples over 344 days

Distinct clustering of the reference samples for PDMS (+0.7 on PC1) and 2NT (-0.65 on PC1) clearly separates their Raman signatures. Within this PCA space, the measurements taken on the SERS substrate span intermediate positions from -0.4 to +0.6 on PC1, reflecting the relative contributions of PDMS and 2NT in the spectra. This projection effectively illustrates the relative concentration of each reference signature. The observations with a stronger 2NT signature cluster near the 2NT reference ($-0.4 < \text{PC1} < -0.2$), while those dominated by PDMS signature shift toward positive PC1 scores, closer to the PDMS reference. These findings confirm PC1 as a reliable metric for evaluating the relative concentration of 2NT vs. the PDMS background. The second principal component (PC2) primarily distinguishes the graphene signature at PC2 = -0.7 from the other two references with positive scores. As a result, SERS spectra from sample "G" align more closely with graphene reference compared to the "U" series.

By normalizing PC1 scores linearly, a quantitative score for analyte detection was created ranging from 0% (no 2NT detected) to 100% (pure 2NT detected). This metric was used to track the time-dependent evolution of the SERS signal, as illustrated in Figure 56b.

The results revealed that both U and G samples initially showed a detection score of around 80%; scores being slightly higher for the unprotected sample U. This observation aligns with the findings of Gong et al., [180], who reported slightly higher enhancement factors for bare metal substrates. This initial difference is attributed to the exponential decay of the near-field electromagnetic EM enhancement; the insertion of the graphene overlayer introduces an additional physical distance between the analyte molecules and the plasmonic silver surface. However, over time, both samples exhibited a decline in signal intensity. Sample G stabilized at a retention score of approximately 29.7%, while sample U degraded completely to zero. This degradation timeline perfectly aligns with literature reports regarding the intrinsic chemical instability of bare SERS substrates [261]. For the unprotected silver, degradation is primarily driven by rapid oxidation and sulfidation upon exposure to ambient air. Furthermore, in this study, the degradation was heavily accelerated by the direct contact between the highly reactive silver surface and the analyte. The strong chemisorption of the thiol (-SH) groups of 2NT initiated metal-catalyzed side reactions that progressively deteriorated the plasmonic nano-antennas, ultimately causing the complete desorption or decomposition of the chemically bonded analyte and a total loss of the SERS signal after 344 days.

The overall decline that was observed in the protected sample (G) can be explained by the presence of intrinsic structural defects in the CVD-grown monolayer, compounded by additional mechanical imperfections introduced during the dry-transfer process. As established in the literature review, localized corrosion can initiate at these grain boundaries and structural defect sites, leading to inhomogeneous coverage and localized plasmonic degradation. However, the remarkable ability to retain 30% of the analyte detection score after nearly a year is directly attributed to two synergistic properties of the graphene overlayer:

(1) Physical and electronic passivation: in regions of complete coverage, the atomically impermeable graphitic lattice shielded the silver nanocubes from atmospheric oxidants and physically separated the reactive metal from the corrosive thiol groups of the analyte, preventing metal-catalyzed degradation [261].

(2) Chemical mechanism: the hexagonal carbon network actively interacted with the aromatic naphthalene ring of the 2NT analyte (composed of two fused benzene rings) via non-covalent $\pi - \pi$ stacking [262]. Driven by the highly delocalized $\pi - electron$ clouds, this interaction enriched the analyte concentration within the near-field and effectively pinned the molecules to the surface. Although these $\pi - \pi$ interactions are weaker than direct metal-thiol covalent bonds, they are highly robust when the substrate itself is an extended aromatic system such as graphene [263, 264]. Chakradhar et al., [265] showed that while the interaction strength between benzene and graphene can be modulated by the underlying substrate, it remains sufficiently robust to delay desorption.

Ultimately, the obtained results quantitatively confirm that while the EM mechanism provides the initial massive signal boost, the CM mediated by the protective graphene overlayer is a critical mechanism responsible for long-term signal retention. This stability is paramount for forensic archiving and environmental monitoring, where evidence must remain stable for retrospective testing over the extended periods.

It is worth mentioning that PCA has limitations, particularly in handling nonlinear combinations of components or variations in spectral characteristics. Peak shifts or new peaks emerging from the molecular bonding can as well reduce PCA's sensitivity, as demonstrated by the 2NT peak shifting from 1,080 cm^{-1} in its crystalline form (reference) to 1,070 cm^{-1} on the SERS substrate [266]. Despite these challenges, PCA proved effective by detecting the 2NT signal (detection score = 30%) in the unprotected sample "U" at day 108, even when the isolated 1,070 cm^{-1} band was no longer detectable, underscoring PCA's capability compared to the manual peak-fitting methods for generalized spectral analysis and long-term monitoring.

CONCLUSIONS

This dissertation addresses the critical challenges in the synthesis, multi-spectroscopic characterization, and graphene-metal hybrid SERS sensing application. By bridging fundamental growth with applied sensor stability, the research leads to the following general conclusions:

1. The study established that the uniformity of graphene growth on polycrystalline nickel foils is fundamentally governed by the nucleation site density. While standard PECVD processes are limited by the variable diffusion rates of the underlying crystal grains, this work demonstrated that pre-seeding the surface with nickel nanoparticles effectively decouples the growth mechanism from the substrate's crystallographic orientation. This strategy lowers the energy activated for carbon precipitation, enabling the synthesis of high-quality bilayer graphene films even under carbon-rich conditions.
2. Nickel-encapsulated graphitic shells were successfully synthesized via a two-step dewetting and PECVD process. XPS analysis confirmed that a minimum growth duration of 20 minutes is required to achieve a hermetic graphitic seal that fully reduces the surface oxides and prevents re-oxidation. Furthermore, the structural quality of these shells was found to be governed by two orthogonal physical mechanisms: shell thickness (driven by catalytic volume) and graphitization (driven by growth duration). Consequently, these features must be tracked separately: infrared absorbance ($\mathrm{Abs(IR)}$), the Raman $\mathrm{I(2D{:}\,D)}$ ratio are the deterministic proxies for shell thickness/flake density, whereas Abs(Vis:UV), $\mathrm{I}(\mathrm{D}_{\mathbf{1}}^{\star}{:}\,\mathrm{D}_{\mathbf{2}}^{\star})$, and D band width ($\mathrm{W(D)}$) from Raman isolates the degree of crystalline ordering.
3. The research validated the physical interchangeability of TAS and Raman spectroscopy for characterizing disordered carbon. Significant inter-metric correlations confirm that ultrafast carrier thermalization dynamics are governed by the same defect densities that dictate phonon lifetimes. Specifically, the TAS peak intensity was established as a robust, non-destructive proxy for crystallinity strongly correlating with Raman G-band width ($r = -0.8$), while the TAS slow decay ratio ($\mathrm{A}_2/(\mathrm{A}_1 + \mathrm{A}_2)$) inversely tracks shell thickness (correlating with the Raman $\mathrm{I(2D{:}\,D)}$ ratio) enabling the use of TAS as a rapid alternative to conventional Raman analysis.
4. The optimized nickel-encapsulated graphitic shells were proven to function as stable UV-SERS platforms, overcoming the rapid oxidation that is typically associated with transition metals. The study concludes that the graphitic shell provides a sealed barrier that preserves the metallic nickel core for over two years. The successful detection of adenine at 325 nm is driven by SERRS, a synergistic effect where the excitation wavelength simultaneously aligns with the UV plasmonic resonance of nickel core and the intrinsic electronic transition of the analyte, while the carbon shell facilitates target adsorption via $\pi - \pi$ stacking.
5. Finally, the integration of monolayer graphene on resonant silver lattice arrays extends the SERS signal stability from weeks to over one year. While the massive EM of the underlying silver lattice inevitably degrades over time due to the

localized sulfidation and oxidation, the graphene overlayer effectively provides both physical and electronic passivation, thereby preserving the chemical enhancement. As quantified by PCA derived analyte detection score, this sustained non-covalent $\pi - \pi$ interaction between the aromatic analyte and the graphitic sensor surface is the primary mechanism allowing for ~30% signal retention after 344 days.

Future Direction

Building on the foundations established in this dissertation, the following directions are proposed for the future research:

- The laser-ablated nickel foils yielded porous nanoflake-like carbon structures. Future work should focus on decorating these high-surface-area scaffolds with noble metal nanoparticles (Ag/Au) to create hierarchical 3D-SERS substrates.
- While this work demonstrated the feasibility of UV-SERS on nickel, future studies should focus on fabricating periodic nickel arrays to systematically quantify enhancement factors and establish the limits of detection for biological analytes.
- A deeper theoretical investigation (e.g., DFT modeling) is required to elucidate the precise degradation kinetics at the graphene-silver interface and optimize the π-π stacking interactions for specific classes of aromatic analytes.

SANTRAUKA

Įvadas

Grafeno, anglies monoatominio sluoksnio, kuris yra daugelio anglies alotropų struktūrinis elementas, technologija ir tyrimai žymi reikšmingą etapą kietojo kūno fizikoje. Grafenas yra žinomas dėl savo išskirtinių savybių, įskaitant didelį elektronų judrį, rekordinį šilumos laidumą, mechanines savybes bei nepralaidumą dujoms. Šios unikalios savybės paskatino išsamius tyrimus ir kitų, naujų dvimačių (2D) medžiagų šeimų srityje.

Unikalios grafeno savybės sukėlė didžiulį mokslinį susidomėjimą ir lėmė jo integravimą į naujas pažangias technologijas ir taikymus. Tarp perspektyviausių iš šių taikymų paminėtini naujos kartos nanofotoniniai jutikliai, ypač struktūros, skirtos paviršiaus sustiprintos Ramano sklaidos (SERS) matavimams. SERS naudojamos plazmoninės nanostruktūros leidžia smarkiai sustiprinti molekulių Ramano signalą ir taip užtikrinti itin jautrų jų aptikimą. Grafeno cheminis inertiškumas ir unikalios elektroninės savybės daro jį idealiu kandidatu hibridinėms SERS platformoms, kurios pasižymi stabilumu ir našumu. SERS padėklų ilgaamžiškumas yra lemiamas veiksnys siekiant išlaikyti jų jautrumą. Jei ilgainiui šie padėklai degraduoja ar praranda savo stiprinimo savybes, analizės rezultatai tampa nepatikimi.

Šios disertacijos tikslas – sukurti stabilias ir patikimai apibūdintas grafeno pagrindu veikiančias hibridines struktūras, taikytinas SERS reikmėms analitės pėdsakams aptikti. Disertacijoje sprendžiami trys uždaviniai, su kuriais susiduriama kuriant ir taikant tokias struktūras. Pirmasis uždavinys skirtas grafeno struktūrų sintezės iššūkiams spręsti, antrasis orientuotas į patikimos validavimo sistemos sukūrimą, o trečiasis uždavinys susijęs su struktūrų taikymais.

Sintezės iššūkis: Naudojant plazmos indukuoto cheminio garų nusodinimo (PECVD) techniką, sudėtinga užtikrinti aukštos kokybės, tolygų grafeno sluoksnių augimą ant polikristalinio katalizatoriaus. Pavyzdžiui, nikelis ir varis yra plačiausiai naudojami katalizatoriai žemos temperatūros grafeno sintezei. Tačiau pagrindinis iššūkis, susijęs su šiomis polikristalinėmis folijomis, yra nekontroliuojamas, atsitiktinis anglies atomų branduolių susidarymas, kurį lemia padėklo grūdų orientacijų skirtumai bei grūdų ribos ir kuris apsunkina tolygaus sluoksnio formavimą.

Apibūdinimo iššūkis: Ramano sklaidos spektroskopija tradiciškai naudojama kaip standartinė anglies alotropinių atmainų apibūdinimo technika. Tačiau jos patikimumas mažėja tiriant itin netvarkingus arba tankiai supakuotus mažus grafeno lakštus, tokius kaip vertikaliai orientuoti grafeno lakštai ar lenktos kupolo formos struktūros. Problema ypač išryškėja sluoksnio sudėtyje esant amorfinei angliai. Dėl netvarkingos tokių struktūrų prigimties pastebimi liuminescencinio fono trukdžiai, todėl įprasta Ramano analizė tampa nepatikima.

SERS padėklų stabilumo iššūkis: Nanofotoninės jutiklinės technikos pažanga įtvirtino SERS kaip galingą analizės įrankį, kuriame paprastai naudojamos tauriųjų metalų nanostruktūros, leidžiančios aptikti molekules smarkiai sustiprinant Ramano signalą. Tačiau čia susiduriama su plazmoninių nanostruktūrų jautrumo oksidacijai ir sulfidacijai problema, kuri ypač aktuali naudojant struktūras vandeninėje aplinkoje.

Toliau pateikti tyrimų uždaviniai remiantis trimis atvejų analizėmis:

Grafeno sintezė ant polikristalinio Ni folijos naudojant PECVD. Ištirti angliavandenilių srauto režimo įtaką plazmos indukuoto cheminio garų nusodinimo (PECVD) procese, auginant grafeno sluoksnius ant nikelio katalizinio paviršiaus, ir įvertinti katalizatoriaus paviršiaus poveikį nusodintos plėvelės kokybei.

Grafitinio sluoksnio kapsuliuotų nikelio nanodalelių sintezė ir išsamus apibūdinimas jas taikant SERS matavimams. Suformavome įvairiais technologiniais režimais grafitiniu sluoksniu padengtų nikelio nanodalelių bandinius, kuriuos naudojome kaip modelį spektroskopinių metodų rinkiniui tirti. Tyrimai apėmė Ramano spektroskopiją, ultravioletinę–matomąją-artimąją infraraudonąją (UV–Vis–NIR) spektroskopiją ir dinaminės absorbcijos spektroskopiją (TAS). Taikyta koreliacinė analizė siekiant sukurti sistemą netvarkingo grafitinio sluoksnio, kapsuliuojančio nikelio branduolį, kokybei vertinti. Ultravioletinės paviršiaus sustiprintos Ramano spektroskopijos galimybių tyrimas buvo atliktas naudojant adenino modelinę analitę esant ~325 nm žadinimui, kuris artimai sutampa su nikelio dalelių paviršiaus plazmonų rezonanso dažniu.

Jutiklių, paremtų grafenu dengtomis rezonansinėmis tvarkingomis sidabro nanodalelių dvimatėmis struktūromis, kūrimas SERS matavimams. Ši užduotis apėmė monosluoksnio grafeno gamybą, jo sausą perkėlimą ant periodinių sidabro nanodalelių masyvų, kuriems būdingas paviršiaus gardelės rezonansas, ir hibridinio jutiklio sudarymą. Sukurto jutiklio ilgalaikio stabilumo tyrimai buvo atlikti naudojant 2-naftalenetiolį (2NT) kaip analitę, taikant pagrindinių komponentų analizę (PCA) siekiant kiekybiškai įvertinti analitės signalų stabilumą per ilgą laikotarpį.

Mokslinio naujumo aspektai yra daugialypiai ir gali būti apibendrinti taip:

- Optimalaus katalitinio paviršiaus paruošimas tolygiam grafeno sluoksnio auginimui PECVD būdu, naudojant Ni nanodalelių išankstinį nusodinimą ant polikristalinių Ni folijų.
- Pirmą kartą sukurta daugelio spektroskopijų koreliacinė metodika defektuotiems grafitiniams apvalkalams apibūdinti, kuri įgalino nustatyti patikimas sluoksnių metrikas ir atskleidė jų tarpusavio koreliacijas, leidžiančias pakaitomis naudoti papildomus spektroskopinius metodus.
- Sukurta nikeliu kapsuliuoto grafito struktūra kaip naujoviška platforma UV-SERS matavimams.
- Naudojant grafeno dengiantįjį sluoksnį ant rezonansinių sidabro masyvų, skirtų ilgalaikiams stebėjimams, pademonstruotas metus trunkantis SERS signalo stabilumas.

Pagrindiniai ginamieji teiginiai:

- Išankstinis polikristalinių nikelio folijų padengimas nikelio nanodalelėmis sumažina anglies nusodinimui reikalingą aktyvacijos energiją ir iš esmės atsieja grafeno augimo mechanizmą nuo padėklo kristalografinės orientacijos.

- Patikima daugelio spektroskopijų metodika, integruojanti duomenis iš Ramano spektroskopijos, UV-Vis-nIR spektroskopijos ir dinaminės absorbcijos spektroskopijos, leidžia keičiamai naudoti šias technikas defektinių grafitinių struktūrų kokybei vertinti. Infraraudonoji sugertis (Abs IR) ir Ramano I(2D:D) santykis yra deterministiniai apvalkalo storio ir (arba) lakštų tankio rodikliai, o Abs Vis:UV, $I(D^{*}_{1}:D^{*}_{2})$ ir D juostos plotis (W (D)) Ramano spektruose patikimai nusako kristališkumo laipsnį.
- Reikšmingos Ramano, UV-Vis-nIR ir TAS tarpusavio metrikų koreliacijos patvirtina, kad šie vienas kitą papildantys metodai leidžia tirti tuos pačius pagrindinius struktūrinius defektus netvarkingoje anglyje. TAS smailės intensyvumas gali būti naudojamas kaip pakaitinis kristališkumo rodiklis (stipriai koreliuojantis su G juostos pločiu), o TAS lėtojo slopimo amplitudžių santykis (A_2 /(A_1+A_2)) atvirkščiai priklauso nuo apvalkalo storio (koreliuojantis su Ramano I(2D:D)). Šie ryšiai patvirtina pakaitinį šių metodų naudojimą neardomajam kokybės vertinimui.
- Nikeliu kapsuliuoto grafito hibridinė struktūra gali būti naudojama kaip potenciali platforma UV-SERS matavimams, joje grafitinis apvalkalas užtikrina ilgalaikę apsaugą nuo oksidacijos ir palengvina cheminį sustiprinimą (π–π sanklodą).
- Sėkmingai integravus grafeno viršutinį sluoksnį su rezonansiniu sidabro masyvu, sukurta ilgalaikė stabili SERS platforma nuolatiniam Ramano signalo aptikimui naudojant matomo diapazono lazerį.

Eksperimentinių detalių ir rezultatų santrauka iš kiekvieno atvejo tyrimo pateikiama pagal spręstus uždavinius

Grafeno sintezė ant polikristalinės Ni folijos naudojant PECVD

Tyrimai buvo skirti grafeno plėvelių nusodinimo ant ekonomiškai efektyvių polikristalinių nikelio padėklų procesui optimizuoti, naudojant įvairius paviršiaus inžinerijos metodus.

Padėklo paruošimas: polikristalinės nikelio folijos buvo pagamintos elektrocheminiu nusodinimu sulfamatiniame elektrolite, joms buvo būdinga polikristalinė struktūra (kubinė centruotojo paviršiaus gardelė, registruotos trys pagrindinės kristalografinės orientacijos: Ni(2 0 0), Ni(2 2 0) ir Ni(1 1 1)).

Tyrime buvo nagrinėtos ir palygintos keturios paviršiaus paruošimo strategijos prieš PECVD procesą:

- Neapdorota Ni folija: naudota kaip atskaitos bandinys.
- Argono atmosferoje atkaitinta Ni folija: iš anksto nusodinta nikelio plėvelė (6 nm), apdorota terminiu atkaitinimu argono aplinkoje esant 500° C temperatūrai 1 valandą.
- Iš anksto Ni dalelėmis padengta Ni folija: Ni dalelės (vidutinis dydis ~80 nm) buvo nusodintos ant folijos paviršiaus per 24 valandas iš suspensijos (sudarytos iš 100 μL Ni nanodalelių (0,0007 g Ni) 5 mL dimetilsulfoksido).
- Lazeriu abliuota Ni folija: paviršius buvo abliuotas naudojant 1064 nm bangos ilgio lazerį mikrostruktūroms sukurti (50 W galia, 20 kHz dažniu, 10 μm intervalais ir 100 mm/s skenavimo greičiu).

Skirtingai paruoštos Ni folijos buvo įdėtos į mikrobangų plazmos cheminio nusodinimo įrenginį (IPLAS gamintojo) ant metalinio padėklo, siekiant užtikrinti tolygesnį padėklo kaitinimą. Prieš PECVD procesą buvo naudojama vandenilio plazma (20 sccm vandenilio dujų maždaug 5 minutes, esant 750°C temperatūrai) oksido sluoksniui pašalinti. Plazmos galia buvo nustatyta 1,4 kW, o slėgis palaikomas 30 mbar. Metanas buvo pridėtas po atkaitinimo proceso, naudojant 15 sccm, sluoksnis buvo auginamas maždaug 10 minučių, esant 770°C temperatūrai.

Sluoksnių, suformuotų ant papildomai neapdorotų mėginių, optinių vaizdų analizė parodė netolygų grafeno augimą. Žinoma, kad šis netolygumas atsiranda dėl grūdų orientacijos įtakos anglies nusodinimui PECVD proceso metu.

Argono aplinkoje atkaitintame mėginyje taip pat buvo pastebėtos ryškesnės grūdų ribos, o grafeno domenai pastebimi atskiruose grūduose.

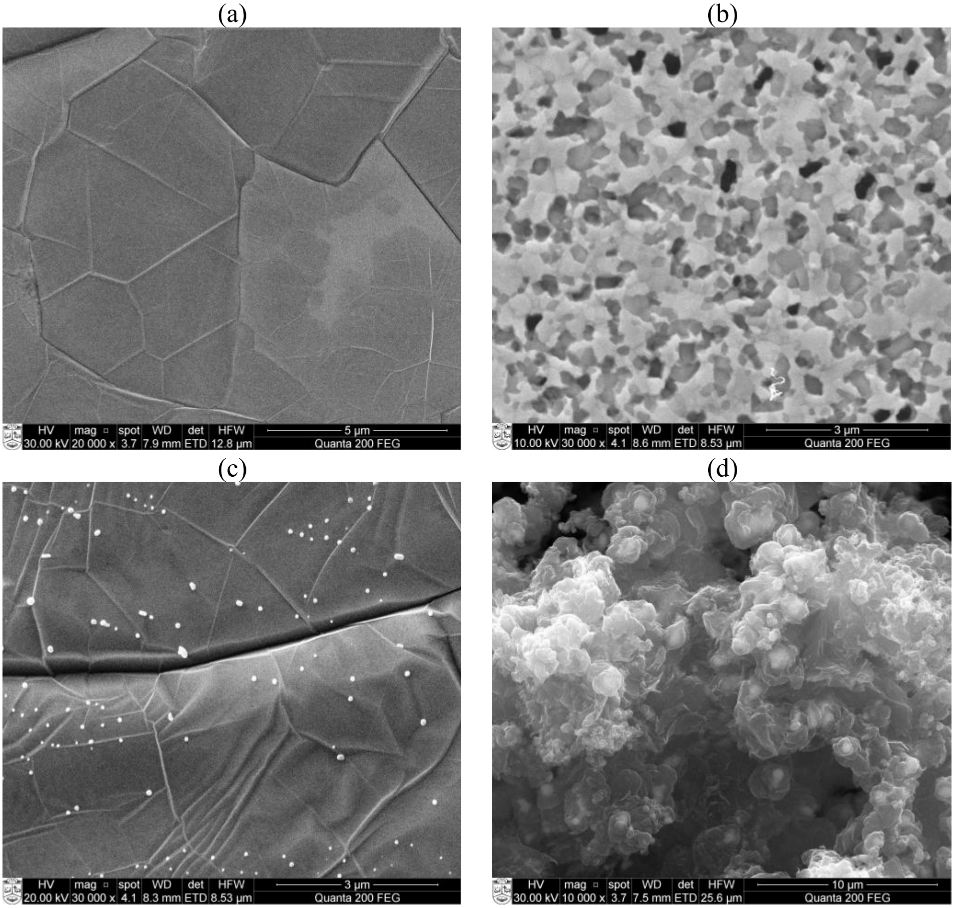

57 pav. Nikelio folijos paviršiaus SEM vaizdai po grafeno auginimo: (a) neapdorota, (b) termiškai argone atkaitinta plėvelė ant folijos, (c) dalelėmis padengta ir (d) lazeriu abliuota Ni folija

Nikelio folijos mėginyje, kuris prieš PECVD buvo abliuotas lazeriu, dėl abliacijos proceso atsiradęs paviršiaus šiurkštumas neleido vertinti grūdų ribų ir jų įtakos sluoksnio augimui. Susidarė būdingos medžiagos sankaupos pakraščiuose palei lazerio skenavimo linijas, sudarančios mikrostruktūras primenančias mikrostruktūras, susijusias su Ni oksidais. Po anglies sluoksnio nusodinimo SEM vaizdų analizė parodė, kad grafeno nanolakštai susidarė ir užauga virš abliuotų vietų kraštų.

Išankstinis nikelio folijų apdorojimas Ni nanodalelių nusodinimu sėkmingai sukūrė energetiškai palankias branduolių susidarymo vietas. SEM vaizdai patvirtino, kad dėl to visoje folijoje vienodai susidarė vientisas didelių domenų grafenas, kurį lydėjo būdingos raukšlės, priskiriamos įtempių relaksacijai.

Ramano matavimai (Renishaw InVia spektrometru, naudojant 532 nm žadinimą, 50× objektyvą ir 2,25 mW lazerio galią, su 4 µm lazerio pluošto skersmeniu) buvo nuosekliai atliekami vizualiai panašiose pilkose srityse visuose keturiuose padėkluose, siekiant tiesioginio rezultatų palyginimo. Didesnis vidutinis tvarkingų domenų matmuo registruotas bandiniuose, kuriuose Ni nanodalelės buvo nusodintos ant Ni folijos. Juose užregistruota siauresnė 2D juosta (pusplotis (FWHM) ~40 cm^{-1}), didesnis I(2D:G) santykis bei mažesnis I(D:G) santykis (<0,1), rodantys geresnę grafeno kokybę PECVD būdu užaugintose plėvelėse. Ant dalelėmis nusodintos folijos augantys domenai pasižymėjo aukštos kokybės dvisluoksnės struktūros savybėmis. Dalelėmis padengto bandinio apskaičiuotas dydis yra šiek tiek mažesnis (~1378 nm), jį lemia tankus paviršiaus raukšlių tinklas.

Kita vertus, reikšmingas D juostos indėlis, pastebėtas iš anksto atkaitintuose ir lazeriu abliuotuose bandiniuose, patvirtina, kad šios gausios defektų Ni topologijos riboja augimą, iš esmės skatindamos itin fragmentuotų nanokristalinių grafeno domenų formavimąsi.

Galiausiai, siekiant perkelti ant šiurkščių folijų pastebėtą morfologiją ant dielektrinio padėklo (tai buvo pagrindinis II atvejo analizės tikslas), tyrimas baigtas lyginamuoju SiO_2 padėklų tyrimu taikant optimalų dujų srautų režimą. Tai patvirtino, kad plėvelės terminio apdorojimo (angl. *dewetting*) metodas yra esminė II atvejo analizės metodika.

Grafitinio apvalkalo kapsuliuotų nikelio nanodalelių sintezė UV-SERS matavimams

Tyrimai buvo skirti netvarkingų grafitinių struktūrų, kapsuliuojančių nikelio nanodaleles (NiNPs), gamybai, visapusiškam kokybės įvertinimui ir pritaikymo galimybėms nustatyti. Šiais tyrimais siekta sukurti patikimą daugelio spektroskopijų metodiką, skirtą didelio defektiškumo grafitinių apvalkalų kokybei įvertinti.

Šiame atvejo tyrime buvo naudota pilna faktorinė schema, kintant dviem nepriklausomiems įvesties veiksniams: pradiniam nominaliam Ni nusodinimo sluoksnio storiui (serijos A–D: 4, 6, 8, 10 nm) ir vėlesniam anglies nusodinimo laikui (10, 20, 40, 60 min). Mėginiai buvo žymimi pagal seriją ir trukmę (pvz., C|60 žymi seriją C, 60 min).

Ypač plonos Ni plėvelės (6- 10nm) buvo nusodintos nuolatinės srovės magnetroniniu dulkinimu ant silicio dioksido padėklų. Šios plėvelės vėliau buvo termiškai apdorotos (angl. *dewetting*) 500˚C temperatūroje 1 valandą naudojant argono dujas (99,9999%) kvarco krosnyje, kur ištisinės plėvelės virto izoliuotomis Ni salelių sritimis.

Siekiant apsaugoti susidariusias Ni saleles nuo tiesioginio plazmos poveikio ir perteklinio ėsdinimo, prieš anglies sluoksnio nusodinimą PECVD kameroje ant padėklų buvo uždėtas specialiai pagamintas apsauginis plieninis skydas. Padėklas buvo kaitinamas iki 500°C, po to 10 minučių įleidžiamas vandenilis (200 sccm srautu), siekiant pašalinti oksiduotą sluoksnį ir toliau skatinti Ni salelių izoliavimą. Tuo pat metu metanas buvo pridėtas kaip pirmtakas 75 sccm srautu, išlaikant pastovų vandenilio srautą. Tyrimams naudotos ankstesniuose tyrimuose nustatytos technologinės sąlygos.

Atominių jėgų mikroskopijos rezultatai parodė stiprią 99% tiesinę koreliaciją tarp pradinės nominalios Ni plėvelės storio ir galutinio grafitinių apvalkalų šiurkštumo (RMS). Tai leido daryti prielaidą, kad storesnės pradinės plėvelės lėmė labiau sugrupuotų Ni salelių formavimąsi ir storesnių apvalkalų susidarymą.

SEM tyrimai patvirtino, kad suformuotos Ni salelės po anglies nusodinimo buvo sėkmingai transformuotos į kapsuliuotą morfologiją su grafitiniais apvalkalais. Anglies apvalkalai sluoksniavosi vienas ant kito tose vietose, kur salelių tankis buvo didesnis, taip didindami vertikaliųjų struktūrų tūrį. EDS tyrimai patvirtino izoliuotų Ni nanodalelių, kapsuliuotų anglies apvalkalais, buvimą. XPS duomenys patvirtino, kad pradinis atkaitinimas vandeniliu sėkmingai pašalino Ni oksido sluoksnį, o hibridizuota grafitinė anglis yra vyraujantis komponentas anglies apvalkaluose (82%–87%).

Šis tyrimas leido sukurti naują sistemą, skirtą netvarkingų grafitinių struktūrų kokybei vertinti, integruojant ir koreliuojant tris skirtingas spektroskopijos metodikas: Ramano spektroskopiją, UV-Vis-nIR spektroskopiją ir skirtuminės sugerties spektroskopiją (TAS). Atlikta koreliacinė analizė, siekiant išanalizuoti visų spektroskopijos metodų rezultatus, įskaitant paklaidos įverčius. Duomenų rinkinį sudarė 14 stebėjimų su dviem nepriklausomais įvesties veiksniais ir 107 priklausomais metrikos duomenimis, gautais iš spektroskopijos duomenų. Buvo apskaičiuoti Pirsono koreliacijos koeficientai (r) ir p vertės, skirtos dvipusiam reikšmingumo testui, daugiausia dėmesio skiriant stiprių koreliacijų $|r| \geq 0{,}5$ nustatymui, kai p vertės yra mažesnės nei 0,05.

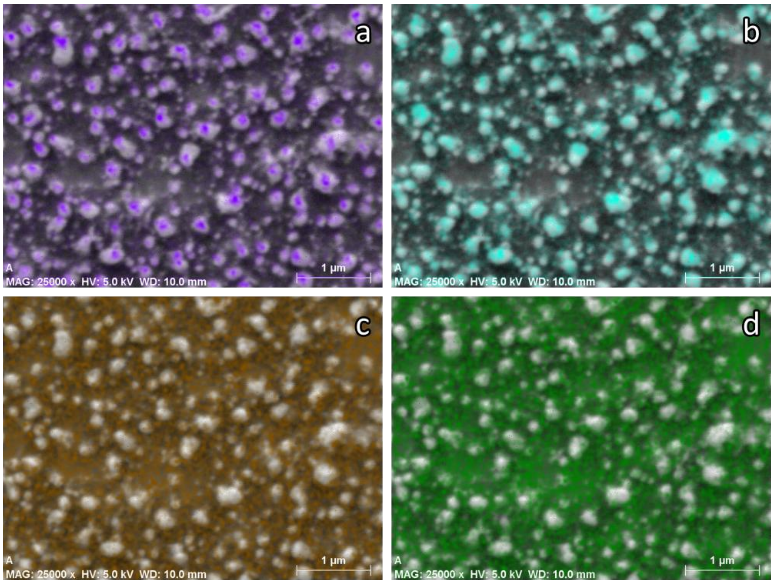

58 pav. B|60 bandinio EDS elementų pasiskirstymo žemėlapiai, rodantys (a) Ni, (b) anglies, (c) silicio ir (d) deguonies pasiskirstymą

Tyrimuose naudota pagrindinių komponentų analizė, siekiant sumažinti didelio skaičiaus metrikų, gautų iš įvairių spektroskopijos metodų, matmenį, palengvinant aiškesnį ryšių tarp 107 metrikų ir dviejų įvesties veiksnių (Ni plėvelės nominalaus storio ir anglies nusodinimo trukmės) bei pagrindinių grafitinių apvalkalų savybių interpretavimą.

Išsami Ramano analizė apėmė spektrų atskyrimą naudojant 11 smailių, atsižvelgiant į ryškias ir mažiau ryškias juostas. Pagrindinių komponentų analizė parodė, kad D juosta yra patikimesnis atskaitos taškas Ramano juostoms normalizuoti grafitinių apvalkalų spektruose, leidžiantis pagerinti palyginimų tikslumą. Gauti toliau nurodyti pagrindiniai rezultatai.

I(D:G) santykis, kuris dažnai naudojamas defektų tankiui įvertinti, mažėjo, apvalkalams storėjant. Be to, I(D:Q) santykis, kurį kai kurie tyrimai naudoja išimtinai defektams vertinti, didesnėms nusodinimo trukmėms rodė didėjimo tendenciją. Antra vertus, žinoma, kad I(D:G) ir I(D:Q) santykiai, esant didelėms defektų koncentracijoms, pasiekia maksimalią vertę ir esant tam tikram defektų lygiui, vėliau pradeda mažėti. Darbe nustatyta, kad I(2D:D) santykis, kuris šiai sistemai yra tikslesnė metrika, turi stiprią teigiamą koreliaciją su nominaliu Ni plėvelės storiu. Šis rezultatas leido daryti prielaidą, kad storesnės plėvelės lėmė didesnį grafitinių lakštų tankį bei didesnę netvarką. Be to, įvertinus mažiau ryškias juostas, nustatyta, kad santykinis $\mathrm{I}(\mathrm{D}_1'':\mathrm{D}_2'')$ intensyvumas (arba plotas), esantis 1000-1300 cm^{-1} dažnių diapazone, rodo teigiamą koreliaciją su nominaliais storiais ir anglies struktūrų defektiškumo padidėjimą.

Kaip žinoma, $\mathrm{D1}^{\star}$ juosta, esanti apie $1450\ \mathrm{cm}^{-1}$, ir $\mathrm{D2}^{\star}$ juosta, esanti apie $1500\ \mathrm{cm}^{-1}$ Ramano spektre, yra siejamos su amorfine anglimi. Nustatyta, kad santykiniai intensyvumo santykiai I(D1*:D) ir I(D2*:D) mažėjo, ilgėjant sluoksnio augimo trukmei. Jų intensyvumų (arba plotų) santykis I(D1*:D2*) taip pat parodė stiprią neigiamą koreliaciją ($r = -0{,}72$) su augimo trukme. Amorfinės anglies juostų intensyvumo sumažėjimas rodo, kad ilgesnis augimas skatina geresnę grafitizaciją.

UV-ViS-nIR spektroskopija buvo naudota sugerties metrikai suformuoti, siekiant nustatyti koreliaciją su struktūriniais kintamaisiais. Sugertis infraraudonojoje srityje, Abs(IR), teigiamai koreliavo su nominaliu storiu ($r = 82\%$). Ši išvada patvirtina jos tinkamumą vertinant lakštų tankio raidą. Abs(Vis:UV) stipriai didėjo ilgėjant augimo trukmei ir rodė stiprią neigiamą koreliaciją su W(G), o tai patvirtina jos veiksmingumą vertinant kristališkumą.

TAS buvo naudojama ultrasparčių krūvininkų dinamikai tirti, nustatant būdingas gyvavimo trukmes, susijusias su elektronų-fononų sklaida (τ_1) ir fononų-fononų sąveika (τ_2). Nustatytas TAS smailių intensyvumo ir Ramano metrikų ryšys. Smailės A_2 intensyvumas rodė mažėjimo tendenciją, didėjant nominaliam storiui, ir pasižymėjo neigiama koreliacija su Ramano metrikos I(2D:D) santykiniu intensyvumu. Ši koreliacija leidžia daryti prielaidą, kad absoliutus A_2 intensyvumas yra jautrus grafitinių lakštų tankiui ir mažėja, didėjant šiam tankiui.

Absoliutus TAS signalo smailės intensyvumas stipriai ir neigiamai koreliavo su G modos pločiu Ramano spektre (W(G), $r = -0{,}84$). Jis taip pat neigiamai koreliavo su amorfinės anglies santykiu I(D1*:D2*). Ši koreliacija patvirtino, kad didesnis TAS smailės intensyvumas patikimai rodo žemesnį amorfinės anglies lygį ir dėl to didesnį kristališkumą apvalkaluose. Kai kurios iš šių metrikų jau buvo eksperimentiškai patvirtintos literatūroje, kaip aptarta anksčiau, tačiau dalis jų yra šio darbo naujumas, leidžiantis tiksliau įvertinti defektuotas struktūras.

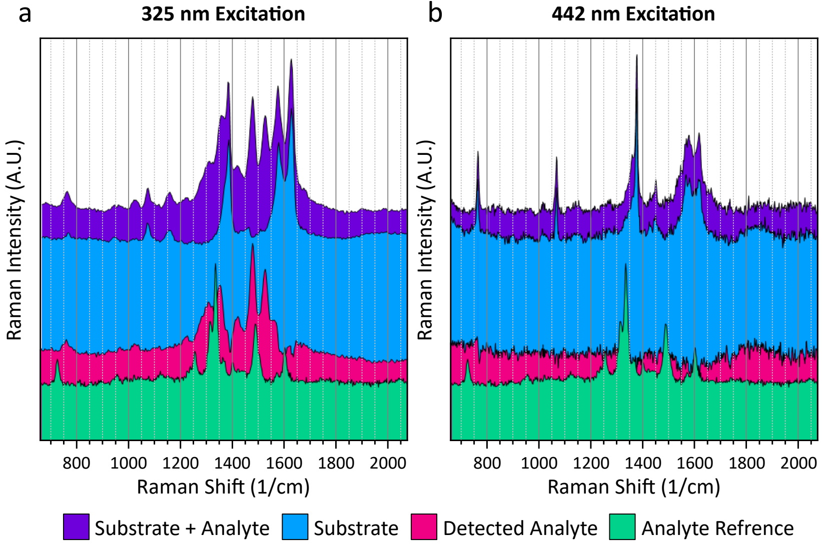

59 pav. Adenino SERS aptikimas ant nikeliu kapsuliuoto grafito (A|40 bandinys): (a) rezonansinis žadinimas esant 325 nm, rodantis sustiprinimą, ir (b) nerezonansinis kontrolinis matavimas esant 442 nm

UV-SERS taikymo galimybių tyrimai

Daugelio spektroskopijų analizė patvirtino $A|40$ mėginį kaip optimalią struktūrą UV–SERS bandymams. Nikeliu kapsuliuotas grafitas buvo patikrintas kaip perspektyvi naujoviška struktūra UV-SERSmatavimams. Ypač svarbu tai, kad šis matavimas buvo atliktas praėjus dvejiems metams po pradinės padėklo sintezės. Šiuo laikotarpiu bandinys buvo laikomas standartinėmis laboratorijos sąlygomis.

Tyrimai pademonstravo sustiprintą adenino molekulių aptikimą, naudojant 325 nm žadinimo lazerį. Adeninas buvo pasirinktas, nes UV srityje pastebima jo stipri sugertis. SERS sustiprinti buvo panaudotas nikelio nanodalelių paviršiaus lokalizuotų plazmonų rezonansas, kuris spektrine sudėtimi buvo artimas 325 nm žadinimo bangos ilgiui. Grafitinis apvalkalas sudarė stabilų apsauginį barjerą nikelio nanodalelėms ir neleido joms oksiduotis. Mėginys buvo efektyvus praėjus net ir vieneriems metams po jo pagaminimo, skirtingai nei neapsaugotos nikelio nanodalelės, kurių atveju signalo stiprinimas nebuvo registruotas. Kontrolinio eksperimento metu, naudojant nerezonansinį 442 nm lazerį, jokių aptinkamų adenino smailių nebuvo. Tai patvirtino, kad signalo sustiprinimas buvo specifinis UV srityje ir rezonansinis.

Sėkmingą adenino aptikimą esant 325 nm žadinimui lemia SERRS (paviršiaus sustiprinta rezonansinė Ramano sklaida) – sinergetinis efektas, kai žadinimo bangos ilgis vienu metu sutampa su nikelio branduolio UV plazmonų rezonansu ir analitės savitaisiais elektroniniais šuoliais.

Jutiklio, pagrįsto grafenu padengtais tvarkingais dvimačiais rezonansiniais sidabro nanodalelių masyvais, kūrimas ilgalaikiams SERS matavimams

Tyrimai buvo skirti ilgaamžiam SERS jutikliui, galinčiam užtikrinti ilgalaikį nuolatinį stebėjimą, sukurti, integruojant apsauginį grafeno monosluoksnį ant rezonansinių plazmoninių masyvų.

Tyrimu buvo siekiama užtikrinti ilgalaikį SERS signalo stabilumą, būdingą tradicinėms tauriųjų metalų SERS platformoms (paprastai sidabro) dėl jų jautrumo oksidacijai ir sulfidacijai aplinkos sąlygomis. Tam naudota grafeno monosluoksnio plėvelė, kuri veikia kaip nepralaidus barjeras virš periodinių nanodalelių masyvų.

Sidabras buvo sintetinamas modifikuotu poliolio metodu, gaunant monodispersinius nanokubelius (AgNPs), kurių vidutinis dydis yra 77 ±3 nm. Dvimačiai periodiniai rezonansiniai AgNPs masyvai buvo suformuoti ant polidimetilsiloksano (PDMS) kaukės, naudojant kapiliarinio nusodinimo (angl. *capillarity-assisted assembly*) metodiką. Buvo naudojamas institute pagamintas įrenginys, kuriame PDMS kaukei judant 1 µm/s greičiu iš koloidinio AgNP tirpalo nanodalelėmis buvo užpildytos dvimačio PDMS kaukės rašto gaudyklės.

Monosluoksnio grafeno plėvelė buvo sintetinama ant komercinės vario (Cu) folijos, naudojant PECVD metodą. Folija buvo atkaitinta 500° C temperatūroje 1 valandą, skatinant Cu_2O sluoksnio susidarymą ant paviršiaus. Ši oksidacija atlieka lemiamą vaidmenį valdant grafeno domenų branduolių susidarymo tankį ant vario, taip palengvinant didesnės ir vientisesnės grafeno plėvelės augimą. Nusodinto sluoksnio I(2D:G) santykis buvo ~2,68 ir patvirtino monosluoksnę struktūrą, nepaisant didelės defektų koncentracijos. Šis monosluoksnis vėliau buvo perkeltas ant suformuoto AgNP masyvo, naudojant sauso perkėlimo metodą su polivinilo alkoholio (PVA) plėvele.

Stabilumo tyrimams buvo paruoštos dvi mėginių grupės: neapsaugotas (U) kontrolinis mėginys ir perkeltu grafenu (G) apsaugotas mėginys. Kaip modelinė analitė ilgalaikiam stebėjimui naudota 2-naftalentolis (2NT) – paprasta aromatinė molekulė su išplėstine π-konjuguota sistema. SERS matavimai buvo atliekami naudojant 532 nm lazerio žadinimo šaltinį. AgNP masyvai buvo pagaminti taip, kad pasižymėtų ryškia paviršiaus gardelės rezonanso (SLR) smaile, registruojama netoli 570 nm. Ši SLR smailė buvo optimaliai suderinta su 2NT analitės Ramano signalo Stokso poslinkiu, esančiu bangų ilgio diapazone nuo 556 iki 580 nm.

Tiek „U“ (neapsaugoti), tiek „G“ (grafenu padengti) mėginiai buvo panardinti į 10^{-4} M 2NT tirpalą. Matavimai buvo registruojami aštuoniais laiko momentais per laikotarpį, apimantį nuo 1 dienos iki 344 dienų po pradinio poveikio analitei. Ypač svarbu pažymėti, kad padėklai nebuvo pakartotinai veikiami šviežia analite kiekvieno matavimo metu.

SLR derinimas ir selektyvus stiprinimas

Gamybos procesas lėmė AgNP masyvų, pasižyminčių stipria SLR smaile apie 570 nm, susidarymą. 2NT Ramano signalo analizė buvo sutelkta į tris būdingas smailes: I smailę, esančią apytiksliai 766 cm^{-1}, II smailę, esančią 1082 cm^{-1}, ir III smailę, esančią 1380 cm^{-1}.

I smailė, esanti už SLR sustiprinimo diapazono ribų, buvo naudojama kaip vidinė atskaita, II ir III smailės, esančios SLR rezonanso srityje (556–580 nm), buvo selektyviai sustiprintos SLR efektu. Apskaičiuotas sustiprinimo koeficientas II smailei buvo apytiksliai ×8,92±0,78, o III smailei – ×3,54±0,26, patvirtinant selektyvaus stiprinimo efektą, susijusį su suderintu SLR.

Ilgalaikio stabilumo kiekybinė analizė

Siekiant kiekybiškai stebėti sudėtingus spektrinius pokyčius beveik metus trukusio tyrimo metu, pagrindinių komponentų analizė (PCA) buvo pritaikyta didelės apimties spektrinių duomenų rinkiniui. Pirmieji du pagrindiniai komponentai paaiškino beveik 94% visos variacijos. Gautos išvados patvirtina, kad PC1 yra patikima metrika, skirta santykinei 2NT koncentracijai vertinti, palyginti su PDMS fonu. Antrasis pagrindinis komponentas (PC2) visų pirma atskiria grafeno požymį esant PC2 = –0,7 nuo kitų dviejų atskaitos taškų, turinčių teigiamus koeficientus.

Neapsaugotas mėginys ('U') iš pradžių turėjo stiprų aptikimo balą (~ 80%), tačiau jo signalas stabiliai mažėjo, tapdamas neatskiriamas nuo PDMS fono po 300 dienų. Šis signalo praradimas buvo priskirtas neapsaugotų sidabro nanodalelių paviršiaus degradacijai (oksidacijai ir sulfidacijai). Priešingai, grafenu apsaugotas mėginys ('G') išlaikė stabilų SERS požymį. Po 100 dienų jis išlaikė ~ 40% pradinio aptikimo balo, o signalas stabilizavosi maždaug 29,7% po 344 dienų.

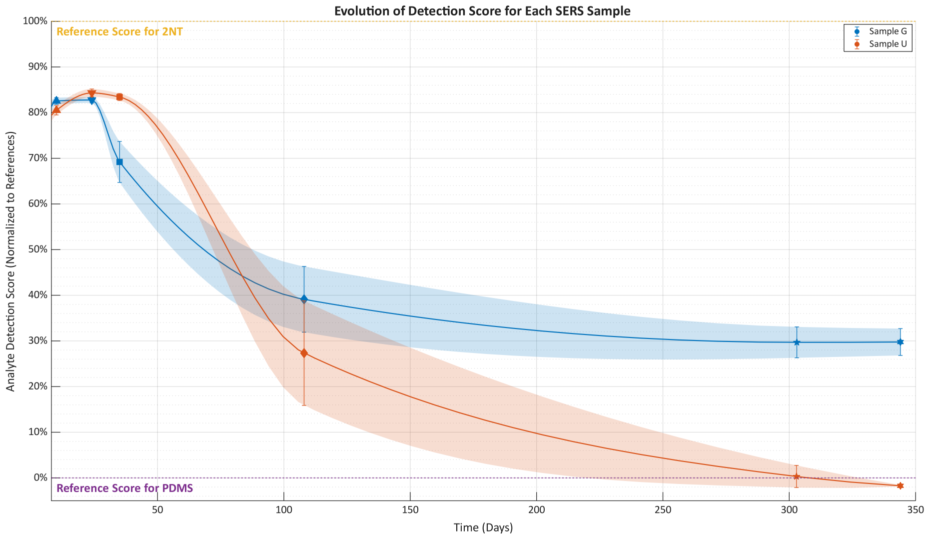

60 pav. Apskaičiuoti analitės aptikimo balai apsaugotuose (G) ir neapsaugotuose (U) bandiniuose per 344 dienas

Ilgalaikis SERS signalo stabilumas grafenu apsaugotame mėginyje per 344 dienas rodo cheminio sustiprinimo vaidmenį per ilgesnį laikotarpį ir grafeno apsauginį vaidmenį nuo aplinkos degradacijos. Būdingas grafeno cheminis inertiškumas ir nepralaidumas sėkmingai apsaugojo po juo esančias AgNPs (sidabro nanodaleles) nuo oksidacijos ir sulfidacijos. Naftaleno žiedas, sudarytas iš dviejų benzeno žiedų, dėl delokalizuotų elektronų debesų π–π sąveikos užtikrino papildomą ryšį su grafenu. Nors šios π–π sąveikos yra silpnesnės nei tiolio grupių su metalo dalelėmis sudaryti kovalentiniai ryšiai, jos tampa reikšmingesnės, kai pats padėklas yra aromatinė sistema, kaip grafenas.

Išvados ir ateities kryptys

Atlikus tyrimus, buvo gautos naujos hibridinės grafeno pagrindo struktūros ir sukurtos analitinės metodikos, jas galima apibendrinti taip:

1. Tyrimas patvirtino, kad grafeno augimo ant polikristalinių nikelio folijų tolygumą iš esmės lemia branduolių susidarymo vietų tankis. Nors standartinius plazmos indukuoto cheminio garų nusodinimo (PECVD) procesus riboja kintantys anglies difuzijos greičiai apatiniuose kristalų grūduose. Šiame darbe pademonstruota, kad išankstinis paviršiaus padengimas nikelio nanodalelėmis efektyviai atsieja augimo mechanizmą nuo padėklo kristalografinės orientacijos. Ši strategija sumažina anglies nusodinimui reikalingą aktyvacijos energiją ir leidžia susintetinti aukštos kokybės dvisluoksnes grafeno plėveles net ir anglies prisotintomis sąlygomis.

2. Analizuojant itin netvarkingų grafitinių struktūrų kokybės vertinimą, šiame tyrime pirmą kartą sukurta daugelio spektroskopijų koreliacinė metodika, skirta patikimam nikelio nanodaleles kapsuliuojančių grafitinių apvalkalų įvertinimui. Integravus išsamios Ramano spektroskopijos (įskaitant mažiau ryškias juostas, būdingas amorfinei angliai), UV-Vis-nIR spektroskopijos ir skirtuminės sugerties

spektroskopijos duomenis, buvo atliktas sistemingas koreliacinis tyrimas. Taikant šį daugelio spektroskopijų metodą, buvo nustatytos patikimos metrikos kiekvienai iš trijų naudotų technikų ir atskleistos reikšmingos tarpusavio koreliacijos. Šios koreliacijos įgalina pakaitinį papildomų spektroskopinių metodų naudojimą netvarkingoms grafitinėms struktūroms apibūdinti. Nustatyta, kad TAS smailės intensyvumas yra patikimas ir neardomasis kristališkumo rodiklis, stipriai koreliuojantis su Ramano G juostos pločiu (r = -0,8), o TAS lėtojo slopimo amplitudžių santykis (A_2 /(A_1+A_2)) atvirkščiai atspindi apvalkalo storį (koreliuojantį su Ramano I(2D:D) santykiu), taip įgalinant TAS naudojimą kaip greitą alternatyvą įprastinei Ramano analizei.

Buvo parodyta, kad nikeliu kapsuliuoto grafito bandinys gali būti naudojamas kaip potenciali nanostruktūra UV-SERS matavimams, taip praplėsdama SERS reikmėms naudojamų metalų diapazoną. Naudojant 325 nm žadinimo bangos ilgį, kuris sutapo su nikelio nanodalelių plazmonų rezonansu, ši nanostruktūra efektyviai stiprino adenino molekulių Ramano signalą šioje srityje.

3. Ištirtas monosluoksnio grafeno, kaip dengiančiojo sluoksnio, vaidmuo ant periodinių sidabro nanodalelių (AgNP) masyvų, naudojamų kaip SERS padėklas. AgNP masyvams, kurie buvo pagaminti taip, kad ties 570 nm būtų ryški SLR smailė, suderinta optimaliam modelinės analitės (2NT) signalo stiprinimui, grafeno dengiantysis sluoksnis smarkiai pagerino ilgalaikį signalo stabilumą, išspręsdamas esminę problemą, kylančią dėl neapsaugotų metalo nanostruktūrų oksidacijos ir sulfidacijos.

Stabilumas buvo kiekybiškai įvertintas naudojant PCA analizę beveik vienerius metus. PCA rezultatai parodė, kad grafenu apsaugoti bandiniai išlaikė stabilų, maždaug 29,7 % siekiantį analitės aptikimo balą ilgai po to, kai neapsaugoti kontroliniai bandiniai visiškai prarado signalą. Šis stabilumas patvirtina nanostruktūros ilgaamžiškumą ir sėkmingą grafeno apsauginės barjerinės funkcijos bei plazmoninio rezonanso integraciją, sukuriant ilgaamžę SERS platformą, tinkamą ilgalaikio stebėjimo taikymams.

Ateities darbais ir tolesniu tyrimų krypties vystymu būtų galima patobulinti sintezę, išplėsti taikymo sritis ir pagilinti fundamentinį supratimą apie grafeno pagrindo sistemas. Šie tyrimai galėtų apimti:

- Sistemingą PECVD auginimo parametrų optimizavimą siekiant toliau gerinti grafeno vienalytiškumą ant polikristalinių Ni folijų.
- Ateities tyrimuose, remiantis ant lazeriu apdorotų folijų stebėtomis porėtomis, nanodribsnių pavidalo struktūromis, reikėtų sutelkti dėmesį į šių struktūrų taikymą naujomis SERS platformomis, dekoruojant jų didelio paviršiaus ploto struktūras tauriųjų metalų nanodalelėmis.

LIST OF REFERENCES

[1] DASTMALCHI, P.; A. HADDADPOUR and G. VERONIS. Nanophotonics: devices for manipulating light at the nanoscale. In: *Nanolithography: The Art of Fabricating Nanoelectronic and Nanophotonic Devices and Systems* [online]. 2014. vol. 7, no. 5, pp. 376–398. Available from: https://doi.org/10.1533/9780857098757.376. [viewed 2026-02-19].

[2] ETCHEGOIN, P.G. and E.C. LE RU. Basic Electromagnetic Theory of SERS. In: [online]. 2010. Available from: https://doi.org/10.1002/9783527632756.CH1. [viewed 2025-09-24].

[3] ZOZULYA, A.; A. ZYUBIN and I. SAMUSEV. A review for DFT in chemical mechanism of SERS studies. In: *Royal Society Open Science* [online]. 2025. vol. 12, no. 6. Available from: https://doi.org/10.1098/RSOS.242000. [viewed 2025-09-24].

[4] MOSIER-BOSS, P.A. Review of SERS substrates for chemical sensing. In: *Nanomaterials* [online]. 2017. vol. 7, no. 6. Available from: https://doi.org/10.3390/nano7060142. [viewed 2026-02-08].

[5] HAN, Y.; R. LUPITSKYY; T.M. CHOU; C.M. STAFFORD; H. DU et al. Effect of oxidation on surface-enhanced raman scattering activity of silver nanoparticles: A quantitative correlation. In: *Analytical Chemistry* [online]. 2011. vol. 83, no. 15, pp. 5873–5880. Available from: https://doi.org/10.1021/ac2005839. [viewed 2026-02-08].

[6] MA, L.; J. WANG; C. REN; P. JU; Y. HUANG et al. Detection of corrosion inhibitor adsorption via a surface-enhanced Raman spectroscopy (SERS) silver nanorods tape sensor. In: *Sensors and Actuators B: Chemical* [online]. 2020. vol. 321, p. 128617. Available from: https://doi.org/10.1016/J.SNB.2020.128617. [viewed 2026-04-20].

[7] NOVOSELOV, K.S.; D. JIANG; F. SCHEDIN; T.J. BOOTH; V. V. KHOTKEVICH et al. Two-dimensional atomic crystals. In: *Proceedings of the National Academy of Sciences of the United States of America* [online]. 2005. vol. 102, no. 30, pp. 10451–10453. Available from: https://doi.org/10.1073/PNAS.0502848102. [viewed 2025-03-27].

[8] CAO, Y.; Y. CHENG and M. SUN. [online]. .[place not known]: Taylor & Francis, 2023. Available from: https://doi.org/10.1080/05704928.2021.1910286. [viewed 2024-12-08].

[9] RAMOS-BERDULLAS, N.; N. OTERO and M. MANDADO. Graphene molecules as platforms for SERS detection: A future perspective. In: *Handbook of Graphene* [online]. [place not known]: Wiley Blackwell, 2019. pp. 431–464. ISBN 9781119468455Available from: https://doi.org/10.1002/9781119468455.ch100. [viewed 2025-05-13].

[10] JIANG, T.; X. WANG; S. TANG; J. ZHOU; C. GU et al. Seed-mediated synthesis and SERS performance of graphene oxide-wrapped Ag nanomushroom. In: *Scientific Reports* [online]. 2017. vol. 7, no. 1, pp. 1–9. Available from: https://doi.org/10.1038/s41598-017-10262-9. [viewed 2024-12-04].

[11] GONG, T.; Y. ZHU; J. ZHANG; W. REN; J. QUAN et al. Study on surface-enhanced Raman scattering substrates structured with hybrid Ag nanoparticles and few-layer graphene. In: *Carbon* [online]. 2015. vol. 87, no. C, pp. 385–394. Available from: https://doi.org/10.1016/j.carbon.2015.02.055. [viewed 2025-02-20].

[12] GAO, N.; T. YANG; T. LIU; Y. ZOU and J. JIANG. Graphene oxide wrapped individual silver nanocomposites with improved stability for surface-enhanced Raman

scattering. In: *RSC Advances* [online]. 2015. vol. 5, no. 69, pp. 55801–55807. Available from: https://doi.org/10.1039/c5ra08180g. [viewed 2026-02-07].

[13] HOLMAN, A.P. and D. KUROUSKI. Surface-enhanced Raman spectroscopy in forensic analysis. In: *Reviews in Analytical Chemistry* [online]. 2024. vol. 43, no. 1. Available from: https://doi.org/10.1515/revac-2023-0079. [viewed 2026-02-08].

[14] MUEHLETHALER, C.; M. LEONA and J.R. LOMBARDI. Review of Surface Enhanced Raman Scattering Applications in Forensic Science. In: *Analytical Chemistry* [online]. 2016. vol. 88, no. 1, pp. 152–169. Available from: https://doi.org/10.1021/acs.analchem.5b04131. [viewed 2026-02-08].

[15] TALAIKIS, M.; L. MIKOLIŪNAITĖ; V. ŠABLINSKAS; S. ADOMAVIČIŪTĖ-GRABUSOVĖ; G. SIRGĖDAITĖ et al. Recent advances in biomolecular analysis by ultraviolet surface-enhanced resonance Raman spectroscopy: A review. In: *Chemija* [online]. 2025. vol. 36, no. 3, pp. 139–149. Available from: https://doi.org/10.6001/chemija.2025.36.3.4. [viewed 2026-02-21].

[16] REMEIKIENĖ, A.; I. MATULAITIENĖ; A. SELSKIS; M. TALAIKIS and G. NIAURA. Electrochemical UV-SERS of adenine on cobalt electrode. In: *Spectrochimica Acta Part A: Molecular and Biomolecular Spectroscopy* [online]. 2025. vol. 330, p. 125733. Available from: https://doi.org/10.1016/J.SAA.2025.125733. [viewed 2025-10-09].

[17] ZHENG, J.; X. LIU; M. TIAN; Y. SU and L. LI. Hybrid metal-dielectric gratings (HMDGs) as an alternative UV-SERS substrate †. In: *Phys. Chem. Chem. Phys* [online]. 2023. vol. 25, p. 15257. Available from: https://doi.org/10.1039/d3cp01911j. [viewed 2025-10-09].

[18] TALAIKIS, M.; L. MIKOLIŪNAITĖ; V. ŠABLINSKAS; S. ADOMAVIČIŪTĖ-GRABUSOVĖ; G. SIRGĖDAITĖ et al. Recent advances in biomolecular analysis by ultraviolet surface-enhanced resonance Raman spectroscopy: A review. In: *Chemija* [online]. 2025. vol. 36, no. 3, pp. 139–149. Available from: https://doi.org/10.6001/chemija.2025.36.3.4. [viewed 2026-02-21].

[19] YANG, G.; L. LI; W.B. LEE and M.C. NG. Structure of graphene and its disorders: a review. In: *Science and Technology of Advanced Materials* [online]. 2018. vol. 19, no. 1, pp. 613–648. Available from: https://doi.org/10.1080/14686996.2018.1494493. [viewed 2025-05-10].

[20] URADE, A.R.; I. LAHIRI and K.S. SURESH. Graphene Properties, Synthesis and Applications: A Review. In: *JOM 2022 75:3* [online]. 2022. vol. 75, no. 3, pp. 614–630. Available from: https://doi.org/10.1007/s11837-022-05505-8. [viewed 2026-02-05].

[21] GEIM, A.K. Graphene: Status and Prospects: In: *Science* [online]. 2009. Vol 324, no 5934, pp. 1530-1534. Available from: https://doi.org/10.1126/science.1158877. [viewed 2024-09-02].

[22] KUMAR, V. Linear and Nonlinear Optical Properties of Graphene: A Review. In: *Journal of Electronic Materials* [online]. 2021. vol. 50, no. 7, pp. 3773-3799. Available from: https://link.springer.com/article/10.1007/s11664-021-08904-w.

[23] CHOI, W. and J.W. LEE. Graphene: Synthesis and Applications. In: *Graphene: Synthesis and Applications* [online]. 2016. pp. 1–357. Available from: https://doi.org/10.1201/b11259. [viewed 2025-05-10].

[24] CHOI, J.H.; J. LEE; M. BYEON; T.E. HONG; H. PARK et al. Graphene-Based Gas Sensors with High Sensitivity and Minimal Sensor-to-Sensor Variation. In: *ACS Applied Nano Materials* [online]. 2020. vol. 3, no. 3, pp. 2257–2265. Available from: https://doi.org/10.1021/acsanm.9b02378. [viewed 2022-09-06].

[25] MOROZOV, S. V.; K.S. NOVOSELOV; F. SCHEDIN; D. JIANG; A.A. FIRSOV et al. Two-dimensional electron and hole gases at the surface of graphite. In: *Physical Review B* [online]. 2005. vol. 72, no. 20, p. 201401. Available from: https://doi.org/10.1103/PhysRevB.72.201401. [viewed 2026-02-17].

[26] GEIM, A.K. and K.S. NOVOSELOV. THE RISE OF GRAPHENE. In: nature materials [online]. 2007. Available from: https://www.nature.com/articles/nmat1849.

[27] BARTELMESS, J. and S. GIORDANI. Carbon nano-onions (multi-layer fullerenes): Chemistry and applications. In: *Beilstein Journal of Nanotechnology* [online]. 2014. vol. 5, no. 1, pp. 1980–1998. Available from: https://doi.org/10.3762/bjnano.5.207. [viewed 2023-08-01].

[28] LABBAYE, T.; E. KOVACEVIC; T. LECAS; M.R. AMMAR; A. CANIZARÈS et al. Enhancement of catalytic effect for CNT growth at low temperature by PECVD. In: *Applied Surface Science* [online]. 2018. vol. 453, pp. 436–441. Available from: https://doi.org/10.1016/j.apsusc.2018.05.059.

[29] LIU, W.W.; S.P. CHAI; A.R. MOHAMED and U. HASHIM. Synthesis and characterization of graphene and carbon nanotubes: A review on the past and recent developments. In: *Journal of Industrial and Engineering Chemistry* [online]. 2014. vol. 20, no. 4, pp. 1171–1185. Available from: https://doi.org/10.1016/j.jiec.2013.08.028. [viewed 2023-06-29].

[30] ZHENG, W.; X. ZHAO and W. FU. Review of Vertical Graphene and its Applications: *American Chemical Society*, 2021. Available from: https://doi.org/10.1021/acsami.0c19188.

[31] INAGAKI, M. and F. KANG. Graphene derivatives: graphane, fluorographene, graphene oxide, graphyne and graphdiyne. In: *Journal of Materials Chemistry A* [online]. 2014. vol. 2, no. 33, pp. 13193–13206. Available from: https://doi.org/10.1039/C4TA01183J. [viewed 2025-05-10].

[32] SURESH, I.; N. NESAKUMAR; J.B.B. RAYAPPAN and A.J. KULANDAISAMY. Recent advances in the synthesis and functionalization of carbon-based functional nanomaterials. In: *Design, Applications, and Devices* [online]. 2023. pp. 33–77. Available from: https://doi.org/10.1016/B978-0-323-91783-4.00012-7. [viewed 2023-12-04].

[33] PERATHONER, S. and G. CENTI. Advanced Nanocarbon Materials for Future Energy Applications. In: *Emerging Materials for Energy Conversion and Storage* [online]. 2018. pp. 305–325. Available from: https://doi.org/10.1016/B978-0-12-813794-9.00009-0. [viewed 2025-05-11].

[34] SHEKA, E.F.; Ye.A. GOLUBEV and N.A. POPOVA. Raman Scattering by sp^2 Amorphous Carbons. In: [online]. 2020. Available from: http://arxiv.org/abs/2002.09913. [viewed 2023-10-11].

[35] CARPENE, E.; E. MANCINI; C. DALLERA; D. SCHWERT; C. RONNING et al. Ultrafast carrier dynamics in tetrahedral amorphous carbon: Carrier trapping versus electron-hole recombination. In: *New Journal of Physics* [online]. 2007. vol. 9, no. 11, p. 404. Available from: https://doi.org/10.1088/1367-2630/9/11/404. [viewed 2024-01-17].

[36] LU, X.; M. YU; H. HUANG and R.S. RUOFF. Tailoring graphite with the goal of achieving single sheets. In: *Nanotechnology* [online]. 1999. vol. 10, no. 3, p. 269. Available from: https://doi.org/10.1088/0957-4484/10/3/308. [viewed 2025-04-04].

[37] KUMAR, N.; R. SALEHIYAN; V. CHAUKE; O. JOSEPH BOTLHOKO; K. SETSHEDI et al. Top-down synthesis of graphene: A comprehensive review. In:

FlatChem [online]. 2021. vol. 27, p. 100224. Available from: https://doi.org/10.1016/j.flatc.2021.100224. [viewed 2023-02-05].

[38] URADE, A.R.; I. LAHIRI and K.S. SURESH. Graphene Properties, Synthesis and Applications: A Review. In: *JOM 2022 75:3* [online]. 2022. vol. 75, no. 3, pp. 614–630. Available from: https://doi.org/10.1007/S11837-022-05505-8. [viewed 2025-03-27].

[39] BAHRI, M.; S.H. GEBRE; M.A. ELAGUECH; F.T. DAJAN; M.G. SENDEKU et al. Recent advances in chemical vapour deposition techniques for graphene-based nanoarchitectures: From synthesis to contemporary applications. In: *Coordination Chemistry Reviews* [online]. 2023. vol. 475, p. 214910. Available from: https://doi.org/10.1016/j.ccr.2022.214910. [viewed 2023-05-05].

[40] WANG, H.; E. GAO; P. LIU; D. ZHOU; D. GENG et al. Facile growth of vertically-aligned graphene nanosheets via thermal CVD: The experimental and theoretical investigations. In: *Carbon* [online]. 2017. vol. 121, pp. 1–9. Available from: https://doi.org/10.1016/j.carbon.2017.05.074. [viewed 2023-02-13].

[41] ZAFAR, M.A. and M. V. JACOB. Plasma-based synthesis of graphene and applications: a focused review. In: *Reviews of Modern Plasma Physics* [online]. 2022. vol. 6, no. 1, pp. 1–38. Available from: https://doi.org/10.1007/s41614-022-00102-3. [viewed 2023-02-17].

[42] HAN, Z.J.; A.T. MURDOCK; D.H. SEO and A. BENDAVID. Recent progress in plasma-assisted synthesis and modification of 2D materials. In: *2D Materials* [online]. 2018. vol. 5, no. 3, p. 032002. Available from: https://doi.org/10.1088/2053-1583/aabb81. [viewed 2023-02-05].

[43] LEE, X.J.; B.Y.Z. HIEW; K.C. LAI; L.Y. LEE; S. GAN et al. Review on graphene and its derivatives: Synthesis methods and potential industrial implementation. In: *Journal of the Taiwan Institute of Chemical Engineers* [online]. 2019. vol. 98, pp. 163–180. Available from: https://doi.org/10.1016/J.JTICE.2018.10.028. [viewed 2025-03-25].

[44] KAINDL, R.; G. JAKOPIC; R. RESEL; J. PICHLER; A. FIAN et al. Synthesis of Graphene-layer Nanosheet Coatings by PECVD. In: *Materials Today: Proceedings* [online]. 2015. vol. 2, no. 8, pp. 4247–4255. Available from: https://doi.org/10.1016/J.MATPR.2015.09.010. [viewed 2022-02-21].

[45] WANG, X.C.; B. WANG; H. XIE; Al -; M. SEO et al. Molecular beam epitaxy of graphene on ultra-smooth nickel: growth mode and substrate interactions. In: *New Journal of Physics* [online]. 2014. vol. 16, no. 9, p. 093055. Available from: https://doi.org/10.1088/1367-2630/16/9/093055. [viewed 2025-05-02].

[46] BO, Z.; Y. YANG; J. CHEN; K. YU; J. YAN et al. [online]. .[place not known]: [publisher not known], 2013. Available from: https://doi.org/10.1039/c3nr33449j.

[47] MA, J.; J.C. RICHLEY; M.N.R. ASHFOLD and Y.A. MANKELEVICH. Probing the plasma chemistry in a microwave reactor used for diamond chemical vapor deposition by cavity ring down spectroscopy. In: *Journal of Applied Physics* [online]. 2008. vol. 104, no. 10, p. 103305. Available from: https://doi.org/10.1063/1.3021095. [viewed 2025-09-10].

[48] LI, N.; Z. ZHEN; R. ZHANG; Z. XU; Z. ZHENG et al. Nucleation and growth dynamics of graphene grown by radio frequency plasma-enhanced chemical vapor deposition. In: *Scientific Reports* [online]. 2021. vol. 11, no. 1, pp. 1–10. Available from: https://doi.org/10.1038/s41598-021-85537-3. [viewed 2023-01-26].

[49] JANKAUSKAS, Š.; Š. MEŠKINIS; N. ŽURAUSKIENĖ and A. GUOBIENĖ. Influence of Synthesis Parameters on Structure and Characteristics of the Graphene Grown Using PECVD on Sapphire Substrate. In: *Nanomaterials* [online]. 2024.

vol. 14, no. 20, p. 1635. Available from: https://doi.org/10.3390/NANO14201635/S1. [viewed 2025-04-01].

[50] MEŠKINIS, Š.; A. LAZAUSKAS; Š. JANKAUSKAS; A. GUOBIENĖ and R. GUDAITIS. Advancing Graphene Synthesis: Low-Temperature Growth and Hydrogenation Mechanisms Using Plasma-Enhanced Chemical Vapor Deposition. In: *Molecules* [online]. 2025. vol. 30, no. 1, p. 33. Available from: https://doi.org/10.3390/MOLECULES30010033/S1. [viewed 2025-04-01].

[51] WU, S.; D. HUANG; H. YU; S. TIAN; A. MALIK et al. Molecular understanding of the effect of hydrogen on graphene growth by plasma-enhanced chemical vapor deposition. In: *Physical Chemistry Chemical Physics* [online]. 2022. vol. 24, no. 17, pp. 10297–10304. Available from: https://doi.org/10.1039/D1CP04510E. [viewed 2025-04-04].

[52] YANG, K.; J. LIU; R. JIANG; Y. GONG; B. ZENG et al. Effect of the Pressure of Reaction Gases on the Growth of Single-Crystal Graphene on the Inner Surfaces of Copper Pockets. In: *Micromachines* [online]. 2020. vol. 11, no. 12, p. 1101. Available from: https://doi.org/10.3390/MI11121101. [viewed 2025-04-04].

[53] RAJACKAITĖ, E.; D. PECKUS; R. GUDAITIS; T. TAMULEVIČIUS; Š. MEŠKINIS et al. The evolution of properties with deposition time of vertical graphene nanosheets produced by microwave plasma-enhanced chemical vapor deposition. In: *Surfaces and Interfaces* [online]. 2021. vol. 27, p. 101529. Available from: https://doi.org/10.1016/j.surfin.2021.101529. [viewed 2023-04-28].

[54] HWANGBO, Y.; C.K. LEE; A.E. MAG-ISA; J.W. JANG; H.J. LEE et al. Interlayer non-coupled optical properties for determining the number of layers in arbitrarily stacked multilayer graphenes. In: *Carbon* [online]. 2014. vol. 77, pp. 454–461. Available from: https://doi.org/10.1016/j.carbon.2014.05.050. [viewed 2025-01-27].

[55] BRUNA, M.; A.K. OTT; M. IJÄS; D. YOON; U. SASSI et al. Doping dependence of the Raman spectrum of defected graphene. In: *ACS Nano* [online]. 2014. vol. 8, no. 7, pp. 7432–7441. Available from: https://doi.org/10.1021/nn502676g. [viewed 2023-09-25].

[56] DAS, D.K.; S.K. SAHOO; P. PUROHIT and S. SAHOO. A study on the tensile force and shear strain of trilayer graphene. In: *The European Physical Journal Applied Physics* [online]. 2021. vol. 93, no. 3, p. 30404. Available from: https://doi.org/10.1051/EPJAP/2021200357. [viewed 2026-04-20].

[57] ODAHARA, G.; S. OTANI; C. OSHIMA; M. SUZUKI; T. YASUE et al. Macroscopic single-domain graphene sheet on Ni(111). In: *Surface and Interface Analysis* [online]. 2011. vol. 43, no. 12, pp. 1491–1493. Available from: https://doi.org/10.1002/SIA.3742. [viewed 2025-05-02].

[58] FAN, T.; C. YAN; J. LU; L. ZHANG and J. CAI. The effect of copper substrate's roughness on graphene growth process via PECVD. In: *Materials Research Express* [online]. 2018. vol. 5, no. 4, p. 045604. Available from: https://doi.org/10.1088/2053-1591/aab909. [viewed 2023-01-26].

[59] ZHENG, S.; G. ZHONG; X. WU; L. D'ARSIÈ and J. ROBERTSON. Metal-catalyst-free growth of graphene on insulating substrates by ammonia-assisted microwave plasma-enhanced chemical vapor deposition. In: *RSC Advances* [online]. 2017. vol. 7, no. 53, pp. 33185–33193. Available from: https://doi.org/10.1039/c7ra04162d. [viewed 2025-05-30].

[60] XU, S.; L. ZHANG; B. WANG and R.S. RUOFF. Chemical vapor deposition of graphene on thin-metal films. In: *Cell Reports Physical Science* [online]. 2021. vol. 2,

no. 3, p. 100372. Available from: https://doi.org/10.1016/j.xcrp.2021.100372. [viewed 2022-04-13].

[61] CHUGH, S.; R. MEHTA; N. LU; F.D. DIOS; M.J. KIM et al. Comparison of graphene growth on arbitrary non-catalytic substrates using low-temperature PECVD. In: *Carbon* [online]. 2015. vol. 93, pp. 393–399. Available from: https://doi.org/10.1016/J.CARBON.2015.05.035. [viewed 2025-05-30].

[62] DONG, Y.; S. GUO; H. MAO; C. XU; Y. XIE et al. The Growth of Graphene on Ni–Cu Alloy Thin Films at a Low Temperature and Its Carbon Diffusion Mechanism. In: *Nanomaterials* [online]. 2019. vol. 9, no. 11, p. 1633. Available from: https://doi.org/10.3390/NANO9111633. [viewed 2025-04-07].

[63] YAN, Z.; J. LIN; Z. PENG; Z. SUN; Y. ZHU et al. Toward the synthesis of wafer-scale single-crystal graphene on copper foils. In: *ACS Nano* [online]. 2012. vol. 6, no. 10, pp. 9110–9117. Available from: https://doi.org/10.1021/nn303352k. [viewed 2026-02-23].

[64] MUÑOZ, R. and C. GÓMEZ-ALEIXANDRE. Review of CVD synthesis of graphene. In: *Chemical Vapor Deposition* [online]. 2013. vol. 19, nos. 10–12, pp. 297–322. Available from: https://doi.org/10.1002/cvde.201300051. [viewed 2026-02-06].

[65] HAN, G.H.; F. GÜNEŞ; J.J. BAE; E.S. KIM; S.J. CHAE et al. Influence of copper morphology in forming nucleation seeds for graphene growth. In: *Nano Letters* [online]. 2011. vol. 11, no. 10, pp. 4144–4148. Available from: https://doi.org/10.1021/NL201980P. [viewed 2025-04-24].

[66] KONDRASHOV, I.; M. KOMLENOK; P. PIVOVAROV; S. SAVIN; E. OBRAZTSOVA et al. Preparation of copper surface for the synthesis of single-layer graphene. In: *Nanomaterials* [online]. 2021. vol. 11, no. 5, p. 1071. Available from: https://doi.org/10.3390/nano11051071. [viewed 2023-02-03].

[67] LI, Y.; Y. WU; Y. ZHOU; J. LI; Y. DUAN et al. Diffusion, Nucleation, and Self-Optimization in the Forming Process of Graphene in Annealed Nickel-Carbon Alloy. In: *Journal of Physical Chemistry C* [online]. 2017. vol. 121, no. 38, pp. 21001–21010. Available from: https://doi.org/10.1021/acs.jpcc.7b06620. [viewed 2023-02-14].

[68] HUANG, L.; Q.H. CHANG; G.L. GUO; Y. LIU; Y.Q. XIE et al. Synthesis of high-quality graphene films on nickel foils by rapid thermal chemical vapor deposition. In: *Carbon* [online]. 2012. vol. 50, no. 2, pp. 551–556. Available from: https://doi.org/10.1016/j.carbon.2011.09.012. [viewed 2023-01-31].

[69] WEATHERUP, R.S.; B. DLUBAK and S. HOFMANN. Kinetic control of catalytic CVD for high-quality graphene at low temperatures. In: *ACS Nano* [online]. 2012. vol. 6, no. 11, pp. 9996–10003. Available from: https://doi.org/10.1021/NN303674G. [viewed 2025-04-24].

[70] DAHAL, A. and M. BATZILL. Graphene-nickel interfaces: A review. In: *Nanoscale* [online]. 2014. vol. 6, no. 5, pp. 2548–2562. Available from: https://doi.org/10.1039/c3nr05279f. [viewed 2023-02-24].

[71] CHENG, T.; Z.Z. LIU; Z.Z. LIU and F. DING. The Mechanism of Graphene Vapor-Solid Growth on Insulating Substrates. In: *ACS Nano* [online]. 2021. vol. 15, no. 4, pp. 7399–7408. Available from: https://pubs.acs.org/doi/10.1021/acsnano.1c00776. [viewed 2023-07-03].

[72] KHALID, A.; M.A. MOHAMED and A.A. UMAR. Graphene growth at low temperatures using RF-plasma enhanced chemical vapour deposition. In: *Sains Malaysiana* [online]. 2017. vol. 46, no. 7, pp. 1111–1117. Available from: https://doi.org/10.17576/jsm-2017-4607-14. [viewed 2025-04-23].

[73] HIRAMATSU, M.; M. NAITO; H. KONDO and M. HORI. Fabrication of Graphene-Based Films Using Microwave-Plasma-Enhanced Chemical Vapor Deposition. In: *Japanese Journal of Applied Physics* [online]. 2013. vol. 52, no. 1S, p. 01AK04. Available from: https://doi.org/10.7567/JJAP.52.01AK04. [viewed 2026-02-04].

[74] GOTTLIEB, S.; N. WÖHRL; S. SCHULZ and V. BUCK. Simultaneous synthesis of nanodiamonds and graphene via plasma enhanced chemical vapor deposition (MW PE-CVD) on copper. In: *SpringerPlus* [online]. 2016. vol. 5, no. 1, p. 568. Available from: https://doi.org/10.1186/s40064-016-2201-x. [viewed 2026-02-04].

[75] JAFARI, A.; M. GHORANNEVISS; M.R. HANTEHZADEH and A. BOOCHANI. Effect of plasma power on growth of multilayer graphene on copper using plasma enhanced chemical vapour deposition. In: *Journal of Chemical Research* [online]. 2016. vol. 40, no. 1, pp. 40–43. Available from: https://doi.org/10.3184/174751916X14497648744542. [viewed 2026-02-02].

[76] VANPAEMEL, J.; M.H. VAN DER VEEN; D.J. COTT; M. SUGIURA; I. ASSELBERGHS et al. Dual Role of Hydrogen in Low Temperature Plasma Enhanced Carbon Nanotube Growth. In: *Journal of Physical Chemistry C* [online]. 2015. vol. 119, no. 32, pp. 18293–18302. Available from: https://doi.org/10.1021/acs.jpcc.5b04689. [viewed 2026-02-04].

[77] GAO, J.; J. YIP; J. ZHAO; B.I. YAKOBSON and F. DING. Graphene nucleation on transition metal surface: structure transformation and role of the metal step edge. In: *ACS PublicationsJ Gao, J Yip, J Zhao, BI Yakobson, F DingJournal of the American Chemical Society, 2011•ACS Publications* [online]. 2011. vol. 133, no. 13, pp. 5009–5015. Available from: https://doi.org/10.1021/ja110927p. [viewed 2026-02-05].

[78] RYBIN, M.G.; I.I. KONDRASHOV; A.S. POZHAROV; V.C. NGUYEN; N.M. PHAN et al. In Situ Control of CVD Synthesis of Graphene Film on Nickel Foil. In: *Physica Status Solidi (B) Basic Research* [online]. 2018. vol. 255, no. 1, p. 1700414. Available from: https://doi.org/10.1002/pssb.201700414. [viewed 2023-01-24].

[79] ZHANG, Y.; T. GAO; S. XIE; B. DAI; L. FU et al. Different growth behaviors of ambient pressure chemical vapor deposition graphene on Ni(111) and Ni films: A scanning tunneling microscopy study. In: *Nano Research* [online]. 2012. vol. 5, no. 6, pp. 402–411. Available from: https://doi.org/10.1007/s12274-012-0221-6. [viewed 2026-02-06].

[80] KIM, H.; C. MATTEVI; M.R. CALVO; J.C. OBERG; L. ARTIGLIA et al. Activation energy paths for graphene nucleation and growth on Cu. In: *ACS Nano* [online]. 2012. vol. 6, no. 4, pp. 3614–3623. Available from: https://doi.org/10.1021/nn3008965. [viewed 2026-02-05].

[81] ZHANG, Y.; L. GOMEZ; F.N. ISHIKAWA; A. MADARIA; K. RYU et al. Comparison of graphene growth on single-crystalline and polycrystalline Ni by chemical vapor deposition. In: *Journal of Physical Chemistry Letters* [online]. 2010. vol. 1, no. 20, pp. 3101–3107. Available from: https://doi.org/10.1021/JZ1011466. [viewed 2025-05-02].

[82] IWASAKI, T.; H.J. PARK; M. KONUMA; D.S. LEE; J.H. SMET et al. Long-range ordered single-crystal graphene on high-quality heteroepitaxial Ni thin films grown on MgO(111). In: *Nano Letters* [online]. 2011. vol. 11, no. 1, pp. 79–84. Available from: https://doi.org/10.1021/NL102834Q. [viewed 2025-05-02].

[83] ENTANI, S.; Y. MATSUMOTO; M. OHTOMO; P. V. AVRAMOV; H. NARAMOTO et al. Precise control of single- and bi-layer graphene growths on epitaxial Ni(111) thin film. In: *Journal of Applied Physics* [online]. 2012. vol. 111, no. 6, p. 64324. Available from: https://doi.org/10.1063/1.3694662/365738. [viewed 2025-05-02].

[84] KOZLOVA, J.; A. NIILISK; H. ALLES and V. SAMMELSELG. Discontinuity and misorientation of graphene grown on nickel foil: Effect of the substrate crystallographic orientation. In: *Carbon* [online]. 2015. vol. 94, pp. 160–173. Available from: https://doi.org/10.1016/J.CARBON.2015.06.023. [viewed 2025-05-02].

[85] HUANG, M.; B. DENG; F. DONG; L. ZHANG; Z. ZHANG et al. Substrate Engineering for CVD Growth of Single Crystal Graphene. In: *Small Methods* [online]. 2021. vol. 5, no. 5, p. 2001213. Available from: https://doi.org/10.1002/SMTD.202001213. [viewed 2025-05-02].

[86] THIELE, S.; A. REINA; P. HEALEY; J. KEDZIERSKI; P. WYATT et al. Engineering polycrystalline Ni films to improve thickness uniformity of the chemical-vapor-deposition-grown graphene films. In: *Nanotechnology* [online]. 2010. vol. 21, no. 1, p. 015601. Available from: https://doi.org/10.1088/0957-4484/21/1/015601. [viewed 2022-04-01].

[87] KICIŃSKI, W. and S. DYJAK. Transition metal impurities in carbon-based materials: Pitfalls, artifacts and deleterious effects. In: *Carbon* [online]. 2020. vol. 168, pp. 748–845. Available from: https://doi.org/10.1016/j.carbon.2020.06.004. [viewed 2023-09-05].

[88] KIM, Y.; W. SONG; S.Y. LEE; C. JEON; W. JUNG et al. Low-temperature synthesis of graphene on nickel foil by microwave plasma chemical vapor deposition. In: *Applied Physics Letters* [online]. 2011. vol. 98, no. 26, p. 263106. Available from: https://doi.org/10.1063/1.3605560. [viewed 2022-10-26].

[89] HAN, J.; Y. MA; M. WANG; Z. TONG; J. SUHR et al. Nano-and micro-engineered vertical graphene/Ni for superior optical absorption. In: *Applied Surface Science* [online]. 2022. vol. 606, p. 154922. Available from: https://doi.org/10.1016/j.apsusc.2022.154922. [viewed 2023-01-12].

[90] YU, K.; G. LU; Z. BO; S. MAO and J. CHEN. Carbon nanotube with chemically bonded graphene leaves for electronic and optoelectronic applications. In: *Journal of Physical Chemistry Letters* [online]. 2011. vol. 2, no. 13, pp. 1556–1562. Available from: https://doi.org/10.1021/jz200641c. [viewed 2022-05-09].

[91] CHEN, R.; Y. XUE; X. XU; H. YANG; T. QIU et al. Lithography-free synthesis of periodic, vertically-aligned, multi-walled carbon nanotube arrays. In: *Nanotechnology* [online]. 2022. vol. 33, no. 6, p. 9. Available from: https://doi.org/10.1088/1361-6528/ac345a. [viewed 2023-04-18].

[92] LOSURDO, M.; M.M. GIANGREGORIO; P. CAPEZZUTO and G. BRUNO. Graphene CVD growth on copper and nickel: Role of hydrogen in kinetics and structure. In: *Physical Chemistry Chemical Physics* [online]. 2011. vol. 13, no. 46, pp. 20836–20843. Available from: https://doi.org/10.1039/c1cp22347j. [viewed 2026-02-04].

[93] KANG, F. and M. INAGAKI. *Materials Science and Engineering of Carbon: Characterization* [online]. [place not known]: Elsevier, 2016. 1–318 pp. ISBN 9780128052563 Available from: https://doi.org/10.1016/B978-0-12-805256-3.01001-1. [viewed 2025-05-12].

[94] LI, Z.; L. DENG; I.A. KINLOCH and R.J. YOUNG. Raman spectroscopy of carbon materials and their composites: Graphene, nanotubes and fibres. In: *Progress in Materials Science* [online]. 2023. vol. 135, p. 101089. Available from: https://doi.org/10.1016/j.pmatsci.2023.101089. [viewed 2023-06-26].

[95] LIN, L.; X. BI; Y. GU; F. WANG and J. YE. Surface-enhanced Raman scattering nanotags for bioimaging. In: *Journal of Applied Physics* [online]. 2021. vol. 129,

no. 19, p. 191101. Available from: https://doi.org/10.1063/5.0047578. [viewed 2025-09-22].

[96] WAN, F.; L. DU; W. CHEN; P. WANG; J. WANG et al. A Novel Method to Directly Analyze Dissolved Acetic Acid in Transformer Oil without Extraction Using Raman Spectroscopy. In: *Energies 2017, Vol. 10, Page 967* [online]. 2017. vol. 10, no. 7, p. 967. Available from: https://doi.org/10.3390/EN10070967. [viewed 2025-09-22].

[97] SMITH, E. and G. DENT. Modern raman spectroscopy: A practical approach. In: *Modern Raman Spectroscopy: A Practical Approach* [online]. 2019. pp. 1–241. Available from: https://doi.org/10.1002/0470011831. [viewed 2025-05-11].

[98] BEAMS, R.; L. GUSTAVO CANÇADO and L. NOVOTNY. Raman characterization of defects and dopants in graphene. In: *Journal of Physics Condensed Matter* [online]. 2015. vol. 27, no. 8, p. 083002. Available from: https://doi.org/10.1088/0953-8984/27/8/083002. [viewed 2023-08-02].

[99] MALARD, L.M.; M.A. PIMENTA; G. DRESSELHAUS and M.S. DRESSELHAUS. Raman spectroscopy in graphene. In: *Physics Reports* [online]. 2009. vol. 473, nos. 5–6, pp. 51–87. Available from: https://doi.org/10.1016/j.physrep.2009.02.003. [viewed 2023-08-02].

[100] JAWHARI, T.; A. ROID and J. CASADO. Raman spectroscopic characterization of some commercially available carbon black materials. In: *Carbon* [online]. 1995. vol. 33, no. 11, pp. 1561–1565. Available from: https://doi.org/10.1016/0008-6223(95)00117-V. [viewed 2023-11-30].

[101] BÎRU, E.I. and H. IOVU. Graphene Nanocomposites Studied by Raman Spectroscopy. In: *Raman Spectroscopy* [online]. 2018. Available from: https://doi.org/10.5772/intechopen.73487. [viewed 2023-03-30].

[102] REICH, S. and C. THOMSEN. Raman spectroscopy of graphite. In: *Philosophical Transactions of the Royal Society A: Mathematical, Physical and Engineering Sciences* [online]. 2004. vol. 362, no. 1824, pp. 2271–2288. Available from: https://doi.org/10.1098/rsta.2004.1454. [viewed 2023-08-02].

[103] DRESSELHAUS, M.S.; G. DRESSELHAUS; R. SAITO and A. JORIO. Raman spectroscopy of carbon nanotubes. In: *Physics Reports* [online]. 2005. vol. 409, no. 2, pp. 47–99. Available from: https://doi.org/10.1016/j.physrep.2004.10.006. [viewed 2022-08-11].

[104] THOMSEN, C. and S. REICH. Double resonant raman scattering in graphite. In: *Physical Review Letters* [online]. 2000. vol. 85, no. 24, pp. 5214–5217. Available from: https://doi.org/10.1103/PhysRevLett.85.5214. [viewed 2025-05-07].

[105] FERRARI, A. and J. ROBERTSON. Interpretation of Raman spectra of disordered and amorphous carbon. In: *Physical Review B - Condensed Matter and Materials Physics* [online]. 2000. vol. 61, no. 20, pp. 14095–14107. Available from: https://doi.org/10.1103/PhysRevB.61.14095. [viewed 2024-01-03].

[106] YUAN, R.; Y. GUO; I. GURGAN; N. SIDDIQUE; Y.S. LI et al. Raman spectroscopy analysis of disordered and amorphous carbon materials: A review of empirical correlations. In: *Carbon* [online]. 2025. vol. 238, p. 120214. Available from: https://doi.org/10.1016/J.CARBON.2025.120214. [viewed 2025-03-28].

[107] TUINSTRA F and KOENIG JL. Raman Spectrum of Graphite. In: *Journal of Chemical Physics* [online]. 1970. vol. 53, no. 3, pp. 1126–1130. Available from: https://doi.org/10.1063/1.1674108. [viewed 2023-12-07].

[108] SCHUEPFER, D.B.; F. BADACZEWSKI; J.M. GUERRA-CASTRO; D.M. HOFMANN; C. HEILIGER et al. Assessing the structural properties of graphitic and non-graphitic carbons by Raman spectroscopy. In: *Carbon* [online]. 2020. vol. 161,

pp. 359–372. Available from: https://doi.org/10.1016/j.carbon.2019.12.094. [viewed 2023-09-07].

[109] ORTS MERCADILLO, V.; H. IJIJE; L. CHAPLIN; I.A. KINLOCH and M.A. BISSETT. Novel techniques for characterising graphene nanoplatelets using Raman spectroscopy and machine learning. In: *2D Materials* [online]. 2023. vol. 10, no. 2, p. 025018. Available from: https://doi.org/10.1088/2053-1583/acc080. [viewed 2023-08-02].

[110] TEJASVI, R. Properties of Carbon-Based Nanomaterials and Techniques for Characterization. In: *Carbon-based Nanomaterials for Green Applications* [online]. [place not known]: wiley, 2024. pp. 21–55. ISBN 9781394243426Available from: https://doi.org/10.1002/9781394243426.ch2. [viewed 2025-05-12].

[111] COUZI, M.; J.L. BRUNEEL; D. TALAGA and L. BOKOBZA. A multi wavelength Raman scattering study of defective graphitic carbon materials: The first order Raman spectra revisited. In: *Carbon* [online]. 2016. vol. 107, no. 107, pp. 388–394. Available from: https://doi.org/10.1016/j.carbon.2016.06.017. [viewed 2023-09-28].

[112] MOSEENKOV, S.I.; V.L. KUZNETSOV; N.A. ZOLOTAREV; B.A. KOLESOV; I.P. PROSVIRIN et al. Investigation of Amorphous Carbon in Nanostructured Carbon Materials (A Comparative Study by TEM, XPS, Raman Spectroscopy and XRD). In: *Materials* [online]. 2023. vol. 16, no. 3, p. 1112. Available from: https://doi.org/10.3390/ma16031112. [viewed 2023-09-07].

[113] MACHADO, L.R.P.; M.O.S. SILVA; J.L.E. CAMPOS; D.L. SILVA; L.G. CANÇADO et al. Deep-learning-based denoising approach to enhance Raman spectroscopy in mass-produced graphene. In: *Journal of Raman Spectroscopy* [online]. 2022. vol. 53, no. 5, pp. 863–871. Available from: https://doi.org/10.1002/jrs.6317. [viewed 2024-09-17].

[114] HAYNES, C.L. and R.P. VAN DUYNE. Plasmon-sampled surface-enhanced Raman excitation spectroscopy. In: *Journal of Physical Chemistry B* [online]. 2003. vol. 107, no. 30, pp. 7426–7433. Available from: https://doi.org/10.1021/jp027749b. [viewed 2025-02-18].

[115] CERF, A.; G. MOLNÁR and C. VIEU. Novel approach for the assembly of highly efficient SERS substrates. In: *ACS Applied Materials and Interfaces* [online]. 2009. vol. 1, no. 11, pp. 2544–2550. Available from: https://doi.org/10.1021/am900476d. [viewed 2022-10-31].

[116] ZHANG, N.; L. TONG and J. ZHANG. Graphene-based enhanced raman scattering toward analytical applications. In: *Chemistry of Materials* [online]. 2016. vol. 28, no. 18, pp. 6426–6435. Available from: https://doi.org/10.1021/acs.chemmater.6b02925. [viewed 2024-12-08].

[117] DANIEL, M.C. and D. ASTRUC. [online]. .[place not known]: [publisher not known], 2004. Available from: https://doi.org/10.1021/cr030698+. [viewed 2025-01-09].

[118] RU, E.C. LE and B. AUGUIÉ. Enhancement Factors: A Central Concept during 50 Years of Surface-Enhanced Raman Spectroscopy. In: [online]. 2013. Available from: https://doi.org/10.1021/acsnano.4c01474. [viewed 2025-09-24].

[119] RU, E.C. LE and B. AUGUIÉ. Enhancement Factors: A Central Concept during 50 Years of Surface-Enhanced Raman Spectroscopy. In: *ACS Nano* [online]. 2024. vol. 18, no. 14, pp. 9773–9783. Available from: https://doi.org/10.1021/ACSNANO.4C01474. [viewed 2025-09-24].

[120] KUMAR, S.; K. TOKUNAGA; K. NAMURA; T. FUKUOKA and M. SUZUKI. Experimental Evidence of a Twofold Electromagnetic Enhancement Mechanism of Surface-Enhanced Raman Scattering. In: *Journal of Physical Chemistry C* [online].

2020. vol. 124, no. 38, pp. 21215–21222. Available from: https://doi.org/10.1021/acs.jpcc.0c07930. [viewed 2025-02-19].

[121] PUSTOVIT, V.N. and T. V. SHAHBAZYAN. Microscopic theory of surface-enhanced Raman scattering in noble-metal nanoparticles. In: *Physical Review B* [online]. 2006. vol. 73, no. 8, p. 085408. Available from: https://doi.org/10.1103/PhysRevB.73.085408. [viewed 2025-09-24].

[122] CHAUDHRY, I.; G. HU; H. YE and L. JENSEN. Toward Modeling the Complexity of the Chemical Mechanism in SERS. In: *ACS nano* [online]. 2024. vol. 18, no. 32, pp. 20835–20850. Available from: https://doi.org/10.1021/acsnano.4c07198. [viewed 2026-02-21].

[123] CHEN, R. and L. JENSEN. Interpreting the chemical mechanism in SERS using a Raman bond model. In: *Journal of Chemical Physics* [online]. 2020. vol. 152, no. 2, p. 24126. Available from: https://doi.org/10.1063/1.5138204. [viewed 2026-02-21].

[124] CHENAL, C.; R.L. BIRKE and J.R. LOMBARDI. Determination of the degree of charge-transfer contributions to surface-enhanced Raman spectroscopy. In: *ChemPhysChem* [online]. 2008. vol. 9, no. 11, pp. 1617–1623. Available from: https://doi.org/10.1002/cphc.200800221. [viewed 2026-02-21].

[125] KRAVETS, V.G.; A. V. KABASHIN; W.L. BARNES and A.N. GRIGORENKO. Plasmonic Surface Lattice Resonances: A Review of Properties and Applications. In: *Chemical Reviews* [online]. 2018. vol. 118, no. 12, pp. 5912–5951. Available from: https://doi.org/10.1021/acs.chemrev.8b00243. [viewed 2022-05-04].

[126] KATAJA, M.; T.K. HAKALA; A. JULKU; M.J. HUTTUNEN; S. VAN DIJKEN et al. Surface lattice resonances and magneto-optical response in magnetic nanoparticle arrays. In: *Nature Communications* [online]. 2015. vol. 6. Available from: https://doi.org/10.1038/ncomms8072. [viewed 2022-05-01].

[127] KHLEBTSOV, B.N.; A.M. BUROV; S. V. ZARKOV and N.G. KHLEBTSOV. Surface-enhanced Raman scattering from Au nanorods, nanotriangles, and nanostars with tuned plasmon resonances. In: *Physical Chemistry Chemical Physics* [online]. 2023. vol. 25, no. 45, pp. 30903–30913. Available from: https://doi.org/10.1039/d3cp04541b. [viewed 2025-02-17].

[128] JUODENAS, M.; T. TAMULEVIČIUS; J. HENZIE; D. ERTS and S. TAMULEVIČIUS. Surface Lattice Resonances in Self-Assembled Arrays of Monodisperse Ag Cuboctahedra. In: *ACS Nano* [online]. 2019. vol. 13, no. 8, pp. 9038–9047. Available from: https://doi.org/10.1021/ACSNANO.9B03191. [viewed 2024-08-20].

[129] ESTEBAN, R.; R.W. TAYLOR; J.J. BAUMBERG and J. AIZPURUA. How chain plasmons govern the optical response in strongly interacting self-assembled metallic clusters of nanoparticles. In: *Langmuir* [online]. 2012. vol. 28, no. 24, pp. 8881–8890. Available from: https://doi.org/10.1021/LA300198R. [viewed 2024-08-20].

[130] DENG, S.; R. LI; J.E. PARK; J. GUAN; P. CHOO et al. Ultranarrow plasmon resonances from annealed nanoparticle lattices. In: *Proceedings of the National Academy of Sciences of the United States of America* [online]. 2020. vol. 117, no. 38, pp. 23380–23384. Available from: https://doi.org/10.1073/PNAS.2008818117. [viewed 2024-12-10].

[131] TÖRMÄ, P.; M.J. HUTTUNEN; K. DOLGALEVA and R.W. BOYD. Ultra-strong polarization dependence of surface lattice resonances with out-of-plane plasmon oscillations. In: *Optics Express, Vol. 24, Issue 25, pp. 28279-28289* [online]. 2016. vol. 24, no. 25, pp. 28279–28289. Available from: https://doi.org/10.1364/OE.24.028279. [viewed 2025-02-12].

[132] KHINEVICH, N.; M. JUODĖNAS; A. TAMULEVIČIENĖ; T. TAMULEVIČIUS; M. TALAIKIS et al. Wavelength-tailored enhancement of Raman scattering on a resonant plasmonic lattice. In: *Sensors and Actuators B: Chemical* [online]. 2023. vol. 394, p. 134418. Available from: https://doi.org/10.1016/J.SNB.2023.134418. [viewed 2024-08-07].

[133] CHARCONNET, M.; C. KUTTNER; J. PLOU; J.L. GARCÍA-POMAR; A. MIHI et al. Mechanically Tunable Lattice-Plasmon Resonances by Templated Self-Assembled Superlattices for Multi-Wavelength Surface-Enhanced Raman Spectroscopy. In: *Small Methods* [online]. 2021. vol. 5, no. 10, p. 2100453. Available from: https://doi.org/10.1002/smtd.202100453. [viewed 2025-02-17].

[134] ALAM, K.; K.M. KABUSURE; B.O. ASAMOAH; T. NUUTINEN; M. BAAH et al. Double resonant plasmonic lattices for Raman studies. In: *Nanoscale* [online]. 2020. vol. 12, no. 45, pp. 23166–23172. Available from: https://doi.org/10.1039/D0NR05255H. [viewed 2025-03-19].

[135] RAGHEB, I.; M. BRAÏK; S. LAU-TRUONG; A. BELKHIR; A. RUMYANTSEVA et al. Surface Enhanced Raman Scattering on Regular Arrays of Gold Nanostructures: Impact of Long-Range Interactions and the Surrounding Medium. In: *Nanomaterials 2020, Vol. 10, Page 2201* [online]. 2020. vol. 10, no. 11, p. 2201. Available from: https://doi.org/10.3390/NANO10112201. [viewed 2025-02-17].

[136] WEITZ, D.A.; S. GAROFF and T.J. GRAMILA. Excitation spectra of surface-enhanced Raman scattering on silver-island films. In: *Optics Letters* [online]. 1982. vol. 7, no. 4, p. 168. Available from: https://doi.org/10.1364/ol.7.000168. [viewed 2025-02-18].

[137] FÉLIDJ, N.; J. AUBARD; G. LÉVI; J.R. KRENN; A. HOHENAU et al. Optimized surface-enhanced Raman scattering on gold nanoparticle arrays. In: *Applied Physics Letters* [online]. 2003. vol. 82, no. 18, pp. 3095–3097. Available from: https://doi.org/10.1063/1.1571979. [viewed 2025-02-17].

[138] MCFARLAND, A.D.; M.A. YOUNG; J.A. DIERINGER and R.P. VAN DUYNE. Wavelength-scanned surface-enhanced Raman excitation spectroscopy. In: *Journal of Physical Chemistry B* [online]. 2005. vol. 109, no. 22, pp. 11279–11285. Available from: https://doi.org/10.1021/jp050508u. [viewed 2025-02-18].

[139] LI, Y.; Q. LIAO; W. HOU and L. QIN. Silver-Based Surface Plasmon Sensors: Fabrication and Applications. In: *International Journal of Molecular Sciences 2023, Vol. 24, Page 4142* [online]. 2023. vol. 24, no. 4, p. 4142. Available from: https://doi.org/10.3390/IJMS24044142. [viewed 2024-08-06].

[140] TONG, Q.; W. WANG; Y. FAN and L. DONG. Recent progressive preparations and applications of silver-based SERS substrates. In: *TrAC Trends in Analytical Chemistry* [online]. 2018. vol. 106, pp. 246–258. Available from: https://doi.org/10.1016/J.TRAC.2018.06.018. [viewed 2024-08-06].

[141] JUODĖNAS, M.; D. PECKUS; T. TAMULEVIČIUS; Y. YAMAUCHI; S. TAMULEVIČIUS et al. Effect of Ag Nanocube Optomechanical Modes on Plasmonic Surface Lattice Resonances. In: *ACS Photonics* [online]. 2020. vol. 7, no. 11, pp. 3130–3140. Available from: https://pubs.acs.org/doi/10.1021/acsphotonics.0c01187. [viewed 2024-12-09].

[142] RYCENGA, M.; C.M. COBLEY; J. ZENG; W. LI; C.H. MORAN et al. Controlling the synthesis and assembly of silver nanostructures for plasmonic applications. In: *Chemical Reviews* [online]. 2011. vol. 111, no. 6, pp. 3669–3712. Available from: https://doi.org/10.1021/CR100275D. [viewed 2024-09-02].

[143] Chu, B. H.; B. J. NICOLASI; C.F. Lo, W. STRUPINSKI; S. J. PEARTON; F. REN. Effect of Coated Platinum Thickness on Hydrogen Detection Sensitivity of Graphene-Based Sensors. In: *Electrochemical and Solid-State Letters* [online]. 2011. vol.14, no.7, K43-K45. Available from: https://iopscience.iop.org/article/10.1149/1.3589250. [viewed 2022-09-27].

[144] YADAV, S.; M. TALAIKIS; Y. V. RYABCHIKOV; M. ZIEGLER; G. NIAURA et al. Copper-Based Multiwavelength UV Surface Enhanced Raman Spectroscopy. In: *Advanced Optical Materials* [online]. 2025. vol. 13, no. 18. Available from: https://doi.org/10.1002/ADOM.202500078. [viewed 2025-10-02].

[145] GHOPRY, S.A.; B. LIU; A. SHULTZ and J.Z. WU. Tuning Fermi Energy of Graphene Using Platinum Nanoparticles and Ultraviolet Irradiation to Increase Charge Transfer for Surface-Enhanced Raman Spectroscopy. In: *ACS Applied Nano Materials* [online]. 2023. vol. 6, no. 23, pp. 21626–21633. Available from: https://doi.org/10.1021/ACSANM.3C03532. [viewed 2025-10-02].

[146] YADAV, S.; M. TALAIKIS; Y. V. RYABCHIKOV; M. ZIEGLER; G. NIAURA et al. Copper-Based Multiwavelength UV Surface Enhanced Raman Spectroscopy. In: *Advanced Optical Materials* [online]. 2025. vol. 13, no. 18. Available from: https://doi.org/10.1002/ADOM.202500078. [viewed 2025-10-09].

[147] DAS, R. and R.K. SONI. Rhodium nanocubes and nanotripods for highly sensitive ultraviolet surface-enhanced Raman spectroscopy. In: *Cite this: Analyst* [online]. 2018. vol. 143, p. 2310. Available from: https://doi.org/10.1039/c8an00341f. [viewed 2025-10-09].

[148] SULTAN, M.F. An investigation of the influence of the graphene layers number on the performance of surface plasmon resonance biosensors with various thicknesses of silver. In: *Journal of Optics (India)* [online]. 2024. vol. 53, no. 5, pp. 4893–4900. Available from: https://doi.org/10.1007/s12596-024-01754-9. [viewed 2025-01-06].

[149] PÉRON, O.; E. RINNERT; M. LEHAITRE; P.C. CRASSOUS; C. COMPERE. Detection of polycyclic aromatic hydrocarbon (PAH) compounds in artificial sea-water using surface-enhanced Raman scattering (SERS). In: *Talanta* [online]. 2009. Available from: https://doi.org/10.1016/j.talanta.2009.03.043. [viewed 2026-02-08].

[150] YANG, M.C.; A. HARDIANSYAH; Y.W. CHENG; H.L. LIAO; K.S. WANG et al. Reduced graphene oxide nanosheets decorated with core-shell of Fe3O4-Au nanoparticles for rapid SERS detection and hyperthermia treatment of bacteria. In: *Spectrochimica Acta Part A: Molecular and Biomolecular Spectroscopy* [online]. 2022. vol. 281, no. 1, p. 121578. Available from: https://doi.org/10.1016/j.saa.2022.121578. [viewed 2026-02-07].

[151] IMCHEN, S.; N.S. SINGH; A.P. SINGH; L. BORAH and A. PUZARI. From synthesis to SERS (Surface Enhanced Raman Scattering): exploring the potential of crystalline ZnBTC MOFs for trace detection of toxic organic dyes. In: *Emergent Materials* [online]. 2025. vol. 8, no. 6, pp. 4309–4320. Available from: https://doi.org/10.1007/s42247-025-01058-z. [viewed 2026-02-08].

[152] POURMADADI, M.; H.S. DINANI; F.S. TABAR; K. KHASSI; S. JANFAZA et al. Properties and Applications of Graphene and Its Derivatives in Biosensors for Cancer Detection: A Comprehensive Review. In: *Biosensors 2022, Vol. 12, Page 269* [online]. 2022. vol. 12, no. 5, p. 269. Available from: https://doi.org/10.3390/BIOS12050269. [viewed 2025-02-03].

[153] BHATT, S.; V.D. PUNETHA; R. PATHAK and M. PUNETHA. Two-Dimensional Carbon Nanomaterial-Based Biosensors: Micromachines for Advancing the Medical Diagnosis. In: *Advanced Structured Materials* [online]. 2023. vol. 190, pp. 181–225.

Available from: https://link.springer.com/chapter/10.1007/978-3-031-28942-2_9. [viewed 2025-02-03].

[154] CAO, Y.; Y. CHENG and M. SUN. Graphene-based SERS for sensor and catalysis. In: *Applied Spectroscopy Reviews* [online]. 2023. vol. 58, no. 1, pp. 1–38. Available from: https://doi.org/10.1080/05704928.2021.1910286. [viewed 2025-02-03].

[155] ZHAO, Y.; X.G. LI; X. ZHOU and Y.N. ZHANG. Review on the graphene based optical fiber chemical and biological sensors. In: *Sensors and Actuators B: Chemical* [online]. 2016. vol. 231, pp. 324–340. Available from: https://doi.org/10.1016/J.SNB.2016.03.026. [viewed 2025-02-03].

[156] BUNCH, J.S.; S.S. VERBRIDGE; J.S. ALDEN; A.M. VAN DER ZANDE; J.M. PARPIA et al. Impermeable atomic membranes from graphene sheets. In: *Nano Letters* [online]. 2008. vol. 8, no. 8, pp. 2458–2462. Available from: https://doi.org/10.1021/nl801457b. [viewed 2024-12-27].

[157] ZHOU, Q.; M. JIN; W. WU; L. FU; C. YIN et al. Graphene-Based Surface-Enhanced Raman Scattering (SERS) Sensing: Bibliometrics Based Analysis and Review. In: *Chemosensors 2022, Vol. 10, Page 317* [online]. 2022. vol. 10, no. 8, p. 317. Available from: https://doi.org/10.3390/CHEMOSENSORS10080317. [viewed 2024-08-06].

[158] LAI, H.; F. XU; Y. ZHANG and L. WANG. Recent progress on graphene-based substrates for surface-enhanced Raman scattering applications. In: *Journal of Materials Chemistry B* [online]. 2018. vol. 6, no. 24, pp. 4008–4028. Available from: https://doi.org/10.1039/C8TB00902C. [viewed 2024-08-06].

[159] NURROHMAN, D.T. and N.F. CHIU. A Review of Graphene-Based Surface Plasmon Resonance and Surface-Enhanced Raman Scattering Biosensors: Current Status and Future Prospects. In: *Nanomaterials 2021, Vol. 11, Page 216* [online]. 2021. vol. 11, no. 1, p. 216. Available from: https://doi.org/10.3390/NANO11010216. [viewed 2024-08-06].

[160] TOPSAKAL, M.; H. AAHIN and S. CIRACI. Graphene coatings: An efficient protection from oxidation. In: *Physical Review B* [online]. 2012. vol. 85, no. 15, p. 155445. Available from: https://doi.org/10.1103/PhysRevB.85.155445. [viewed 2026-02-07].

[161] LOSURDO, M.; I. BERGMAIR; B. DASTMALCHI; T.H. KIM; M.M. GIANGREGROIO et al. Graphene as an Electron Shuttle for Silver Deoxidation: Removing a Key Barrier to Plasmonics and Metamaterials for SERS in the Visible. In: *Advanced Functional Materials* [online]. 2014. vol. 24, no. 13, pp. 1864–1878. Available from: https://doi.org/10.1002/ADFM.201303135. [viewed 2023-02-16].

[162] CHEN, S.; L. BROWN; M. LEVENDORF; W. CAI; S.-Y. JU et al. Oxidation Resistance of Graphene-Coated Cu and Cu/Ni Alloy. In: [online]. 2011. Available from: https://doi.org/10.1021/nn103028d. [viewed 2026-02-07].

[163] YU, F. *Graphene based coatings for corrosion protection*. DTU Nanotech, 2018.

[164] SUZUKI, S. and M. YOSHIMURA. Chemical Stability of Graphene Coated Silver Substrates for Surface-Enhanced Raman Scattering. In: *Scientific Reports* [online]. 2017. vol. 7, no. 1, p. 14851. Available from: https://doi.org/10.1038/s41598-017-14782-2. [viewed 2026-02-07].

[165] LIU, Y.; Y. HU and J. ZHANG. Few-Layer Graphene-Encapsulated Metal Nanoparticles for Surface-Enhanced Raman Spectroscopy. In: [online]. 2014. Available from: https://doi.org/10.1021/jp500751a. [viewed 2026-02-21].

[166] XU, W.; X. LING; J. XIAO; M.S. DRESSELHAUS; J. KONG et al. Surface enhanced Raman spectroscopy on a flat graphene surface. In: *Proceedings of the National Academy of Sciences of the United States of America* [online]. 2012. vol. 109, no. 24,

pp. 9281–9286. Available from: https://doi.org/10.1073/pnas.1205478109. [viewed 2026-02-21].

[167] XU, S.; J. WANG; Y. ZOU; H. LIU; G. WANG et al. High performance SERS active substrates fabricated by directly growing graphene on Ag nanoparticles. In: *RSC Advances* [online]. 2015. vol. 5, no. 110, pp. 90457–90465. Available from: https://doi.org/10.1039/c5ra18333b. [viewed 2026-02-21].

[168] ZHANG, Z.; Y. LEE; M.F. HAQUE; J. LEEM; E.Y. HSIEH et al. Plasmonic sensors based on graphene and graphene hybrid materials. In: *Nano Convergence 2022 9:1* [online]. 2022. vol. 9, no. 1, pp. 1–24. Available from: https://doi.org/10.1186/S40580-022-00319-5. [viewed 2024-12-27].

[169] LIN, J.; N. ZHANG; L. TONG and J. ZHANG. Enhanced Raman Scattering on Graphene and beyond. In: *ACS Symposium Series* [online]. [place not known]: American Chemical Society, 2016. pp. 97–119. ISBN 9780841232013Available from: https://doi.org/10.1021/bk-2016-1246.ch005. [viewed 2024-12-27].

[170] ZHANG, N.; L. TONG and J. ZHANG. Graphene-based enhanced raman scattering toward analytical applications. In: *Chemistry of Materials* [online]. 2016. vol. 28, no. 18, pp. 6426–6435. Available from: https://doi.org/10.1021/ACS.CHEMMATER.6B02925. [viewed 2024-12-08].

[171] LING, X.; L. XIE; Y. FANG; H. XU; H. ZHANG et al. Can graphene be used as a substrate for Raman enhancement? In: *Nano Letters* [online]. 2010. vol. 10, no. 2, pp. 553–561. Available from: https://doi.org/10.1021/nl903414x. [viewed 2024-12-29].

[172] LING, X. and J. ZHANG. First-layer effect in graphene-enhanced raman scattering. In: *Small* [online]. 2010. vol. 6, no. 18, pp. 2020–2025. Available from: https://doi.org/10.1002/smll.201000918. [viewed 2024-12-29].

[173] DAI, Z.G.; X.H. XIAO; W. WU; Y.P. ZHANG; L. LIAO et al. Plasmon-driven reaction controlled by the number of graphene layers and localized surface plasmon distribution during optical excitation. In: *Light: Science & Applications 2015 4:10* [online]. 2015. vol. 4, no. 10, pp. e342–e342. Available from: https://doi.org/10.1038/lsa.2015.115. [viewed 2024-12-07].

[174] WANG, W.; Y. ZHANG and Y.B. WANG. Noncovalent π-π interaction between graphene and aromatic molecule: Structure, energy, and nature. In: *Journal of Chemical Physics* [online]. 2014. vol. 140, no. 9. Available from: https://doi.org/10.1063/1.4867071. [viewed 2026-02-07].

[175] BIROJU, R.K.; B.C. MAREPALLY; P. MALIK; S. DHARA; S. GENGAN et al. Defective Graphene/Plasmonic Nanoparticle Hybrids for Surface-Enhanced Raman Scattering Sensors. In: *ACS Omega* [online]. 2023. vol. 8, no. 4, pp. 4344–4356. Available from: https://doi.org/10.1021/acsomega.2c07706. [viewed 2026-02-07].

[176] YU, X.; H. CAI; W. ZHANG; X. LI; N. PAN et al. Tuning chemical enhancement of SERS by controlling the chemical reduction of graphene oxide nanosheets. In: *ACS Nano* [online]. 2011. vol. 5, no. 2, pp. 952–958. Available from: https://doi.org/10.1021/nn102291j. [viewed 2026-02-07].

[177] KONG, X. and Q. CHEN. The positive influence of boron-doped graphene with pyridine as a probe molecule on SERS: A density functional theory study. In: *Journal of Materials Chemistry* [online]. 2012. vol. 22, no. 30, pp. 15336–15341. Available from: https://doi.org/10.1039/c2jm32050a. [viewed 2026-02-07].

[178] ZHANG, C.; K. LIN; Y. HUANG and J. ZHANG. Graphene-Ag hybrids on laser-textured Si surface for SERS detection. In: *Sensors (Switzerland)* [online]. 2017.

vol. 17, no. 7, p. 1462. Available from: https://doi.org/10.3390/s17071462. [viewed 2024-08-06].

[179] OSVÁTH, Z.; A. PÁLINKÁS; G. PISZTER and G. MOLNÁR. Synthesis and Characterization of Graphene–Silver Nanoparticle Hybrid Materials. In: *Materials 2020, Vol. 13,* [online]. 2020. vol. 13, no. 20, pp. 1–8. Available from: https://doi.org/10.3390/ma13204660. [viewed 2026-02-21].

[180] GONG, T.; Y. LUO; C. ZHAO; W. YUE; J. ZHANG et al. Highly reproducible and stable surface-enhanced Raman scattering substrates of graphene-Ag nanohole arrays fabricated by sub-diffraction plasmonic lithography. In: *OSA Continuum* [online]. 2019. vol. 2, no. 3, p. 582. Available from: https://doi.org/10.1364/osac.2.000582. [viewed 2025-02-19].

[181] LIU, X.; J. WANG; Y. WU; T. FAN; Y. XU et al. Compact Shielding of Graphene Monolayer Leads to Extraordinary SERS-Active Substrate with Large-Area Uniformity and Long-Term Stability. In: *Scientific Reports* [online]. 2015. vol. 5, p. 17167. Available from: https://doi.org/10.1038/srep17167. [viewed 2026-02-21].

[182] LI, J.F.; Y.F. HUANG; Y. DING; Z.L. YANG; S.B. LI et al. Shell-isolated nanoparticle-enhanced Raman spectroscopy. In: *Nature 2010 464:7287* [online]. 2010. vol. 464, no. 7287, pp. 392–395. Available from: https://doi.org/10.1038/nature08907. [viewed 2026-02-23].

[183] LI, J.F. and Z.Q. TIAN. Shell-Isolated Nanoparticle-Enhanced Raman Spectroscopy (SHINERS). In: *Wiley Blackwell 6* [online]. 2014. vol. 9781118359020, pp. 163–192. Available from: https://doi.org/10.1002/9781118703601.ch8. [viewed 2026-02-07].

[184] JIN, C.; H. ZHENG and J. CHEN. Advances in the Application of Graphene and Its Derivatives in Drug Delivery Systems. In: *Pharmaceuticals 2025, Vol. 18,* [online]. 2025. vol. 18, no. 9. Available from: https://doi.org/10.3390/ph18091245. [viewed 2026-02-23].

[185] LI, J.F.; J.R. ANEMA; T. WANDLOWSKI and Z.Q. TIAN. Dielectric shell isolated and graphene shell isolated nanoparticle enhanced Raman spectroscopies and their applications. In: *Chemical Society Reviews* [online]. 2015. vol. 44, no. 23, pp. 8399–8409. Available from: https://doi.org/10.1039/c5cs00501a. [viewed 2026-02-23].

[186] LING, X. and J. ZHANG. Interference Phenomenon in Graphene-Enhanced Raman Scattering. In: *J. Phys. Chem. C* [online]. 2011. vol. 115, pp. 2835–2840. Available from: https://doi.org/10.1021/jp111502n. [viewed 2026-02-23].

[187] ZHANG, N.; L. TONG and J. ZHANG. Graphene-Based Enhanced Raman Scattering toward Analytical Applications. In: [online]. 2016. Available from: https://doi.org/10.1021/acs.chemmater.6b02925. [viewed 2026-02-23].

[188] ATTA, S.; T. SHARAF and T. VO-DINH. Rapid Solution-Based SERS Detection of Pesticides Using Graphene Oxide-Coated Silver–Gold Nanostars. In: *ACS applied nano materials* [online]. 2024. vol. 7, no. 10, p. 11518. Available from: https://doi.org/10.1021/acsanm.4c01122. [viewed 2026-02-21].

[189] WU, X.; Y. XING; K. ZENG; K. HUBER and J.X. ZHAO. Study of Fluorescence Quenching Ability of Graphene Oxide with a Layer of Rigid and Tunable Silica Spacer. In: *Langmuir* [online]. 2017. Vol 34, no 2, pp. 603-611. Available from: https://pubs.acs.org/doi/10.1021/acs.langmuir.7b03465.

[190] ZHANG, N.; K. ZHANG; M. ZOU; R.A. MANIYARA; T.A. BOWEN et al. Tuning the Fermi Level of Graphene by Two-Dimensional Metals for Raman Detection of Molecules. In: *ACS Nano* [online]. 2024. vol. 18, no. 12, pp. 8876–8884. Available from: https://doi.org/10.1021/acsnano.3c12152. [viewed 2026-02-21].

[191] GAO, L.; W. REN; B. LIU; R. SAITO; Z.S. WU et al. Surface and Interference Coenhanced Raman Scattering of Graphene. In: *ACS Nano* [online]. 2009. vol. 3, no. 4, pp. 933–939. Available from: https://doi.org/10.1021/nn8008799. [viewed 2026-02-23].

[192] LING, X. and J. ZHANG. Interference Phenomenon in Graphene-Enhanced Raman Scattering. In: *J. Phys. Chem. C* [online]. 2011. vol. 115, pp. 2835–2840. Available from: https://doi.org/10.1021/jp111502n. [viewed 2026-02-23].

[193] ZHOU, H.; W.J. YU; L. LIU; R. CHENG; Y. CHEN et al. Chemical vapour deposition growth of large single crystals of monolayer and bilayer graphene. In: *Nature Communications* [online]. 2013. vol. 4, no. 1, pp. 1–8. Available from: https://doi.org/10.1038/ncomms3096. [viewed 2025-02-13].

[194] HASEGAWA, M.; K. TSUGAWA; R. KATO; Y. KOGA; M. ISHIHARA et al. High quality and large-area graphene synthesis with a high growth rate using plasma-enhanced CVD. In: *Synthesiology English edition* [online]. 2016. vol. 9, no. 3, pp. 124–138. Available from: https://doi.org/10.5571/syntheng.9.3_124. [viewed 2026-02-06].

[195] GUDAITIS, R.; A. LAZAUSKAS; Š. JANKAUSKAS and Š. MEŠKINIS. Catalyst-Less and Transfer-Less Synthesis of Graphene on Si(100) Using Direct Microwave Plasma Enhanced Chemical Vapor Deposition and Protective Enclosures. In: *Materials* [online]. 2020. vol. 13, no. 24, pp. 1–16. Available from: https://doi.org/10.3390/MA13245630. [viewed 2023-01-09].

[196] TAO, A.; P. SINSERMSUKSAKUL; P. YANG; A. TAO; P. SINSERMSUKSAKUL et al. Polyhedral Silver Nanocrystals with Distinct Scattering Signatures**. In: *Angew. Chem. Int. Ed* [online]. 2006. vol. 45, pp. 4597–4601. Available from: https://doi.org/10.1002/anie.200601277. [viewed 2025-02-21].

[197] NI, S.; L. ISA and H. WOLF. Capillary assembly as a tool for the heterogeneous integration of micro- and nanoscale objects. In: *Soft Matter* [online]. 2018. vol. 14, no. 16, pp. 2978–2995. Available from: https://doi.org/10.1039/c7sm02496g.

[198] JUODĖNAS, M.; N. KHINEVICH; G. KLYVIS; J. HENZIE; T. TAMULEVIČIUS et al. Lasing in an Assembled Array of Silver Nanocubes. In: [online]. 2024. Available from: https://arxiv.org/abs/2405.11908v1. [viewed 2024-12-09].

[199] SHIVAYOGIMATH, A.; P.R. WHELAN; D.M.A. MACKENZIE; B. LUO; D. HUANG et al. Do-It-Yourself Transfer of Large-Area Graphene Using an Office Laminator and Water. In: *Chemistry of Materials* [online]. 2019. vol. 31, no. 7, pp. 2328–2336. Available from: https://doi.org/10.1021/ACS.CHEMMATER.8B04196. [viewed 2025-11-07].

[200] MAZET, V. Background correction. In: *Annual Reports on Analytical Atomic Spectroscopy* [online]. [place not known]: [publisher not known], 1983. Available from: https://doi.org/10.1039/AA9831300052. [viewed 2025-01-24].

[201] CAMPOS, J.L.E.; H. MIRANDA; C. RABELO; E. SANDOZ-ROSADO; S. PANDEY et al. Applications of Raman spectroscopy in graphene-related materials and the development of parameterized PCA for large-scale data analysis. In: *Journal of Raman Spectroscopy* [online]. 2018. vol. 49, no. 1, pp. 54–65. Available from: https://doi.org/10.1002/jrs.5225. [viewed 2024-04-11].

[202] SILVA, D.L.; J.L.E. CAMPOS; T.F.D. FERNANDES; J.N. ROCHA; L.R.P. MACHADO et al. Raman spectroscopy analysis of number of layers in mass-produced graphene flakes. In: *Carbon* [online]. 2020. vol. 161, pp. 181–189. Available from: https://doi.org/10.1016/J.CARBON.2020.01.050. [viewed 2024-04-11].

[203] SUN, J.; T. RATTANASAWATESUN; P. TANG; Z. BI; S. PANDIT et al. Insights into the Mechanism for Vertical Graphene Growth by Plasma-Enhanced Chemical Vapor Deposition. In: *ACS Applied Materials and Interfaces* [online]. 2022. vol. 14, no. 5, pp. 7152–7160. Available from: https://doi.org/10.1021/ACSAMI.1C21640. [viewed 2022-09-17].

[204] SEMAK, V. and A. MATSUNAWA. The role of recoil pressure in energy balance during laser materials processing. In: *Journal of Physics D: Applied Physics* [online]. 1997. vol. 30, no. 18, p. 2541. Available from: https://doi.org/10.1088/0022-3727/30/18/008. [viewed 2025-05-06].

[205] KODA, K.; W. KOBAYASHI; H. IMAI and M. TSUKAMOTO. Formation of microstructures on ni film surface by nanosecond laser irradiation. In: *Applied Physics A: Materials Science and Processing* [online]. 2018. vol. 124, no. 3, pp. 1–6. Available from: https://doi.org/10.1007/S00339-018-1635-0. [viewed 2025-05-06].

[206] MOUN, M.; A. VASDEV; R. PUJAR; K. PRIYA MADHURI; U. MOGERA et al. Enhanced electrical transport through wrinkles in turbostratic graphene films. In: *Applied Physics Letters* [online]. 2021. vol. 119, no. 3, p. 33102. Available from: https://doi.org/10.1063/5.0056212/41788. [viewed 2025-05-06].

[207] FERRARI, A.C. and D.M. BASKO. Raman spectroscopy as a versatile tool for studying the properties of graphene. In: *Nature Nanotechnology 2013 8:4* [online]. 2013. vol. 8, no. 4, pp. 235–246. Available from: https://doi.org/10.1038/nnano.2013.46. [viewed 2025-05-07].

[208] HAO, Y.; Y. WANG; L. WANG; Z. NI; Z. WANG et al. Probing layer number and stacking order of few-layer graphene by Raman Spectroscopy. In: *Small* [online]. 2010. vol. 6, no. 2, pp. 195–200. Available from: https://doi.org/10.1002/SMLL.200901173. [viewed 2025-05-13].

[209] CANÇADO, L.G.; M.G. DA SILVA; E.H. MARTINS FERREIRA; F. HOF; K. KAMPIOTI et al. Disentangling contributions of point and line defects in the Raman spectra of graphene-related materials. In: *2D Materials* [online]. 2017. vol. 4, no. 2, p. 025039. Available from: https://doi.org/10.1088/2053-1583/AA5E77. [viewed 2023-06-23].

[210] GOHIER, A.; C.P. EWELS; T.M. MINEA and M.A. DJOUADI. Carbon nanotube growth mechanism switches from tip- to base-growth with decreasing catalyst particle size. In: *Carbon* [online]. 2008. vol. 46, no. 10, pp. 1331–1338. Available from: https://doi.org/10.1016/j.carbon.2008.05.016. [viewed 2025-04-23].

[211] BOWER, C.; O. ZHOU; W. ZHU; D.J. WERDER and S. JIN. Nucleation and growth of carbon nanotubes by microwave plasma chemical vapor deposition. In: *Applied Physics Letters* [online]. 2000. vol. 77, no. 17, pp. 2767–2769. Available from: https://doi.org/10.1063/1.1319529. [viewed 2024-02-01].

[212] BOWER, C.; O. ZHOU; W. ZHU; D.J. WERDER and S. JIN. Nucleation and growth of carbon nanotubes by microwave plasma chemical vapor deposition. In: *Applied Physics Letters* [online]. 2000. vol. 77, no. 17, pp. 2767–2769. Available from: https://doi.org/10.1063/1.1319529. [viewed 2023-06-29].

[213] HE, C.N.; C.S. SHI; X.W. DU; J.J. LI and N.Q. ZHAO. TEM investigation on the initial stage growth of carbon onions synthesized by CVD. In: *Journal of Alloys and Compounds* [online]. 2008. vol. 452, no. 2, pp. 258–262. Available from: https://doi.org/10.1016/j.jallcom.2006.11.016. [viewed 2023-09-07].

[214] QIU, L. and F. DING. Contact-Induced Phase Separation of Alloy Catalyst to Promote Carbon Nanotube Growth. In: *Physical Review Letters* [online]. 2019. vol. 123, no. 25,

p. 256101. Available from: https://doi.org/10.1103/PhysRevLett.123.256101. [viewed 2023-09-19].

[215] BOLTON, K.; F. DING and A. ROSÉN. Atomistic simulations of catalyzed carbon nanotube growth. In: *Journal of Nanoscience and Nanotechnology* [online]. [place not known]: J Nanosci Nanotechnol, 2006. pp. 1211–1224. Available from: https://doi.org/10.1166/jnn.2006.145. [viewed 2024-05-10].

[216] HANIFF, M.A.S.M.; H.W. LEE; D.C.S. BIEN; I.H.A. AZID; M.W. LEE et al. Formation of Co, Fe, and Co-Fe nanoparticles through solid-state dewetting in the presence of hydrogen plasma and their electrical properties. In: *Vacuum* [online]. 2014. vol. 101, pp. 371–376. Available from: https://doi.org/10.1016/j.vacuum.2013.10.015. [viewed 2023-09-17].

[217] LEE, M.W.; M.A.S.M. HANIFF; A.S. TEH; D.C.S. BIEN and S.K. CHEN. Effect of Co and Ni nanoparticles formation on carbon nanotubes growth via PECVD. In: *Journal of Experimental Nanoscience* [online]. 2015. vol. 10, no. 16, pp. 1232–1241. Available from: https://doi.org/10.1080/17458080.2014.994679. [viewed 2022-07-05].

[218] BULYARSKIY, S. V.; E.P. KITSYUK; A. V. LAKALIN; A.A. PAVLOV and R.M. RYAZANOV. Carbon Solubility in a Nickel Catalyst with the Growth of Carbon Nanotubes. In: *Russian Microelectronics* [online]. 2020. vol. 49, no. 1, pp. 25–29. Available from: https://doi.org/10.1134/S1063739720010059. [viewed 2023-07-18].

[219] TIEN, H.W.; Y.L. HUANG; S.Y. YANG; J.Y. WANG and C.C.M. MA. The production of graphene nanosheets decorated with silver nanoparticles for use in transparent, conductive films. In: *Carbon* [online]. 2011. vol. 49, no. 5, pp. 1550–1560. Available from: https://doi.org/10.1016/j.carbon.2010.12.022. [viewed 2024-09-17].

[220] HUANG, Y.L.; H.W. TIEN; C.C.M. MA; S.Y. YANG; S.Y. WU et al. Effect of extended polymer chains on properties of transparent graphene nanosheets conductive film. In: *Journal of Materials Chemistry* [online]. 2011. vol. 21, no. 45, pp. 18236–18241. Available from: https://doi.org/10.1039/c1jm13790e. [viewed 2024-09-17].

[221] BERTÓTI, I.; M. MOHAI and K. LÁSZLÓ. Surface modification of graphene and graphite by nitrogen plasma: Determination of chemical state alterations and assignments by quantitative X-ray photoelectron spectroscopy. In: *Carbon* [online]. 2015. vol. 84, no. 1, pp. 185–196. Available from: https://doi.org/10.1016/j.carbon.2014.11.056. [viewed 2023-11-30].

[222] KOMISSAROV, I. V.; N.G. KOVALCHUK; V.A. LABUNOV; K. V. GIREL; O. V. KOROLIK et al. Nitrogen-doped twisted graphene grown on copper by atmospheric pressure CVD from a decane precursor. In: *Beilstein Journal of Nanotechnology* [online]. 2017. vol. 8, no. 1, pp. 145–158. Available from: https://doi.org/10.3762/bjnano.8.15. [viewed 2023-10-13].

[223] BAYEV, V.G.; J.A. FEDOTOVA; J. V. KASIUK; S.A. VOROBYOVA; A.A. SOHOR et al. CVD graphene sheets electrochemically decorated with “core-shell” Co/CoO nanoparticles. In: *Applied Surface Science* [online]. 2018. vol. 440, pp. 1252–1260. Available from: https://doi.org/10.1016/j.apsusc.2018.01.245. [viewed 2024-09-17].

[224] BIESINGER, M.C. Accessing the robustness of adventitious carbon for charge referencing (correction) purposes in XPS analysis: Insights from a multi-user facility data review. In: *Applied Surface Science* [online]. 2022. vol. 597, p. 153681. Available from: https://doi.org/10.1016/j.apsusc.2022.153681. [viewed 2024-09-17].

[225] LI, S.; T. XIE; L. MA; B. LI; D. LIU et al. Advanced bifunctional bionic neural network-like architecture constructed by multi-scale carbon nanotubes nanocomposites for enhanced microwave absorption. In: *Composites Part B:*

Engineering [online]. 2024. vol. 284, p. 111714. Available from: https://doi.org/10.1016/j.compositesb.2024.111714. [viewed 2024-09-17].

[226] LIU, Y.; S. WU; C. FAN; X. WANG; F. LIU et al. Variations in surface functional groups, carbon chemical state and graphitization degree during thermal deactivation of diesel soot particles. In: *Journal of Environmental Sciences (China)* [online]. 2023. vol. 124, pp. 678–687. Available from: https://doi.org/10.1016/j.jes.2022.01.007. [viewed 2023-10-11].

[227] LEI, Z.; X. ZHANG; L. MA; B. ZHENG; Y. LIU et al. Broadband microwave absorption and antibiosis effect of Cu@C@Fe3O4 nanocomposites. In: *Journal of Alloys and Compounds* [online]. 2024. vol. 1003, p. 175497. Available from: https://doi.org/10.1016/j.jallcom.2024.175497. [viewed 2024-09-17].

[228] KOUKETSU, Y.; T. MIZUKAMI; H. MORI; S. ENDO; M. AOYA et al. A new approach to develop the Raman carbonaceous material geothermometer for low-grade metamorphism using peak width. In: *Island Arc* [online]. 2014. vol. 23, no. 1, pp. 33–50. Available from: https://doi.org/10.1111/IAR.12057. [viewed 2023-10-11].

[229] NEGRI, F.; E. DI DONATO; M. TOMMASINI; C. CASTIGLIONI; G. ZERBI et al. Resonance Raman contribution to the D band of carbon materials: Modeling defects with quantum chemistry. In: *Journal of Chemical Physics* [online]. 2004. vol. 120, no. 24, pp. 11889–11900. Available from: https://doi.org/10.1063/1.1710853. [viewed 2023-09-11].

[230] YOSHIDA, A.; Y. KABURAGI and Y. HISHIYAMA. Full width at half maximum intensity of G band in first order Raman spectrum of carbon material as a parameter for graphitization-a study with pyrolytic carbons. In: *Tanso* [online]. 2006. vol. 2006, no. 221, pp. 2–7. Available from: https://doi.org/10.7209/tanso.2006.2. [viewed 2023-12-06].

[231] ECKMANN, A.; A. FELTEN; A. MISHCHENKO; L. BRITNELL; R. KRUPKE et al. Probing the nature of defects in graphene by Raman spectroscopy. In: *Nano Letters* [online]. 2012. vol. 12, no. 8, pp. 3925–3930. Available from: https://doi.org/10.1021/nl300901a. [viewed 2023-06-23].

[232] TAN, P.H.; Y.M. DENG and Q. ZHAO. Temperature-dependent Raman spectra and anomalous Raman phenomenon of highly oriented pyrolytic graphite. In: *Physical Review B - Condensed Matter and Materials Physics* [online]. 1998. vol. 58, no. 9, pp. 5435–5439. Available from: https://doi.org/10.1103/PhysRevB.58.5435. [viewed 2023-12-05].

[233] FERRARI, A.C.; J.C. MEYER; V. SCARDACI; C. CASIRAGHI; M. LAZZERI et al. Raman spectrum of graphene and graphene layers. In: *Physical Review Letters* [online]. 2006. vol. 97, no. 18, p. 187401. Available from: https://doi.org/10.1103/PhysRevLett.97.187401. [viewed 2023-11-30].

[234] JORIO, A. Raman Spectroscopy in Graphene-Based Systems: Prototypes for Nanoscience and Nanometrology. In: *ISRN Nanotechnology* [online]. 2012. vol. 2012, pp. 1–16. Available from: https://doi.org/10.5402/2012/234216. [viewed 2023-09-14].

[235] WU, J. Bin; M.L. LIN; X. CONG; H.N. LIU and P.H. TAN. Raman spectroscopy of graphene-based materials and its applications in related devices. In: *Chemical Society Reviews* [online]. 2018. vol. 47, no. 5, pp. 1822–1873. Available from: https://doi.org/10.1039/c6cs00915h. [viewed 2022-06-08].

[236] KUZNETSOV, V.L.; S.N. BOKOVA-SIROSH; S.I. MOSEENKOV; A. V. ISHCHENKO; D. V. KRASNIKOV et al. Raman spectra for characterization of defective CVD multi-walled carbon nanotubes. In: *physica status solidi (b)* [online].

2014. vol. 251, no. 12, pp. 2444–2450. Available from: https://doi.org/10.1002/PSSB.201451195. [viewed 2023-08-01].

[237] JIANG, J.; R. PACHTER; A.E. ISLAM; B. MARUYAMA and J.J. BOECKL. Defect-induced Raman spectroscopy in single-layer graphene with boron and nitrogen substitutional defects by theoretical investigation. In: *Chemical Physics Letters* [online]. 2016. vol. 663, pp. 79–83. Available from: https://doi.org/10.1016/j.cplett.2016.09.067. [viewed 2024-01-24].

[238] LÓPEZ-DÍAZ, D.; M. LÓPEZ HOLGADO; J.L. GARCÍA-FIERRO and M.M. VELÁZQUEZ. Evolution of the Raman Spectrum with the Chemical Composition of Graphene Oxide. In: *Journal of Physical Chemistry C* [online]. 2017. vol. 121, no. 37, pp. 20489–20497. Available from: https://doi.org/10.1021/acs.jpcc.7b06236. [viewed 2024-01-18].

[239] SINGH, S.; Z. Bin JUNAID; V. VYAS; T.S. KALYANWAT and S.S. RANA. Identification of vacancy defects in carbon nanotubes using vibration analysis and machine learning. In: *Carbon Trends* [online]. 2021. vol. 5, p. 100091. Available from: https://doi.org/10.1016/j.cartre.2021.100091. [viewed 2024-04-03].

[240] EL-BARBARY, A.; H. TELLING; P. EWELS; I. HEGGIE and R. BRIDDON. Structure and energetics of the vacancy in graphite. In: *Physical Review B - Condensed Matter and Materials Physics* [online]. 2003. vol. 68, no. 14, p. 144107. Available from: https://doi.org/10.1103/PhysRevB.68.144107. [viewed 2024-04-03].

[241] ROY, D.; M. CHHOWALLA; H. WANG; N. SANO; I. ALEXANDROU et al. Characterisation of carbon nano-onions using Raman spectroscopy. In: *Chemical Physics Letters* [online]. 2003. vol. 373, nos. 1–2, pp. 52–56. Available from: https://doi.org/10.1016/S0009-2614(03)00523-2. [viewed 2023-08-01].

[242] VENEZUELA, P.; M. LAZZERI and F. MAURI. Theory of double-resonant Raman spectra in graphene: Intensity and line shape of defect-induced and two-phonon bands. In: *Physical Review B - Condensed Matter and Materials Physics* [online]. 2011. vol. 84, no. 3. Available from: https://doi.org/10.1103/PhysRevB.84.035433. [viewed 2023-11-30].

[243] VAUTARD, F.; S. OZCAN; F. PAULAUSKAS; J.E. SPRUIELL; H. MEYER et al. Influence of the carbon fiber surface microstructure on the surface chemistry generated by a thermo-chemical surface treatment. In: *Applied Surface Science* [online]. 2012. vol. 261, pp. 473–480. Available from: https://doi.org/10.1016/j.apsusc.2012.08.038. [viewed 2023-11-30].

[244] HERZIGER, F.; C. TYBORSKI; O. OCHEDOWSKI; M. SCHLEBERGER and J. MAULTZSCH. Double-resonant la phonon scattering in defective graphene and carbon nanotubes. In: *Physical Review B - Condensed Matter and Materials Physics* [online]. 2014. vol. 90, no. 24, p. 245431. Available from: https://doi.org/10.1103/PhysRevB.90.245431. [viewed 2023-11-02].

[245] LEE, A.Y.; K. YANG; N.D. ANH; C. PARK; S.M. LEE et al. Raman study of D* band in graphene oxide and its correlation with reduction. In: *Applied Surface Science* [online]. 2021. vol. 536, p. 147990. Available from: https://doi.org/10.1016/j.apsusc.2020.147990. [viewed 2023-10-04].

[246] COUZI, M.; J.L. BRUNEEL; D. TALAGA and L. BOKOBZA. A multi wavelength Raman scattering study of defective graphitic carbon materials: The first order Raman spectra revisited. In: *Carbon* [online]. 2016. vol. C, no. 107, pp. 388–394. Available from: https://doi.org/10.1016/J.CARBON.2016.06.017. [viewed 2023-10-17].

[247] SADEZKY, A.; H. MUCKENHUBER; H. GROTHE; R. NIESSNER and U. PÖSCHL. Raman microspectroscopy of soot and related carbonaceous materials:

Spectral analysis and structural information. In: *Carbon* [online]. 2005. vol. 43, no. 8, pp. 1731–1742. Available from: https://doi.org/10.1016/J.CARBON.2005.02.018. [viewed 2023-09-28].

[248] CHOI, Y.C.; K.I. MIN and M.S. JEONG. Novel method of evaluating the purity of multiwall carbon nanotubes using raman spectroscopy. In: *Journal of Nanomaterials* [online]. 2013. vol. 2013. Available from: https://doi.org/10.1155/2013/615915. [viewed 2023-07-14].

[249] FERRARI, A.C. and D.M. BASKO. Raman spectroscopy as a versatile tool for studying the properties of graphene. In: *Nature nanotechnology* [online]. 2013. vol. 8, no. 4, pp. 235–246. Available from: https://doi.org/10.1038/NNANO.2013.46. [viewed 2023-10-02].

[250] BACKES, C.; K.R. PATON; D. HANLON; S. YUAN; M.I. KATSNELSON et al. Spectroscopic metrics allow in situ measurement of mean size and thickness of liquid-exfoliated few-layer graphene nanosheets. In: *Nanoscale* [online]. 2016. vol. 8, no. 7, pp. 4311–4323. Available from: https://doi.org/10.1039/c5nr08047a. [viewed 2023-12-26].

[251] BREUSING, M.; C. ROPERS and T. ELSAESSER. Ultrafast carrier dynamics in graphite. In: *Physical Review Letters* [online]. 2009. vol. 102, no. 8, p. 086809. Available from: https://doi.org/10.1103/PHYSREVLETT.102.086809. [viewed 2023-11-30].

[252] MALIC, E.; T. WINZER; F. WENDLER; S. BREM; R. JAGO et al. Carrier Dynamics in Graphene: Ultrafast Many-Particle Phenomena. In: *Annalen der Physik* [online]. 2017. vol. 529, no. 11, p. 1700038. Available from: https://doi.org/10.1002/andp.201700038. [viewed 2024-01-16].

[253] SONG, J.C.W.; M.Y. REIZER and L.S. LEVITOV. Disorder-assisted electron-phonon scattering and cooling pathways in graphene. In: *Physical Review Letters* [online]. 2012. vol. 109, no. 10, p. 106602. Available from: https://doi.org/10.1103/PHYSREVLETT.109.106602. [viewed 2023-09-15].

[254] BRIDA, D.; A. TOMADIN; C. MANZONI; Y.J. KIM; A. LOMBARDO et al. Ultrafast collinear scattering and carrier multiplication in graphene. In: *Nature Communications* [online]. 2013. vol. 4, no. 1, pp. 1–9. Available from: https://doi.org/10.1038/ncomms2987. [viewed 2023-12-15].

[255] RAJACKAITĖ, E.; D. PECKUS; R. GUDAITIS; M. ANDRULEVIČIUS; T. TAMUIUS et al. Transient absorption spectroscopy as a promising optical tool for the quality evaluation of graphene layers deposited by microwave plasma. In: *Surface and Coatings Technology* [online]. 2020. vol. 395, p. 125887. Available from: https://doi.org/10.1016/j.surfcoat.2020.125887. [viewed 2022-09-12].

[256] HUANG, K.C.; J. MCCALL; P. WANG; C.S. LIAO; G. EAKINS et al. High-Speed Spectroscopic Transient Absorption Imaging of Defects in Graphene. In: *Nano Letters* [online]. 2018. vol. 18, no. 2, pp. 1489–1497. Available from: https://doi.org/10.1021/ACS.NANOLETT.7B05283. [viewed 2023-07-07].

[257] SINNOKROT, M.O.; E.F. VALEEV and C.D. SHERRILL. Estimates of the ab initio limit for π-π interactions: The benzene dimer. In: *Journal of the American Chemical Society* [online]. 2002. vol. 124, no. 36, pp. 10887–10893. Available from: https://doi.org/10.1021/JA025896H. [viewed 2025-11-04].

[258] JUODĖNAS, M.; D. PECKUS; T. TAMULEVIČIUS; Y. YAMAUCHI; S. TAMULEVIČIUS et al. Effect of Ag Nanocube Optomechanical Modes on Plasmonic Surface Lattice Resonances. In: *ACS Photonics* [online]. 2020. vol. 7, no. 11,

pp. 3130–3140. Available from: https://doi.org/10.1021/ACSPHOTONICS.0C01187. [viewed 2024-08-19].

[259] AGARWAL, N.R.; A. LUCOTTI; M. TOMMASINI; F. NERI; S. TRUSSO et al. SERS detection and DFT calculation of 2-naphthalene thiol adsorbed on Ag and Au probes. In: *Sensors and Actuators B: Chemical* [online]. 2016. vol. 237, pp. 545–555. Available from: https://doi.org/10.1016/J.SNB.2016.06.143. [viewed 2024-11-05].

[260] SON, J.; G.H. KIM; Y. LEE; C. LEE; S. CHA et al. Toward Quantitative Surface-Enhanced Raman Scattering with Plasmonic Nanoparticles: Multiscale View on Heterogeneities in Particle Morphology, Surface Modification, Interface, and Analytical Protocols. In: *Journal of the American Chemical Society* [online]. 2022. vol. 144, no. 49, pp. 22337–22351. Available from: https://doi.org/10.1021/JACS.2C05950. [viewed 2025-02-18].

[261] OSVÁTH, Z.; A. PÁLINKÁS; G. PISZTER and G. MOLNÁR. Synthesis and Characterization of Graphene–Silver Nanoparticle Hybrid Materials. In: *Materials 2020, Vol. 13, Page 4660* [online]. 2020. vol. 13, no. 20, p. 4660. Available from: https://doi.org/10.3390/MA13204660. [viewed 2023-04-13].

[262] ARSHAD, F.; F. NABI; S. IQBAL and R.H. KHAN. Applications of graphene-based electrochemical and optical biosensors in early detection of cancer biomarkers. In: *Colloids and Surfaces B: Biointerfaces* [online]. 2022. vol. 212, p. 112356. Available from: https://doi.org/10.1016/J.COLSURFB.2022.112356. [viewed 2025-02-02].

[263] KARTON, A. π–π interactions between benzene and graphene by means of large-scale DFT-D4 calculations. In: *Chemical Physics* [online]. 2022. vol. 561, p. 111606. Available from: https://doi.org/10.1016/J.CHEMPHYS.2022.111606. [viewed 2024-12-07].

[264] LECHNER, C. and A.F. SAX. Adhesive forces between aromatic molecules and graphene. In: *Journal of Physical Chemistry C* [online]. 2014. vol. 118, no. 36, pp. 20970–20981. Available from: https://doi.org/10.1021/jp505894p. [viewed 2024-12-07].

[265] CHAKRADHAR, A.; N. SIVAPRAGASAM; M.T. NAYAKASINGHE and U. BURGHAUS. Adsorption kinetics of benzene on graphene: An ultrahigh vacuum study. In: *Journal of Vacuum Science & Technology A: Vacuum, Surfaces, and Films* [online]. 2016. vol. 34, no. 2. Available from: https://doi.org/10.1116/1.4936337/246171. [viewed 2025-02-03].

[266] YAGHOBIAN, F.; T. KORN and C. SCHÜLLER. Frequency Shift in Graphene-Enhanced Raman Signal of Molecules. In: *ChemPhysChem* [online]. 2012. vol. 13, no. 18, pp. 4271–4275. Available from: https://doi.org/10.1002/CPHC.201200642. [viewed 2025-03-23].

CURRICULUM VITAE AND DESCRIPTION OF CREATIVE ACTIVITIES

Marjan Monshi
Ph.D. in Physics | Materials Researcher & Open Science Advocate
Kaunas, Lithuania | www.linkedin.com/in/marjan-monshi
|marjan.monshi@ktu.lt | ORCID: 0000-0002-6655-1935

Professional Summary

Physics Ph.D. specializing in the synthesis of 2D materials (PECVD graphene) and the design of hybrid metal-graphene SERS platform for sensing application. Strong expertise in advanced spectroscopic quality assessment, paired with a commitment to advancing Open Science, FAIR data management, and sustainable manufacturing practices.

Education

Ph.D. in Physics | Kaunas University of Technology, Lithuania | ***2020 – 2025***

- **Focus:** Design, synthesis, and multi-spectroscopic quality assessment of hybrid metal-graphene SERS substrates for stable analyte detection.

MSc in Materials Engineering: Ceramics | Azad University, Isfahan, Iran | *2012 – 2015*

BSc in Materials Engineering: Ceramics | Azad University, Isfahan, Iran | *2008 – 2012*

Professional and Academic Experience

Research Data Manager, *Research Information Services, Library, Kaunas University of Technology, Lithuania | Aug 2024 – Present*

- **Focus:** Empowering early-career researchers through the promotion of Open Science initiatives and data management support.

Contract Materials Researcher, *Invisible Loudspeaker Company (UAB), Lithuania | Jun 2022 – Present*

- **Focus:** Conducting mechanical testing and structural characterization on material samples to guide product development. Leading sustainability research to transition the company toward eco-friendly, green manufacturing processes.

Doctoral Researcher, *Kaunas University of Technology, Lithuania | 2020 – 2025*

- **Focus:** Synthesized graphene-based material via plasma-enhanced chemical vapor deposition (PECVD). Developed and optimized hybrid metal-graphene plasmonic structures for surface-enhanced Raman spectroscopy (SERS), validating substrate quality through comprehensive multi-spectroscopic analysis for stable optical sensing application.

Public Relations Committee Member, *Doctoral Student Society, Kaunas University of Technology, Lithuania | Sep 2022 – 2024*

- **Focus:** Coordinated strategic outreach, event promotion, and science communication campaigns to enhance community engagement and interdisciplinary networking among doctoral candidates.

Technical Expertise

- **Nanomaterial Synthesis & Fabrication:** PECVD graphene synthesis, graphene transfer techniques (wet/dry), magnetron sputtering (PVD), capillary-assisted particle assembly (CAPA), SERS substrate design.
- **Spectroscopy & Optoelectronics:** Raman spectroscopy (quality assessment & analyte detection), transient absorption spectroscopy (TAS), UV-Vis-nIR spectroscopy, x-ray photoelectron spectroscopy (XPS), spectroscopic ellipsometry.
- **Structural Characterization:** scanning electron microscopy (SEM/EDS), atomic force microscopy (AFM), x-ray diffraction (XRD), mechanical testing.
- **Data Analysis & Computational Skills:** principal component analysis (PCA), multivariate statistical correlation, MATLAB, OriginPro, Gwyddion.
- **Research & Data Management:** open science advocacy, FAIR data principles, reproducibility practices, scientific communication

Honors and Awards

- **Finalist, "Tyrėjų Grand Prix" (Researchers' Grand Prix)** | Science Popularization Competition, Vilnius | *2024*
- **Scholarship for the Most Active Ph.D. Student** | Department of Physics, KTU | *2023*
- **Best Presentation Award** | Ph.D. Days, Doctoral Student Society, KTU | *2021, 2022*
- **Doctoral Scholarship** | Government of the Republic of Lithuania | *2020 – 2024*.

LIST OF SCIENTIFIC PAPERS AND SCIENTIFIC CONFERENCES

Publications related to the topic of the dissertation

1. **MONSHI, M.**; M. MOUSSAVI; N. KHINEVICH; T. TAMULEVIČIUS; A. TAMULEVIČIENĖ; J. HENZIE; M. JUODĖNAS and S. TAMULEVIČIUS. Graphene-Enhanced Resonant Arrays of Silver Nanoparticles for Sustained Detection of Raman Signature. *The Journal of Physical Chemistry C*, 129, 2025, 33, 14983-14992.
2. **MONSHI, M.**; M. MOUSSAVI; D. PECKUS; E. RAJACKAITĖ; A. VASILIAUSKAS; M. ANDRULEVIČIUS; T. TAMULEVIČIUS and S. TAMULEVIČIUS. Correlation study of graphitic shell encapsulated nickel: A multi-spectroscopic approach. *Carbon*, 232, 2025, 119704.
3. PECKUS, D.; R. GUDAITIS; E. RAJACKAITĖ; **M. MONSHI**; Š. MEŠKINIS and S. TAMULEVIČIUS. The quality studies of vertical graphene nanosheets catalyst-free microwave plasma-enhanced chemical vapor deposited on glass and fused silica. *Physica B: Condensed Matter*, 662, 2023, 414957.

Conferences (poster and presentation)

1. **MONSHI, M**. and S. TAMULEVICIUS. Simple and low-cost Ni particles assembly as catalyst in carbon nanotube production using plasma enhanced chemical vapor deposition. In: *Advanced materials and technologies: book of abstracts of 24th international Conference-School, 22-26 August 2022, Palanga, Lithuania*. Kaunas: Kaunas University of Technology, 2022, A-P27, pp. 63–63. ISSN 2669-1930.
2. **MONSHI, M.**; A. VASILIAUSKAS; E. RAJACKAITĖ and S. TAMULEVIČIUS. Ni thin films as a catalyst in graphene growth by plasma-enhanced CVD. In*: Advanced materials and technologies: book of abstracts of 23rd international Conference-School, 23-27 August 2021, Palanga, Lithuania*. Kaunas: Kaunas University of Technology, 2021, B-P36, pp. 66–66. ISSN 2669-1930.
3. TAMULEVIČIUS, T.; K. MIDVERIS; G. KLYVIS; T. KLINAVIČIUS; **M. MONSHI**; M. MOUSSAVI; A. TAMULEVIČIENĖ; M. JUODĖNAS; D. PECKUS; J. HENZIE and S. TAMULEVIČIUS. Self-assembled plasmonic lattices and their applications. In: *Molecular Plasmonic 2025, 15-17 May 2025, Leibniz IPHT, Jena, Germany*. Jena: Leibniz Institute of Photonic Technology, 2025, pp. 15–15.
4. MOUSSAVI, M.; **M. MONSHI**; G. KLYVIS and S. TAMULEVIČIUS. Enhanced detection of lithium battery electrolyte vapors using graphene protected SERS substrate with silver nano particles. In: *Joint international conference "Functional materials and nanotechnologies + Nanotechnology and innovation in the Baltic Sea region ", FM&NT–NIBS 2024, Tartu, Estonia, 6-9 October 2024*. Tartu: Estonian Physical Society, 2024, P14, pp. 1–1.
5. **MONSHI, M.**; M. MOUSSAVI; D. PECKUS and S. TAMULEVIČIUS. Transient absorption spectroscopy quality study of graphene grown on a seeding layer of Ni. In: *E-MRS Spring meeting 2023: 40th anniversary: May 29 - June 2, 2023,*

Strasbourg, France. Strasbourg: European materials research society, 2023, 01127, pp. 1–1.

6. **MONSHI, M.** and S. TAMULEVIČIUS. Experimental observation of important parameters in local density of particles in contact line of capillary assembly process. In: *Chemistry and Chemical Technology: proceedings of international scientific conference, Kaunas, 2022*. Kaunas: Kaunas University of technology, 2022, pp. 146–146. ISSN 2538-7359.
7. **MONSHI, M.** Investigating graphene growth by plasma-enhanced CVD using various catalyst thicknesses. In: *Graphene 2021: Graphene and 2DM international conference, November 2-5, 2021*, *virtual.* [S.l.]: [s.n], 2021, ePoster 67, pp. 67–69.
8. **MONSHI, M.**; M. MOUSSAVI; N. KHINEVICH; T. TAMULEVIČIUS; A. TAMULEVIČIENĖ; J. HENZIE; M. JUODĖNAS and S. TAMULEVIČIUS. Graphene-Enhanced Plasmonic Arrays for Long-Term, Stable SERS Detection. In: *8th International Conference "Nanotechnology and Innovation in the Baltic Sea Region" (NIBS 2025), October 20–22, 2025 at Plön Castle, Germany*. [S.l.]: [s.n.], 2025.
9. **MONSHI, M.** Multispectroscopic Approach to Graphite-Encapsulated Metal Nanoparticles. Presented at: *European Doctorate in Physics and Chemistry of Advanced Materials (PCAM) Network Seminar*, 2025-01-16.

Internships and Schools

1. **Research Internship (PCAM Network)**: NanoSYD Research Center, Mads Clausen Institute, University of Southern Denmark (SDU), Sønderborg, Denmark. (February 2025).
2. **The Extreme Light Infrastructure (ELISS) Summer School:** Focused on laser-based research and applications. Szeged, Hungary. (September 2024).
3. **Micro and Nano Sensors Summer School:** Organized by the Technical University of Denmark (DTU). (August 2023).

ACKNOWLEDGEMENT

Reaching the completion of this doctoral journey is an achievement I owe to the unwavering support, guidance, and collaboration of many individuals and institutions. I am profoundly grateful to have endured through the complexities and challenges along the way, even when the path felt overwhelming.

Academic Guidance and Granting

My deepest gratitude is reserved for my research supervisor, Prof. Dr. Hab. Sigitas Tamulevičius. Thank you for granting me the opportunity to conduct this research at Kaunas University of Technology, for your comprehensive vision, invaluable scientific mentorship, and the constant professional trust you placed, particularly through periods of uncertainty.

Scientific Collaboration and Technical Support

I extend my sincere gratitude to all the colleagues at the Institute of Materials Science, Kaunas University of Technology, for creating a supportive and collaborative environment. I am as well thankful to my co-authors for their wonderful contributions, which were invaluable to my work. I am deeply grateful for being a part of the PCAM European Doctorate Network. My experience at the Mads Clausen Institute, University of Southern Denmark, under the supervision of Prof. Günter Rubahn and Dr. Fiutowski, proved to be a pivotal and enriching aspect of my doctoral studies.

My profound thanks are due to the experimental support from the Center for Physical Sciences and Technology, Lithuania, particularly from Prof. Gediminas Niaura and Dr. Martynas Talaikis.

I wish to acknowledge the administrative staff of the Doctoral School at Kaunas University of Technology for their unwavering support from the very beginning of this academic journey.

I am deeply grateful to the members of the Dissertation Defence Board and the reviewers for their valuable time, diligence, and constructive insights, which were instrumental in refining the quality of this dissertation. My thanks as well go to the editorial staff for their assistance in the final preparation of this disseration.

Personal Dedication and Support

On a deeply personal note, this work is infused with the memory of my beloved mother. She was the one who constantly encouraged me to gain new experiences and urged me to step out of my comfort zone to see the world beyond the familiar. My heart has been broken since she left this world at the very beginning of this journey; yet, her belief in my bravery remained the spark that kept me going. I as well carry with me the memory of my grandmothers and grandfather, whom I lost during these years. The love they planted within me will remain forever.

I owe deep gratitude to my father, whose lifelong dedication to science laid the foundation that inspired me to follow in his footsteps. While I was fortunate to benefit from his guidance throughout my earlier education, this doctoral journey was a path I undertook independently; taking a step to stand on my own within the vision he inspired. My heartfelt thanks go to my parents-in-law, whose kindness and unwavering encouragement reminded me that true family is not defined by blood alone. Their presence and support throughout this long academic endeavor have been deeply meaningful.

My final and most profound gratitude goes to my life partner Maziar, who have been my constant guiding mentor through the demanding years of this research and my greatest source of strength in life. There is no doubt that I could not have completed this doctorate without your exceptional support and presence by my side.

APPENDICES

Comprehensive Matrix of Pearson Correlations

The table presented below provides supporting evidence for the Case Study II and includes complete dataset of the multi-spectroscopic correlation. This table lists every relationship investigated between the input factors and the 107 derived spectroscopic metrics. It distinguishes between statistically significant correlations (highlighted) and those found to be negligible, providing the full statistical context for the metric selection process described in the dissertation.

Table S1. Comprehensive matrix of Pearson correlations identified between the input synthesis factors and spectroscopic metrics; this table includes inter-metric correlations across Raman, UV-Vis-nIR, and TAS techniques; significant correlations (two-tailed test, $p < 0.05$) are highlighted; the metrics explicitly selected for the quality evaluation framework in the main text are bolded and bordered

			Transient Absorption Spectroscopy						UV-Vis-nIR Spectroscopy						
	Thickness	Duration	τ_1	τ_2	$A_1 + A_2$	A_1	A_2	$\frac{A_2}{(A_1 + A_2)}$	λ_{max}	Abs_{UV}	Abs_{Vis}	Abs_{IR}	Abs(UV − IR)	Abs(Vis − IR)	Abs(Vis:UV)
Thickness	-	6 %	10%	65%	-2%	5 %	-75%	-77%	37%	66%	73%	82%	52%	61%	34%
Duration	6 %	-	-35%	43%	36%	38%	-6%	-46%	23%	-38%	-22%	-2%	-53%	-35%	71%
τ_1	10%	-35%	-	1 %	-18%	-16%	-33%	1 %	-19%	1 %	-5%	7 %	-3%	-14%	3 %
τ_2	65%	43%	1 %	-	19%	24%	-51%	-64%	22%	18%	21%	38%	6 %	7 %	29%
$A_1 + A_2$	-2%	36%	-18%	19%	-	-	48%	-44%	47%	-43%	-31%	-20%	-50%	-37%	45%
A_1	5 %	38%	-16%	24%	-	-	41%	-51%	51%	-39%	-27%	-14%	-48%	-34%	48%
A_2	-75%	-6%	-33%	-51%	48%	41%	-	49%	-14%	-61%	-62%	-71%	-51%	-50%	-20%
$A_2/(A_1 + A_2$	-77%	-46%	1 %	-64%	-44%	-51%	49%	-	-39%	-27%	-42%	-61%	-7%	-26%	-70%
λ_{max}	37%	23%	-19%	22%	47%	51%	-14%	-39%	-	9 %	19%	25%	0 %	12%	38%
Abs_{UV}	66%	-38%	1 %	18%	-43%	-39%	-61%	-27%	9 %	-	97%	88%	97%	97%	-14%
Abs_{Vis}	73%	-22%	-5%	21%	-31%	-27%	-62%	-42%	19%	97%	-	95%	89%	97%	9 %
Abs_{IR}	82%	-2%	7 %	38%	-20%	-14%	-71%	-61%	25%	88%	95%	-	74%	84%	34%
Abs(UV	52%	-53%	-3%	6 %	-50%	-48%	-51%	-7%	0 %	97%	89%	74%	-	94%	-36%
Abs(Vis	61%	-35%	-14%	7 %	-37%	-34%	-50%	-26%	12%	97%	97%	84%	94%	-	-11%
Abs(UV:IR)	-43%	-68%	-8%	-39%	-41%	-46%	35%	77%	-43%	1 %	-19%	-45%	24%	3 %	-97%
Abs(Vis:IR)	-12%	-56%	-37%	-34%	-39%	-42%	20%	48%	-23%	34%	24%	-7%	51%	46%	-73%
Abs(Vis:UV)	34%	71%	3 %	29%	45%	48%	-20%	-70%	38%	-14%	9 %	34%	-36%	-11%	-
A(T:Q)	-11%	38%	1 %	-3%	38%	39%	5 %	-20%	52%	-37%	-24%	-20%	-43%	-25%	38%
W(D_1'')	-47%	-27%	25%	-13%	-13%	-16%	22%	56%	-9%	-36%	-48%	-58%	-22%	-37%	-47%
A(D_1'':T)	50%	-42%	48%	28%	-11%	-7%	-41%	-25%	-1%	46%	38%	44%	43%	30%	-9%
A(D_1'':Q)	43%	-26%	50%	29%	10%	14%	-36%	-32%	25%	20%	18%	26%	16%	10%	5 %
I(D_1'':Q)	29%	20%	-7%	19%	26%	28%	-20%	-40%	61%	27%	40%	44%	16%	34%	39%
A(D_1'':G)	34%	-46%	57%	21%	-12%	-10%	-33%	-9%	-5%	24%	13%	19%	25%	8 %	-19%
I(D_1'':G)	27%	-41%	5 %	0 %	-42%	-40%	-33%	7 %	5 %	80%	74%	66%	80%	75%	-19%
I(D_1'':D)	55%	-34%	14%	18%	-28%	-24%	-47%	-28%	0 %	88%	86%	85%	82%	81%	0 %

	Thickness	Duration	Transient Absorption Spectroscopy						UV-Vis-nIR Spectroscopy						
			τ_1	τ_2	$A_1 + A_2$	A_1	A_2	$\frac{A_2}{(A_1 + A_2)}$	$\lambda_{\max}$	$\mathrm{Abs}_{\mathrm{UV}}$	$\mathrm{Abs}_{\mathrm{Vis}}$	$\mathrm{Abs}_{\mathrm{IR}}$	Abs(UV − IR)	Abs(Vis − IR)	Abs(Vis:UV)
$\mathrm{A}(\mathrm{D}_1'':\mathrm{D}_2'')$	59%	-24%	36%	44%	-1%	3 %	-43%	-42%	0 %	51%	47%	57%	44%	36%	6 %
$\mathrm{I}(\mathrm{D}_1'':\mathrm{D}_2'')$	54%	3 %	-5%	37%	4 %	7 %	-32%	-47%	10%	66%	70%	78%	54%	59%	27%
$\mathrm{W}(\mathrm{D}_2'')$	-40%	44%	-48%	-6%	58%	55%	52%	-3%	20%	-60%	-55%	-54%	-58%	-52%	8 %
$\mathrm{A}(\mathrm{D}_2'':\mathrm{T})$	-49%	-39%	30%	-54%	-26%	-29%	19%	61%	-10%	-31%	-41%	-55%	-17%	-28%	-42%
$\mathrm{A}(\mathrm{D}_2'':\mathrm{Q})$	-28%	9 %	19%	-29%	16%	16%	10%	11%	33%	-41%	-34%	-37%	-39%	-30%	12%
$\mathrm{I}(\mathrm{D}_2'':\mathrm{Q})$	-27%	6 %	23%	-29%	12%	12%	8 %	12%	32%	-38%	-32%	-35%	-36%	-27%	11%
$\mathrm{A}(\mathrm{D}_2'':\mathrm{G})$	-54%	-25%	27%	-42%	-16%	-20%	27%	58%	-16%	-50%	-59%	-69%	-36%	-46%	-38%
$\mathrm{I}(\mathrm{D}_2'':\mathrm{G})$	-52%	-38%	28%	-42%	-34%	-37%	20%	69%	-23%	-33%	-45%	-60%	-17%	-31%	-53%
$\mathrm{I}(\mathrm{D}_2'':\mathrm{D})$	-17%	-69%	49%	-41%	-54%	-55%	-15%	53%	-16%	18%	4 %	-11%	31%	15%	-52%
$\mathrm{A}(\mathrm{D}_{1+2}'':\mathrm{T})$	-14%	-64%	59%	-33%	-32%	-32%	-8%	42%	-10%	0 %	-15%	-23%	11%	-7%	-45%
$\mathrm{A}(\mathrm{D}_{1+2}'':\mathrm{Q})$	-11%	-1%	36%	-16%	18%	19%	-3%	-1%	40%	-30%	-25%	-25%	-31%	-24%	13%
$\mathrm{A}(\mathrm{D}_{1+2}'':\mathrm{G})$	-40%	-40%	45%	-33%	-20%	-22%	14%	52%	-17%	-39%	-51%	-59%	-26%	-41%	-42%
C(D)	42%	32%	-51%	42%	-5%	-3%	-22%	-40%	-11%	44%	49%	51%	37%	45%	13%
W(D)	20%	-70%	42%	-9%	-56%	-55%	-41%	21%	-19%	63%	49%	37%	71%	55%	-47%
A(D:T)	-20%	73%	-71%	11%	50%	49%	39%	-18%	27%	-41%	-29%	-25%	-46%	-30%	33%
A(D:Q)	-13%	48%	-14%	-2%	42%	43%	11%	-21%	53%	-39%	-24%	-20%	-45%	-25%	41%
I(D:Q)	-22%	57%	-19%	-4%	49%	49%	21%	-19%	48%	-54%	-38%	-32%	-60%	-40%	45%
A(D:G)	-57%	27%	-16%	-17%	18%	15%	46%	35%	-8%	-81%	-81%	-85%	-72%	-72%	-13%
I(D:G)	-63%	24%	-23%	-20%	9 %	5 %	49%	46%	-17%	-75%	-78%	-85%	-64%	-67%	-24%
$\mathrm{W}(\mathrm{D}_1^\star)$	23%	-49%	69%	-20%	-32%	-29%	-42%	-2%	-2%	48%	44%	44%	46%	40%	-2%
$\mathrm{A}(\mathrm{D}_1^\star:\mathrm{T})$	30%	-66%	35%	-14%	-57%	-55%	-43%	13%	-14%	83%	71%	61%	86%	74%	-35%
$\mathrm{A}(\mathrm{D}_1^\star:\mathrm{Q})$	18%	-44%	38%	-10%	-29%	-27%	-35%	7 %	27%	50%	46%	39%	51%	48%	-18%
$\mathrm{I}(\mathrm{D}_1^\star:\mathrm{Q})$	7 %	-31%	0 %	-14%	-20%	-19%	-17%	12%	36%	40%	40%	27%	43%	47%	-21%
$\mathrm{A}(\mathrm{D}_1^\star:\mathrm{G})$	8 %	-74%	45%	-28%	-64%	-63%	-34%	37%	-15%	64%	49%	36%	71%	55%	-48%
$\mathrm{I}(\mathrm{D}_1^\star:\mathrm{G})$	-11%	-76%	15%	-37%	-71%	-73%	-14%	61%	-23%	54%	36%	14%	69%	51%	-73%
$\mathrm{I}(\mathrm{D}_1^\star:\mathrm{D})$	30%	-69%	17%	-13%	-60%	-59%	-39%	17%	-17%	86%	74%	60%	92%	80%	-45%
$\mathrm{A}(\mathrm{D}_1^\star:\mathrm{D}_2^\star)$	10%	-74%	43%	-27%	-68%	-67%	-34%	37%	-24%	65%	51%	38%	73%	57%	-49%
$\mathrm{I}(\mathrm{D}_1^\star:\mathrm{D}_2^\star)$	10%	-73%	19%	-25%	-69%	-70%	-27%	41%	-25%	72%	58%	41%	82%	66%	-58%
$\mathrm{W}(\mathrm{D}_2^\star)$	40%	-40%	46%	2 %	-23%	-19%	-49%	-20%	12%	73%	69%	71%	67%	62%	5 %
$\mathrm{A}(\mathrm{D}_2^\star:\mathrm{T})$	45%	-38%	16%	0 %	-16%	-13%	-41%	-27%	17%	84%	82%	80%	78%	79%	4 %
$\mathrm{A}(\mathrm{D}_2^\star:\mathrm{Q})$	15%	13%	8 %	0 %	29%	32%	-16%	-32%	64%	10%	21%	24%	2 %	18%	35%
$\mathrm{I}(\mathrm{D}_2^\star:\mathrm{Q})$	1 %	29%	-12%	-4%	36%	38%	1 %	-26%	61%	-14%	1 %	1 %	-20%	0 %	35%
$\mathrm{A}(\mathrm{D}_2^\star:\mathrm{G})$	3 %	-54%	40%	-32%	-24%	-22%	-26%	14%	21%	44%	38%	29%	48%	41%	-18%
$\mathrm{I}(\mathrm{D}_2^\star:\mathrm{G})$	-51%	-43%	-14%	-47%	-37%	-41%	25%	68%	-17%	-11%	-24%	-49%	9 %	-3%	-71%
$\mathrm{I}(\mathrm{D}_2^\star:\mathrm{D})$	47%	-57%	15%	-1%	-39%	-36%	-46%	-13%	-1%	90%	84%	74%	90%	86%	-24%
$\mathrm{A}(\mathrm{D}_{1+2}^\star:\mathrm{T})$	40%	-53%	26%	-7%	-37%	-34%	-44%	-8%	3 %	87%	80%	74%	85%	80%	-15%
$\mathrm{A}(\mathrm{D}_{1+2}^\star:\mathrm{Q})$	17%	-6%	20%	-4%	11%	14%	-24%	-21%	56%	25%	32%	31%	20%	30%	19%
$\mathrm{A}(\mathrm{D}_{1+2}^\star:\mathrm{G})$	6 %	-69%	45%	-31%	-49%	-48%	-32%	29%	0 %	59%	47%	35%	65%	52%	-37%
W(G)	-23%	-60%	-3%	-28%	-70%	-72%	-8%	63%	-36%	41%	22%	-4%	59%	40%	-84%
A(G:T)	57%	-7%	-5%	24%	-4%	-1%	-37%	-45%	9 %	76%	79%	83%	65%	70%	21%
A(G:Q)	16%	38%	-6%	13%	41%	43%	-10%	-42%	64%	-5%	11%	17%	-16%	5 %	48%
I(G:Q)	19%	46%	-2%	16%	51%	54%	-9%	-51%	66%	-13%	5 %	17%	-27%	-4%	62%
I(G:D)	64%	-24%	21%	25%	-14%	-10%	-50%	-45%	3 %	80%	81%	86%	70%	72%	16%

	Thickness	Duration	Transient Absorption Spectroscopy						UV-Vis-nIR Spectroscopy						
			τ_1	τ_2	$A_1 + A_2$	A_1	A_2	$\frac{A_2}{(A_1 + A_2)}$	$\lambda_{\max}$	$\mathrm{Abs}_{\mathrm{UV}}$	$\mathrm{Abs}_{\mathrm{Vis}}$	$\mathrm{Abs}_{\mathrm{IR}}$	Abs(UV − IR)	Abs(Vis − IR)	Abs(Vis:UV)
C(D′)	-4%	22%	-22%	12%	-54%	-55%	-10%	29%	-44%	3%	-1%	-3%	5%	1%	-18%
W(D′)	49%	-10%	-35%	22%	-17%	-15%	-32%	-33%	-1%	79%	79%	71%	76%	79%	-7%
A(D′:T)	-53%	3%	8%	-28%	-7%	-10%	29%	47%	-17%	-67%	-71%	-78%	-56%	-61%	-25%
A(D′:Q)	-37%	24%	11%	-22%	16%	15%	18%	14%	16%	-60%	-53%	-54%	-57%	-49%	12%
I(D′:Q)	-37%	20%	20%	-25%	15%	14%	18%	16%	12%	-62%	-56%	-56%	-59%	-53%	12%
A(D′:G)	-52%	-1%	13%	-26%	-5%	-8%	31%	46%	-21%	-67%	-72%	-78%	-55%	-61%	-27%
I(D′:G)	-56%	-12%	19%	-31%	-15%	-19%	30%	57%	-26%	-60%	-68%	-77%	-46%	-56%	-38%
I(D′:D)	-46%	-26%	36%	-34%	-24%	-26%	15%	54%	-20%	-48%	-57%	-64%	-36%	-47%	-35%
C($G^{\star}$)	-26%	8%	20%	13%	11%	11%	5%	14%	10%	-63%	-66%	-63%	-57%	-64%	-15%
W($G^{\star}$)	73%	23%	-22%	43%	7%	12%	-52%	-72%	31%	66%	76%	85%	51%	64%	41%
A($G^{\star}$:T)	79%	36%	-32%	56%	1%	6%	-58%	-69%	36%	61%	71%	80%	46%	58%	42%
A($G^{\star}$:Q)	53%	57%	-33%	45%	31%	36%	-38%	-67%	72%	18%	35%	44%	3%	26%	56%
I($G^{\star}$:Q)	31%	65%	-23%	31%	41%	44%	-23%	-56%	73%	-15%	3%	15%	-29%	-6%	62%
A($G^{\star}$:G)	68%	56%	-42%	60%	8%	13%	-53%	-67%	44%	33%	44%	55%	20%	33%	45%
I($G^{\star}$:G)	30%	46%	-48%	37%	-12%	-10%	-33%	-22%	24%	-4%	-2%	1%	-7%	-4%	9%
I($G^{\star}$:D)	82%	0%	-7%	42%	-25%	-20%	-70%	-55%	18%	78%	81%	87%	67%	71%	21%
I($G^{\star}$: 2D)	65%	37%	-45%	32%	-20%	-15%	-60%	-53%	34%	51%	59%	62%	40%	53%	31%
C(2D)	60%	30%	-48%	39%	8%	12%	-39%	-64%	21%	46%	54%	60%	35%	45%	31%
W(2D)	-60%	-46%	30%	-48%	-31%	-36%	32%	76%	-29%	-28%	-41%	-57%	-11%	-25%	-57%
A(2D:T)	-47%	-24%	25%	-22%	-2%	-6%	43%	61%	-14%	-49%	-57%	-60%	-39%	-52%	-29%
A(2D:Q)	-22%	33%	8%	-8%	37%	37%	15%	-6%	47%	-49%	-38%	-34%	-53%	-38%	32%
I(2D:Q)	7%	59%	-6%	20%	56%	58%	0%	-43%	66%	-40%	-22%	-8%	-52%	-30%	61%
A(2D:G)	-56%	-10%	18%	-24%	0%	-3%	41%	55%	-17%	-69%	-75%	-81%	-57%	-66%	-31%
I(2D:G)	-30%	15%	-14%	11%	3%	1%	23%	31%	-7%	-59%	-65%	-66%	-50%	-60%	-25%
A(2D:D)	-22%	-56%	55%	-22%	-31%	-33%	8%	53%	-25%	-10%	-23%	-28%	0%	-18%	-39%
I(2D:D)	70%	-25%	21%	38%	-20%	-16%	-57%	-42%	3%	74%	72%	78%	65%	61%	10%
C(D+D′)	-42%	31%	-31%	-17%	-2%	-5%	33%	26%	-31%	-57%	-56%	-60%	-51%	-50%	-6%
W(D+D′)	52%	-44%	26%	12%	-40%	-37%	-52%	-25%	-21%	88%	84%	80%	84%	80%	-9%
A(D+D′:T)	6%	-60%	71%	-1%	-33%	-32%	-25%	11%	-43%	6%	-4%	-4%	10%	-4%	-31%
A(D+D′:Q)	-9%	22%	25%	-2%	30%	32%	-3%	-18%	39%	-39%	-28%	-23%	-44%	-30%	31%
I(D+D′:T)	-23%	34%	12%	-8%	39%	39%	16%	-9%	38%	-60%	-49%	-43%	-63%	-50%	32%
A(D+D′:G)	-42%	-25%	40%	-19%	-12%	-14%	19%	41%	-31%	-57%	-64%	-68%	-46%	-57%	-33%
I(D+D′:G)	-57%	-13%	14%	-23%	-6%	-10%	37%	55%	-24%	-67%	-75%	-83%	-53%	-64%	-41%
I(D+D′:D)	-2%	-49%	47%	-8%	-12%	-12%	-5%	16%	-17%	-24%	-31%	-35%	-18%	-26%	-31%
C(2D′)	-51%	12%	-6%	-31%	-12%	-15%	29%	49%	-14%	-64%	-68%	-73%	-55%	-60%	-17%
W(2D′)	62%	-10%	-1%	30%	-9%	-5%	-49%	-55%	4%	81%	85%	88%	70%	76%	21%
A(2D′:T)	-29%	-6%	45%	-8%	1%	1%	0%	3%	-24%	-48%	-47%	-42%	-47%	-48%	7%
A(2D′:Q)	-18%	18%	32%	-6%	22%	23%	-3%	-16%	16%	-45%	-36%	-29%	-49%	-38%	32%
I(2D′:Q)	-31%	14%	35%	-17%	22%	22%	14%	5%	11%	-63%	-57%	-52%	-63%	-56%	19%
I(2D′:G)	-52%	-21%	33%	-25%	-10%	-13%	29%	51%	-30%	-61%	-69%	-75%	-49%	-60%	-35%
I(2D′:D)	-23%	-24%	41%	-18%	-1%	-2%	10%	18%	-23%	-49%	-52%	-53%	-43%	-47%	-13%

UDK 546.26:544.174.5+539.2](043.3)

SL344. 2025-04-21, 18 leidyb. apsk. l. Tiražas 14 egz. Užsakymas 055. Išleido Kauno technologijos universitetas, K. Donelaičio g. 73, 44249 Kaunas Spausdino leidyklos „Technologija“ spaustuvė, Studentų g. 54, 51424 Kaunas